Influences of cell shape in microbial communities

William Peter Joseph Smith

Department of Computer Science

University of Oxford

This thesis is submitted for the degree of

Doctor of Philosophy

Balliol College June 2017

For Rebecca

Declaration

I hereby declare that, except where specific reference is made to the work of others, the contents of this thesis are original and my own work. Where research has been carried out in collaboration with other authors, I indicate this explicitly. This thesis has not been submitted in whole or in part for consideration for any other degree or qualification in this, or any other university.

William Peter Joseph Smith

June 2017

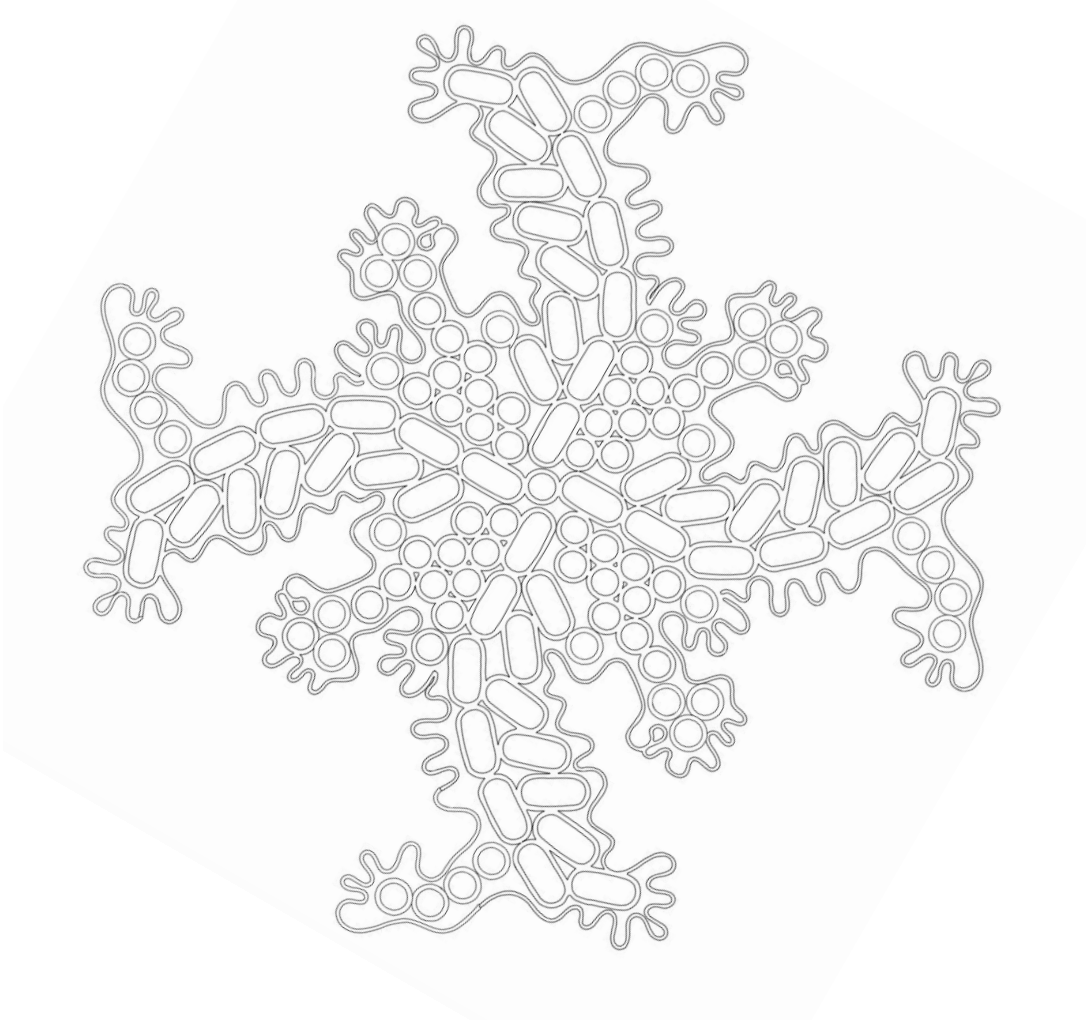

"Divide et impera"

Artwork by Beth McMillan

2016

Acknowledgements

My time at Oxford has been made immeasurably more enjoyable and productive thanks to some truly wonderful people.

I am superlatively grateful to each of my supervisors—James, Joe, Kevin and Yohan—for the support and guidance they have provided throughout my DPhil. Their patience, collective wisdom and generosity of time have kept me hale, happy and reasonably sane (pending further tests). Guys: the phrase "above and beyond" applies in so many ways. Thank you all for indulging me that very first coffee-table meeting on cell shape – who would have guessed that this is where we'd end up? I hope it's been as much fun for you as it has been for me.

I owe a huge debt of thanks to Tim Rudge, Niall Murphy, Jonas Schluter and Wook Kim, for many productive discussions and tech support phone-calls, and for helping me to get set up at the very beginning of my project. As well as the brilliant teaching staff at the Oxford DTC, I would also like to thank Izzy Frost, David Nelson, Helen Byrne, Sara Mitri, Christian Picioreanu, Oskar Hallatschek, Daniel Unterweger, David Kay, Brian Woods, Romain Briandet, Lucas Andrade Meirelles, Carey Nadell, Dianne Newman, Knut Drescher and Nick Trefethen: my work, and my development both as a person and as a researcher, have benefitted enormously from your encouragement and insight. Thank you all.

I am also very thankful to all of my physical chemistry students at Balliol, and particularly to my project student Edmund Wrigley. You guys are unbelievably smart and made me think a lot harder about what it was that I was doing! Outside of my

academic life, I have been supported throughout by friends and family. Thanks to Beth, Ali, Paul, Izzy and Kathryn from the DTC; to Chris, Adam, Matt, Lou, Ollie, Hannah, Andrew, Ol, Nat, Kate and Paul for being there for me when the going got tough. I wish you all natural 20s with every roll you make.

I am indebted to the Engineering and Physical Sciences Research Council (EPSRC, grant EP/G03706X/1), to the DTC, and to the Calleva Research Center, for funding my DPhil research. I am similarly grateful to L'Institut de Mećanique des Fluides de Toulouse (IMFT) for allowing me to use their computing resources, and both to Balliol College and the Computer Science department for their generosity with travel funding. I look forward to continuing to pursue science, thanks to PostDoc funding from Kevin Foster and Laurie Comstock.

Finally, thank you to Rebecca, to whom this thesis is dedicated, for being my bestie.

TL;DR: Thanks, ants. *Thants.*

Abstract

By growing together in dense communities, microorganisms (microbes) have a huge impact on human life. Microbes also come in a wide variety of shapes, but we have yet to understand the importance of these shapes for community biology. How are multi-species communities, such as biofilms and colonies, affected by the morphologies of constituent cells? Which morphologies might these environments select for in turn?

To address these questions, we use individual-based modelling to investigate the effects of cell shape on patterning and evolution within microbial communities. We develop a flexible simulation framework, coupling a continuum model of the biofilm chemical environment to a cellular-level description of biofilm growth mechanics. This modelling system allows competitions between different microbial cell shapes to be simulated and studied, in different community contexts.

Our models predict that cell shape can strongly affect spatial structure and patterning within competitive communities. Rod cells perform better at colonising surfaces and the expanding edges of colonies, while round cells are better at dominating the upper surface of a community. Our predictions are supported by experiments using *Escherichia coli* and *Pseudomonas aeruginosa* bacteria, and demonstrate that particular shapes can confer a selective advantage in communities.

In summary, the work presented in this thesis predicts and examines new mechanisms of self-organisation driven by cell shape, demonstrating a new significance for microbial morphology as a means for cells to succeed in a dense and competitive environment.

Lay summary

The shapes of living organisms are sculpted by the environments in which they live. Around us, we can observe plants and animals whose forms are suited to their function. But what about microscopic life forms – how do their shapes help them to get an edge over their competitors? Currently, we understand that microbes adopt certain shapes in order to achieve certain goals, resulting in a rich catalogue of weird and wonderful forms. However, little is known about the role of cell shape inside microbial communities (dense, slimy mounds of cells attached to a surface), where cells face a fierce struggle for space and nutrients. Understanding how these communities develop is a high priority, not least because unchecked growths can endanger human health.

This thesis involves simulating communities of microbes using computer models, which describe the pushing forces between cells as they grow and divide, as well as their struggle for limited food. Unlike previous models, ours allows different microbial shapes to be pitted against each other in a battle for dominance, helping us to understand the selective advantages that particular cell shapes can confer under different circumstances. Supported by experimental tests, our models show that shape can have unexpected effects on cells' positioning, and, consequently, their survival and reproduction.

Table of contents

List of figures

List of tables

Nomenclature

Roman Symbols

2-D	2-Dimensional
3-D	3-Dimensional
CFU	Colony-forming units
CG	Conjugate Gradient
CPU	Central Processing Unit
CSLM	Confocal Scanning Laser Microscopy
DM	Davis Minimal
DNA	DeoxyriboNucleic Acid
DS	Dynamical Systems
EM	Epifluorescent Microscopy
EPS	Extracellular Polymeric Substance
FEM	Finite Element Method
FISH	Fluorescence In-Situ Hyrbridisation
GFP	Green Fluorescent Protein

GPU	Graphical Processing Unit
HPLC	High-Performance Liquid Chromatography
IbM	Individual-Based Model
LB	Lysogeny Broth
MS	Mass Spectrometry
NMR	Nuclear Magnetic Resonance
ODE	Ordinary Differential Equation
PBS	Phosphate-Buffered Saline
PDE	Partial Differential Equation
qPCR	Quantitative Polymerase Chain Reaction
RDE	Reaction-Diffusion Equation
RFP	Red Fluorescent Protein
RNA	RiboNucleic Acid
RPM	Rotations Per Minute
SEM	Scanning Electron Microscopy
T6SS	Type VI Secretion System

1

Introduction

> "The number of these animalcules in the scurf of a man's teeth are so many that we believe they exceed the number of men in a kingdom."
>
> *Antony van Leeuwenhoek, 1632-1723* [274]

At this very moment, we are surrounded by invisible life-forms, moving and growing unseen. They are inside us, outside us and around us, on our skin and in our mouths [253, 150], and in the air we breathe [39]. They are a fundamental part of us, and yet have lived on this planet far longer than we have [114].

What are these invisible beings? They are microbes: tiny single-celled organisms, too small to see with the naked eye, but visible through the lens of a microscope. Since their discovery by the Dutch scientist Antony Van Leeuwenhoek in the 17th century [274], we have learned that our world teems with microbial life. Microbes rank among the most abundant organisms on Earth [138], and have managed to colonise practically every environment on the planet [176]. Habitats thought too extreme to support life, such as arctic snows and deep sea vents, have been found brimming with microbes [260, 118].

Although they sometimes live alone, microbes are, by and large, gregarious organisms, and are often found living alongside each other in dense communities [169]. This thesis is all about microbial communities, and this introductory chapter is intended as a brief primer on them. Here, we explain what these communities are, and why it is important that we study and understand them. We then provide an overview of rest of the thesis, which begins with a literature review that defines our specific topic of interest: the influence of cell shape in microbial communities.

1.1 What are microbial communities?

We once thought of microbes as being predominantly solitary organisms [281]. The realisation that the majority of microbes actually live in large, surface-attached communities, has transformed the field of microbiology over the past 60 years [114]. Estimated to comprise over 90% of all microbial biomass [228], these aggregates can be found in virtually all natural, industrial and medical ecosystems [65].

Microbial communities can form on virtually any surface with access to moisture [66], and so appear in all sorts of contexts in nature: in aquifers and the soil [70], in lakes and in rivers [102]; on, and even inside, other living organisms, including plants and mammals [240, 253]. Communities are often found playing key roles in all of these different ecosystems [282], and in some cases can grow large enough to see with the naked eye. Figure 1.1 shows some common examples of microbial communities taken from various environments.

A common example of a microbial community is a biofilm, which consists of a large number of microbes attached to a surface, protected by a gel-like layer of cellular secretions known collectively as EPSs (Extracellular Polymeric Substances) [65, 114]. Microbes in a biofilm absorb chemicals that diffuse into the structure from the external environment, using them to create biomass, to grow and to divide. It is believed that

most microbial life on the planet exists in some form of biofilm, making this type of community particularly significant in the study of microbiology.

So, what is it like to live in a microbial community? Communities from many different natural ecosystems display a number of similar characteristics. One such characteristic is spatial heterogeneity, particularly in the chemical species present in the community. High cell densities create intense demand for solutes, resulting in steep chemical gradients – and so the conditions experienced by microbes often vary significantly over small lengthscales [265]. Strong chemical gradients consequently influence community spatial structure—the arrangement of microbes and EPS in space—by

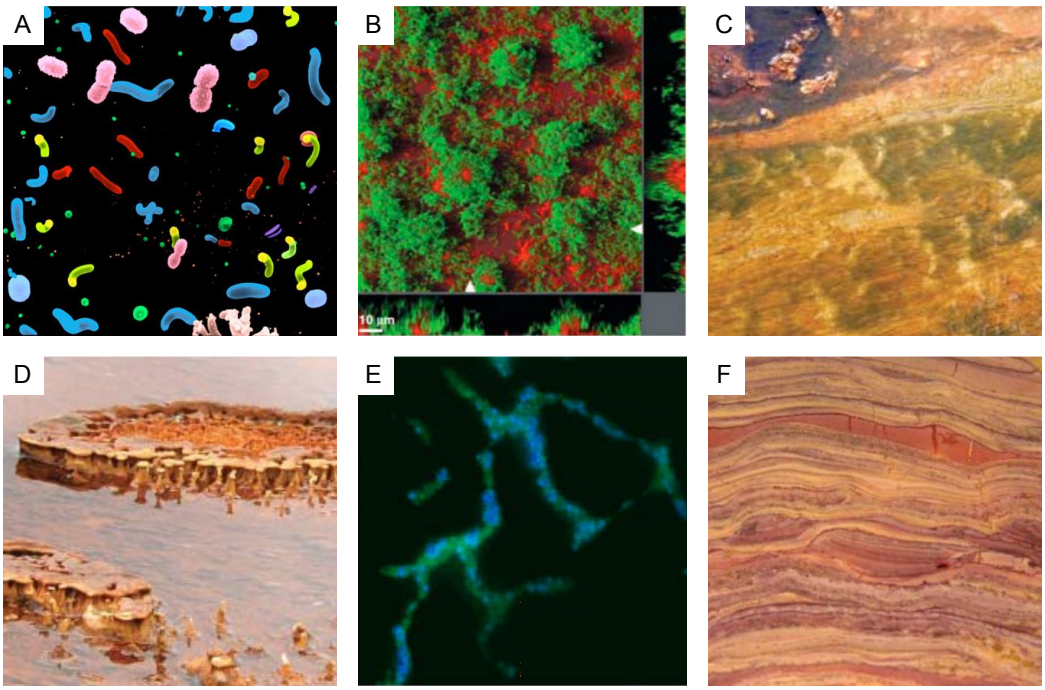

Fig. 1.1 Microbes can live in a low-density planktonic state (A), but more frequently live alongside one another in dense communities (B). Microbial communities occur in various natural contexts: examples include “streamers” in rivers (C) and “mushrooms” in lakes (D). In some cases, community growth may involve a close association with a host organism: (E) shows a community growing on a bean leaf. As well as high cell densities, communities are typified by rich spatial structure, as visible in a 2-billion-year-old stromatolite fossil (F). Images taken with permission from references [139] (A), [191] (B,E,F) and [114] (C,D).

creating instabilities at its growing boundaries [105], and can lead to a loss of diversity through genetic bottlenecking events [151, 191].

A second important characteristic is the potential for strong social interactions. Microbes are social organisms in the sense that they interact, often *via* the secretion of diffusing chemicals [26]. The very high cell densities found in communities allow individual microbes to interact with many neighbours at once [190]. These interactions can facilitate coordinated and synchronised behaviour [160, 294], mediated through communication systems such as quorum sensing [185, 71]. Collectively, microbes can also increase their biological fitness—their capacity to grow and reproduce—by collaborating to produce 'public goods' [281], such as digestive enzymes [213] and scavenger molecules [62].

A third characteristic is strong competition. Microbes growing in communities often have strong metabolic overlap, meaning that they compete for the same limited foodstuffs [169, 63, 190]. This resource competition can in turn drive the development of aggressive strategies, such as toxin secretion [294, 171, 17, 63], and the emergence of 'cheating', where microbes exploit the public goods of rival strains without paying the metabolic costs of their production [199, 226].

Each of these factors—steep chemical gradients, strong social interactions and fierce competition—can be decisive in controlling the composition and development of microbial communities. The complex interplay between physical, chemical and biological processes underlying these behaviours create the potential for a rich variety of emergent phenomena – but also make comprehending and predicting community properties far from trivial [114].

1.2 The importance of microbial communities

1.2.1 Why study microbial communities?

Whether we realise it or not, humans are constantly interacting with microbial communities. Through collective action, they can have profound influences on our lives, with consequences both good and for bad. For example, aggregates of microbes cause a host of problems in industrial settings: blocking pipes [53], impeding shipping vessels [251], and damaging machinery [161]. Losses of energy and resources from nuisance biofilms have been estimated to cost the USA alone over 1 Billion USD per year [279]. In medical contexts, microbial communities have an enormous capacity to aid or threaten human health. For example, biofilms are notorious pathogens, accounting for some 80% of all chronic infections [289]. These films can collect on and degrade implanted devices such as catheters and artificial joints [78], and are a major factor in chronic wounds [25], ear and heart infections [10, 111], tooth decay and gum disease [229], prostatitis [179] and cystic fibrosis [196, 124]. By understanding microbial communities better, therefore, we can develop and improve therapies for treating these illnesses.

In other circumstances, the development of a microbial community can be highly desirable. Many industrial processes involve the deliberate culturing of biofilms, harnessing their ability to degrade harmful chemical species for applications such as water treatment and bioremediation [207]. The formidable metabolic powers possessed by microbes can be used to create useful products such as ethanol or electricity, using bioreactors and microbial fuel cells [75, 230].

Many multicellular organisms also benefit from symbiotic relationships with microbial groups, outsourcing parts of their metabolism to hosted communities [195]. Notable examples include the nitrogen-fixing bacteria that live in the root nodules of leguminous plants [59, 240], and, closer to home, the microbiota that line the mammalian gut

[125, 253]. Humans rely on these biofilms to process nutrients, block infections from pathogens [256] and to train their immune system [19, 243].

Finally, microbial communities serve as an important scientific tool, providing a test-bed with which to probe fundamental questions about the nature of life, such as the evolution of sociality [200, 199, 191, 63]. Because communities comprise the dominant habitat for microorganisms, understanding this particular context of growth is essential for understanding microbes themselves, and the various roles they play in our planet's ecosystems [282].

1.2.2 Methods for studying communities

As a consequence of their importance, microbial communities have received a huge amount of attention from researchers over the past 60 years. Today, a wide range of experimental and theoretical techniques are used to study them at various levels of detail [283]. Some of the methods commonly used are shown on the graph in Figure 1.2, plotted according to the scales and complexity levels for which they provide most insight.

As shown in Figure 1.2 (magenta ellipses), experimental techniques such as proteomics, metabolomics and genomics—collectively known as 'omics'—respectively enable the study of proteins, metabolic intermediates and genomes associated with individual microorganisms [60, 164]. These techniques are supported by a spectrum of analytical tools, such as HPLC (High-Performance Liquid Chromatography), MS (Mass Spectrometry), NMR (Nuclear Magnetic Resonance) spectroscopy, and X-ray crystallography [119, 3].

The realisation of the significance of social interactions between microbes has emphasised the importance of also studying community-level interactions, achieved by examining naturally-occurring communities (*in situ* methods), or by culturing communities on laboratory media (*in vitro*) using agar plates, microfluidic devices and

chemostats [144, 69]. Likewise, 'gnotobiotic' model organisms, such as mice and chickens, are used to study host-associated communities (*in vivo*) [175].

Community-level analyses are increasing facilitated by 'meta-omics' methods, qPCR ([quantitative] Polymerase Chain Reaction) and flow cytometry techniques, which allow high-throughput analysis of genes, proteins and metabolites [306]. The spatial arrangement of microbes in a community can be interrogated using confocal microscopy, and labelling techniques such as FISH (Fluorescence *In Situ* Hybridisation) [23].

Experimental investigations of microbial communities are widely supported by a range of theoretical frameworks and techniques (Figure 1.2, green ellipses) [279, 147]. Computational and mathematical models complement experimental approaches by integrating empirical findings, analysing and parameterising mechanisms underlying processes of interest, and by predicting behaviour in new scenarios. Ideally, experiments and models should work together synergistically – happily, there are

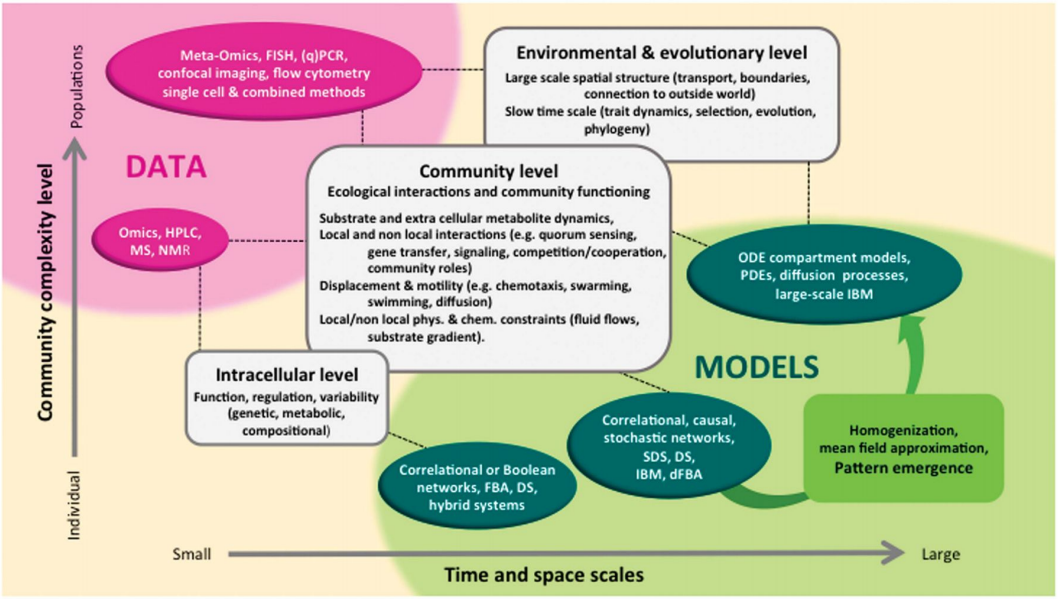

Fig. 1.2 Various methods have been developed to study different phenomena in microbial communities. Here, experimental (magenta) and theoretical (green) methods are sorted according to the spatio-temporal scales and the levels of community complexity they include (horizontal and vertical axes respectively). Diagram reproduced with permission from Reference [283]. Acronyms are defined in the main text, and in the nomenclature section at the front of this thesis.

many examples of successful model-experiment synergy in the field of microbiology (Figure 1.2, white boxes) [283].

For example: on a cellular scale, FBA (Flux-Balance Analysis) and DS (Dynamical Systems) approaches provide mechanistic descriptions of processes inside microbial cells, while correlational and causal network models are used to study interactions between cellular components [148]. Network models are also used to describe ecological interactions between large numbers of species in communities, such as those found in the human gut [44, 68].

On larger scales, analytical ODE (Ordinary Differential Equation) descriptions were among the first models of microbial communities, and aimed to describe substrate kinetics and utilisation in biofilms [235]. Advances in computing allowed the explicit modelling of community spatial structure using CA (Cellular Automaton) and PDE (Partial Differential Equation) approaches, facilitating mechanistic descriptions of community dynamics and structural development [224]. During the drive to predict and understand biofilm structure, the emergence of the IbM (Individual-Based Model) proved hugely influential, providing a more biologically-detailed representation of social interactions between populations of microorganisms in a community [154, 297, 122]. We discuss IbM approaches further in Chapters 2 and 3.

1.3 What this thesis is about

Microbial cells come in many different shapes and sizes. Cells range in shape from simple forms, such as rods and cocci (spheres), to more exotic branched, spiral or filamentous shapes [258, 300, 158]. Scale diagrams of some of the microbial shapes found in nature, shown in Figure 1.3, indicate some of this variation.

Shape is understood to be important for microbes, as particular shapes may help them to survive and thrive in different environments [299–301, 218]. However, we do not yet understand what the effects of cell shape are in microbial communities. This

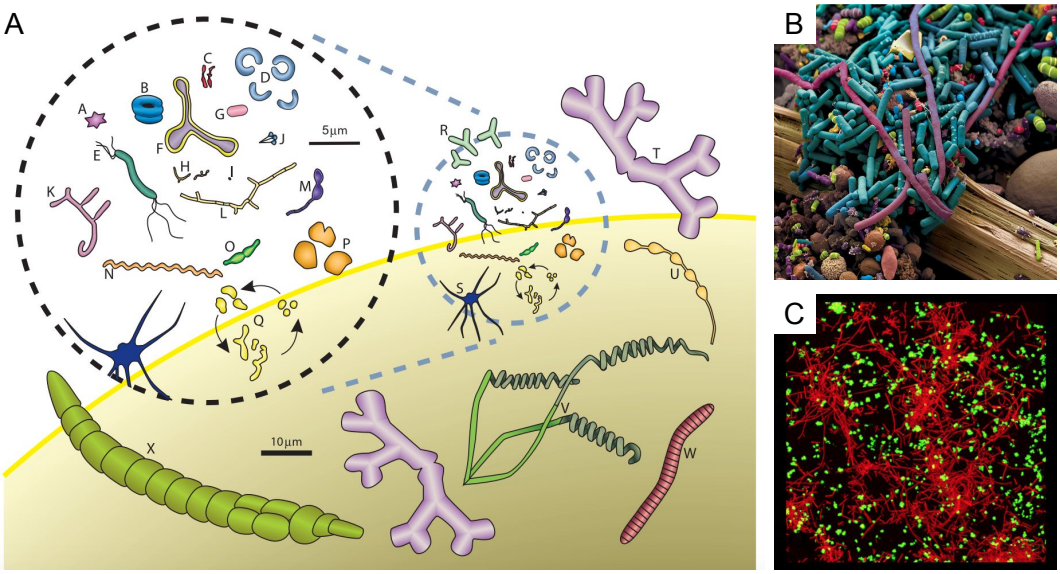

Fig. 1.3 A scaled diagram depicting various microbial species (A) shows the wide range of shapes and sizes adopted. Different shapes frequently grow alongside one another in microbial communities, such as those found in the human intestine (B, false-colour scanning electron micrograph) and in two-species biofilms grown in a laboratory (C, confocal micrograph). Images taken with permission from references [300], [174] and [244] respectively.

constitutes a significant gap in our knowledge, as many microbial communities are known to contain cells of many different shapes [57, 204, 262]. Further, experiments have shown that cell shape can affect spatial patterning and self-organisation in dense groups of microbes, by modulating mechanical interactions between neighbouring cells [157, 276, 238].

The aim of this thesis is to address this ambiguity, and explore what consequences cellular shape might have in the context of a community. To that end, we develop computational models to study the effects of cell shape in microbial communities. We apply these models in different biological contexts in order to explore the consequences and value of cell shape, supporting our findings with experimental data.

Here we give a brief overview of the content of each chapter. The layout of the thesis, summarised in Figure 1.4, is as follows:

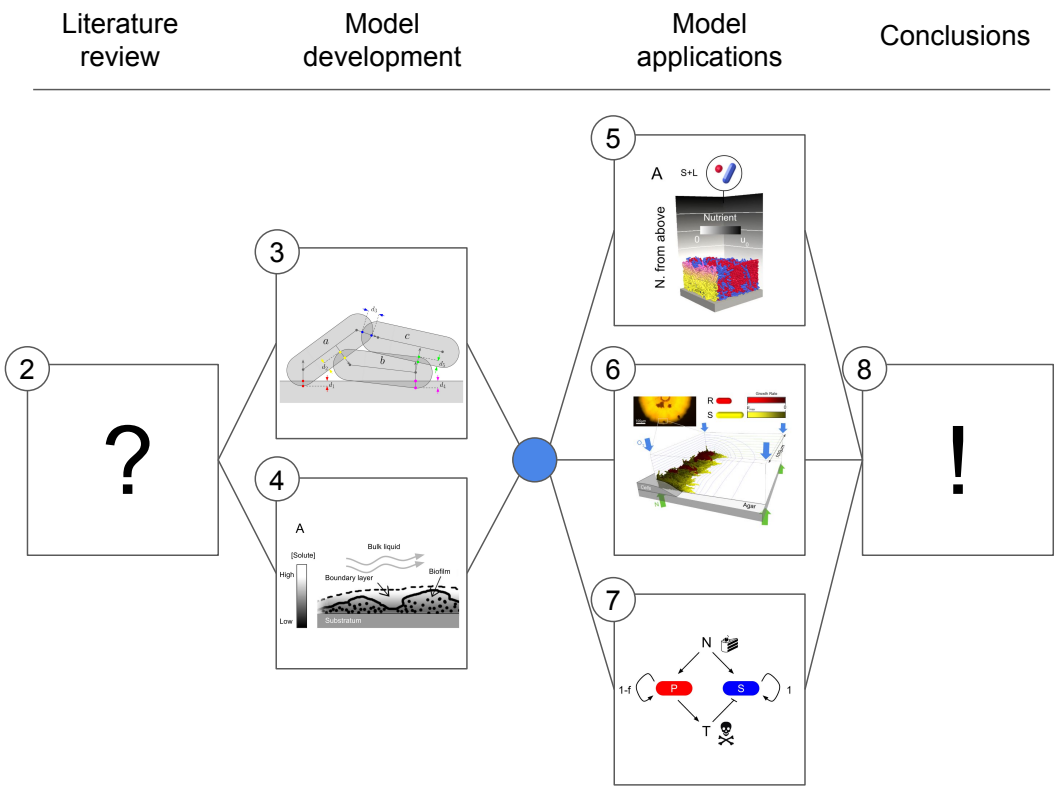

Fig. 1.4 Diagram summarising the layout of this thesis. Subsequent chapters are shown as numbered boxes (2-8), grouped into four stages (columns). First, we review the literature on cell shape in microbial communities (2), and argue for the use of individual-based modelling tools to explore shape effects further. We show how to combine an existing physics engine (3) with a solute modelling system (4) to create a hybrid individual-based model, with which to investigate cell shape (blue circle). We then apply this model in three separate scenarios (5,6,7). Finally, we summarise and discuss our findings, and suggest future directions for research (8).

- **Chapter 2**: Here we provide a detailed literature review summarising what is known about microbial cell shape, and how it might serve to influence community properties. Citing evidence of shape effects, we argue in favour of investigating the role of cell shape in communities such as biofilms. We define specific research questions and examine potential experimental and theoretical methodologies to answer them.

- **Chapter 3**: Individual-based models are an important theoretical tool for studying microbial communities, but until recently have focussed purely on spherical

shapes. In this chapter, we review computational methods for including non-spherical shapes in individual-based models. We select a particular model (the Rudge model), define its underlying assumptions, and give a detailed account of its derivation and parameterisation. We also discuss how the model can be extended to include periodic boundary conditions.

- **Chapter 4**: The Rudge model provides a detailed description of biomechanical interactions in a community, but omits solute transport. In this chapter we show how to model solute transport, and solve the resulting equations using the finite element method. We verify the scheme using convergence tests, and show how to couple the solute and mechanics representations to create a hybrid model like that used in previous studies, but with variable cell shape. This hybrid model framework then forms the basis for the studies presented in Chapters 5, 6 and 7.

- **Chapter 5**: Here, we use the hybrid model to study the properties of communities containing different mixtures of cell shapes. We show that cell shape can strongly affect spatial patterning and strain fitness within biofilms, and characterise a novel mechanism for generating emergent layered biofilm structures. We also validate our model predictions with image analysis of bacterial colonies, grown using differently-shaped strains of *Escherichia coli*.

- **Chapter 6**: In this chapter, we move focus from the bulk of a biofilm to the edge of a microbial colony, using our model to understand an experimental system for studying antibiotic resistance in *Pseudomonas aeruginosa* bacteria. We show that cell elongation (filamentation) in response to antibiotic exposure can provide bacteria with a competitive advantage, again by altering colony spatial structure. Importantly, this patterning occurs *via* a different mechanism to that reported in Chapter 5.

- **Chapter 7**: Here we present a preliminary study, examining the role of shape-driven patterning in controlling social interactions within a community. We extend our model to include aggressive microbial phenotypes, which produce bacteriocins (diffusing toxins) to attack rival cells. We implement, analyse and extend an existing model of toxin secretion, but find that cell shape has only a limited effect on the dynamics of community competition.

- **Chapter 8**: In this final chapter, we provide a synopsis and discussion of our findings, and an evaluation of their impact for microbial community research. We also suggest directions for future work in this field.

2

Literature review: the impact of microbial shape

Abstract

Why study cell shape in microbial communities? The literature review presented in this chapter provides the motivation for the thesis, reviewing our current understanding of cell shape, and summarising evidence for its influences in communities. We argue that cell shape is an important but overlooked factor deserving further analysis, and examine methods that could be used to study its role in the community context. We conclude by defining the research questions of this thesis, and outline our strategy for addressing them.

2.1 Introduction

In the previous chapter, we introduced microbial communities and commented on their importance for science, technology and human health. This chapter builds on that general introduction and goes into specifics. Reviewing and commenting on the scientific literature of the field, we define the 'what', 'why' and 'how' of our studies:

- What is our current understanding of the role of bacterial shape?
- Why might cell shape be important in microbial communities?
- How can we investigate the impact of cell shape in this context?

These are the questions that we answer in Sections 2.2, 2.3 and 2.4 of this chapter. Overall, the purpose of this review is three-fold:

1. To motivate our study into the effects of cell shape;

2. To examine the scientific literature –

   (a) To define what is currently known and unknown about cell shape; and

   (b) To determine suitable methods for its study;

3. To define the research questions that we will address in this thesis.

2.2 What is the role of microbial shape?

In the previous chapter, we discussed the wide variety of morphologies displayed by microbes. Much research has been devoted to the question of how and why microbes have adopted this marvellous catalogue of forms. Although our molecular description of microbial morphogenesis is far from complete [92, 303, 86], studies using simple model organisms—predominantly rod and coccoidal bacteria—are establishing a general consensus [302]. Most bacteria make a cell wall out of peptidoglycan that helps them keep their shape, and morphogenesis is governed through coordinated activity of multiple cytoskeletal complexes acting on this structure [46, 210, 48, 272].

2.2.1 Does microbial shape have a function?

While the 'how' of cell shape is an interesting question in its own right, in this thesis we will be focussing more on the question of 'why' [299, 302]. Why did microbes arrive at this enormous catalogue of diversity? Is it all incidental, or does it have some function? Several pieces of evidence suggest that the shapes we see in microbes are adaptations, serving functions that benefit these organisms in different contexts. Here we review the evidence supporting this hypothesis.

Firstly, we observe that shape is consistent, but responsive. Microbes have a wide range of morphologies, yet within any particular genus, cell shape is tightly conserved for a given set of environmental conditions [301]. This suggests that, while microbes have a potentially vast range of morphologies to choose from, they only adopt the

optimum form for a given situation [299]. Further, when environments change, certain microbes are observed to change shape in response – a phenomenon known as pleiomorphism [104, 206]. Common examples include cell elongation in response to nutrient-poor environments [277] or during pathogenesis [136], and divergence in cell size in response to the threat of predation (the bimodal effect) [217]. Certain shapes are also found to be particularly prevalent in particular environments: for instance, cells living in high-viscosity habitats are often found to be helical in shape [90, 20, 236].

Secondly, shape is under regulatory control. While not all microbes display pleiomorphism, in all cases shape is tightly controlled through robust regulatory networks [272, 86]. Since regulatory infrastructure is generally costly, this implies that selection exists to maintain control of cell shape – in turn implying that cells can maximise their fitness by adopting particular shapes in particular circumstances [300]. After all, why bother regulating a trait that has no bearing on fitness?

Thirdly, shape is evolutionarily convergent. Most microorganisms belong to one of two domains of living organisms: bacteria and archaea. Bacteria and archaea are fundamentally different organisms [288], yet have evolved a similar catalogue of cell shapes [301, 158]. In particular, coccal morphologies appear to have evolved independently numerous times [258, 270]. This suggests that there may be some common mechanism that selects these morphologies, and that the habitats these organisms share make similar morphologies adaptive.

2.2.2 What is the function of microbial shape?

For the reasons stated above, we currently understand shape to be an adaptive trait – one that serves some function, or functions, for microorganisms. Various hypotheses have been put forward as to what these functions are. The cartoon shown in Figure 2.1 summarises some of the rationales collated in the excellent reviews by Kevin Young [300, 301].

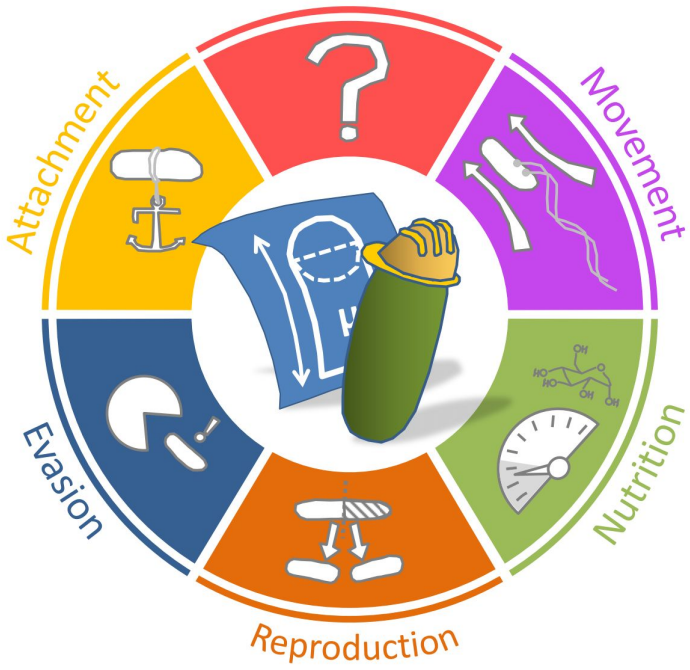

Fig. 2.1 The wheel of shape function. The cartoons shown above summarise proposed functions of cell shape. Reading clockwise from top right, particular cell shapes are thought to benefit cells in multiple ways: enabling more efficient motility or dispersal ('Movement'); increasing nutrient access ('Nutrition'); enabling reliable cell division ('Reproduction'); evading or disrupting predation threats ('Evasion'); and resisting shear forces on surfaces ('Attachment'). This list is likely to be incomplete, and so a blank sector is reserved for additional functions as yet unknown (top).

Some of the earliest work on the functional value of shape concerned its effect on microbial motility. While life in sessile communities dominates, many microbes spend at least some of their existence in a motile state, using appendages such as flagella to swim and feed [188]. Rod-shaped morphologies are thought to be optimum for swimming [61], and experiments show that disrupting cell shape alone is enough to impair motility [269]. Some cell shapes are also thought to facilitate passive motility (dispersion), by allowing cells to be carried along on fluid currents [83], or to resist movement by allowing firmer attachment to fixed surfaces [300, 84].

Cell shape affects the rate at which microbes can exchange solutes—particularly nutrients—with their surroundings, as a cell's surface area constrains the number of importer (or exporter) protein complexes that can operate simultaneously [149].

Additionally, because microbes lack active internal transport systems, their shape and size are constrained by the need for fast internal mixing and diffusion [172]. Microbes respond to reductions in nutrient by changing shape, elongating or branching in a manner thought to improve their nutrient access [250, 277].

Finally, most microbes reproduce asexually by dividing in two (binary fission) [275, 225], which places constraints on cell shape. Symmetrical, non-random morphologies make it easier for cells to duplicate and partition their genetic material between daughter cells [300]. Many microbes also face predation (bacterivory) from larger organisms, such as protists and the immune cells of animals [95, 41]. By adopting awkward sizes and shapes, microorganisms can make it more difficult for a predator to engulf or trap them [217, 232], and thus increase their chances of survival.

2.3 Does microbial shape affect communities?

Far from being an incidental attribute, then, there is much evidence to suggest cell shape has a functional value, helping microbes to survive and thrive in different situations. There is, however, a gap in our understanding here. While the surveys discussed in the previous section focus on the functional effects of shape for individual cells, much less attention has been paid to the potential functions of shape in groups of cells.

Given the importance of community life for microbes, any effects operating at the collective level would be expected to have a strong influence on their evolution. Further, shape is likely to have particularly strong effects in communities, because living together in close physical contact could make direct mechanical interactions between different shapes particularly significant [103].

Recent studies have illustrated the impact of individual cell shape on collective behaviours in microbial groups. Figure 2.2 depicts some of these effects in cartoon form, and shows examples pertaining to each case. Firstly, collectives of rod-shaped

cells can behave very differently to those of spherical cells: when rod-shaped motile bacteria collide on a surface, steric interactions lead to their axes becoming aligned (Figure 2.2-A). For example, when *Bacillus subtilis* bacteria swarm together at high enough cell densities, steric alignment leads to cluster formation (Figures 2.2-B, C; [54, 261]), allowing cells to move efficiently together in raft-like collectives [300]. While spherical cells can also partake in collective motion [231], the speed and size of motile clusters is thought to depend strongly on cell shape [219, 263, 131, 261].

The orientational ordering produced by steric interactions also affects how groups of sessile cells grow and expand (Figure 2.2-D). As shown by experiments in which rod-shaped *Escherichia coli* grow in microfluidic chambers, steric alignment leads to orientational ordering at high cell densities [276, 177], helping to direct growth forces along the axis of the chamber (Figures 2.2-E, F; [276, 56]). In a 2007 study using various chamber shapes, Cho *et al*. further suggested that this self-organisation aided growth by efficiently guiding bacteria towards chamber exits and relieving internal growth pressure [56].

Finally, cell shape can influence spatial patterning in microbial communities, by controlling so-called 'buckling' interactions (Figure 2.2-G; [35]). In 2013, Rudge *et al*. showed that lines of rod-shaped *E. coli* cells buckle under growth forces, folding neighbouring cell groups into one another to create a fractal-like boundary (Figure 2.2-H; [238]). By contrast, repeating the experiment using a coccal mutant of *E. coli* produced a smooth boundary (Figure 2.2-I). This result matches the predictions of previous models of cell buckling, which suggest that lines of shorter cells are much less stable and so buckle on much shorter lengthscales [35].

By influencing biomechanical interactions between microbes, the cell shapes present in a group may have far-reaching consequences for its properties and prospects [103] – yet we know little about how self organisation processes vary with shape parameters. We have also yet to test how different shapes interact together in mixed-species communities.

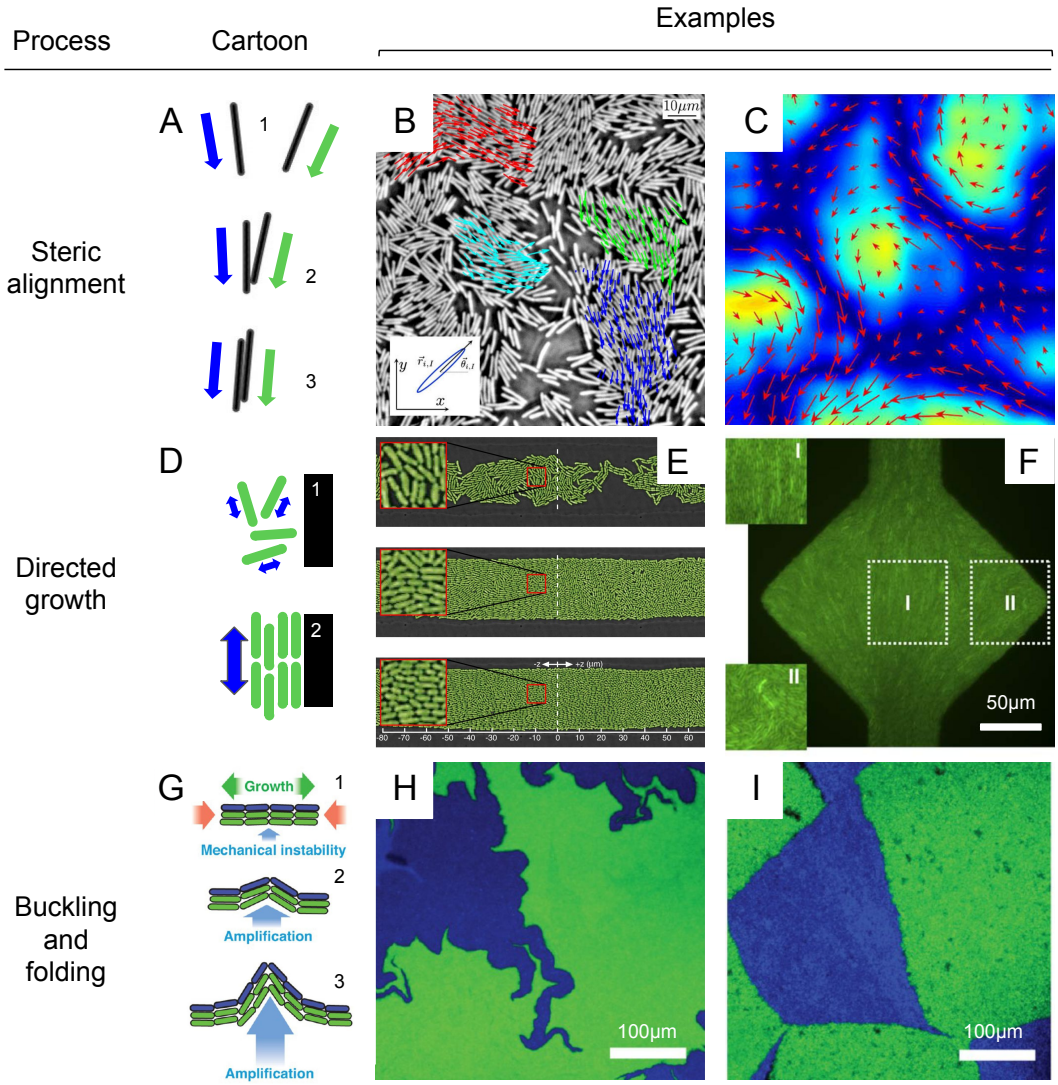

Fig. 2.2 Influences of cell shape in microbial collectives. Experiments suggest that cell shape could influence community properties by modulating 3 types of process: steric alignment between cells (A, B, C), directed growth (D, E, F) and buckling and folding interactions (G, H, I). Cartoons (A, D, G) summarise how each process works, supported by experimental examples using motile *Bacillus subtilis* (B, C) and sessile *Escherichia coli* bacteria (E, F, H, I). Steric alignment leads to cluster formation and collective motility, as shown by cell velocity arrows (B) and vorticity colormap (C). For immotile cells, directed growth also develops at high density (E) and is influenced by solid surfaces (F). Finally, rod-cell buckling folds neighbouring cell groups into each other (H, blue and green), creating a fractal-like boundary. Mutant coccal cells buckle on shorter lengthscales and create a smooth boundary (I). Images (B, C), (E, F) and (G, H, I) adapted with permission from references [54, 261], [276, 56], and [238] respectively.

As a result, we have yet to comprehend what functional value, if any, cell shape might offer to microbes living in communities. One of the major factors hampering our understanding of morphology is the absence of comparative studies, where the properties of microbial communities are measured systematically for different constituent cell shapes. In the next section, we examine experimental and theoretical approaches that might be used to devise such comparisons.

2.4 How can we study cell shape in communities?

To examine the impact of cell shape in a microbial community, we require a system in which cellular morphology can be varied whilst controlling other variables, and in which dependent effects, such as spatial patterning, can be observed and measured. Both experimental and theoretical methods offer ways in which to achieve this goal. Here we examine some of the options, and discuss their suitability.

2.4.1 Experimental approaches

To make a comparison based on cell shape fair, we require methods to control and vary microbial morphology in isolation of other variables, on the community scale. Differences in community properties (or indeed, lack thereof) can then be attributed directly to imposed changes in cell shape.

One such method is to grow cells inside microscopic chambers with the desired shape – a technique used previously to study the effects of cell morphology on flagellar motility [269]. Because the synthesis of new microbial cell wall is in part directed by mechanical stress [272], the microbe then adapts its shape to that of the chamber, and maintains that shape once removed from it. Unfortunately however, this technique is very difficult to scale to the number of cells typically comprising communities, as the morphological changes induced are not heritable [269].

Instead of trying to directly control the shape of a particular strain of microbe, another solution might be to conduct a meta-analysis of cell shape effects, pooling data from communities composed of various pairings of differently-shaped species. Clearly, any particular pair of species will differ in many ways other than shape. However, by comparing a large number of different mixed-species communities, each having a common pairing of cell shapes, one might be able to average out intrinsic differences in microbes, leaving cell shape *per se* as the only differential variable separating the two groups. Nevertheless, it is unclear how large sample sizes would have to be in order to achieve this convergence, and whether the range of species required could practicably be cultured *in vitro* [158].

A third method for manipulating microbial cell shape is through genetic modification. Altering cell shape by mutating genes encoding morphogenic protein complexes often causes unwanted side effects, potentially crippling the cell's ability to grow and divide robustly [18, 303]. However this does not always seem to be the case: in 2014, Monds *et al*. reported a library of *E. coli* mutants with a range of different cell aspect ratios, but with near-identical growth rates [193]. Recent biotechnological advances such as this offer new ways to survey the effects of cell shape in communities.[1]

2.4.2 Theoretical approaches

As discussed in the previous chapter, computational modelling is used extensively to study and understand microbial communities. These models support experimental work by integrating observations, helping to interpret data, and predicting behaviour under new circumstances.

Major themes in community modelling include the development of community structure [224, 146, 28], its interactions with liquid flow [266, 221, 69], chemical trans-

[1] A *fourth* route to manipulating microbes' shape *in vivo* is through the control of their chemical environment – alterations to which can induce morphological changes [21]. We examine this concept further in Chapter 6, where we study the elongation of *Pseudomonas aeruginosa* bacteria in response to antibiotic exposure.

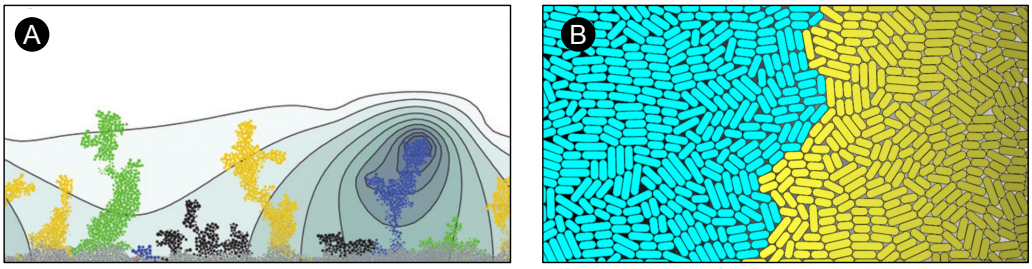

Fig. 2.3 Approaches for investigating cell shape effects in microbial communities. Individual-based models (IbMs, A) can incorporate detailed representations of the chemical and biological processes governing community development, but have largely neglected detailed physical modelling of non-spherical cell shapes. Models incorporating non-spherical cell shapes have recently been developed (B), and could be combined with the IbM approach to examine cell shape effects and functions at the community level. Images A and B taken from references [43] and [239] respectively.

port and transformation [291, 72, 165], and ecological interactions between constituent microbes [201, 147, 198]. As we noted in Chapter 1, these investigations draw upon a range of computational modelling methods, using both continuum (e.g. ODEs [147, 279] and PDEs [6, 7]) and discrete representations (e.g. cellular automata [222, 123], network-based [44, 68] and particle-based methods [297, 159]) of community features, in order to study phenomena of interest.

Of these, a particularly important type of computational model is the so-called agent-based or individual-based model (IbM). Broadly speaking, IbMs represent a system of interest using a large number of discrete objects (the individuals or agents), each programmed with a set of rules about how it responds to different environmental conditions [163]. This rule-based approach distinguishes IbMs from other modelling techniques, such as systems of differential equations, which prescribe the global behaviour of the system [163].

Individual-based models are a major tool in the study of microbial communities [89, 121, 197, 122, 198]. Figure 2.3-A shows an example of an individual-based model in which different strains microbes attack each other with diffusing toxins. IbMs like this one have been used to study a wide range of community phenomena,

including social interactions [30, 31], gene transfer dynamics [183, 173, 96], and the development of spatial structure [199, 192]. They are ideally suited to testing the functional value of a trait, such as cell shape, in the context of a competitive community, where resources such as nutrients are often limiting. However, for all of this chemical and biological detail, most existing IbMs model only spherical cell shapes.

Meanwhile, new methods for dealing with the mechanics of non-spherical cell shapes have been recently introduced, as part of studies examining the biomechanics and self-organisation of microbial groups [219, 56, 276, 239, 88, 106]. As a result, we now have access to a range of computational tools with which to systematically vary cell shape in simulations. We discuss these methods further in Chapter 3.

Currently, most models incorporating non-spherical shapes lack the capacity to simulate the chemical environment of a microbial community. However, combining one of these systems (for instance, the Rudge model pictured in Figure 2.3-B [239]) with the detailed chemical transport models used in traditional IbMs now offers a way to test the competitive value of cell shape in a community. We show how to construct such a model in Chapter 4.

To summarise: in both experimental and theoretical approaches, cell shape is not an easy variable to work with, and this may partly explain the apparent gap in our understanding of its influence and purpose. Yet on both fronts there are ways forward. Combining the chemically-detailed community representations of existing IbMs with biomechanical models of non-spherical cell shapes offers new insights into the role of cell morphology, while newly-published 'morphotype libraries' have the potential to test cell shape effects *in vitro*.

2.5 Research questions

The canon of literature suggests that cell shape is of fundamental importance to microbes, but we still have little understanding of its potential effects and functions in communities. Experimental and theoretical studies suggest that shape may produce several types of emergent phenomena in communities, where many groups of different cell shapes interact together at high density. The full biological implications of cell shape, and these emergent effects, have therefore yet to be explored. Given the ubiquity and importance of microbial collectives, we should seek to further investigate cell shape's role in communities.

Following these observations, therefore, we undertake to address the following research questions in this thesis:

1. Does cell shape influence collective behaviour in a dense community, such as a colony or biofilm?
   (a) containing particular shapes?
   (b) containing mixtures of different shapes?
2. What features of the community does it influence?
3. By what mechanism(s) do such effects occur?
4. How do these effects affect competition in a community?
5. What implications does this raise for our picture of shape function?

To do this, we will use a combination of the methods listed to study cell shape, focussing primarily on the development of computational modelling tools, but also considering experimental approaches as a methods to test model predictions. Our goals can therefore be summarised as:

1. To create an individual-based modelling framework that incorporates both cell shape and the other solute interactions that drive so much of community dynamics;

2. To use said model to simulate competition scenarios between different cell shapes;

3. Where possible, to support the model's findings with experimental tests, using morphotype cell libraries to vary cell shape in isolation of other variables.

2.6 Conclusions

In this chapter, we have discussed evidence showing that microbial shape is important, and the ways in which particular shapes might benefit microbial life. A review of the scientific literature highlights a substantial gap in our understanding: while we know that communities often contain microbes of different shapes, we still rationalise the function of shape in terms of its effects at the individual level. Experimental evidence, meanwhile, suggests that shape is able to influence interactions in communities, by controlling self-organisation, spatial patterning and mixing – yet to date, few systematic studies of cell shape effects have been carried out.

Recent advances in modelling and biotechnology could now enable systematic studies of mixed-shape communities, opening the way to understanding shape's role. To that end, we will focus in this thesis on the creation and application of individual based models incorporating different cellular shapes, and devise experimental tests of their predictions. We begin this process in the next chapter, by choosing and defining a biomechanical model of rod-shaped cell growth dynamics.

3

Individual-based modelling of biomechanical interactions in a microbial community

Abstract

This chapter summarises our methodology for modelling mechanical interactions between non-spherical microbes in the colony environment. Here, we review individual-based approaches for representing non-spherical cell shapes, and provide a detailed description of the model of Rudge *et al*. and its implementation as the open-source software CellModeller. We also discuss our extensions CellModeller, proposing schemes to represent periodic boundary conditions and cell cycles for microbes of different shapes. The resulting model forms the basis for work presented in this thesis.

3.1 Introduction

Computational modelling is being used extensively to study and understand microbial communities [89, 122, 283]. As discussed in Chapter 1, these models support experimental work by integrating observations, helping to interpret data, and predicting behaviour under new circumstances. When it comes to cell shape, so-called "individual-based" models (IbMs) can offer new insights into the role of cell shape in microbial collectives, providing a theoretical framework to complement experimental investigations.

In this methodological chapter, we discuss individual-based modelling techniques and systems for simulating mechanical interactions between non-spherical cell shapes. Of these models, we identify one in particular—the model of Rudge *et al*. [239]-–which fulfils the requirements of this project, and which accordingly forms the basis for the

modelling framework detailed in this thesis. We describe the model's assumptions, formulation and implementation in detail, before covering modifications to the scheme necessary for the work presented in this thesis.

3.2 Individual-based models including cellular shape

How should cell shape be incorporated into an individual-based model? Many existing IbM frameworks incorporate a spatially-explicit representation of cell shape – that is, they consider cells to be objects with specific geometries, with physical rules about how they move in space and interact with other cells. Here, we review the techniques used to describe the interactions between discrete cells of different shapes.

3.2.1 Methods and representations

Until recently, most IbMs focussed entirely on spherical morphologies [153, 154, 297, 159] – and for a good reason. The assumption of spherical geometry—representing bacterial cells or cell clusters of coccal morphology—is a useful simplification: with it, cell rotational degrees of freedom can be ignored, so that cell movements consist only of translational motion. It also makes it easier to compute cell-cell interactions, and less computer memory is used in storing the configuration of the system [154, 297]. Consequently, spherical cell models continue to enjoy widespread application, being used to model bacterial communities [154, 297, 7, 295], as well as other systems such as eukaryotic tissues [215, 187] and tumours [246].

Now however, methods for dealing with the mechanics of more complex shapes are being introduced. So far, the vast majority of these models are based on rod-shaped morphologies [276, 239, 88, 209, 106, 267], but some methodologies also extend to more complex cell shapes [227, 50]. In any case, the ability to include non-spherical cells is a critical step forward, allowing a range of cell shapes to be modelled using

a single system [267]. These recent developments therefore offer new methods for comparing different cell shapes, in the context of a microbial community.

Interactions between non-spherical cells are generally treated using one of two methods:

- **Force-based methods**, in which cell movements are calculated by summing forces on cells, computed as functions of relative cell orientation. Net forces are then integrated in time to compute cell movements each simulation step [215].
- **Constraint-based methods**, which exchange an explicit description of intercellular forces for a set of biophysical constraints, detailing what properties simulated cell configurations ought to have. Many of these methods are based on mechanical relaxation, and define procedures that move cells into a state of mechanical equilibrium [297, 239].

In some cases, it is possible to model a system of interest using both methods, and such studies have been used to check their equivalence [99].

As well as different methods for describing cell-cell mechanical interactions, we also find a range of geometric representations used to approximate the shape of microbial cells. Figure 3.1 provides a visual comparison of some of cell representations found in the literature, grouped by the approach used to simulate mechanical interactions. The representations chosen for cell geometries and interactions are hardly independent: as might be expected, some combinations work much more naturally together than others. For example, force-based models of rod-shaped cells (Figure 3.1, A-C) often represent cell-cell interactions using some variety of particle-spring network, reducing non-spherical objects to a system of connected spheres. Three popular methods here include:

- The sphere chain method, where cell bending and compression are accounted for by internal springs (Figure 3.1-A) [106];

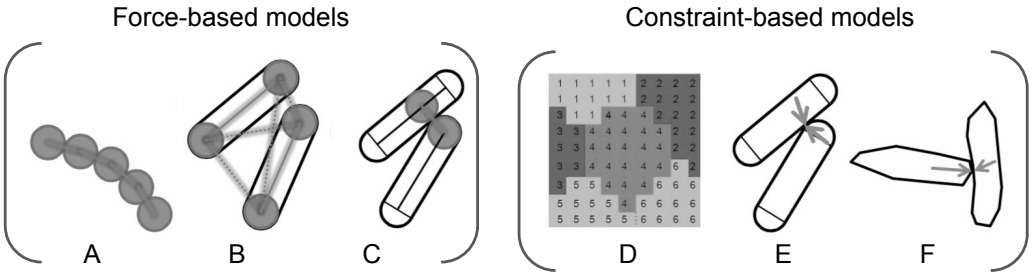

Fig. 3.1 Representations of non-spherical (polar) cells using Force-based (left) and Constraint-based (right) approaches. Force-based methods often approximate rod-shaped cells using collections of spherical particles, placed along the length of the cell (A), at the cell tips (B) or at the point of closest approach between two line segments (C). Forces between particles are combined to compute overall cell movements. Constraint-based representations include on-lattice cellular Potts models (D) and off-lattice capsule (E) and vertex (F) systems. As the name suggests, these models substitute explicit forces for constraints, such as overlap minimisation, whose resolution creates realistic configurations of cells.

- The end-sphere method, where neighbouring cell poles are connected with springs (Figure 3.1-B) [267];
- The closest sphere method, where forces are computed for pairs of spheres placed at the points of closest approach between neighbouring cells (Figure 3.1-C) [88].

By contrast, common representations for rod cells in constraint-based models (Figure 3.1, D-E) include:

- Cellular Potts methods, representing cells as collections of adjacent lattice elements with a particular state (Figure 3.1-D) [227];
- Rigid-body methods, which model rod cells as inflexible elastic capsules (Figure 3.1-E) [239, 209];
- Vertex-based methods, where cells are represented as polygons bound by a number of mobile vertices, which move to minimise energy functions (also used to simulate tissue mechanics (Figure 3.1-E) [187].

Both force-based and constraint-based methods have their own distinct strengths and weaknesses, and both approaches remain popular. Force-based models tend to be easier to compose and interpret, because they are based on parameters with a clear interpretation. By contrast, it is not always clear exactly what combination of biophysical rules will produce a realistic simulation of collective phenomena, and therefore constraint-based approaches are harder to construct.

Physical quantities of interest, such as stress or strain, are also easier to extract from force-based simulations. However, by effectively coarse-graining out the dynamics of relaxation processes and focussing only on equilibrium states, constraint-based methods can be less susceptible to numerical instabilities, and so can admit larger timesteps (so, fewer calculations per unit of time simulated). Constraint-based methods can therefore offer higher performance, and may help to group many unmeasurable physical parameters into effective parameter clusters.

3.2.2 The Rudge model

As we have seen, recent developments in individual-based modelling have created a range of possible approaches for investigating cell-shape effects. Given all of this choice, which model do we pick? To identify the most suitable framework for our studies, we need to identify selection criteria and then review the properties of these models with respect to those criteria. Three critical factors to check are:

- **Realism**. The model should adequately and demonstrably emulate the biophysics of a real bacterial colony.
- **Performance**. The model implementation should minimise cost of computational operations and memory usage, in order to maximise the range of spatial and temporal scales that can be simulated.

- **Accessibility**. To be effective, the model software should be freely available, and easy to modify and combine with other computational tools.

Of the resources available at time of writing, the open-source colony modelling software CellModeller provides a good match with these prerequisites [239, 238]. Designed by Tim Rudge, Paul Steiner, Andrew Philips and Jim Haseloff, CellModeller is a program under continuous development, documented online at http://haselofflab.github.io/CellModeller/. The underlying biophysical model, which we will refer to as the Rudge model, represents microbial cells as growing capsules, and simulates cell biomechanics using a constraint-based scheme. This scheme, combined with a high-performance parallel implementation in OpenCL, allows communities with large populations to be simulated quickly: for example, the growth of a 10^5-cell colony from a single cell can be simulated in only 3 hours of real time [239]. Because the user interface of CellModeller is primarily written in Python, it can also easily be adapted and interfaced with other pieces of scientific software.

Further, the Rudge model has already been validated using experimental data in previous publications, as highlighted in Figure 3.2. Here, we show a comparison between confocal images of growing *Escherichia coli* bacterial colonies (Figure 3.2, A-C) and colonies simulated using CellModeller (Figure 3.2, A-C) – demonstrating that the model can reproduce the bulk geometry of a developing colony over time [239]. On similar lengthscales, the model can also reproduce spatial patterning effects in two-strain communities, such as the fractal-like strain boundaries that develop in colonies of rod-shaped cells (Figure 3.2, G-K, [238]).

Overall then, the Rudge model—and its implementation, CellModeller—provide suitable means for simulating biomechanical interactions between non-spherical cells, and can therefore be used as the basis for a community model incorporating mixed cell shapes. Accordingly, we devote the remainder of this chapter to examining it in detail. We begin with a derivation of Rudge's model from starting assumptions,

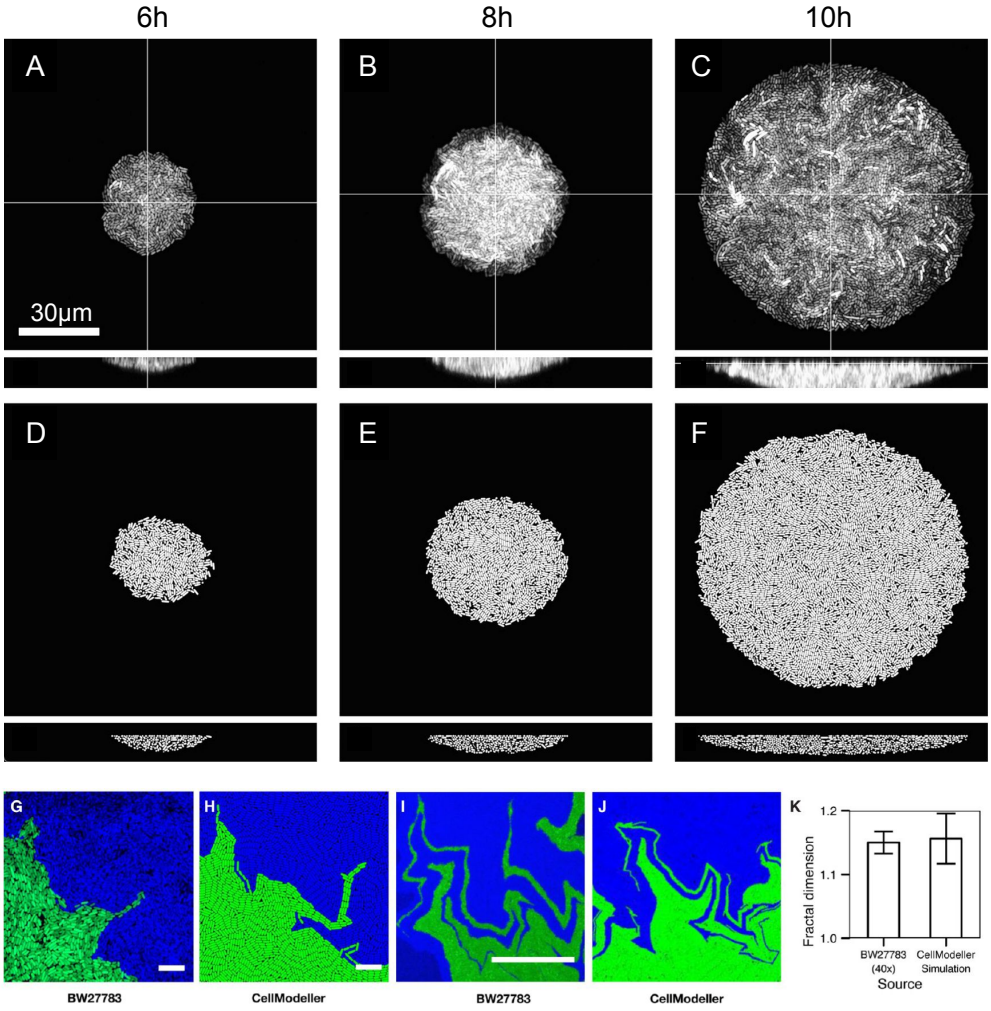

Fig. 3.2 Confocal images (A-C) of BW27783 *E. coli* colonies grown at room temperature show similar geometries to those in CellModeller simulations (D-F), which reproduce both colony width (top) and depth (bottom) properties at comparable time points. Simulated colonies also reproduce effects such as fractal boundary patterning (G-J) between adjacent clonal cell groups, shown with blue and green fluorescent markers. Boundary fractal dimension measurements (K) found in confocal images are mirrored by simulations. Scale bars in A-F and G-J correspond to 30 and 10 μm respectively; figures reproduced with permission from references [239] (A-F) and [238] (G-K).

and proceed to discuss its implementation and parameterisation in the CellModeller software. Finally, we conclude by showing how the model can be adapted to include additional features, such as a shape-independent growth model, and periodic boundary conditions.

3.3 Model derivation

Here we provide a derivation of the Rudge model, beginning with an overview of the model's underlying assumptions, as illustrated in Figure 3.3.

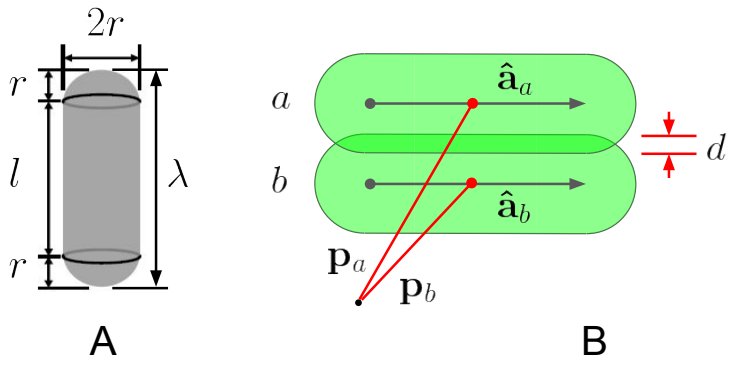

Fig. 3.3 In the model of Rudge *et al.* [239], bacterial cells are represented as growing 3-dimensional capsules (A) of fixed radius r, variable segment length l_i, and variable tip-to-tip length λ_i. Each capsule has a position vector $\mathbf{p}_i$ (B) and a unit axis vector $\hat{\mathbf{a}}_i$. Cell movement is overdamped and driven by elastic repulsion between elongating cells, as represented by a set of constraints that minimise overlap distances d.

3.3.1 Model assumptions

The model rests on five sets of assumptions:

1. **Cells**. The colony is comprised of n discrete cells, each labelled with a unique index i. These cells are represented by inflexible elastic capsules[1]. Each capsule

[1] A capsule is a cylinder with hemispherical ends, equivalent to the locus of points at distance r from a line segment of length l. We refer to cell segments later on, as they can be used to identify which cells are in physical contact.

has a variable segment length l_i, a fixed radius r, and a variable tip-to-tip length $\lambda_i = l_i + 2r$, as shown in Figure 3.3-A. Its location, orientation and length in Cartesian space are given by a position vector, $\mathbf{p}_i$ and a unit axis vector, $\hat{\mathbf{a}}_i$, respectively, summarised by the generalised coordinate $\tilde{\mathbf{p}}_i = (\mathbf{p}_i, \hat{\mathbf{a}}_i, l_i)^\top$.[2] Thus, each cell has a total of seven degrees of freedom.

2. **Growth**. Each cell's unconstrained growth rate is proportional to its segment length l_i, so that $\frac{dl_i}{dt} = \mu l_i$, where μ represents the cell's intrinsic growth rate.[3] However, cellular growth is also constrained by intercellular forces, so that $\frac{dl_i}{dt} \leq \mu l_i$ according to the mechanical pressures cell i experiences. These mechanical growth constraints are parameterised by the number Γ, defined as

$$\Gamma = \frac{\text{Energetic cost of moving cells}}{\text{Energetic cost of constraining cell growth}}. \tag{3.1}$$

3. **Division**. Each capsule cell divides by symmetric binary fission once its tip-to-tip length λ_i exceeds a threshold, λ_{div}. Every cell has its threshold length drawn randomly at birth, from a fixed uniform distribution on the interval $[2l_0 + 4r,\ 2l_0 + 4r + \xi_l]$, with the noise parameter ξ_l representing variability in cell division length. The parameter l_0, the minimum cell segment length at birth, controls cell shape. Upon division, the parent cell is replaced with two daughter cells of length $\lambda_{\text{div}}/2$, placed inside the parent cell silhouette. Division therefore conserves the tip-to-tip length of the parent cell, λ, but not its volume or segment length. Daughter cells inherit the orientation vector $\hat{\mathbf{a}}$ of the parent cell, perturbed by random noise $\xi_{\hat{\mathbf{a}}}$ representing the effects of inhomogeneities in the medium and cellular division machinery.

[2] The complete set of generalised cell coordinates, $\{\tilde{\mathbf{p}}_i(t)\}$, at a particular time t, is known as the cell configuration.

[3] We will assume that all cells grow at the same constant rate μ for the time being. We go on to lift this assumption in Chapter 4.

4. **Medium**. Cells are implicitly surrounded by a medium of extracellular polymeric material (EPS). Drag forces between cells and the EPS matrix dominate inertia, so that cells move only when subjected to a net force. Drag forces acting on any point on the cell are proportional and opposite to that point's velocity. Cell movement is also constrained by planar elastic surfaces, such as the basal surface on which the colony sits.

5. **Dynamics**. Colony expansion occurs over a series of discrete, short timesteps of length Δt. Cellular growth is much slower than mechanical relaxation, so that the colony remains in mechanical quasi-equilibrium as it expands. This timescale separation allows the cell configuration to be updated in five consecutive steps each timestep Δt:

   (a) Allow each cell i to elongate by $\Delta l_i = \mu_i l_i \Delta t$, where l_i is the current cell segment length;

   (b) Divide any cells whose total lengths exceed their assigned values of λ_{div};

   (c) Identify cells whose surfaces overlap (representing a non-equilibrium configuration) and quantify these m contact instances with a set of overlap distances $\{d_k\}$;

   (d) Move and/or shorten the cells so as to remove overlap (restoring an equilibrium configuration).

   (e) Replace any cell ready for division with two daughter cells, positioned roughly inside the parent cell silhouette, but with orientational noise added.

The variables of this model are collated for reference in Table 3.1. Using the assumptions listed above, we can derive a model to simulate the dynamics of a large system of growing cells. The major result to establish is how to carry out stage (d) – the restoration of mechanical equilibrium to a configuration of overlapping cells.

Table 3.1 Variables of the Rudge model

Variable	Symbol	Units
Time	t	s
Number of cells	n	
Number of cell overlaps	m	
For each cell i:		
position vector	$\mathbf{p}_i = (p_x, p_y, p_z)^\top$	µm
orientation unit vector	$\hat{\mathbf{a}}_i = (a_x, a_y, a_z)^\top$	µm
segment length	l_i	µm
generalised coordinate	$\tilde{\mathbf{p}}_i = (\mathbf{p}_i, \hat{\mathbf{a}}_i, l_i)^\top$	µm
tip-to-tip length	$\lambda_i = l_i + 2r$	µm
volume	$V_i = \frac{4}{3}\pi r^3 + l_i \pi r^2$	µm^3

3.3.2 Constraint formulation

Our goal is to specify a set of n generalised movement vectors, $\Delta\tilde{\mathbf{p}} = (\Delta\tilde{\mathbf{p}}_1, \ldots, \Delta\tilde{\mathbf{p}}_n)^\top$, that remove all overlaps $\mathbf{d}$ present in a configuration $\{\tilde{\mathbf{p}}_i\}$ of n cells. The crux of the Rudge model is a constraint equation specifying how to do this, written in the form of a cost function,

$$\text{total cost} = \text{overlap cost} + \text{movement cost}. \tag{3.2}$$

The correct cell movements $\Delta\tilde{\mathbf{p}}$ for a given set of overlaps $\mathbf{d}$ are those which minimise the cost function – i.e. which minimise cell overlap with the smallest possible movement of cells (Figure 3.3-B). The inclusion of the movement constraint is necessary in order to evaluate a unique solution to the overlap problem. We go on to show this explicitly in Section 3.3.4.

In practise, it is easier to work not with the cell movements themselves, but with the time-integrated forces (impulses, $\tilde{\mathbf{j}}$) necessary to produce them. The Rudge model formulates the cost function in Equation (3.2) as an energy minimisation problem,

$$E_{\text{total}}(\tilde{\mathbf{j}}) = \underbrace{E_{\text{overlap}}(\tilde{\mathbf{j}} \mid \mathbf{d})}_{\text{Cost of remaining overlap}} + \alpha \underbrace{E_{\text{movement}}(\tilde{\mathbf{j}})}_{\text{Cost of moving cells}}, \tag{3.3}$$

where α is a weighting constant controlling the relative importance of the overlap and movement constraints. We now proceed to define the energy functions E_{overlap} and E_{movement}, before using these results compute the minimum-energy solution to Equation (3.3) above. To do this, we draw upon the equations of motion for capsules in a viscous medium [239], included for reference in Appendix A.

3.3.3 Energetic cost of cell movement

To define E_{movement} in Equation (3.3), we compute the work done by cells moving through the medium. Consider first an individual cell acted on by a linear force $\mathbf{F}_{\text{lin}}$, over a path S. The work, W_{lin}, performed by this linear force is

$$W_{\text{lin}} = \int_S \mathbf{F}_{\text{lin}} \cdot d\mathbf{r} \approx \mathbf{F}_{\text{lin}} \cdot \Delta\mathbf{p}, \tag{3.4}$$

where $\Delta\mathbf{p}$ is the linear displacement of the cell. Here we have assumed that the force is approximately constant over the path S, allowing it to be taken out of the integral. We can use the same assumption to relate work to an applied linear impulse, $\mathbf{j}_{\text{lin}}$, using

$$\mathbf{j}_{\text{lin}} = \int_{t_0}^{t_1} \mathbf{F}_{\text{lin}}\, dt \approx \mathbf{F}_{\text{lin}} \Delta t, \tag{3.5}$$

where $\Delta t = t_1 - t_0$ corresponds to the simulation timestep. Combining this result with Equation (3.4) gives

$$W_{\text{lin}} = \frac{1}{\Delta t} \mathbf{j}_{\text{lin}} \cdot \Delta\mathbf{p}. \tag{3.6}$$

In the Rudge model, cells can undergo rotation ($\Delta\hat{\mathbf{a}}$) and compression (Δl) as well as translation ($\Delta\mathbf{p}$), and the work associated with each of these degrees of freedom needs to be taken into account. By analogy to Equation (3.6), we can say

$$W_{\text{rot}} = \frac{1}{\Delta t} \mathbf{j}_{\text{rot}} \cdot \Delta\hat{\mathbf{a}}, \quad \text{and} \tag{3.7}$$

$$W_{\text{gro}} = \frac{1}{\Delta t} j_{\text{gro}} \Delta l, \tag{3.8}$$

where the impulses $\mathbf{j}_{\text{rot}}$ and j_{gro} correspond to time integrals of rotational and compressive forces acting on the cell, by analogy to Equation (3.5).

The total work W_{tot} performed by a generalised combination of these impulses, $\tilde{\mathbf{j}} = (\mathbf{j}_{\text{lin}}, \mathbf{j}_{\text{ang}}, j_{\text{gro}})^\top$, is therefore

$$W_{\text{tot}} = W_{\text{lin}} + W_{\text{rot}} + W_{\text{gro}} = \frac{1}{\Delta t} \begin{bmatrix} \mathbf{j}_{\text{lin}} \\ \mathbf{j}_{\text{ang}} \\ j_{\text{gro}} \end{bmatrix} \cdot \begin{bmatrix} \Delta\mathbf{p} \\ \Delta\hat{\mathbf{a}} \\ \Delta l \end{bmatrix} = \frac{1}{\Delta t}\, \tilde{\mathbf{j}} \cdot \Delta\tilde{\mathbf{p}}, \tag{3.9}$$

where $\Delta\tilde{\mathbf{p}} = (\Delta\mathbf{p}, \Delta\hat{\mathbf{a}}, \Delta l)^\top$ denotes a change in the cell's generalised coordinates in response to $\tilde{\mathbf{j}}$. The work done in moving a system of n cells, equivalent to E_{movement}, can be computed in exactly the same way,

$$E_{\text{movement}} = \sum_{i=1}^{n} W_{\text{tot},i} = \frac{1}{\Delta t} \begin{bmatrix} \tilde{\mathbf{j}}_1 \\ \vdots \\ \tilde{\mathbf{j}}_n \end{bmatrix} \cdot \begin{bmatrix} \Delta\tilde{\mathbf{p}}_1 \\ \vdots \\ \Delta\tilde{\mathbf{p}}_n \end{bmatrix} = \frac{1}{\Delta t}\, \tilde{\mathbf{j}} \cdot \Delta\tilde{\mathbf{p}}, \tag{3.10}$$

where above we have changed the meanings of $\tilde{\mathbf{j}}$ and $\Delta\tilde{\mathbf{p}}$ to denote vectors of generalised impulses and coordinate changes, respectively, for all of the n cells.

Finally, we can simplify Equation (3.10) by rewriting $\Delta\tilde{\mathbf{p}}$ in terms of $\tilde{\mathbf{j}}$. This is equivalent to computing the movement of a set of cells produced by the application of a set of impulses: as shown in Appendix A.1, Equation (A.16),

$$\Delta\tilde{\mathbf{p}} = \mathbf{D}\tilde{\mathbf{j}}, \tag{3.11}$$

where $\mathbf{D}$ is a block diagonal matrix encoding the impulse response of a set of n cells. Combining this result with Equation (3.10) gives us the required result,

$$E_{\text{movement}} = \frac{1}{\Delta t}\tilde{\mathbf{j}}^\top \mathbf{D}\tilde{\mathbf{j}}. \tag{3.12}$$

3.3.4 Energetic cost of cell overlap

As well as minimising cell movement, Equation (3.3) requires us to minimise overlap between cells, and with other simulations objects such as hard surfaces. We therefore need a geometric definition of what $\{d_k\}$ is for a given configuration of cells and surfaces, in order to compute E_{overlap}. Here we show how to do this, applying the method to some simple cell configurations by way of example.

Cell-cell overlap

We must first define cell-cell overlaps geometrically. Figure 3.4-A shows a way of parameterising the overlap between a pair of capsules with indices a and b. For this and any pair of capsules, we can define the shortest possible vector connecting their line segments as $\mathbf{s}_{a,b} = s_{a,b}\hat{\mathbf{n}}$.[4] Here, $\hat{\mathbf{n}}$ is unit vector parallel to $\mathbf{s}_{a,b}$, summarising the relative orientation of the two cells in space. If it is the case that

$$s_{a,b} < r_a + r_b, \tag{3.13}$$

i.e. the connecting path is shorter than the sum of the cell's radii, then the cells are overlapping, as shown in Figure 3.4-A. In this case, we refer to $\hat{\mathbf{n}}$ as the contact vector for this pair of cells, and assign it an index $k = 1$.

The points at which $\hat{\mathbf{n}}_1$ intersects each cell's surface are termed the contact points, labelled as $\mathbf{q}_a$ and $\mathbf{q}_b$ in Figure 3.4-A. The overlap distance for this pair of cells, d_1, is then defined as

$$d_1 = |\mathbf{q}_b - \mathbf{q}_a| = \hat{\mathbf{n}}_1 \cdot (\mathbf{q}_b - \mathbf{q}_a) = q_{b,\hat{\mathbf{n}}_1} - q_{a,\hat{\mathbf{n}}_1}. \tag{3.14}$$

How will d_1 change when generalised impulses, $\tilde{\mathbf{j}}$, are applied to capsules a and b? To compute the answer, we project the movement of each contact point onto the contact

[4] We use the convention that the shortest path vector $\mathbf{s}_{a,b}$ points away from the cell of lower index.

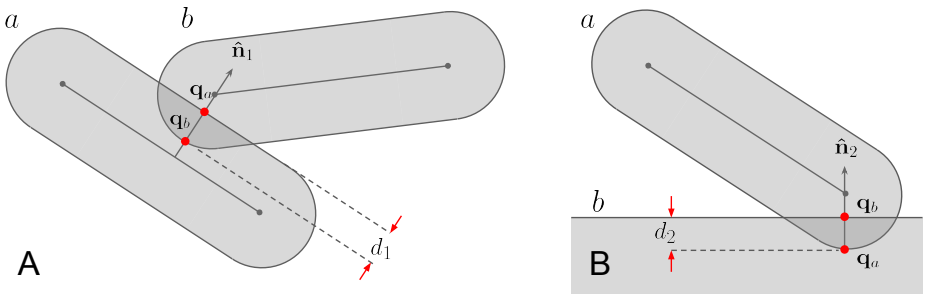

Fig. 3.4 In the Rudge model, overlaps between neighbouring cells a and b (A) are parameterised by a contact unit normal vector $\hat{\mathbf{n}}$, on which lie a pair of surface contact points ($\mathbf{q}_a$, $\mathbf{q}_b$), shown in red. To resolve the overlap we require that $\mathbf{q}_a$ and $\mathbf{q}_b$ move along $\hat{\mathbf{n}}$ such that their separation d is reduced to zero. (B) Overlaps between cells and surfaces (B) are parameterised in much the same way, except that surfaces are immobile. 3-D cells are shown as 2-D silhouettes for clarity.

vector $\hat{\mathbf{n}}_1$. In Appendix A.2, we show that the movement of a surface point, $\Delta q_{\hat{\mathbf{n}}}$, along a particular unit vector, $\hat{\mathbf{n}}$, is given by

$$\Delta q_{\hat{\mathbf{n}}} = \left(\mathbf{C}_{\hat{\mathbf{n}},\mathbf{q},i}\mathbf{D}_i\right)\tilde{\mathbf{j}}_i, \tag{3.15}$$

where $\mathbf{C}_{\hat{\mathbf{n}},\mathbf{q},i}$ and $\mathbf{D}_i$ are respectively a vector of dimensions 1-by-7, and a matrix of dimensions 7-by-7.[5] Using this result, we can rewrite Equation (3.14) to define the change in overlap, Δd_1, caused by applying generalised impulses $\tilde{\mathbf{j}}_a$, $\tilde{\mathbf{j}}_b$ to cells a and b respectively,

$$\Delta d_1 = \Delta q_{a,\hat{\mathbf{n}}_1} - \Delta q_{b,\hat{\mathbf{n}}_1} \tag{3.16}$$

$$= \left(\mathbf{C}_{\hat{\mathbf{n}}_1,\mathbf{q}_a,a}\mathbf{D}_a\right)\tilde{\mathbf{j}}_a - \left(\mathbf{C}_{\hat{\mathbf{n}}_1,\mathbf{q}_b,b}\mathbf{D}_b\right)\tilde{\mathbf{j}}_b. \tag{3.17}$$

Cell-surface overlap

Overlaps between cells and fixed planar surfaces can be described in much the same way as between cells. Figure 3.4-B shows a way of parameterising the overlap between

[5] Note that $\mathbf{D}_i$ is related to $\mathbf{D}$ in Equation (3.11), according to Appendix A, Equation (A.18).

a capsule a and an infinite planar surface b; we will assign this overlap with contact index $k = 2$. Equations 3.13 and 3.17 still apply, except that the contact normal vector $\mathbf{n}_2$ must be perpendicular to the face of the surface. Since the surface is fixed, its corresponding contact point $\mathbf{z}_b$ is immobile and $\Delta z_{b,\hat{\mathbf{n}}_2} = 0$. Thus, Δd_2 depends only upon the impulse applied to cell a, i.e.

$$\Delta d_2 = \Delta z_{a,\hat{\mathbf{n}}_2} = \left(\mathbf{C}_{\hat{\mathbf{n}}_2,\mathbf{z}_a,a}\mathbf{D}_a\right)\tilde{\mathbf{j}}_a. \tag{3.18}$$

A system of many overlaps

We can now generalise these constraints to any system of contacts between cells and surfaces. As an example, Figure 3.5 shows a set of three capsule cells and a surface, connected by five overlaps.

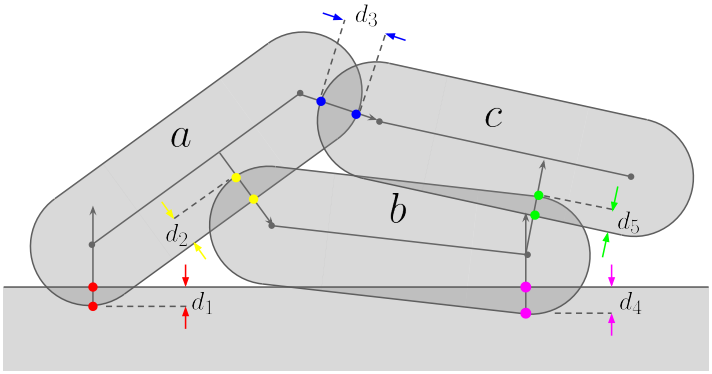

Fig. 3.5 An example contact system, showing overlaps between three capsule cells (a-c) and one surface. Each overlap is assigned a unique index and color, and is shown with its corresponding contact vector (arrows), surface point pair (colored dots) and overlap distance (d_1-d_5). The constraints for this system can be found in Equations (3.19) and (3.20). Note that, by convention, contact vectors point from low to high cell index. Overlap distances have been exaggerated; 3-D cells are shown as 2-D silhouettes for clarity.

As before, we can write down the constraints for this example system, allowing us to specify the impulses required to resolve all five overlaps simultaneously. These are

$$\begin{bmatrix} \mathbf{C}_{a,1}\mathbf{D}_a & 0 & 0 \\ \mathbf{C}_{a,2}\mathbf{D}_a & -\mathbf{C}_{b,2}\mathbf{D}_b & 0 \\ \mathbf{C}_{a,3}\mathbf{D}_a & 0 & -\mathbf{C}_{c,3}\mathbf{D}_c \\ 0 & \mathbf{C}_{b,4}\mathbf{D}_b & 0 \\ 0 & \mathbf{C}_{b,5}\mathbf{D}_b & -\mathbf{C}_{c,5}\mathbf{D}_c \end{bmatrix} \begin{bmatrix} \tilde{\mathbf{j}}_a \\ \tilde{\mathbf{j}}_b \\ \tilde{\mathbf{j}}_c \end{bmatrix} = \begin{bmatrix} \Delta d_1 \\ \Delta d_2 \\ \Delta d_3 \\ \Delta d_4 \\ \Delta d_5 \end{bmatrix} \tag{3.19}$$

which can be factorised as

$$\underbrace{\begin{bmatrix} \mathbf{C}_{a,1} & 0 & 0 \\ \mathbf{C}_{a,2} & -\mathbf{C}_{b,2} & 0 \\ \mathbf{C}_{a,3} & 0 & -\mathbf{C}_{c,3} \\ 0 & \mathbf{C}_{b,4} & 0 \\ 0 & \mathbf{C}_{b,5} & -\mathbf{C}_{c,5} \end{bmatrix}}_{\text{Overlap matrix } \mathbf{C}} \underbrace{\begin{bmatrix} \mathbf{D}_a & 0 & 0 \\ 0 & \mathbf{D}_b & 0 \\ 0 & 0 & \mathbf{D}_c \end{bmatrix}}_{\text{Drag matrix } \mathbf{D}} \underbrace{\begin{bmatrix} \tilde{\mathbf{j}}_a \\ \tilde{\mathbf{j}}_b \\ \tilde{\mathbf{j}}_c \end{bmatrix}}_{\text{Impulse vector } \tilde{\mathbf{j}}} = \underbrace{\begin{bmatrix} \Delta d_1 \\ \Delta d_2 \\ \Delta d_3 \\ \Delta d_4 \\ \Delta d_5 \end{bmatrix}}_{\text{Overlap vector } \Delta\mathbf{d}}, \tag{3.20}$$

for this system of overlaps. While the terms of matrices $\mathbf{C}$ and $\mathbf{D}$ (and vectors $\tilde{\mathbf{j}}$ and $\Delta\mathbf{d}$) depend on the exact number and configuration of cells present, the general form

$$\mathbf{CD}\tilde{\mathbf{j}} = \mathbf{A}\tilde{\mathbf{j}} = \Delta\mathbf{d}, \tag{3.21}$$

applies for any system of n cells and m overlaps, where $\mathbf{C}$ is an m-by-$7n$ matrix, and $\mathbf{D}$ a $7n$-by-$7n$ block diagonal matrix. Note that in Equation (3.21) we have introduced the shorthand $\mathbf{A} = \mathbf{CD}$.

We are now ready to define E_{overlap}. Let the sets of overlaps before and after application of impulses $\tilde{\mathbf{j}}$ be denoted $\mathbf{d}_{t_0}$ and $\mathbf{d}_{t_1}$, respectively. Assuming that cells behave elastically, the potential energy U associated with the remaining overlaps $\mathbf{d}_{t_1}$ is given by

$$U = \frac{1}{2}\mathbf{d}_{t_1}^{\top}\mathbf{K}\mathbf{d}_{t_1}, \tag{3.22}$$

which is analogous to the potential energy of a linear spring, $U = Kd^2/2$. In Equation (3.22), $\mathbf{K}$ is a diagonal matrix of cell stiffness coefficients – for the purposes of this thesis, we can assume that all cells and surfaces have the same stiffness, such that $\mathbf{K} = K\mathbf{I}$, with $\mathbf{I}$ representing the identity matrix. Using Equation (3.21), we can write

$$\mathbf{d}_{t_1} = \mathbf{d}_{t_0} + \Delta\mathbf{d} = \mathbf{d} + \mathbf{A}\tilde{\mathbf{j}}, \tag{3.23}$$

and so substitution into Equation (3.22) gives us our definition for the overlap energy function E_{overlap},

$$E_{\text{overlap}} = U = \frac{K}{2}|\mathbf{A}\tilde{\mathbf{j}} + \mathbf{d}|^2. \tag{3.24}$$

At this point, we can identify why minimising the overlap energy alone is not sufficient to specify a unique set of impulses $\tilde{\mathbf{j}}$ that restore a cell configuration to mechanical equilibrium. The problem is that $\mathbf{A}$ is a singular matrix – in other words, there are an infinite number of ways in which to separate cells so that they do not overlap. For instance, the pair of overlapping cells depicted in Figure 3.4-A could be separated by rotating cell b, or by moving a downwards, or b to the right, and so on and so forth. Another way of seeing this is to note that we require a total of $7n$ equations to specify impulse components for each of the system's $7n$ degrees of freedom, where n is the number of cells to be moved. However, each of the m overlap instances constrains movements only along the three components of its contact vector. Since, for most geometrically-feasible arrangements of n cells, $7n > 3m$, $\mathbf{A}$ will generally be rank-deficient, and therefore singular. We therefore need to specify additional constraints to compute a unique solution $\tilde{\mathbf{j}}$, and this is the purpose of the second energy term E_{movement}.

3.3.5 Energy-minimising solution

We have now defined the energy functions $E_{\text{overlap}}(\,\tilde{\mathbf{j}} \mid \mathbf{d}\,)$ and $E_{\text{movement}}(\,\tilde{\mathbf{j}}\,)$, and can therefore rewrite the cost function shown in Equation (3.3) as

$$E_{\text{tot}} = \underbrace{|\mathbf{A}\tilde{\mathbf{j}} + \mathbf{d}|^2}_{\text{overlap energy cost}} + \alpha \underbrace{\left(\frac{1}{\Delta t}\tilde{\mathbf{j}}^\top \mathbf{D}\tilde{\mathbf{j}}\right)}_{\text{movement energy cost}} . \tag{3.25}$$

Above, we have absorbed the $\frac{K}{2}$ factor into the coefficient α, whose value reflects the energy cost of cell movement relative to that of cell movement. We can therefore interpret α as

$$\alpha = \frac{\text{Energetic cost of cell movement}}{\text{Energetic cost of cell overlap}} = \Gamma, \tag{3.26}$$

as stated in the starting assumptions. To minimise the energy associated with this equation, we compute its differential with respect to the impulse set $\mathbf{j}$ and set this to zero, i.e.

$$\frac{dE_{\text{tot}}}{d\tilde{\mathbf{j}}} = \mathbf{0}, \tag{3.27}$$

$$\frac{d}{d\tilde{\mathbf{j}}}\left(|\mathbf{A}\tilde{\mathbf{j}} + \mathbf{d}|^2\right) + \frac{\alpha}{\Delta t}\frac{d}{d\mathbf{j}}\left(\tilde{\mathbf{j}}^\top \mathbf{D}\tilde{\mathbf{j}}\right) = \mathbf{0}, \tag{3.28}$$

$$\mathbf{A}^\top \mathbf{A}\tilde{\mathbf{j}} + \mathbf{A}^\top \mathbf{d} + \frac{\Gamma}{\Delta t}\mathbf{D}\tilde{\mathbf{j}} = \mathbf{0}, \tag{3.29}$$

$$\left(\mathbf{A}^\top \mathbf{A} + \frac{\Gamma}{\Delta t}\mathbf{D}\right)\tilde{\mathbf{j}} = -\mathbf{A}^\top \mathbf{d}. \tag{3.30}$$

which retains the linear form

$$\mathbf{M}\tilde{\mathbf{j}} = \mathbf{b}, \tag{3.31}$$

where $\mathbf{M} = (\mathbf{A}^\top \mathbf{A} + \frac{\Gamma}{\Delta t}\mathbf{D})$, and $\mathbf{b} = -\mathbf{A}^\top \mathbf{d}$. Once the generalised impulses $\tilde{\mathbf{j}}$ have been found using Equation (3.31), the cell movements $\Delta\tilde{\mathbf{p}}$ resolving all m overlaps are given by $\Delta\tilde{\mathbf{p}} = \mathbf{D}\tilde{\mathbf{j}}$ (Equation (3.11)).

Note that, in Equation (3.30), mechanical work is being used as a regularising constraint on cell movement (i.e. matrix $\mathbf{D}$ regularises matrix $\mathbf{A}^\top\mathbf{A}$), so that the physical quantity being minimised in Equation (3.31) is potential energy plus work. However, other regularisation constraints are also feasible: in Appendix B, we present an alternative model in which cell movements are constrained using linear springs. In this case, minimising the total potential energy of the system produces a similar linear problem to Equation (3.30).

3.3.6 Iterative constraint identification

As we have described, an intuitive way of parameterising mechanical constraints for a system of cells (and thereby composing matrix $\mathbf{M}$ in Equation (3.31)) is to identify pairs of cells, or cells and surfaces, which are already in contact. However, knowledge of all the current overlaps is not necessarily sufficient for bringing the system to equilibrium, as resolving existing overlaps may result in the creation of new overlaps with neighbouring cells.

As an example, consider a hypothetical configuration in which two cells are overlapping, with a third non-overlapping cell nearby. Figure 3.6 shows an example of such as system. If we concern ourselves only with existing overlaps, the problem appears to just be that of separating the first two cells (Figure 3.6-A). However, doing so may create new overlap with the third cell (Figure 3.6-B). The 'hidden' constraint here is that the third cell must be moved along with the first two, as shown in Figure 3.6-C.

It is difficult to identify hidden constraints just by examining a given configuration of cells, because it is not clear whether a given cell movement will produce any new overlaps. To circumvent this problem, Rudge *et al*. proposed an iterative scheme to account for new overlaps created by cell movement [239]. This scheme consists of the following steps:

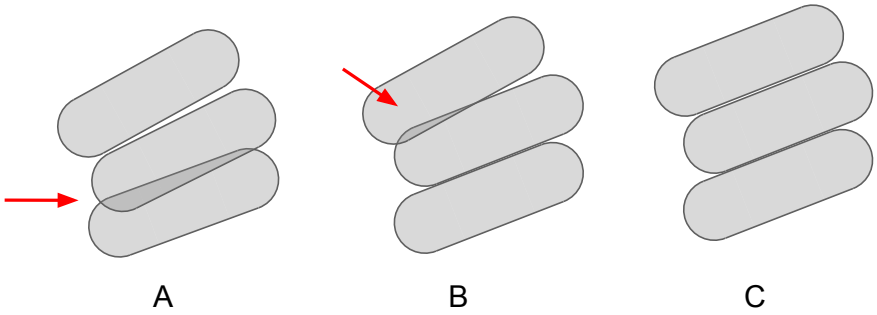

Fig. 3.6 Detecting only existing contacts between cells (A) is insufficient to resolve the cell relaxation problem: cell movements may then create new contacts not visible in the original configuration ('hidden' constraints, B). Logging the first, resolved contact and then repeating the contact-solving process again takes into account both constraints, and solves the relaxation problem fully (C).

1. Test a configuration for overlaps, and determine the impulses needed to resolve those overlaps.

2. If new overlaps are created as a result, then update the contact set to include these new overlaps whilst retaining (and updating) the old ones.

3. Solve this new system as before, logging the impulses required and adding them to the original set. The application of this impulse set creates a predicted configuration that can be tested for new overlaps as before.

4. Repeat the process, until the predicted configuration contains no new overlaps, or the iteration count exceeds a user-specified maximum N_{Con}.

5. Apply the resulting total impulse set to move the cells and resolve all contacts.

In principle, step 4 of the above algorithm should be performed for as many iterations as are necessary, to collect the complete set of constraints pertinant to a given configuration. For the parameters and protocols used in this thesis, however, exceeding the maximum number of iterations N_{Con} does not appear to be catastrophic, as any

overlaps that remain afterwards will always be identified and removed in the next timestep of the simulation.

3.4 CellModeller: parallelised model implementation

Having defined the abstract assumptions and mathematics of the Rudge model, we now move to describing how it is implemented in the CellModeller software package. An important practicality to consider at this point is performance: individual-based models need to be programmed efficiently, so that we can simulate systems containing as many cells as possible (maximum n).

However, Equation (3.31) involves a matrix of size $7n \times 7n$, requiring us to define and save hundreds of billions of floating point numbers for large cell populationes (supposing, for instance, $n = 10^5$). If we assume entries to be of double precision, this matrix would occupy a Terrabyte of information – well beyond the capacities of most desktop computers at the time of writing. To deal with such population sizes, we therefore require a high-performance implementation of this model, which CellModeller provides. Here we give a brief overview of the essential elements of the implementation, focusing on the methods used to improve performance. These elements are as follows:

1. Efficient algorithms for iterative contact-finding and updates;

2. Solving Equation (3.31) using a matrix-free conjugate gradient (CG) method, so that the size scaling is $\mathcal{O}(n \log n)$ instead of $\mathcal{O}(n^2)$ [239];

3. Parallel implementation using OpenCL, for running CellModeller on CPUs (Central Processing Units) or GPUs (Graphics Processing Units).

3.4.1 Efficient algorithms for identifying contacts

Computing cell movements requires us to parameterise cell contacts, as detailed previously. Before solving Equation (3.31), we first need to compile a complete list of all the contacts that appear in a given cell configuration.

This process, known as contact-finding, is computationally intensive. Firstly, since any cell can in principle be in contact with any other cell, we must check $\frac{1}{2}n(n-1)$ cells for contacts ($n-1$ because a cell cannot be in contact with itself; $\frac{1}{2}$ factor to avoid double-counting). Secondly, for each pair of cells to be checked, we must compute the shortest distance between those cells' line segments. Whereas computing the separation between two spheres is easy, algorithms to compute minimum segment separations are more computationally demanding [4], raising contact-finding costs further.

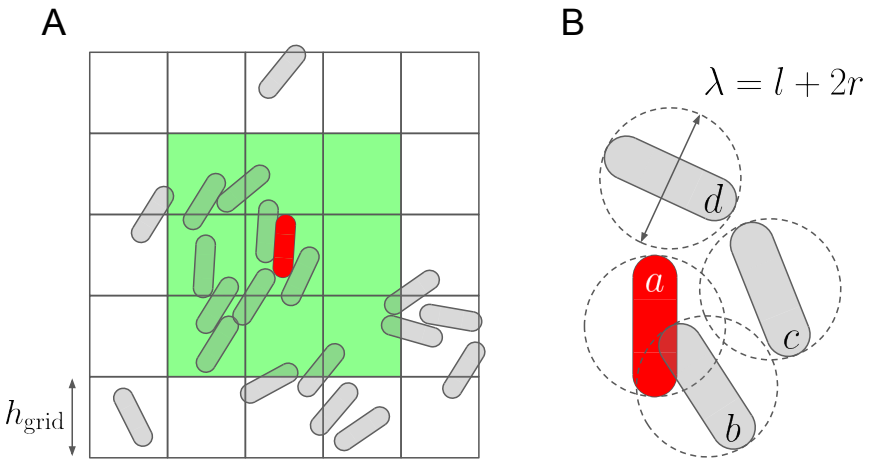

Fig. 3.7 CellModeller employs several methods to speed up the identification of cell-cell contacts. Cells are assigned to elements of a uniform grid (A) on the xy plane; when searching for the contacts of a focal cell (red) one has only to check cells in adjacent grid squares (green shading). Before applying the full shortest-distance algorithm, potentially-touching cell pairs a subjected to a computationally-cheaper bounding spheres test (B), which eliminates geometrically impossible contacts. 3-D cells are shown as 2-D silhouettes for clarity.

CellModeller uses established methods to reduce the computational cost of contact finding. These methods, shown in Figure 3.7, eliminate geometrically-impossible

contacts without having to run the full shortest distance algorithm described in [4]. Firstly, cell x and y coordinates are used to assign each cell to a specific square in a 2-D grid drawn on the xy plane, as shown in Figure 3.7-B.[6] Each grid element has a width h_{grid} slightly larger than the largest possible cell in the simulation, and the grid is expanded each simulation timestep so that the entire cell population always lies inside of it. The search for a focal cell's contacts can then be restricted to only those cells lying in the Moore neighbourhood of its grid square (Figure 3.7-B, green shaded area), since other squares are too far away for contact to be feasible. This reduces the number of contact checks to at most $9np + c$, where p is the maximum cell population of a grid square, and c is the overhead cost of sorting cells into their grid cells. Cells of lower index than the focal cell are ignored so as to avoid double contact-counting. Secondly, for any pair of capsules i, j to be in contact, their cell centres must be within a distance s of one another, where s is given by $(\lambda_i + \lambda_j)/2$; for greater separations, contact is geometrically impossible, regardless of cell orientation, which can consequently be ignored. This constraint gives rise to the so-called "bounding spheres" method, shown in Figure 3.7-C, which eliminates impossible contacts without having to use the more expensive shortest distance algorithm. Cells passing the second test are subjected to the full shortest distance test as described by [4]; cells subsequently found to be overlapping have their contact details $(\hat{\mathbf{n}}_k, d_k)$ stored to compute entries in matrix $\mathbf{A}$ in Equation (3.30).

3.4.2 Matrix-free conjugate gradient method

As discussed, large n makes for large $\mathbf{M}$ – potentially too large to be stored in a computer's memory at all. However, the matrix $\mathbf{M}$ in Equation (3.31) has some useful properties that can be exploited, avoiding the need to define or store it explicitly.

[6] Although the cell grid is 2-dimensional, cells can still move in 3-D. A 3-D gridding system that sorted cells according to their z-coordinate would be even more effective here, but has yet to be implemented in CellModeller.

Since $\mathbf{A}^\top\mathbf{A}$ and $\mathbf{D}$ are both symmetric (each projection matrix in $\mathbf{D}$ is symmetric by definition), $\mathbf{M}$ is also symmetric. $\mathbf{M}$ is also positive-definite, and Equation (3.31) is therefore amenable to being solved using an iterated conjugate gradient method, as described by Saad [241]. Matrix $\mathbf{M}$ only appears in the conjugate gradient algorithm as part of products with other terms, and so we can avoid explicitly defining or storing $\mathbf{M}$ itself.

CellModeller therefore uses the methods of iterated conjugate gradients, allowing up to N_{Sol} iterations to solve Equation (3.31) to within an absolute tolerance of ε_{CG} – i.e. such that

$$|\mathbf{M}\tilde{\mathbf{j}} - \mathbf{b}|_{L2} < \varepsilon_{\text{CG}}. \tag{3.32}$$

If more than N_{Sol} iterations are needed to meet this criterion, CellModeller raises an error message, and the simulation process is terminated.

3.4.3 Parallel programming

The Rudge model requires that numerous different calculations be performed at each timestep of the simulation. Fortunately, many of these calculations can be divided into smaller tasks, which, when carried out concurrently, accelerate computation. As described by Rudge *et al*. [239, 238], the CellModeller mechanics scheme is designed to exploit this property using parallel programming. As well as a frontend written in Python, handling serial operations and the program's user interface, CellModeller has an OpenCL backend that can run parallel processes on different types of CPU or GPU hardware.

Which parts of CellModeller operate in parallel? Figure 3.8 represents the Rudge model implementation as a flow diagram (left column), showing the tasks required for the removal of cell overlaps, and the Python functions responsible for carrying out these tasks (middle column). Broadly speaking, there are three types of operation that are parallelised (functions in **bold text**):

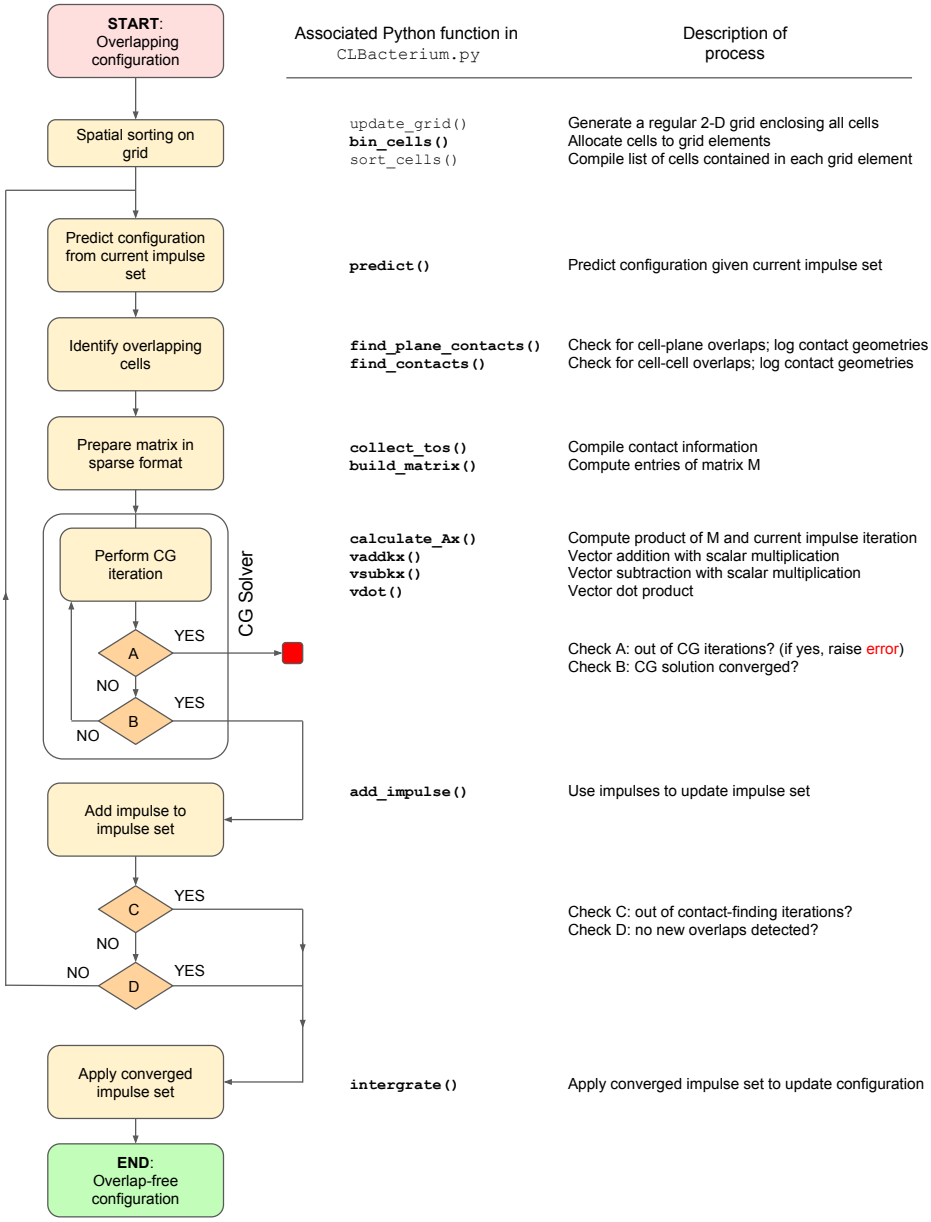

Fig. 3.8 Schematic showing the CellModeller implementation of Rudge's biomechanical model. Coloured boxes in flow chart (left column) indicate the sequence of processes for converting an overlapping cell configuration (top) to a non-overlapping configuration (bottom), to be carried out on each step of a simulation. Associated Python functions are shown (middle column), along with a description of their purpose (right column), for each process. Functions listed in **bold** are written as OpenCL kernels, such that the corresponding task can be completed by multiple OpenCL 'workers' operating in parallel.

1. Calculations regarding cells' spatial arrangement within a given cell configuration (e.g. `bin_cells()`, `find_plane_contacts()`, `find_contacts()`).

2. Compiling entries of the matrix $\mathbf{M}$ in a sparse format (e.g. `collect_tos()`, `build_matrix()`)

3. Individual matrix and vector operations associated with the conjugate gradients (CG) solver (e.g. `calculate_Ax()`), or with handling the resulting solution as part of the iterative search for hidden constraints (e.g `predict()`, `integrate()`, `add_impulse()`).

In these cases, parallelisation is possible because each part of the calculation is independent, and does not require input from, or coordination with, other parts[7] – except for a final synchronisation stage in which results are combined ready for use by subsequent processes. For example, a given pair of cells can be checked to see if they are in contact independently of the positions of all other cells; likewise, each row of a matrix-vector product can be computed independently of all other rows.

By contrast, some elements of the algorithm cannot be parallelised, because of the reliance of one part of the calculation on another. For example, the iterative contact-finding procedure (loop exiting check D in Figure 3.8) and iterative conjugate gradients solver (loop exiting check B) must run in serial, because each iteration depends on the previous step.

At the end of this chapter (Section 3.7), we test the performance of the parallelised scheme for a range of different domain geometries and initial conditions. In agreement with previous publications [239], we find that simulation performance shows impressive (and in some cases, sub-linear) scaling with cell population, but that running the mechanical relaxation scheme (Figure 3.8) is nevertheless the bottleneck to simulation performance. We interpret this as a justification of CellModeller's parallel

[7] In fact, these tasks might therefore be termed 'embarrassingly parallel'.

processing strategy: parallelising the mechanics scheme would likely have given the best improvement in overall performance.

First however, we discuss how the parameters of the model may be determined, and what modifications to the CellModeller implementation are necessary to address the research questions of this thesis.

3.5 Model parameterisation

We have now defined the Rudge model and outlined its implementation in the CellModeller software. However, the model depends on various parameters, values for which need to be defined. Here, we provide an overview of model parameter meanings, and how they can be assigned sensible values.

The parameters of the Rudge model fall into three main groups. These are:

1. Mechanical parameters, associated with the biophysical properties of the cells and their surroundings;

2. Geometric parameters, associated with cell geometry;

3. Numerical parameters, associated with the computational implementation of the model.

Mechanical and geometrical parameters are physical in nature – they correspond to real-world quantities and correspondingly have units which need to be defined. Numerical parameters are non-physical, and pertain more to the performance and stability of the numerical methods used to run model simulations (particularly, the contact iteration process, time stepping, and the iterative conjugate gradients scheme). Table 3.5 summarises the parameters, along with their values, units and sources, for each of these groups. Let us now visit each type of parameter in turn.

Table 3.2 Parameters used in the Rudge model

Parameter	Symbol	Value	Units	Source in [238]
Mechanical:				
Drag coefficient	ζ	1.0	$\mathrm{kg\,m^{-1}\,s^{-1}}$	-
Growth restriction cost	γ	Unspecified	$\mathrm{kg\,s^{-1}}$	-
Combined restriction factor	Γ	0.1	$\mathrm{m^{-1}}$	Assumed
Cell stiffness	K	Unspecified	$\mathrm{kg\,s^{-2}}$	-
Division axis noise	$\xi_{\hat{\mathbf{a}}}$	0.1	%	Assumed
Geometric:				
Min. cell birth length	l_0	1×10^{-6}	m	Measured
Cell radius	r	0.5×10^{-6}	m	Measured
Cell division length noise	ξ_l	1.5×10^{-6}	m	Measured
Cell growth rate	μ	5.58×10^{-4}	$\mathrm{s^{-1}}$	Measured
Numerical:				
Simulation timestep	Δt	45	s	Constrained by μ, r, l_0
Cell grid element size	h_{grid}	6×10^{-6}	m	Constrained by l, r
Max. contact iterations	N_{Con}	8	-	Fitted
Max. CG solver iterations	N_{Sol}	$7n$	-	Fitted
Absolute CG tolerance	$\varepsilon_{\mathrm{CG}}$	0.5×10^{-8}	m	Constrained by r

3.5.1 Mechanical parameters

So far, we have defined four mechanical parameters: the drag coefficient ζ, the growth restriction cost γ, the cell stiffness K, and an orientational noise factor $\xi_{\hat{\mathbf{a}}}$ associated with cell division (Table 3.5). However: only one grouping of these parameters actually appears in the final constraint system (Equation (3.30)): the combined restriction factor $\Gamma = \zeta/\gamma$, which is present both in matrix $\mathbf{D}$ and the coefficient $\frac{\Gamma}{\Delta t}$.

The parameters ζ and γ are difficult to measure directly, and so we cannot know their precise ratio Γ *a priori*. Nevertheless, the assumption that cells move in order to maintain approximate mechanical equilibrium implies that $0 < \Gamma \ll 1$, or else the cell configuration would remain under significant compression during growth. In practice, we find that Γ values between $\frac{1}{10}$ and $\frac{1}{500}$, produce qualitatively similar simulations; if desired, the parameter can be tuned to a particular value that best reproduces a feature of interest, such as boundary fractal dimension [238].

As for the noise parameter $\xi_{\hat{\mathbf{a}}}$, it is found this noise is significant only for symmetry breaking, and its actual value does not matter provided $0 < \xi_{\hat{\mathbf{a}}} \ll 1$ holds. Its primary role is to induce Eulerian buckling, preventing perfectly-aligned chains of cells from

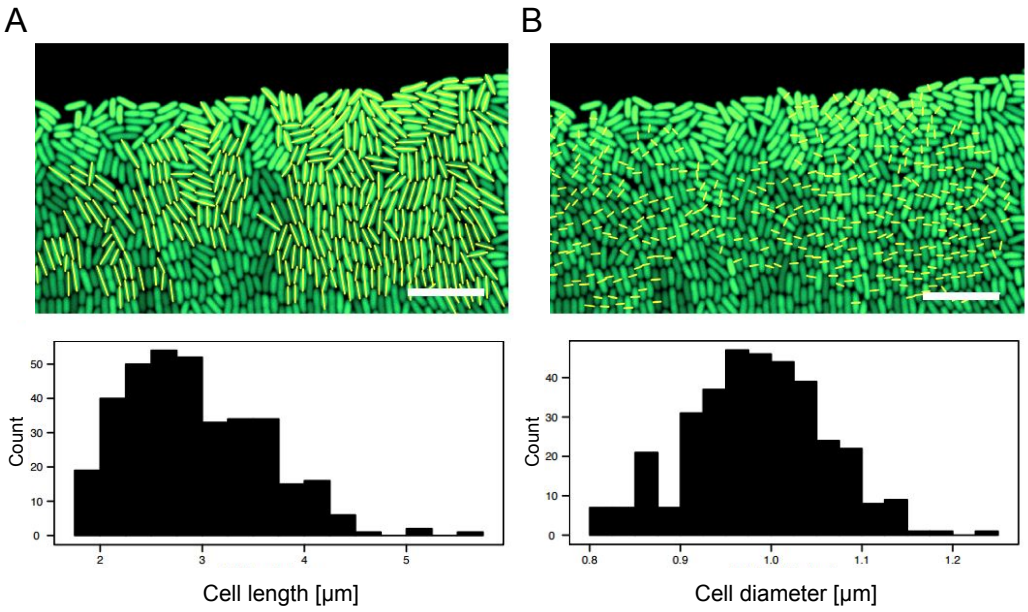

Fig. 3.9 Geometric parameters from the Rudge model can be extracted directly from confocal images of fluorescently-labelled *E. coli* bacteria. Automated image processing can be used to estimate mean cell tip-to-tip length (A) and diameter (B). Scale bars correspond to 10 μm; images and data taken with permission from reference [238].

forming [239]. This property can be exploited to constrain a simulation to a 2-dimensional plane without the use of confining surfaces, since setting the z-component of division axis perturbation vectors to 0 prevents cell buckling in the z direction.

3.5.2 Geometric parameters

The geometric parameters in the model are the minimum cell birth length l_0, the cell radius r, the cell division noise parameter ξ_l and the intrinsic cell growth rate μ (Table 3.5). Fortunately, these parameters are easy to estimate through direct observation. Provided cell outlines are clearly visible, high-resolution microscope images of bacterial colonies can be processed to measure the range of cell lengths and diameters present in a population. We demonstrate this procedure in Figure 3.9.

As shown in Figure 3.9-A, tip-to-tip cell length (λ) measurements in fluorescent BW27783 *E. coli* bacteria follow an approximately lognormal distribution, whose

width can be used to estimate both cell birth length and the variability in division length. Given that the distribution spans the range $2 \leq \lambda \leq 5.5\,\mu\text{m}$ and that cell length is approximately conserved on division, we can estimate that cells divide when they are between $2 \times 2\,\mu\text{m} = 4\,\mu\text{m}$ and $5.5\,\mu\text{m}$. This indicates that $\xi_l \approx 1.5\,\mu\text{m}$ and $l_0 = 2 - 2r \approx 1\,\mu\text{m}$. Diameter measurements (Figure 3.9-B) follow a normal distribution with low variability (10-20%), supporting a model based on a constant cell radius with a value of about $0.5\,\mu\text{m}$. Note that these parameter values are only examples – we go on to use and test a range of microbial shapes (i.e. a range of l_0 and r values) later in this thesis, in Chapters 5-7. Nevertheless, it is instructive to see how these parameters can extracted from microscope images.

Finally, the cell growth rate μ can be inferred from observed doubling times, τ_{growth},

$$\tau_{\text{growth}} = \frac{\ln(2)}{\mu}, \tag{3.33}$$

for a given bacterial species in exponential phase. For example, *E. coli* bacteria can achieve a doubling time of just 20 min when grown on rich media [93], corresponding to a growth rate of $\mu = 5.58 \times 10^{-4}\,\text{s}^{-1}$. However, microbes can only maintain these rapid growth rates so long as nutrient are plentiful; in practice, this is not generally true in microbial communities. We discuss how to account for this later on, in Chapter 4.

3.5.3 Numerical parameters

The five numerical parameters of the Rudge model are the simulation timestep Δt, the cell grid size h_{grid}, the maximum permitted number of contact-finding iterations N_{Con}, the maximum permitted number of conjugate gradient solver iterations N_{Sol}, and the absolute solver tolerance ε_{CG} (Table 3.5). Many of these parameters are directly constrained by the physical parameters defined above: for example, h_{grid} should be slightly larger than the largest value of $\lambda_i = l_i + 2r$ in the simulation, since this excludes the possibility of cells in non-adjacent grid elements from touching

whilst minimising the number of cells in each element that must be checked. Similarly, Δt and $\varepsilon_{\mathrm{CG}}$ are constrained by cell geometry: in the former case, no cell should be able to elongate by more than half the cell radius r in any timestep, as this could cause capsule line segments to intersect (this is undesirible, since then contact data would become degenerate and our overlap constraints would break down). Since cells elongate according to the equation $\Delta l_i = \mu l_i \Delta t$, we have $\max(\Delta l_i) = \mu \Delta t \max(l_i) = \mu \Delta t (2l_0 + 2r + \xi_l)$, limiting the timestep to

$$\Delta t < \frac{r}{2\mu(2l_0 + 2r + \xi_l)}, \tag{3.34}$$

or $\Delta t < 99.6\,\mathrm{s}$ using the *E. coli* parameters discussed above. CellModeller uses a default timestep significantly below this limit at just $\Delta t < 45\,\mathrm{s}$. Likewise, if our requirement that cell overlap be removed is to be meaniningful, we require $0 < \varepsilon_{\mathrm{CG}} \ll r$. In practice, setting a fairly high tolerance of $\varepsilon_{\mathrm{CG}} = 0.01r$ suffices.

Finally we have the iteration limits N_{Con} and N_{Sol}. In the case of N_{Con}, trial-and-error testing indicates that 8 contact-finding iterations is usualy sufficient to identify all contacts in a given system. We have noted previously that, when 8 iterations is not enough, missed-out constraints can be solved in subsequent simulation iterations. Meanwhile, setting N_{Sol} equal to the number degrees of freedom of the current cell population, $7n$, results in satisfactory performance – allowing the simulation more time to solve the constraint problem as its size (and therefore difficulty) increases.

3.6 Extensions to the Rudge model

The Rudge model and its implementation in the software CellModeller provide a useful basis on which to develop our individual-based modelling approach. Certain features of the model, however, benefit from extension or modification. Here we describe and explain how we have adapted CellModeller to suit the purposes of this thesis.

3.6.1 Volume expansion model

For our studies, we require an individual-based model that is able to represent different cell shapes. In order to do this fairly, we need a description of cellular growth that works the same way no matter what a cell's shape – i.e. independent of the value of l_0, the minimum cell segment length at birth. The growth model also needs to agree with biological observations about the way in which microbial cells grow. These requirements necessitate some small changes to the CellModeller cell growth scheme, which we detail here.

In the original version of CellModeller (Section 3.3.1), capsule cells grow *via* exponential elongation of their cylindrical segments, obeying the equation

$$\frac{dl_i}{dt} = \mu l_i, \tag{3.35}$$

where l_i is the cell segment length and μ the intrinsic growth rate, in the absence of mechanical restriction effects. Indeed, there is some experimental evidence to support this model of cellular growth: typically, the hemispherical poles of rod-shaped cells remain inert, and only the cylindrical section of the cell wall undergoes extension [278, 86]. Figure 3.10 ('Growth') provides a diagram of this scheme, showing a parent cell elongating (t_1-t_5) and subsequently dividing.

However, this segment-based growth model creates several problems for cells of different shapes. Firstly, truly round cells have a segment length of zero, which would result in a growth rate of zero according to Equation (3.6.1). Secondly, CellModeller does not conserve cell segment length during cell division events. Daughter cells are placed to fit inside the parent cell silhouette, reducing the total length of growing segment by $2r$, as shown in Figure 3.10 ('Division', left-hand side) As a result, a set of cells with a combined segment length $l_{\text{tot}} = \sum l_i$ will then grow at a rate dependent

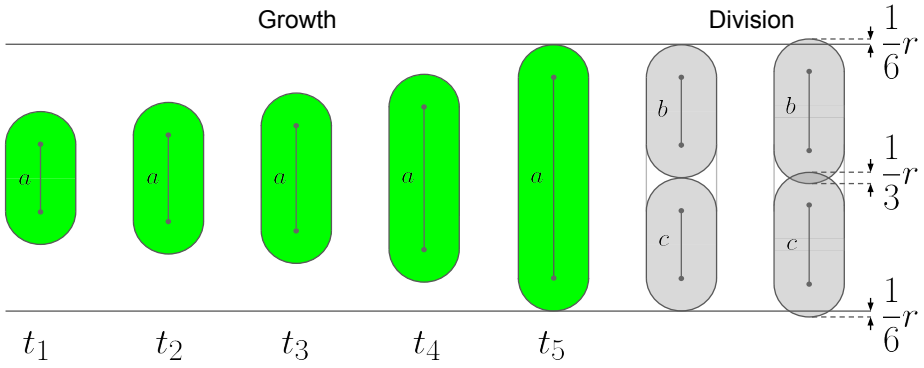

Fig. 3.10 Cell growth and division scheme for the Rudge model. A cell of index a grows in discrete steps t_1-t_5 according to the linearised exponential growth (Green cells). Once it meets a division criterion (doubled length or doubled volume), it divides into two identical daughters (grey cells, b and c). In the original growth-by-length model, both daughters fit within the parent cell silhouette (left pair of grey cells); in the growth-by-volume extra overlap is created (right pair).

on their shape: distributing l_{tot} over many small cells results in more division events and hence more losses than distributing the same l_{tot} over fewer, longer cells.

A more universal variable to associate with cell growth is volume – i.e. the volume enclosed by the cell membrane, equal to $\frac{4}{3}\pi r^3 + l_i \pi r^2$ for a capsule of length l_i and radius r. Provided cell volume is conserved upon cell division, a given total cell volume will always grow in the same way regardless of how it is partitioned into different cell shapes. Moreover, supported by experimental observations, previous individual-based models have used cell volume to describe exponential cell growth [154, 152].

With this in mind, we modified the CellModeller growth scheme as follows:

1. Cells grow according to the equation $\frac{dV_i}{dt} = \mu V_i$, and so increase in segment length by $\frac{dl_i}{dt} = \mu\left(\frac{4}{3}r + l_i\right)$ each timestep Δt;

2. Cell volume is conserved on cell division. Since this requires the daughter cells to be altogether $\frac{2}{3}r$ longer than their parent, new overlaps are created (cell placement is unchanged) as shown in Figure 3.10 ('Division', right-hand side).

Additionally, we modified CellModeller's overlap relaxation scheme to prevent cell growth from being slowed by mechanical pressure. In the original model, cell length is treated as a degree of freedom in the relaxation scheme such that cells reduce their growth rates (elongation Δl per simulation step) in response to mechanical forces from surrounding cells. While there is some experimental evidence that microbes experience such mechanical growth restriction [74], we chose to exclude this effect from the model, such that cell division rates are controlled only by the specific growth parameter μ.[8] We made this decision for two reasons:

1. As yet, there is little information that could be used to parameterise mechanical growth restriction, and to quantify its importance relative to nutrient growth limitations, in biofilm communities.

2. As discussed above, it is important that our growth model allows all cells to grow at the same intrinsic rate irrespective of their shape. Mechanical growth restriction could introduce confounding effects here, unfairly penalising particular shapes because of their different spatial arrangements in cell groups.[9]

Figure 3.11 shows that, in simulations of 2-D colonies, mechanical growth restriction can be controlled through the parameter Γ, which serves as a weighting factor for the length-change degree of freedom Δl in Equation A.16. High values of Γ result in high mechanical restriction, causing significant deviations from exponential growth behaviour (dashed line) and producing smaller colonies (end-state screenshots, right). Whilst setting $\Gamma = 0$ is not possible because of the consequent loss of matrix regularisation in Equation 3.30, low values of Γ (≤ 0.002) suffice to give approximately exponential growth for colonies of up to 10,000 cells. We will therefore use the value

[8] μ may in turn be coupled to the availability of a rate-limiting nutrient, as we go on to explain in Chapter 4

[9] This is not to discount such effects as impossible or uninteresting: indeed, it may be that certain microbial shapes *do* enable faster growth by alleviating growth-limiting mechanical pressure, as suggested in Reference [56]. We leave such questions for future studies, however.

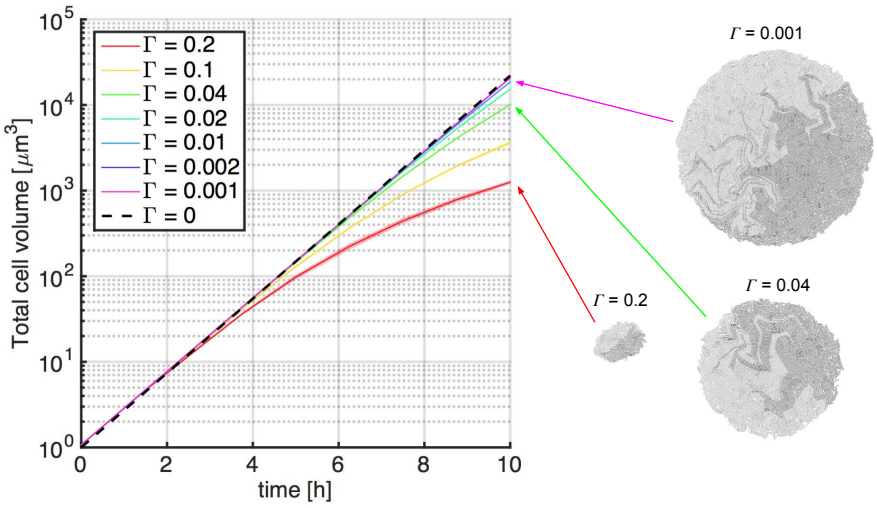

Fig. 3.11 Controlling mechanical restriction through the parameter ratio $\Gamma = \zeta/\gamma$. Simulations of 2-D colonies show that default value of $\Gamma = 0.1$ (yellow trace) results in significant growth restriction, with cells reducing their effective growth rates in response to mechanical compression by neighbouring cells, as shown by deviation from exponential growth behaviour (dashed line). Lower values of Γ make restriction effects less significant, resulting in larger colonies (end-state colony images, right). $\Gamma \leq 0.002$ suffices to give negligible restriction for colonies of this size.

$\Gamma = 0.002$ throughout this thesis, as a means to exclude the mechanical restriction effect built into CellModeller.

3.6.2 Periodic boundary conditions

In computational modelling, limitations in computer power constrain the length- and time-scales that can be simulated. Using a micro-scale model to simulate a macroscopic system is often impractical because of the computational expense involved. A standard work-around to this problem is to approximate the properties of a large system by simulating some smaller, representative section of it. This reduces the computational workload in exchange for some loss of realism.

To be representative, the smaller simulation domain needs to have boundary conditions that reflect what is going on in the full system, so that "edge effects" and other spurious artifacts are avoided. Conventionally, this is achieved by imposing some combination

of periodic boundary conditions on the simulation domain, so that the domain becomes an element in some infinite tessellation of identical elements. This makes the domain effectively edgeless [222, 154, 152, 199].

For an individual-based model, periodic boundary conditions require two features of a computational domain: consistency of motion, and consistency of interaction. Specifically:

1. When an individual leaves the domain by one edge or face of the domain, it must re-enter *via* the opposite face. Its motion must not be affected by this process.

2. Individuals need to be able to interact over opposite faces of the domain just as they would within the domain.

Figure 3.12 shows three diagrams summarising these principles. Individuals (colored capsules) occupy a rectangular domain (blue grid); simulating periodic boundary conditions in the horizontal direction is equivalent to changing the domain topology to that of a cylinder (3.12-A). To achieve this, individuals need to be able to move through opposing borders of the domain seamlessly (3.12-B) as well as interact across them (3.12-C).

In order to extend the CellModeller contact search scheme to a domain that is periodic in the x and y direction, we redefine cells' Moore neighbourhoods so that squares on the edge of the grid are treated as adjacent to those on opposite edges. Cell locations in the grid are also used to extend the conventional contact checks so that cells can interact *via* their minimal images. Figure 3.12-C shows this process in action: when searching for the contacts of the blue cell, the red and green cells are identified as lying in blue's neighbourhood. Blue is too far away to interact with red or green directly, but may still interact with the images of these cells. Using the minimum image convention, the closest image of a cell j to a focal cell i in an xy-periodic domain measuring L_x by

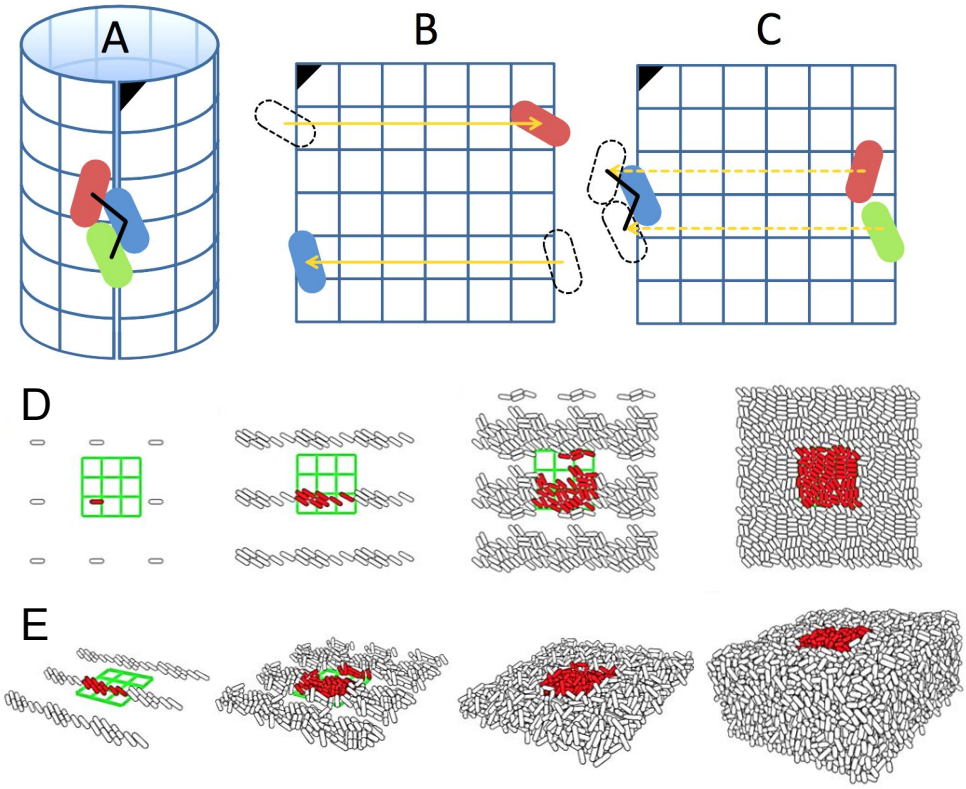

Fig. 3.12 Periodic boundary conditions require continuity in both cell movement and mechanical interactions over opposite borders of the simulation domain (A). To achieve this, cells that leave the domain are moved back onto at the opposite edge (B). Cell contact finding also operates over the domain edges (C). In (D), we show snapshots from an example 2-D periodic simulation using the extended CellModeller scheme. Cells (red) and their nearest images (grey) are both shown; the 3-by-3 cell grid used to compute contacts is highlighted in green. (E) shows an analogous 3-D simulation (periodic in x and y but not z).

L_y can be found at coordinates

$$(\text{Nearest image location})_j = \mathbf{p}_j + a\hat{\mathbf{x}} + b\hat{\mathbf{y}}, \tag{3.36}$$

where $a \in \{-L_x, 0, +L_x\}$, and $b \in \{-L_y, 0, +L_y\}$. The coefficients a and b can be chosen by comparing the grid squares that n and m lie in: if the indices of the squares differ by more than 1 in, say, the x-direction, then i must be closer to j's image than to j itself along this axis. This means that a will be $\pm L_x$, depending on the sign of the difference in the square indices.

Figure 3.12-D and E provide some examples of our periodic boundary condition implementation, showing a sequence of snapshots taken of 2-D (D) and 3-D (E) *xy*-periodic periodic simulations. Here, 'real' cells are highlighted in red, and their nearest images are shown in grey to help verify continuity of cell motion and interaction.

3.7 Example simulations and performance testing

In this final section, we discuss profiling tests to assess the performance of CellModeller in a range of different simulation scenarios. The purpose of these tests is to establish how the program's performance scales with cell group size, and to identify which parts of the program most limit performance.

To this end, we ran four types of CellModeller simulation: box simulations in 2- and 3-D (cells growing upwards in a walled domain) and open simulations in 2- and 3-D (cell movements unconstrained by walls). Box simulations were initiated by placing 100 cells on the base of the box (along a 400 µm line in 2-D, and on a 40 µm-by-40 µm square in 3-D), with randomised cells positions, orientations and volumes. Open simulations began with two such cells placed 6 µm apart. All simulations were run to a fixed end-point of 10,000 cells, and configured to report wallclock and process times alongside normal output configuration files.

The results of these profiling simulations are shown in Figure 3.13, with performance data from box simulations shown on the first row (Figure 3.13-A), and those from open simulations on the second (Figure 3.13-B). The left-hand column shows total simulation ('wallclock') time as a function of increasing cell population (N), indicating higher performance for 2-D simulations than for 3-D simulations, in both rows.[10] This observation may be rationalised as follows: firstly, simulations are less efficient in 3-D because the CellModeller contact-finder (see Section 3.4.1) only sorts cells by location

[10]We note that traces have a staircase-like form in row B: this is due to synchronisation in cell division events, such that all cells periodically divide at approximately the same time, creating huge spikes in the number of cell overlaps (and consequently in the difficulty of the energy minimisation problem).

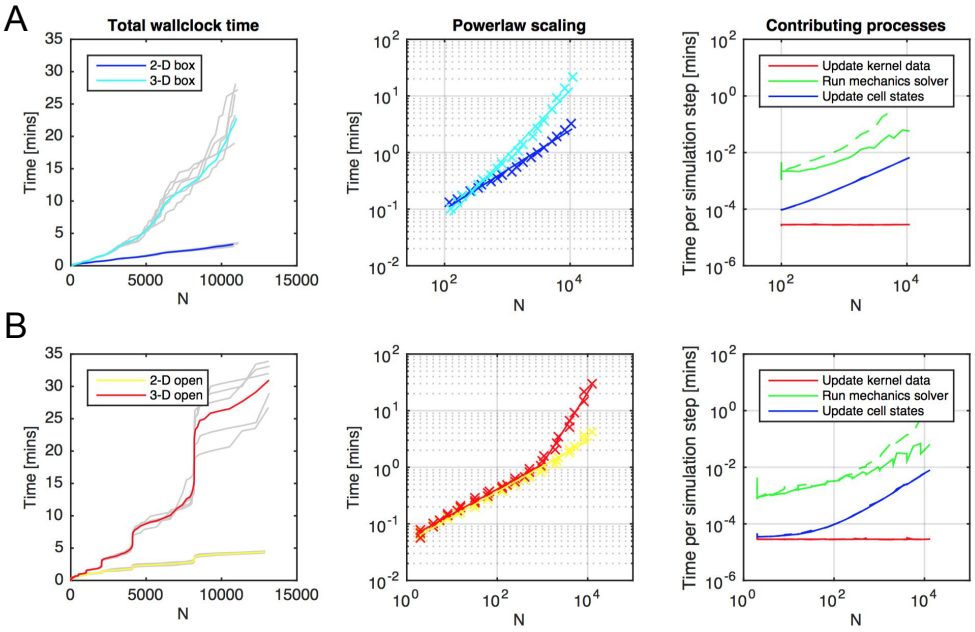

Fig. 3.13 Tests of CellModeller performance as a function of cell count (N) for different simulation types, comparing enclosed (row A) and open domains (row B) in 2 and 3 dimensions. Plots of total simulation time (left column) show that 3-D simulations are generally more computationally intensive than 2-D analogues. Grey traces show individual simulations and coloured lines mark means; sample of 5 simulations per case. Replotting data means on logarithmic axes (middle column, crosses) allows powerlaw-like performance scaling to be quantified using linear regression (fitted lines). Additional logarithmic plots (right column) show individual process durations within simulation timesteps, highlighting the mechanics solver as the overall performance bottleneck. Solid and dashed lines correspond to 2- and 3-D simulations respectively.

along the x and y axes. If a simulated colony expands along the z axis, each element of the cell sorting grid will contain progressively more cells, necessitating more contact checks per cell than in 2-D. Secondly, cell coordination number is higher in 3-D, such that any given cell will have more contacts (i.e. matrix $\mathbf{M}$ is less sparse, and requires more time to compile).

In the middle column of Figure 3.13, we quantify this performance data by replotting trace means on logarithmic axes. Here, each dataset produces an approximately linear trace, suggesting that total computational time t_{tot} can be described by a powerlaw of

the form

$$t_{\text{tot}} = aN^b, \tag{3.37}$$

where N is the number of cells, and where a and b are constants. The exponent b corresponds to the gradient of the line in each case, and summarises how program performance scales with N. Note that for open 3-D simulations (Figure 3.13-B, red crosses), the line gradient suddenly increases around the $N = 1000$ mark, and so we have fitted a separate line for each section of the data.

The values for the scaling exponents are as follows: $b = 0.699$ (2-D box, cyan); $b = 1.151$ (3-D box, blue); $b = 0.448$ (2-D open, yellow). In other words, performance scaling is sub-linear in 2-D, but rises more rapidly with N in 3-D. For the open 3-D simulations (red), $b = 0.440$, rising to $b = 1.260$ for $N > 1000$. In this case, cell group expansion is initially planar (scaling like a 2-D simulation) but later becomes more isotropic (scaling like a 3-D simulation), resulting in two separate powerlaw behaviours.

Finally, in the right-hand column of Figure 3.13 we plot the calculation times associated with the three main processes carried out in each timestep of a CellModeller simulation: updating the backend data available to the OpenCL kernels (red traces), running the mechanics solver (green), and updating frontend cell state data (blue). These data indicate that the mechanics solver is the performance bottleneck, justifying the extensive use of parallel programming in implementing this process.

3.8 Conclusions

Individual-based models provide a natural and powerful tool for investigating the influences of cell morphology within a microbial community. In this chapter, we have discussed tools and techniques which allow non-spherical cell shapes to be incorporated into individual-based models. In particular, we have shown how to

derive, implement and extend one such model, the Rudge model, which describes the dynamics of a growing microbial colony using a constraint-based method.

Implemented as the GPU-accelerated software CellModeller, the Rudge Model allows us to flexibly model mechanical interactions within large microbial communities, containing different cell shapes. We will therefore use CellModeller (along with the modifications described in this chapter) as a basis for further work in the remainder of this thesis. In the next chapter, we discuss methodology for extending the CellModeller framework to incorporate interactions with chemical solutes, in order to create a model that can explore the competitive ramifications of cellular shape.

4

Creating a hybrid model of biofilm development

Abstract

Like all living organisms, microbes need to eat in order to survive and reproduce. The fundamental processes of life, cellular respiration (catabolism) and the biosynthesis of macromolecules (anabolism)—carbohydrates, proteins, lipids, DNA and RNA—all rely upon microbes obtaining a supply of energy and nutrients from their environment [47, 175]. Competition for these resources is a fundamental theme of biology, and is one of the defining characteristics of microbial communities [295, 94, 63].

In the previous chapter, we described an individual-based model for describing interactions between cells of different shapes. In this chapter, we extend this model by coupling cell growth rates to the availability of nutrients, allowing us to simulate competition between differently-shaped strains in a community. We begin by defining partial differential equations for describing nutrient transport and uptake, noting the assumptions made and defining the domain of applicability of the resulting model. We then show how this representation can be implemented and added to the mechanics model described in Chapter 3, creating a 'hybrid framework' that we use in subsequent chapters.

4.1 Introduction

Compared with humans, microbial metabolism is very diverse [212, 175]: microbes can extract energy and nutrients from organic or inorganic compounds [49, 245], from the atmosphere [245, 45], or from sunlight itself [77, 156]. The metabolic strategy

employed by a particular microbe is a crucial determinant of the ecological niches it can inhabit, and the role it plays in its respective ecosystem [148]. Metabolism can also be used to differentiate and classify microbes: for example, many lab-grown bacteria (e.g. *E. coli* and *B. Subtilis*) are chemoheterotrophs[194], meaning that they depend on organic chemicals for their supply of carbon and energy.

The need to absorb nutrients and excrete waste requires all microorganisms to exchange chemicals with their environment – a task they achieve using arrays of transporter proteins embedded in their plasma membranes [109]. Microbes also secrete various products to aid their nutrition, collecting ions with scavenger molecules (e.g. siderophores [205]) and digesting large molecules with extracellular enzymes [22] or enzyme complexes (e.g. cellulosomes [15]).

When microorganisms have a plentiful supply of nutrients, they can grow and divide rapidly, leading to an exponential increase in cell biomass [194, 278]. However, nutrient supplies often become limiting when microbes live together in communities [21], creating the steep solute gradients that are a hallmark of this habitat [264]. As we discussed in Chapter 1, such limitations exert powerful effects on community development – for example, they can alter community structure (the spatial distribution of biomass) by inducing growth instabilities at the community's outer surfaces, producing the 'finger'-like edifices and branched patterns observed in microbial biofilms and colonies [105, 186, 146].

Nutrient scarcity strongly affects the biology and ecology of microbial communities. Rapid cell growth is often limited to the outer surfaces of biofilms, where the supply of limiting resources is richest [191]. This spatial heterogeneity produces a selective pressure that favours any phenotype granting access to these valuable positions. For example, in colonies of *P. aeruginosa*, increased EPS secretion can help improve resource access by pushing secretor phenotypes towards the upper surface of the community [144, 296]. Limited nutrient access also alters the spatio-genetic composition[1]

[1] I.e. the spatial distribution of different strains or species of microbe

of a community: when only a small number of microbes can grow, the community becomes more susceptible to genetic drift – leading to particular genotypes becoming locally 'fixed', and reducing microbial diversity. The link between nutrient limitation and spatial segregation is well-established both experimentally and theoretically [115, 151], and has important consequences for mediating social interactions between microbes in a community [199, 294].

Thus, nutrient limitations are major source of physical and biological heterogeneity in microbial communities, necessitating their inclusion in our model. The individual-based model (CellModeller) described in Chapter 3 extends previous models of microbial communities, by including biomechanical interactions between non-spherical cells – yet it currently lacks the functionality to model nutrient limitations.[2] In order to assess the effects and function of cellular shape in a competitive community environment, therefore, we need to couple CellModeller to a description of nutrient fields.

The objective of this chapter, therefore, is to implement and test a model of solute transport in a biofilm community, and to pair this model with CellModeller to create a framework incorporating both cell shape and solute interactions. We begin first by describing an existing solute interaction model and its boundary conditions, defining its underlying assumptions, and reducing it to a simplified non-dimensional form.

[2]The version of CellModeller published in [239] does contain some functionality for modelling cell-cell chemical interactions, through the exchange of diffusing chemical signals. However, this implementation is insufficient for our purposes, because it makes very restrictive assumptions about the behaviour of chemical fields at the simulation domain boundary.

4.2 Defining a continuum solute transport model

4.2.1 Transport and growth equations

An established method for modelling the distribution of solutes in a biofilm is to define a partial-differential equation of the form

$$\underbrace{\frac{\partial u}{\partial t}}_{\text{Accumulation}} = \underbrace{D\nabla^2 u}_{\text{Diffusion}} + \underbrace{R}_{\text{Reaction}} . \tag{4.1}$$

This reaction-diffusion equation (RDE) describes the variation in a solute's concentration, u, in space $\mathbf{x} = [x, y, z]$ and time t. As the name suggests, this variation is governed by two key processes:

- **Reaction**: the creation or removal of solute molecules, represented by a reaction term $R = R(u, \mathbf{x}, t)$;
- **Diffusion**: the tendency for solute molecules to spread out, moving from regions of high concentration to low. This spreading process is modelled by the Laplacian $\nabla^2 u = \frac{\partial^2 u}{\partial x^2} + \frac{\partial^2 u}{\partial y^2} + \frac{\partial^2 u}{\partial z^2}$, and weighted by the diffusivity parameter D, which controls the rate of spreading out.

Reaction-diffusion equations are widely used in biofilm modelling [291, 290, 279, 147], and many existing IbMs incorporate a continuum description of solute fields using this kind of equation (an approach known as the continuum-discrete or 'hybrid' method) [154, 297, 159]. In this chapter, we will examine a specific instance of this equation, in which u represents the concentration of a rate-limiting nutrient, such as oxygen. In this case, the reaction term R in Equation (4.1) corresponds to nutrient uptake by microbes. Each microbial cell i requires this nutrient in order to grow, and therefore has its specific growth rate, μ_i, coupled to the local nutrient concentration u_i

Variable	Description	Units
u(x,y,z,t)	Nutrient concentration	$\mathrm{kg\,m^{-3}}$
t	Time	s
x,y,z	Cartesian coordinates	m
$\phi(x,y,z,t)$	Local cell volume fraction	—

Table 4.1 Nutrient model variables

using

$$\frac{dV_i}{dt} = \mu_i V_i = \mu_{\max}\left(\frac{u_i}{u_i + K}\right) V_i, \tag{4.2}$$

where V_i represents the volume of cell i, $\mu_{\max}$ is the cell's maximum specific growth rate, and K is a saturation constant. Here, the 'Monod' function, $\mu_{\max} u_i/(u_i + K)$, is an empirical description of microbial growth kinetics, characterising a transition from a 1^{st}-order growth at low nutrient concentration ($u_i \ll K$), to a 0^{th}-order growth at high nutrient concentration ($u_i \gg K$). In essence, it states that microbial growth is saturating, increasing with nutrient availability up to a maximum rate $\mu_{\max}$ [194, 147]. Using this coupling, cell growth rates throughout a biofilm then depend on variations in local nutrient concentration, which we can describe using Equation (4.1). If microbes are consuming nutrient for growth as in Equation (4.2), then the reaction term R in Equation (4.1) is given by

$$R = -\frac{1}{\gamma}\mu_{\max}\left(\frac{u}{u + K}\right)\rho\phi(\mathbf{x},t), \tag{4.3}$$

Here, $\frac{1}{\gamma}$ represents the amount of nutrient consumed per unit cell biomass, ρ the maximum biomass density, and ϕ the local cell volume fraction as a function of space $\mathbf{x}$ and time t. The product $\rho\phi$ approximates the discrete arrangement of cells in space as a continuous density function, and so assumes that concentrations u vary in space on longer lengthscales than those of individual cells. The dependent and independent variables of this model (respectively x, y, z, t and u, ϕ) are summarised in Table 4.1.

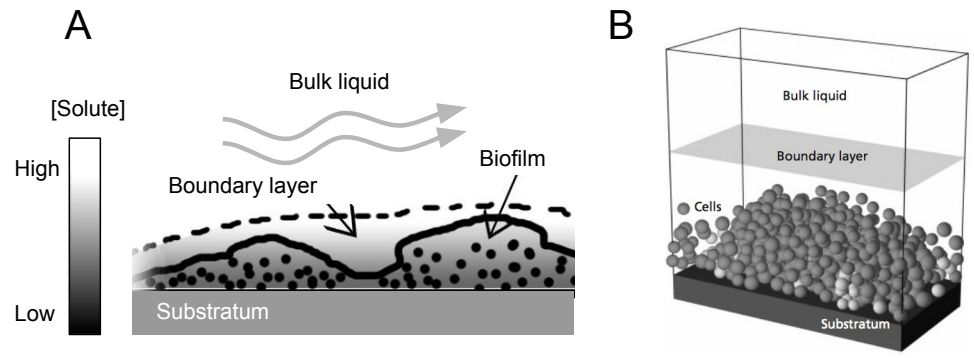

Fig. 4.1 Boundary conditions for biofilm models. Diagram A shows a cross section of a typical biofilm growing in a fluid bath. For a generic solute, advective transport (grey arrows) is rapid in the bulk liquid, but is much slower close to the surface of the biofilm. The result is a boundary layer (dotted line) within which diffusion is the limiting transport process. These observations motivate a simplified model of solute behaviour near the biofilm (B): the bulk liquid acts as an ideal source of solute at some height δ above the top of the biofilm, while the impermeable substratum prevents solute from leaving through the base of the domain. Diagram B taken with permission from [154].

4.2.2 Model domain, boundary conditions and parameters

Having specified equations to describe nutrient transport in a biofilm, we now need to define the domain on which these equations are to be solved, and the values of the physical parameters governing them. In doing so, we must also consider what the behaviour of our model will be at the domain's boundaries, and specify boundary conditions for our solute equations accordingly.

How large should our domain be? Biofilms found in nature often contain billions of microbial cells, and it is therefore not usually possible to model an entire biofilm using individual-based approaches. A typical work-around is to instead model a small 2-D or 3-D section of a biofilm, and assume that the behaviour of this section approximates that of the whole community [222, 223, 154]. In practice, this means solving transport equations on domains with very simple geometries, e.g.

1. 2-dimensional domains spanning $[0, L_x] \times [0, L_z]$, corresponding to a vertical slice through the biofilm;

2. 3-dimensional domains spanning $[0, L_x] \times [0, L_y] \times [0, L_z]$, corresponding to a vertical section of the biofilm.[3]

Assuming an upper population limit of approximately 10^5 cells [239], each with a diameter of roughly 1 µm, our domain size limit can be estimated as

$$L = \sqrt[3]{10^5 \times 1\,\mu m^3} \approx 40\,\mu m \tag{4.4}$$

in 3-D, or $L = \sqrt[2]{10^5 \times 1\,\mu m^2} \approx 300\,\mu m$ in 2-D. While less realistic, 2-D domains therefore allow longer lengthscales to be simulated for the same computational cost.

When specifying the boundary conditions of these domains, we need to account for the processes occurring in their immediate surroundings. Figure 4.1-A depicts a typical context for biofilm growth. The biofilm grows on a fixed surface, and is immersed in a fluid bath, which continuously supplies cells in the biofilm with the nutrients they require for growth. The 'bulk' fluid above the biofilm is flowing and well-mixed, so that the nutrient concentration u is maintained at a constant value u_0 [79]. However, close to the biofilm's surface, fluid flow is reduced, forming a so-called diffusive boundary layer [73, 280]. Within this layer, the supply of nutrient into the biofilm is limited by diffusion, so that $u(\mathbf{x}, t) < u_0$. As the biofilm grows upwards, the position of the boundary layer surface moves upwards with it.

Previous cellular-automata and individual-based biofilm models [222, 154, 297] have approximated these surroundings using the following set of domain boundary conditions:

- Let the domain include both the biofilm and the diffusive boundary layer above it, so that the top surface of the solute domain ($z = L_z$) is the upper surface of the boundary layer, while the bottom surface ($z = 0$) is the beginning of the substratum (Figure 4.1-B).

[3] Note the convention for naming the vertical axis z in both cases.

- Assume that the boundary layer has a flat, horizontal profile, and is of minimum thickness δ. Make the boundary layer track the upper surface of the biofilm (i.e. the cell configuration, $\{\tilde{\mathbf{p}}_i\}$, defined in Chapter 3) by setting $L_z = \delta + \max(p_z)$, where $\max(p_z)$ denotes the z-coordinate of the highest cell in the biofilm.

- Set the Dirichlet boundary condition $u(L_z) = u_0$, representing nutrient supply from the bulk liquid.

- Set $\nabla u \cdot \hat{\mathbf{k}} = 0$ at $z = 0$, where $\hat{\mathbf{k}}$ is the unit vector in the z-direction, representing the impermeability of the substratum to solute flux.

- On the side walls of the domain ($x = 0,\ x = L_x,\ y = 0,\ y = L_y$), impose either

  – Zero-flux boundary conditions, $\nabla u \cdot \hat{\mathbf{n}} = 0$, where $\hat{\mathbf{n}}$ is the unit vector normal to a given boundary, or

  – Periodic boundary conditions, such that

$$u(x = 0) = u(x = L_x), \quad u(y = 0) = u(y = L_y), \tag{4.5}$$

and

$$\left.\frac{\partial u}{\partial x}\right|_{x=0} = \left.\frac{\partial u}{\partial x}\right|_{x=L_x}, \quad \left.\frac{\partial u}{\partial y}\right|_{y=0} = \left.\frac{\partial u}{\partial y}\right|_{y=L_y}. \tag{4.6}$$

These boundary conditions are written for 3-D domains. Analogous boundary conditions apply in 2-D, except that the domain then has zero thickness in the y direction, so that we no longer have to specify boundary conditions at $y = 0$ and $y = L_y$.

This type of nutrient-limited growth model has been used extensively in previous models [222, 154, 297]. It represents a logical and convenient starting point for us, because the parameters governing the model have already been measured, and because the model's behaviour has been validated against experimental data. Some example

parameters for oxygen-limited growth are shown in Table 4.2, listed along with their units and source.

Before using this model, however, it is important to define the assumptions underpinning it, so that we can understand its domain of applicability, as well as the physical meaning of its parameters and variables.

4.2.3 Model assumptions

There are several important assumptions built into this model that we need to be aware of. Firstly, biofilms are heterogeneous systems, containing a multitude of material phases (cells, EPS, bubbles, channels and so forth) and spatial scales [264, 72]. Consequently, models of biofilm transport phenomena, and the physical meanings of their parameters and variables, change according to the spatial scale of interest. The model we have described is a macroscopic picture of transport phenomena: by writing Equations (4.1) and (4.3), we are assuming that the biofilm behaves as a single, homogeneous phase, with a single, spatially-averaged concentration field u. This homogenisation is a reasonable approximation on lengthscales larger than those of individual cells, provided that average concentrations in each phase of the biofilm (cells, medium, etc) remain in equilibrium, and do not change too quickly in space [291, 290].

Parameter	Description	Value	Units	Source
u_0	Bulk oxygen concentration	3.84×10^{-3}	$\mathrm{kg\,m^{-3}}$	[222]
D	Oxygen diffusivity	2.0×10^{-9}	$\mathrm{m^2\,s^{-1}}$	[222]
ρ	Cell biomass density	290	$\mathrm{kg\,m^{-3}}$	[222]
$\mu_{\max}$	Maximum specific growth rate	15.2×10^{-6}	$\mathrm{s^{-1}}$	[222]
K	Monod saturation constant	0.35×10^{-3}	$\mathrm{kg\,m^{-3}}$	[222]
γ	Biomass yield	0.045	—	[222]
δ	Boundary layer thickness	80.0×10^{-6}	m	[222]

Table 4.2 Example parameters for nutrient modelling

However, it is important to remember that other representations apply at different spatial scales. For example, subcellular-scale models of transport have to take into account subcellular-scale details, such as interactions with transported complexes in the cell membrane, and differences in extra- and intra-cellular solute concentrations [291, 290]. On a molecular scale, reaction and transport processes (e.g. Brownian motion, receptor binding) become stochastic instead of deterministic, and a different model then applies [242, 16, 38]. Mathematical techniques such as spatial averaging ('upscaling') can be used to convert between these descriptions and relate effective parameters on each scale [97, 290].

Further, Equation (4.1) also assumes that diffusion is isotropic and constant in space – in reality, it is neither. Biofilms are mostly comprised of water, yet diffusivities measured in biofilms are consistently less than those in aqueous solutions, for solutes of various molecular weights [264]. This is because biofilms are full of cells and other obstacles that make molecular diffusion more tortuous and slow. Further, the nematic ordering effects described in Chapter 3 could also make diffusion anisotropic (so that $D\nabla^2 u$ is replaced with $\nabla \cdot (\mathbf{D} \cdot \nabla u)$, with $\mathbf{D}$ a diffusion tensor), by making it easier for solutes to diffuse in some directions (such as in parallel to a group of axially-aligned cells) than others [56].

In Equation (4.2), cell growth is controlled entirely by the availability of a single nutrient. This assumption may seem to clash with our introductory observation that microbes require multiple substrates to survive. In practice however, the supply of one of these necessary solutes often becomes limiting [194, 152, 21], and so we need consider only its concentration in order to predict cell growth rates [194]. Further, Equation (4.2) supposes that the microbial response to nutrient availability is lag-free and not subject to regulation – i.e. parameters K and $\mu_{\max}$ are fixed, so that growth rate is purely determined by the local nutrient concentration u_i. Cells do not incur maintenance costs, and remain viable indefinitely regardless of nutrient concentration. In other words, a non-growing cell will never die of starvation, and can start growing

once more as soon as its nutrient access improves. These assumptions generally hold for timescales of minutes to days, but are less realistic on longer timescales [21].

Our model neglects several couplings between biofilm development and fluid motion in the bulk liquid. In reality, shear forces from fluid can alter biofilm structure, resulting in streamer formation and biomass detachment [293, 221]. For simplicity however, we ignore hydrodynamic interactions between the bulk fluid and the biofilm, and neglect biomass detachment so that cells are never removed from the computational domain. We also assume that the bulk fluid behaves as a perfect nutrient source, and that the boundary layer has a flat profile independent of the arrangement of cells beneath it.

Having defined the model and its assumptions, we are almost ready to begin implementing it as part of the CellModeller framework. Before we devise a method for solving our model equations, however, we can simplify our model further by converting it to a non-dimensional (unitless) form. This procedure offers several advantages [127, 197]: model variables are scaled in terms of natural units, making their meaning more intuitive, and their values close to unity – reducing the model susceptibility to computational error when solved numerically.

4.2.4 Dimensional analysis

Here we non-dimensionalise Equations (4.1) and (4.2), and identify intrinsic timescales for the processes involved in the nutrient model. We use this analysis to justify a separation of timescales that allow the dynamics of Equation (4.1) to be ignored, and derive dimensionless control parameters that govern model behaviour.

To reiterate, our dimensional equations are

$$\frac{\partial u}{\partial t} = D\nabla^2 u - \frac{1}{\gamma}\mu_{\max}\left(\frac{u}{u+K}\right)\rho\phi(\mathbf{x},t), \tag{4.7}$$

which describes how the nutrient concentration field $u = u(\mathbf{x},t)$ varies in time and space, and

$$\frac{dV_i}{dt} = \mu_{\max}\left(\frac{u_i}{u_i + K}\right)V_i, \tag{4.8}$$

specifying how each rapidly each cell grows, in response to the nutrient concentration it experiences. Beginning with (4.8), we define the unitless variables

$$\bar{t} = t/\tau_d, \quad \bar{V}_i = V_i/l^3, \quad \bar{u}_i = u_i/u_0, \tag{4.9}$$

where τ_d is the minimum cell doubling time given by $\frac{\ln 2}{\mu_{\max}}$, given in s, l is the diameter of a microbial cell in m, and u_0 is the bulk (maximum) substrate concentration in $\mathrm{kg\,m^{-3}}$. Using these scaled variables, we can rewrite (4.8) as

$$\frac{d\bar{V}_i}{d\bar{t}} = (\tau_d \mu_{\max})\frac{\bar{u}_i}{\bar{u}_i + K/u_0}\bar{V}_i, \tag{4.10}$$

which simplifies to

$$\frac{d\bar{V}_i}{d\bar{t}} = \ln 2\frac{\bar{u}_i}{\bar{u}_i + K/u_0}\bar{V}_i. \tag{4.11}$$

To non-dimensionalise (4.7), we can additionally define scaled spatial coordinates

$$\bar{x} = x/l, \quad \bar{y} = y/l, \quad \bar{z} = z/l, \tag{4.12}$$

which gives

$$\frac{1}{\tau_d}\left(\frac{\partial \bar{u}}{\partial \bar{t}}\right) = \frac{D}{l^2}\left(\bar{\nabla}^2\bar{u}\right) - \frac{\rho\mu_{\max}}{\gamma u_0}\left(\frac{\bar{u}}{K/u_0 + \bar{u}}\phi(\mathbf{x},t)\right). \tag{4.13}$$

The model incorporates three key temporal processes in the biofilm: cell growth and division, solute diffusion and solute uptake by cells. Each of these processes takes place on a particular timescale. Table 4.3 compares estimates of these timescales, based on the parameter values listed in Table 4.2. The example parameter values quoted

dictate that substrate diffusion and uptake take place on a much shorter timescale than cell growth. Rewriting (4.13) in terms of τ_{growth}, $\tau_{\text{diffusion}}$ and τ_{uptake}

$$\frac{1}{\tau_{\text{growth}}}\left(\frac{\partial \bar{u}}{\partial \bar{t}}\right) = \frac{1}{\tau_{\text{diffusion}}}\left(\bar{\nabla}^2 \bar{u}\right) - \frac{1}{\tau_{\text{uptake}}}\left(\frac{\bar{u}}{K/u_0 + \bar{u}}\phi(\mathbf{x},t)\right), \tag{4.14}$$

we see that the term $\frac{1}{\tau_{\text{growth}}}$ is so small as to be negligible. This observation leads naturally to the conventional splitting of timescales used in other IbM studies (see, for example, [222, 154, 297, 248]), whereby the time dependence of (4.13) is ignored, and the equation solved to 'pseudo-steady' state:

$$\bar{\nabla}^2 \bar{u} = \left(\frac{\tau_{\text{diffusion}}}{\tau_{\text{uptake}}}\right)\frac{\bar{u}}{K/u_0 + \bar{u}}\phi(\mathbf{x}). \tag{4.15}$$

Physically, this means that the substrate concentration field responds very rapidly to any perturbation to the cell configuration (and therefore ϕ) caused by cell growth, and so depends on cell positions only parametrically. The dimensionless quantity given by

$$\mathscr{D} = \frac{\tau_{\text{diffusion}}}{\tau_{\text{uptake}}} = \frac{l^2 \rho \mu_{\max}}{D\gamma u_0} \tag{4.16}$$

is commonly known as the [second] Damköhler number (or Thiele modulus [222]). This ratio summarises the rate of diffusive substrate transport relative to the substrate uptake rate. An additional parameter cluster $\eta = K/u_0$ controls how the intrinsic cell growth rate drops with diminishing substrate availability. Thus, non-dimensionalisation shows that there are effectively only two independent parameter groupings for Equa-

Process	Timescale	Equation	Value
Cell growth and division	τ_{growth}	$\ln 2/\mu_{\max}$	12.67 h
Solute diffusion	$\tau_{\text{diffusion}}$	l^2/D	0.50 ms
Solute uptake by cells	τ_{uptake}	$\gamma u_0/(\rho \mu_{\max})$	39.2 ms

Table 4.3 Characteristic timescales of dynamic processes

tions (4.7) and (4.8)

$$\bar{\nabla}^2 \bar{u} = \mathscr{D} \frac{\bar{u}}{\eta + \bar{u}} \phi, \quad \text{and} \tag{4.17}$$

$$\frac{d\bar{V}_i}{d\bar{t}} = \frac{\bar{u}_i \ln 2}{\eta + \bar{u}_i} \bar{V}_i. \tag{4.18}$$

Given the pseudo-steady-state nutrient field $\bar{u}$, Equation (4.18) can be solved by evaluating the local nutrient concentration $\bar{u}_i = \bar{u}(\mathbf{x}_i)$ at each cell's centroid $\mathbf{p}_i$, and then updating each cell's volume $\bar{V}_i$ using the linearisation

$$\Delta \bar{V}_i \approx \ln 2 \frac{\bar{u}_i}{\bar{u}_i + \eta} \bar{V}_i \Delta t, \ \forall \ i, \tag{4.19}$$

where Δt corresponds to the simulation timestep. It then falls to us to compute the field $\bar{u}$ by solving Equation (4.17) for a fixed configuration of cells $\{\tilde{\mathbf{p}}_i\}$. At this point, we will drop the $\bar{u}$ notation for clarity, and assume that u implicitly refers to the scaled nutrient concentration (and likewise for our other scaled variables $\bar{l}$, $\bar{V}$, $\bar{x}$, $\bar{y}$, $\bar{z}$, and $\bar{t}$). What is the physical meaning of the Damköhler number $\mathscr{D}$? Equation (4.16) shows how $\mathscr{D}$ can be interpreted as a ratio of model timescales τ, characterising the relative rates of nutrient diffusion and uptake. However, $\mathscr{D}$ can additionally be understood as a ratio of model *lengthscales*, which may be demonstrated as follows.

Suppose we wish to characterise a lengthscale $\mathscr{L}$, over which nutrient concentrations vary significantly with respect to the reference (bulk) concentration u_0. Diffusion increases $\mathscr{L}$ by spreading nutrients over space (see Equation (4.7)), and so we expect $\mathscr{L} \propto D$, the nutrient diffusivity. By contrast, increasing the relative rate of nutrient uptake (by raising ρ, $\mu_{\max}$, or by decreasing γ, u_0) will decrease $\mathscr{L}$ by making nutrient gradients steeper. We therefore expect $\mathscr{L} \propto \gamma u_0 / (\rho \mu_{\max})$. Combining these terms gives a parameter cluster

$$A = \frac{D \gamma u_0}{\rho \mu_{\max}}, \tag{4.20}$$

with overall units m^2, which implies that $\sqrt{A}$ qualifies as our gradient lengthscale $\mathscr{L}$,

$$\mathscr{L} = \sqrt{\frac{D\gamma u_0}{\rho \mu_{\max}}}. \tag{4.21}$$

Finally, we note that the quantity

$$\frac{l^2}{\mathscr{L}^2} = \frac{l^2 \rho \mu_{\max}}{D\gamma u_0} = \mathscr{D}, \tag{4.22}$$

where l is the reference lengthscale we used earlier. This demonstrates that the Damköhler $\mathscr{D}$ is equivalent to a ratio of reference and gradient lengthscales.

This type of analysis can also be used to relate $\mathscr{D}$ to other dimensionless numbers commonly used in biofilm modelling. One such number, Π, is defined as

$$\Pi = \sqrt{\frac{u_0 D\gamma}{\mu_{\max}\rho\delta^2}}, \tag{4.23}$$

and is used to quantify the depth to which nutrients penetrate into a biofilm [199, 43, 197].[4] Using Equation (4.21), we can see that Π may be interpreted as

$$\Pi \equiv \frac{\mathscr{L}}{\delta} = \frac{\text{Nutrient gradient lengthscale}}{\text{Boundary layer thickness}}. \tag{4.24}$$

In other words, nutrient penetration into the biofilm is significant when the gradient lengthscale $\mathscr{L}$ is large relative to the boundary layer thickness δ. We describe further extensions of this lengthscale analysis, applied to the case of diffusing toxins, in Chapter 7.

[4] Note that Π is more commonly written as 'δ', but since we are using δ to denote boundary layer thickness in this thesis, we have relabelled it.

4.3 Solutions using a finite element method

Equation (4.17) is a non-linear elliptic PDE of the form

$$\nabla^2 u = f(u), \tag{4.25}$$

defined on 2- or 3-dimensional domains Ω, and subject to the boundary conditions described in the previous section. In this section, we discuss how to solve this type of equation using finite element methods (FEM), a widely-used approach for solving PDEs numerically [37, 133]. We begin by summarising an iterative scheme—a variant of Newton's method—for solving Equation (4.25), before going on to describe a FEM-implementation of that scheme, using the finite element modelling library FEniCS.

4.3.1 Newton's method

Numerical schemes such as Newton's method can be used to solve Equation (4.25) iteratively [140]. Beginning with some initial solution estimate u^0, Newton's method may be written as a sequence of update steps,

$$u^{k+1} = u^k + \delta u^{k+1}, \;\; k = 0, 1, \ldots \tag{4.26}$$

where δu^{k+1} represents a small perturbation that updates the solution estimate. We can compute δu^{k+1} as follows: substituting Equation (4.26) into the right-hand side of (4.25), we get

$$f(u^{k+1}) = f(u^k + \delta u^{k+1}), \tag{4.27}$$

which can be expanded as

$$f(u^k) = f(u^k) + f'(u^k)\delta u^{k+1} + \mathscr{O}\left((\delta u^{k+1})^2\right) \tag{4.28}$$

$$\approx f(u^k) + f'(u^k)\delta u^{k+1}. \tag{4.29}$$

Similarly, substitution on the left-hand side of (4.25) gives

$$\nabla^2 u^{k+1} = \nabla^2 u^k + \nabla^2 \delta u^{k+1}, \tag{4.30}$$

and so altogether we have

$$\nabla^2 \delta u^{k+1} - f'(u^k)\delta u^{k+1} = -\nabla^2 u^k + f(u^k), \tag{4.31}$$

which has the form of a linear PDE in terms the perturbation δu^{k+1}, assuming that we know the previous solution u^k. This indicates that we can solve non-linear PDEs, such as Equation (4.17) by solving a linear PDE multiple times.

4.3.2 Variational forms

To solve the linear PDE Equation (4.31) using FEM, we rewrite the linear PDE using the calculus of variations [37, 133]. Multiplying by a test function $v = v(\mathbf{x})$ and taking volume integrals over domain Ω results in the so-called weak form

$$\int_\Omega \left(\nabla^2 \delta u^{k+1}\right) v dV - \int_\Omega f'(u^k)\delta u^{k+1} v dV = \int_\Omega f(u^k) v dV - \int_\Omega \left(\nabla^2 u^k\right) v dV \tag{4.32}$$

where dV is an infinitesimal volume element of Ω. Using Gauss' theorem, we can simplify integrals containing second derivatives, such as

$$\int_\Omega \left(\nabla^2 u^k\right) v dV = \int_\Gamma (\nabla u^k \cdot \hat{\mathbf{n}}) v dS - \int_\Omega \nabla u^k \cdot \nabla v dV, \tag{4.33}$$

and similarly for the term in $\nabla^2 \delta u^{k+1} v$. Here, Γ signifies the domain boundary, and $\hat{\mathbf{n}}$ its unit outward normal vector. The boundary integral in Equation (4.33) vanishes when we impose any combination of Dirichlet, periodic or zero-flux conditions on it.[5]

[5]This happens for different reasons in each case. For Dirichlet boundary conditions, we require that $v = 0$ on the boundary. For periodic boundary conditions, the components of the integral may be non-zero, but cancel out overall by definition. For zero-flux conditions, we have $\nabla u^k \cdot \hat{\mathbf{n}} = 0$ [133].

The variational problem is then this: given a previous solution guess u^k, update that guess by finding perturbation δu^{k+1} such that

$$-\int_\Omega (\nabla \delta u^{k+1}) \cdot (\nabla v) dV - \int_\Omega f'(u^k) \delta u^{k+1} v dV \approx \int_\Omega (\nabla u^k) \cdot (\nabla v) dV + \int_\Omega f(u^k) v dV. \quad (4.34)$$

4.3.3 Discrete solutions

To solve Equation (4.34) using finite elements, we divide the domain Ω into a set of discrete, non-overlapping parts called elements, which completely span Ω. We can then replace δu^{k+1} with a discrete approximation δu_h^{k+1}, written as a linear combination of basis functions $\varphi_j = \varphi_j(\mathbf{x})$ defined on N nodes (points) connecting those elements,

$$\delta u_h^{k+1} = \sum^N \alpha_j^{k+1} \varphi_j, \quad (4.35)$$

with each basis function weighted by an unknown coefficient α_j^{k+1} that we aim to determine. Certain choices of basis function qualify as suitable test functions v [133], allowing us to discretise (4.34) as

$$-\sum_j^N \alpha_j^{k+1} \left(\int_\Omega \nabla \varphi_j \cdot \nabla \varphi_i dV \right) - \sum_j^N \alpha_j^{k+1} \left(\int_\Omega f'(u^k) \varphi_j \varphi_i dV \right) = \int_\Omega \nabla u^k \cdot \nabla \varphi_i dV + \int_\Omega f(u^k) \varphi_i dV, \quad i = 1, 2, \ldots, N, \quad (4.36)$$

or in matrix form,

$$-(\mathbf{K} + \mathbf{M})^k \alpha^{k+1} = (\mathbf{b} + \mathbf{c})^k, \quad (4.37)$$

whose elements are defined as

$$K_{ij} = \int_\Omega \nabla\varphi_j \cdot \nabla\varphi_i dV, \tag{4.38}$$

$$M_{ij} = \int_\Omega f'(u^k)\varphi_j\varphi_i dV, \tag{4.39}$$

$$b_i = \int_\Omega \nabla u^k \cdot \nabla\varphi_i dV, \text{ and} \tag{4.40}$$

$$c_i = \int_\Omega f(u^k)\varphi_i dV. \tag{4.41}$$

Each of these integrals can be computed numerically if we already know what the functions φ_i, f and $u^k = f(\alpha^k)$ are. Note that basis functions centered on sections of the domain boundary $\delta\Omega$ where Dirichlet boundary condition apply are *not* suitable test functions because they are non-vanishing at these locations. Where this applies, rows of **K**, **M**, **b** and **c** can be overwritten with known solution values.

We now have a method for approximating discrete solutions to non-linear elliptic PDEs: given an initial solution estimate u^0, we can solve a series of variational problems using FEM to improve that estimate, updating the coefficients α^k until the residual $\Delta^2 u^k - f(u^k)$ is satisfactorily small. Provided the initial iterate u^0 is sufficiently close to the true solution u, Newton's method converges quadratically [55].

4.4 Implementation using FEniCS

To implement this finite element scheme numerically, we used FEniCS, an open-source library for solving PDEs using finite element methods [168, 5]. For our purposes, FEniCS is an ideal modelling tool: it has a front-end written in Python, which can easily be interfaced with CellModeller, but an efficient back-end written in C++. It also contains a large amount of in-built functionality for solving PDEs using finite elements, including meshes, basis functions and numerical solvers. Here we summarise our implementation of the scheme described in Section 4.3 using this library.

4.4.1 Meshes, elements and boundaries

We discretise the 2-D and 3-D domains described in Section 4.2.2 using regular crossed meshes (in-built FEniCS class `RectangleMesh()`) and box meshes (in-built class `BoxMesh()`), as shown in Figure 4.2. Crossed meshes consist of an N_x-by-N_z grid of rectangles of overall dimensions $L_x \times L_z$, each containing four triangular elements of equal area (Figure 4.2-A). Box meshes consist of an N_x-by-N_y-by-N_z grid of cuboids of overall dimensions $L_x \times L_y \times L_z$, each containing six tetrahedral elements of equal volume (Figure 4.2-B). The number of elements along the base of the domain, N_x (and N_y in 3-D) are fixed to give a constant element size $h_x = L_x/N_x$ (and $h_y = L_y/N_y$ in 3-D). The domain height L_z depends on the cell configuration as $L_z = \delta + \max(p_z)$, and so N_z is chosen so as to set the vertical element size $h_z \approx h_x = h_y = h$, using

$$N_z = \lfloor L_z/h \rceil, \tag{4.42}$$

where the operation $\lfloor \cdot \rceil$ denotes rounding to the nearest integer.

We then define basis functions $\{\varphi\}$ on these meshes. Specifically, we use 1st order Lagrange basis functions, selected using the in-built FEniCS class `FunctionSpace`. This choice of basis function makes our discrete solution (Equations (4.26), (4.35) and (4.37)) a piecewise-linear approximation to the true nutrient field u, as defined by Equation (4.17). The boundary conditions specified in Section 4.2.2 are implemented using the FEniCS class `DirichletBC()` for the source boundary condition at $z = L_z$, and custom classes `XPeriodicDomain()` and `XYPeriodicDomain()` for lateral periodic boundary conditions in 2 and 3 dimensions, respectively.[6]

[6]Note that zero-flux boundary conditions are 'natural' (set by default), and do not need to be imposed explicitly [133].

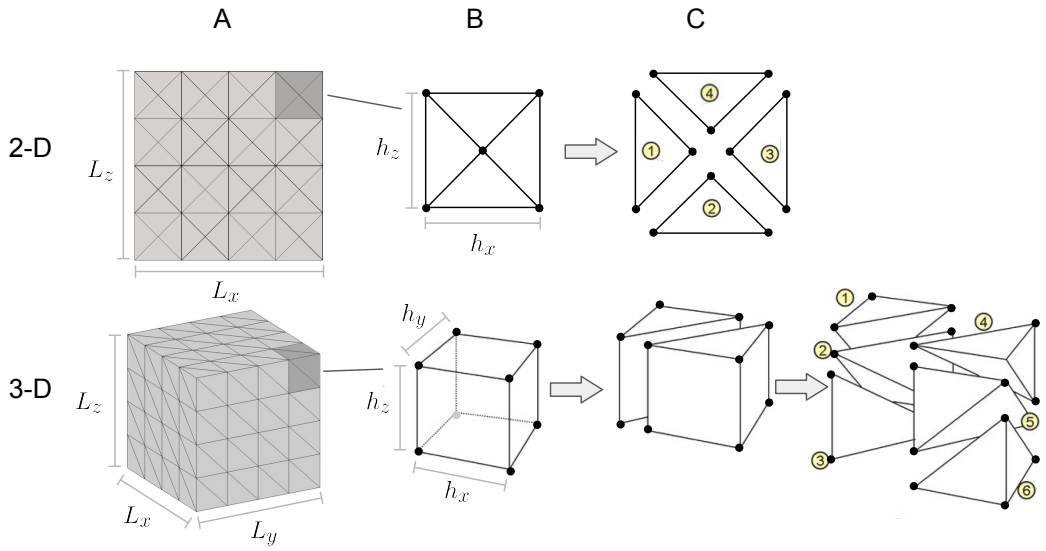

Fig. 4.2 Finite element meshes in 2 and 3 dimensions. Rectangular or cuboidal simulation domains Ω are discretised using regular meshes (A). Each mesh is constructed from multiple copies of a single unit cell (B), which in turn contains multiple simplex elements (C): 4 triangles in the 2-D case, or 6 tetrahedra in the 3-D case. In both cases, the regular structure of the mesh enables efficient element assignment for each microbial cell in the colony.

4.4.2 Defining the volume fraction function

The finite element problem also requires a definition of the cell volume fraction field $\phi(\mathbf{x})$, which needs to be calculated from the cell configuration $\{\mathbf{p}_i\}$ for each simulation timestep.

For each mesh element, we can approximate the local cell volume fraction by evaluating which cells lie in that element, summing their volumes, and dividing by the element volume. This gives an element-wise approximation to ϕ, that can then be supplied to FEniCS as a piece-wise constant function. We then avoid having to compute integrals over $\phi(\mathbf{x})$ in Equations (4.39) and (4.40) for each iteration of the solver scheme – instead, we can read off ϕ from a pre-computed list of values, increasing the computational efficiency of the scheme.

This piece-wise constant approximation of ϕ is expected to be effective provided that $h > l$, where h is the element width and l the characteristic cell size, which places an

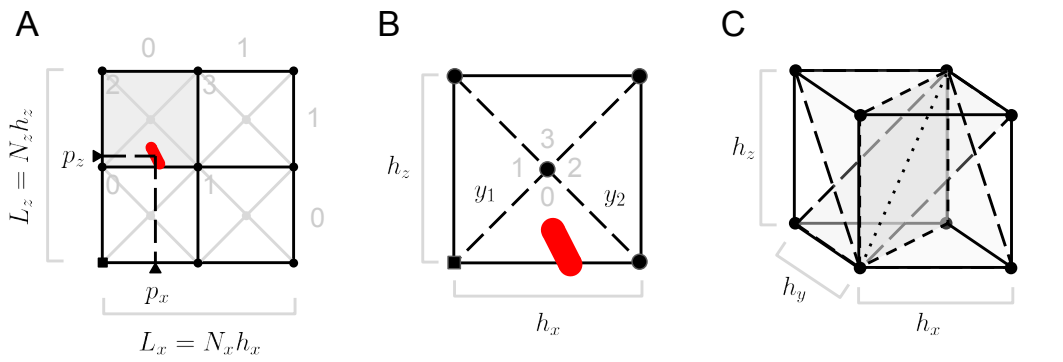

Fig. 4.3 Methodology for computing the cell volume fraction function ϕ by counting capsule cells on finite element meshes, defined by nodes (dots) and connecting edges (lines). We use a 2-part method, demonstrated using a 2-D example in A and B. First, the grid square containing the capsule (red) is assigned (A), by comparing the coordinates of its centroid to the unit cell size. Second, the capsule is assigned to one of the 4 triangular elements within that square (B), by comparing its coordinates (expressed in the frame of the square) to those defining the two mesh diagonals, y_1 and y_2. The square and element indices from A and B are combined to give the global index of the capsules' element. In 3 dimensions, the procedure is similar, except that each unit cube in the grid is divided into 6 tetrahedra by 3 diagonal planes, as shown in C. As before, element indices are determined by computing whether a given cell's centroid lies above or below each of these planes.

upper limit on the resolution of the mesh (i.e. on $1/h$).[7] A more detailed treatment of the problem, in which $\phi(\mathbf{x})$ is represented as a continuous function, would extend this limit further, but is beyond the scope of this thesis.

Because our finite element meshes will generally contain a large number of cells (1000-10,000), it is important that cell element assignment is performed efficiently. We use a two-part assignment process that exploits the regular structure and geometry of our meshes, in order to rapidly define and export the ϕ function:

1. Given a cell's coordinates, assign the unit grid cell to which it belongs;

2. Within that unit grid cell, compute which element the cell lies in.

This process is explained further in Figure 4.3, using a 2-dimensional example. Given an N_x by N_z regular grid of squares, whose dimensions are $L_x \times L_z$, Figure 4.3-A

[7] We test this limit in the next section by using meshes with $h \approx l$, which show satisfactory convergence.

shows how to compute which square a given point $\mathbf{p} = [p_x, p_z]$ lies in. Numbering grid columns along the x axis from 0 to $N_x - 1$ as shown, the point must be in column $\lfloor p_{x,i}/h_x \rfloor$, where $\lfloor\ \rfloor$ denotes the mathematical 'floor' operation (nearest integer rounding towards negative infinity). Similarly, the point's row index is $\lfloor p_{z,i}/h_z \rfloor$. If we number the squares from 0 to $N_x N_z - 1$ going along x then z, then the global index a of the target square is

$$a = \underbrace{\lfloor p_{x,i}/h_x \rfloor}_{\text{column index}} + N_x \underbrace{\lfloor p_{z,i}/h_z \rfloor}_{\text{row index}}. \tag{4.43}$$

A similar procedure applies in 3-dimensions: this time there are three axis indices to count along, giving

$$a = \lfloor p_{x,i}/h_x \rfloor + N_x \lfloor p_{y,i}/h_y \rfloor + N_x N_y \lfloor p_{z,i}/h_z \rfloor. \tag{4.44}$$

The next stage is to calculate which of the elements within square a contains point $\mathbf{p}$. As shown in Figure 4.3-B, each square in a cross mesh contains four triangular elements, separated by two diagonal lines y_1 and y_2. If the origin of the square is $[p_{s,x}, p_{s,z}]$, we can write equations for these lines

$$y_1 = 0 + \frac{h_z}{h_x} x, \quad \text{and} \tag{4.45}$$

$$y_2 = h_z - \frac{h_z}{h_x} x. \tag{4.46}$$

We can then score point $\mathbf{p}$ according to which of the planes it lies above, so that each of the four triangles corresponds to a unique score b, given by

$$b = \mathscr{H}\left((p_{i,z} - p_{s,z}) - \frac{h_z}{h_x}(p_{i,x} - p_{s,x}) \right) + 2\mathscr{H}\left((p_{i,z} - p_{s,z}) + \frac{h_z}{h_x}(p_{i,x} - p_{s,x}) - h_z \right), \tag{4.47}$$

where above we have used the Heaviside function $\mathscr{H}$, defined as

$$\mathscr{H}(x) = \begin{cases} 1, & x > 0, \\ 0, & x \leq 0, \end{cases} \tag{4.48}$$

to compare cell coordinates with those of each plane.

In three dimensions, the arrangement of elements in a grid cell is different, but a similar system can be devised. Figure 4.3-C shows how a cubic grid cell is divided up into six tetrahedral elements of equal volume. These elements are separated by three planes, which pass through the main diagonal axis of the cube. Writing the cube's origin as $[p_{s,x}, p_{s,y}, p_{s,z}]$, we can again score the point $\mathbf{p}$ according to which of the planes it lies above, giving a unique tetrahedron index b,

$$\begin{aligned} b = \mathscr{H}\left(\frac{h_z}{h_y}(p_{y,i} - p_{y,s}) - (p_{z,i} - p_{z,s})\right) \\ + 2\mathscr{H}\left(\frac{h_x}{h_z}(p_{z,i} - p_{z,s}) - (p_{x,i} - p_{x,s})\right) \\ + 4\mathscr{H}\left(\frac{h_y}{h_x}(p_{x,i} - p_{x,s}) - (p_{y,i}) - p_{y,s})\right). \end{aligned} \tag{4.49}$$

In each case, once both a and b are known, the point's absolute element index m can be computed as

$$m = \begin{cases} b + 4a, \text{ (in 2D)}, \\ b + 6a, \text{ (in 3D)}. \end{cases} \tag{4.50}$$

Repeating the procedure for a list of cell positions $\{\mathbf{p}_i\}$ produces a table of element assignments that can then be searched (using Python functions such as `bincount`) to sum the cell volumes (or areas) present in each element. Note that each of these processes uses only the coordinates of cell centroids. We use the assumption that if a cell's centre lies within a particular mesh element, then all of that cell's volume

(or area) is then assigned to that element, even if part of the cell lies within another element. The full procedure used to assign cells to the elements of regular 2- and 3-dimensional meshes are shown in Algorithms 1 and 2.

Data: Cell centroids $\{\mathbf{p_i}\}$, cell areas $\{A_i\}$, regular cross mesh $\mathscr{M}$ of dimensions $[0, L_x] \times [0, L_z]$ with divisions N_x, N_z
Result: Empty list of cell area fractions for each element $\{A_m\} = 0$
Initialise $\{A_m\} = 0$; empty list of cell elements $\{E_i\} = 0$;
for *each cell i* **do**
1. Get rectangle index a:

$$a = \lfloor p_{x,i} N_x / L_x \rfloor + N_x \lfloor p_{z,i} N_z / L_z \rfloor. \tag{4.51}$$

2. Get rectangle origin $\mathbf{p}_a$:

$$\mathbf{p}_a = [L_x \lfloor p_{x,i} N_x / L_x \rfloor / N_x,\ L_z \lfloor p_{z,i} N_z / L_z \rfloor / N_z]. \tag{4.52}$$

3. Get triangle index t:

$$b = \mathscr{H}\left((p_{i,z} - p_{a,z}) - \frac{L_z N_x}{L_x N_z}(p_{i,x} - p_{a,x}) \right) + 2\mathscr{H}\left((p_{i,z} - p_{a,z}) + \frac{L_z N_x}{L_x N_z}(p_{i,x} - p_{a,x}) - \frac{L_z}{N_z}) \right). \tag{4.53}$$

4. Assign cell element index $E_i = b + 4a$.

end
for *each element m* **do**
  for *each cell i* **do**
    if *element* $E_i = m$ **then**
      $A_m \leftarrow A_m + A_i$
    end
  end
  $A_m \leftarrow A_m / (\frac{L_x L_z}{N_x N_z})$
end

Algorithm 1: Cell counting algorithm for crossed 2-D meshes

4.4.3 FEniCS PDE solver

FEniCS contains an in-built version of the Newton's method solver described previously, called using the function `solve()`. The solver performs the iteration procedure in Equation (4.26) automatically, measuring values of the residual $r^k = \nabla^2 u^k - f(u^k)$

Data: Cell centroids $\{\mathbf{p_i}\}$, cell volumes $\{V_i\}$, regular cubic mesh $\mathscr{M}$ of dimensions $[0,L_x]\times[0,L_y]\times[0,L_z]$ with divisions $N_x,\ N_y,\ N_z$
Result: Empty list of cell area fractions for each element $\{V_m\}=0$
Initialise $\{A_m\}=0$; empty list of cell elements $\{E_i\}=0$;
for *each cell i* **do**

1. Get rectangle index a:

$$a = \lfloor p_{x,i}N_x/L_x\rfloor + N_x\lfloor p_{y,i}N_y/L_y\rfloor + N_xN_y\lfloor p_{z,i}N_z/L_z\rfloor. \tag{4.54}$$

2. Get rectangle origin $\mathbf{p}_a$:

$$\mathbf{p}_a = [L_x\lfloor p_{x,i}N_x/L_x\rfloor/N_x,\ L_y\lfloor p_{y,i}N_y/L_y\rfloor/N_y,\ L_z\lfloor p_{z,i}N_z/L_z\rfloor/N_z]. \tag{4.55}$$

3. Get tetrahedron index b:

$$\begin{aligned} b = \mathscr{H}\left(\frac{L_zN_y}{L_yN_z}(p_{y,i}-p_{y,a})-(p_{z,i}-p_{z,a})\right) \\ +2\mathscr{H}\left(\frac{L_xN_z}{L_zN_x}(p_{z,i}-p_{z,a})-(p_{x,i}-p_{x,a})\right) \\ +4\mathscr{H}\left(\frac{L_yN_x}{L_xN_y}(p_{x,i}-p_{x,a})-(p_{y,i})-p_{y,a})\right). \end{aligned} \tag{4.56}$$

4. Assign cell element index $E_i = b+6a$.

end
for *each element m* **do**
  for *each cell i* **do**
    if *element* $E_i = m$ **then**
      $V_m \leftarrow V_m + V_i$
    end
  end
  $V_m \leftarrow V_m/(\frac{L_xL_yL_z}{N_xN_yN_z})$
end

Algorithm 2: Cell counting algorithm for regular 3-D meshes

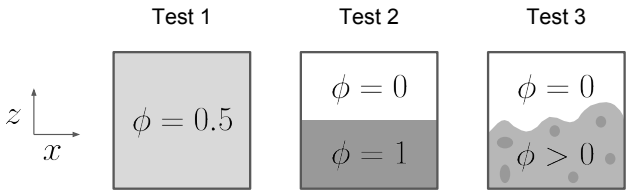

Fig. 4.4 Diagrams depicting test problems 1, 2 and 3, showing vertical 2-D slices through the simulation domain. Shaded areas show the sections of the domain where the cell volume fraction ϕ is non-zero. (1) shows a simple model where ϕ is constant in space. In (2), ϕ is a step function of height z, but invariant in x (and y in 3-D problems). (3) represents the full nutrient modelling problem, where ϕ is taken from a realistic cell configuration generated by CellModeller.

for each iteration k. We control the solver performance using two parameters: the relative solution tolerance ε_n, and the maximum iteration number N_{iter}, set to default values of 1×10^{-6} and 50 respectively. Solver iteration is set to end when either of the following conditions is met: either the relative residual is satisfactorily low, $r^k/r^0 < \varepsilon_n$, or the solver runs out of iterations $k > N_{\text{iter}}$. In the former case, the converged solution u^k is returned; in the latter case, an error is reported and the program terminates.

4.5 Implementation testing

Having shown how to implement the reaction-diffusion solute model using the FEniCS finite element library, we now need to test that implementation. Tests of computational models generally fall into two categories:

1. **Verification**: given a model of some process, has that model been implemented correctly?

2. **Validation**: independent of its implementation, is the model itself a valid representation of the physical processes being modelled?

This section is all about verification – we will look at experimental validation later, in Chapters 5 and 6. Our aim here is to test whether our FEniCS implementation—the

computer code, numerical schemes and the solutions they produce—is able to represent the model to a satisfactory degree of accuracy. The verification scheme presented here consists of subjecting the implementation to three tests of increasing complexity. Figure 4.4 shows diagrams summarising the three test problems, which are as follows:

- **Test problem 1**: Letting $L_x = L_z = 40\,\mu\text{m}$ ($= L_y$ for 3-D problems), assume that the volume fraction function $\phi = 0.5$ over all space (Figure 4.4-1).
- **Test problem 2**: Again using $L_x = L_z = 40\,\mu\text{m}$ ($= L_y$ for 3-D problems), make the ϕ a step function of height z, so that $\phi = 1$ when $z \leq L_z/2$ and zero otherwise (Figure 4.4-2).
- **Test problem 3**: Using domains of similar geometry, compute ϕ from a 'real' configuration of cells $\{\mathbf{p}_i\}$ produced by CellModeller, roughly filling the bottom half of the domain, choosing $L_z = \max(p_{z,i})$.

For each test, we analyse the results of the implementation and use them to decide if the answers provided are correct. If the answers are correct, we will assume that the implementation is correct, and can be applied to other problems on top of the test problem.

In Tests 1 and 2, ϕ is invariant in the x (and y) directions. This in turn makes the transport PDE invariant in x and y, as there is nothing to drive lateral flow of solute. In Test 1, the PDE reduces to a second-order non-linear ODE

$$\frac{d^2u}{dz^2} = \frac{1}{2}\mathscr{D}\left(\frac{u}{u+\eta}\right), \tag{4.57}$$

subject to the boundary conditions

$$\left.\frac{du}{dz}\right|_{z=0} = 0, \quad u(L_z) = 1. \tag{4.58}$$

The same applies for Test 2, except the reaction term $f(\bar{u})$ becomes a step function of height,

$$f(u) = \begin{cases} \left(\frac{\mathscr{D}u}{u+\eta}\right), & z \leq L_z/2 \\ 0, & z > L_z \end{cases} \tag{4.59}$$

In these two cases, the volume fraction function ϕ can be generated directly from the mesh, instead of from a cell configuration specified by CellModeller. The ϕ function generator still needs to be tested however, so we need to feed it a list of cell positions and volumes (areas) accordingly. To do this for Test 1, we place an imaginary cell at the centroid of each mesh element, setting the cell's volume (or area) in each case to be half that of the element. For Test 2, we do this for only the first 50% of mesh elements (corresponding to the bottom half of the domain), setting the volume or area equal to that of the element.

The resulting boundary value problems are difficult to solve analytically, but very simple to solve numerically. We can therefore test the output of the FEniCS PDE implementation against a numerical solution provided by a different numerical solver – one that has already been thoroughly tested, and whose errors are well-defined. For this purpose, we use the Chebfun ODE solver [113, 81], implemented in MATLAB, to compute trusted, high-resolution approximations of the true solution u.[8] The accuracy of our FEniCS solutions u_h can then be quantified using metrics like the L2-norm absolute error, E_{abs}, defined as

$$E_{\text{abs}} = ||u - u_h||_{l_2} \tag{4.60}$$

$$= \left(\int_0^{L_z} (u-u_h)^2 dz\right)^{\frac{1}{2}}, \tag{4.61}$$

[8] Solutions from the Chebfun solver also behave like continuous solutions, which makes computing the integrals in Equations (4.61) and (4.63) straightforward [113, 81].

or the relative error, E_{rel},

$$E_{\text{rel}} = ||u - u_h||_{l_2} / ||u||_{l_2} \tag{4.62}$$

$$= \left(\int_0^{L_z} (u - u_h)^2 dz \right)^{\frac{1}{2}} / \left(\int_0^{L_z} u^2 dz \right)^{\frac{1}{2}}. \tag{4.63}$$

Test 3 represents our most realistic test problem, equivalent to the PDE that FEniCS will actually have to solve during simulations. Here, we compute ϕ as discussed previously from cell configurations generated by CellModeller, in either 2 or 3 dimensions. Both configurations consist of approximately flat layers of cells roughly 20 µm in depth. However, since these cell configurations are not completely homogeneous in x and y, the PDE for Test 3 does not reduce to a simple ODE form, and we have no trusted solution to compare our answers against. However, since we expect ϕ functions to be similar in Tests 2 and 3, we can compare their results and check for any unexpected differences.

For each of the three test problems, we perform two types of analysis, using both 2-D and 3-D domains:

- A parameter sweep using a fixed mesh resolution, varying the bulk solute concentration value u_0 (*via* the Damköhler number $\mathscr{D}$) through four orders of magnitude. This initial comparison helps to establish the form of the solutions u_h to the solute PDE, and their resemblance to the trusted solutions u.

- A convergence test using a mesh discretisation series: a sequence of increasingly fine meshes used to check how the error of our discrete approximations varies with the mesh parameter h. The aim here is to verify that solutions are convergent – i.e. that error can be reduced to an arbitrarily low value by selecting a mesh of appropriate fineness.

The results of these analyses are shown in Figures 4.5 and 4.6 respectively. Here we discuss the behaviour of each in turn.

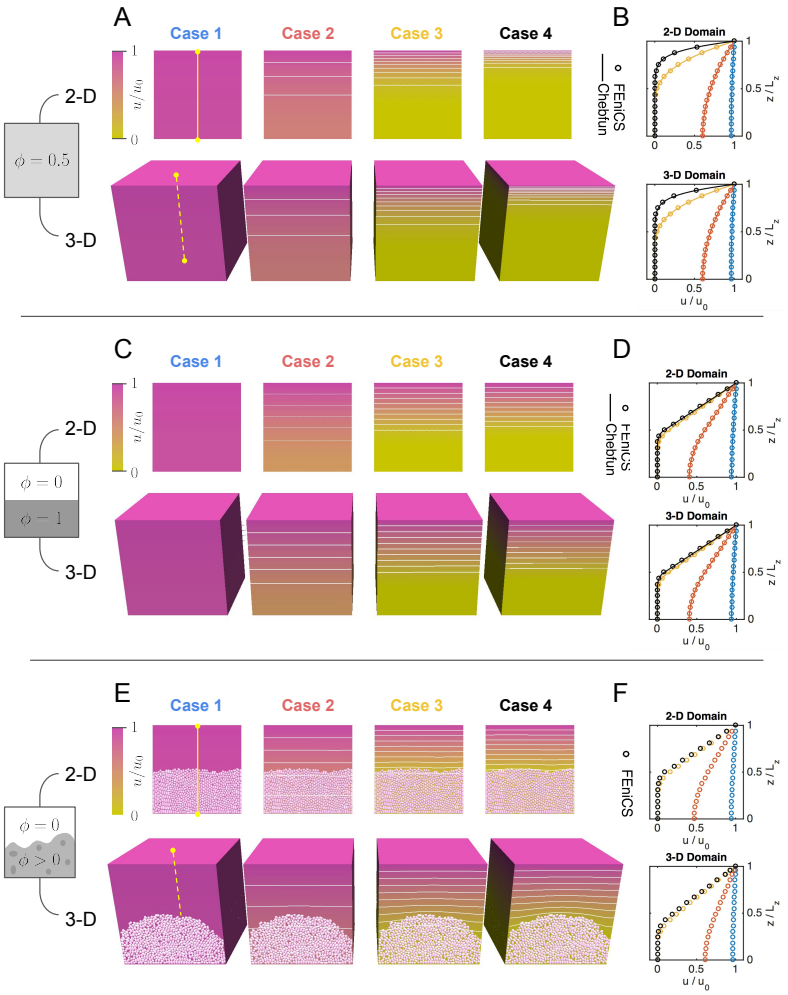

Fig. 4.5 Parameter sweeps for test problems 1 (A, B), 2 (C, D) and 3 (E, F), solved on 2-D (top rows) and 3-D (bottom rows) FEniCS meshes, where $h_x = h_y = h_z = h = 2.5$. Solution plots (A) show variation in scaled solute concentration for decreasing values of bulk concentration parameter u_0, equal to 500, 50, 5 and 0.5 $\mathrm{g\,m^{-3}}$ in Cases 1 through 4 respectively. Contours mark points of equal concentration, from $u/u_0 = 0.1$ to 0.9 in increments of 0.1. In B, we compare these solutions (circles) to trusted solutions produced by the Chebfun ODE solver (solid lines). Traces are colour-coded using case labels in A. FEniCS solutions were measured along the central vertical axis of each mesh, as shown by the yellow lines in A, Case 1. C and D follow the same pattern as A and B, but depict the results of Test 2. In E and F we again plot solutions for the 4 parameter cases, shown alongside the cell configurations used to generate them.

4.5.1 Results I: parameter sweeps

Figure 4.5 shows example solutions on 2- and 3-dimensional meshes for the three test problems (Figure 4.5-A, C, and E for Tests 1, 2 and 3 respectively), using a mesh parameter of $h = 2.5\,\mu\text{m}$ in each case. On these meshes, solutions were generated using $u_0 = 500$, 50, 5 and $0.5\,\text{g}\,\text{m}^{-3}$ (labelled as Cases 1-4), representing a spectrum of nutrient perfusion scenarios from rich feeding to poor feeding. The corresponding dimensionless control parameters are $\mathscr{D} = 0.0001, 0.001, 0.01$ and 0.1, and $\eta = 0.00033, 0.0033, 0.033$ and 0.33, respectively.

For Tests 1 and 2 (Figure 4.5-B,D), we compare the FEniCS solution to the trusted Chebfun solution u. 2- and 3-dimensional FEniCS solutions are converted into 1-D solutions by measuring u_h values along the central vertical axis of the mesh: the line $[L_x/2,\ 0] \to [L_x/2,\ L_z]$ in 2-D, and the line $[L_x/2,\ L_y/2,\ 0] \to [L_x/2,\ L_y/2,\ L_z]$ in 3-D. Because N_x and N_y are always even (by choice), this line always intersects with nodes at the centre of the mesh, whose solution values can be read off.

Going from Case 1 to 4, the supply of nutrient from the bulk liquid to the biofilm diminishes, resulting in increased nutrient gradients and decreased perfusion. In each case however, we see good agreement between FEniCS and Chebfun solutions. We also see good correspondence between the 2- and 3-D solutions, which appear identical. This is as it should be, since our claim was that solutions would be invariant in the x and y dimensions for Tests 1 and 2 – so that solutions in 1, 2 or 3 dimensions should all be equivalent.

In the case of Test 3 (Figure 4.5-E and F), we have no Chebfun solutions to compare with, so we plot the FEniCS solution only. Reassuringly however, the solutions resemble those of Test 2, since the step function approximation to ϕ is similar to that generated by a realistic cell configuration. This correspondence indicates that Test 2 is a good approximation of Test 3 when examining a uniform layer of cells, and so the

agreement with Chebfun solutions in Test 2 is good evidence to suggest the validity of Test 3.

4.5.2 Results II: convergence analysis

Having qualitatively compared our FEniCS solutions against trusted values, we now quantify discrepancies as a function of mesh resolution, beginning with results from Test 1. In Figure 4.6-A, we show 2-D (top) and 3-D (bottom) mesh discretisation series: four increasingly-refined meshes, with h ranging from 10 (left) to 1.25 µm (right). On these meshes, we plot interpolated values of the elementwise cell volume fraction function ϕ, as measured by our on-grid cell counting system.

In Figure 4.6-B, we compare FEniCS and Chebfun solutions to compute the absolute and relative solution error as a function of mesh parameter h, both in 2-D (top) and 3-D (bottom). This procedure is applied for both periodic and non-periodic boundary conditions. In all cases, the error converges quadratically: least-squares fitting to each of the lines in Figure 4.6-B gives a mean gradient of 1.985 in 2D, or 1.997 in the 3-D case.

Figure 4.6-C and D follow the same pattern as 4.6-A and B. In Figure 4.6-D, we see the scheme again becomes approximately quadratically convergent once $h = 5\,\mu\text{m}$ or below. Here the mean convergence gradients are 1.827 (2-D case) and 1.845 (3-D case), excluding the coarsest mesh $h = 10\,\mu\text{m}$. Overall, both observations are consistent with the scheme being quadratically convergent in space.

Finally, Figure 4.6-E and F show similar analyses applied to the results of Test 3. In this case, because cells have fixed coordinates instead of automatically being placed at element centroids, the cell volume fraction function can become patchy at high mesh resolution, as elements are too small to contain any cell's centroid. Although we lack trusted solutions for Test 3, we can still check that our FEniCS solutions are converging to some particular set of values. In Figure 4.6-F, we compare solutions

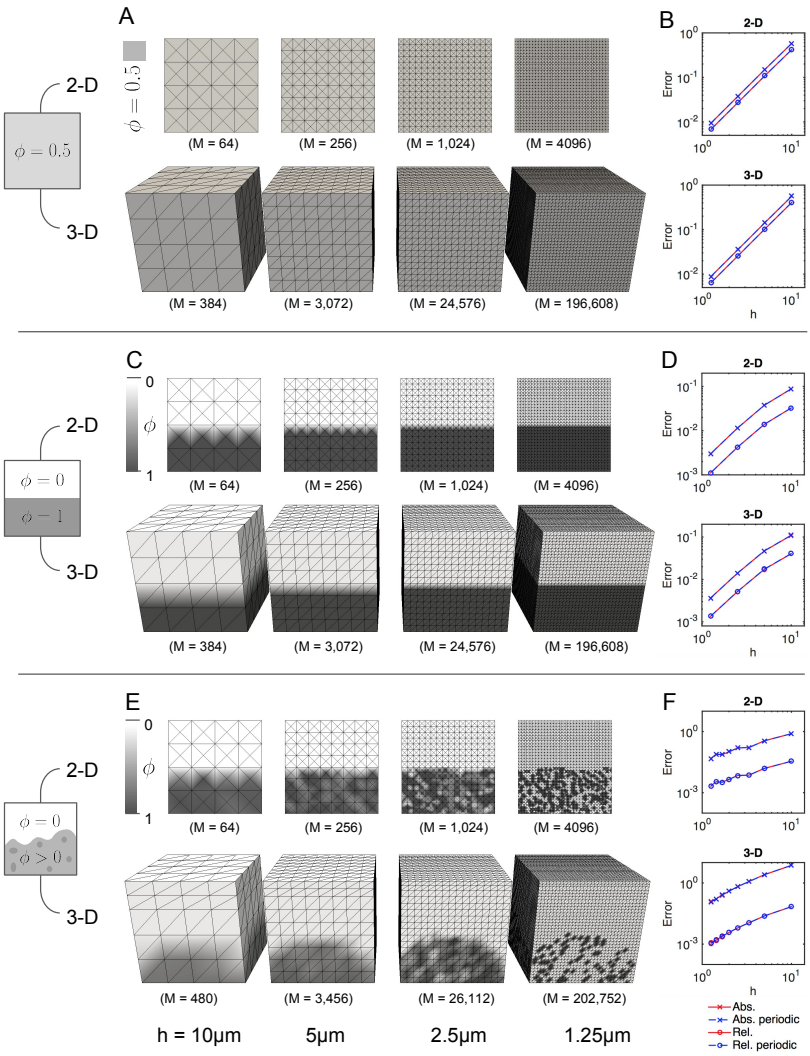

Fig. 4.6 Convergence analysis for test problems 1 (A, B) 2, (C, D) and 3 (E, F), solved on 2-D (top rows) and 3-D (bottom rows) FEniCS meshes. A shows a discretisation series of increasingly refined meshes (left to right: $h = 10$, 5, 2.5 and 1.25 μm) annotated with their element populations M. Meshes are shaded according to the volume fraction field ϕ. In B, we compare periodic and non-periodic solutions evaluated on these meshes to trusted 1-D Chebfun solutions, showing approximately quadratic reduction in the relative error as h is reduced. C and D are analogous to A and B respectively, repeating the same analysis for Test 2. In Test 3, ϕ is evaluated from a real cell configuration, resulting in patchy distributions for low h values (E). In F, we compare solutions to a reference FEniCS solution computed on a very fine mesh, as Test 3 cannot be solved by Chebfun.

on the discretisation series u_h to solutions generated on a very fine mesh u_H, with $H = 1.11\,\mu\text{m} \approx l$. We measure the absolute and relative differences between these solutions using

$$E_{\text{abs}} = \left(\sum_{i=0}^{N} (u_{h,i} - u_{H,i})^2 \right)^{\frac{1}{2}} \tag{4.64}$$

and

$$E_{\text{rel}} = \left(\sum_{i=0}^{N} \left(\frac{u_{h,i} - u_{H,i}}{u_{H,i}} \right)^2 \right)^{\frac{1}{2}}, \tag{4.65}$$

where $\{u_{i,h}\}$ and $\{u_{i,H}\}$ are the N nodal values of the solutions. Plotting these metrics against h shows that solutions are converging to particular values: convergence is quadratic in 3-D (mean gradient of 1.997), but sub-quadratic in 2-D (1.291). Interestingly, we see that convergence is maintained right up until the $h \approx l$ limit.

Overall, these results indicate that a mesh parameter of $\approx 5.0\,\mu\text{m}$ is sufficient to ensure a relative error of 2% or lower in each test case, for both 2- and 3-dimensional problems. We will therefore use this value of h for the remainder of the thesis, unless indicated otherwise.

4.5.3 Fully-coupled hybrid model

Our tests so far have examined the behaviour of solute field solutions for fixed cell coordinates – generated either from the mesh itself (Tests 1 and 2), or by CellModeller (Test 3). In these cases, the interaction between cells and solutes is one-way only. However, the fundamental purpose of our proposed hybrid model is to describe two-way interactions, or feedback, between the cell configuration and the solute fields surrounding it.

As a final test of the framework, we show example simulations where the expanding cell configuration is fully coupled to the solute fields, and *vice-versa*. Beginning with some initial arrangement of cells, the state of the simulation is updated iteratively according to a three-step algorithm:

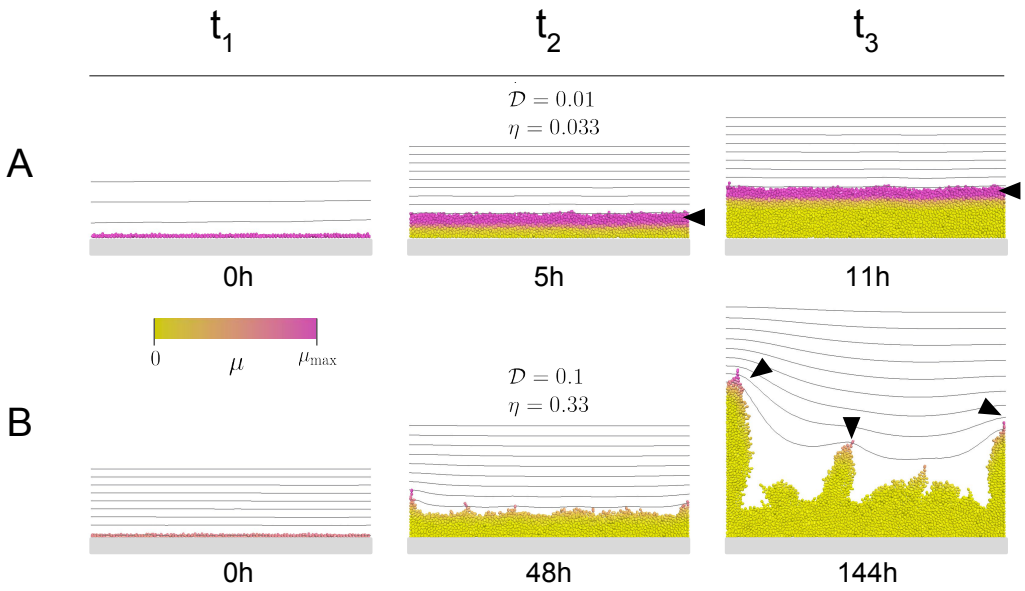

Fig. 4.7 Example simulations demonstrating full coupling between cell growth and solute fields, as described in this chapter. Here we use the completed hybrid model to grow quasi-2-D (L_x = 150 µm, L_y = 5 µm) colonies from cell monolayers (t_1), under 2 contrasting perfusion regimes. In A, the colony front (t_2, black arrow) expands evenly, resulting in a smooth morphology (t_3). In B, we repeat the same simulation with $u_0 = 0.5\,\mathrm{g\,m^{-3}}$, comparing snapshots with similar colony volumes. In this scenario, the advancing front becomes unstable (t_2), generating a branched colony morphology (t_3, black arrows). In each case, cells are coloured by their growth rate according to the colourbar shown. Values of the dimensionless control parameters $\mathscr{D}$ and η are listed (t_2 column), along with the collection time for each snapshot. Contours mark points of equal concentration, from $u/u_0 = 0.1$ to 0.9 in increments of 0.1. Mesh parameter h and boundary layer thickness δ are set to 5 and 40 µm respectively.

1. Computing the nutrient field to pseudo-steady state, given the current cell configuration;

2. Growing and dividing cells, given local nutrient concentrations, according to Equation (4.19);

3. Computing cell movement given a non-equilibrium cell configuration (as described in Chapter 3).

Note that this algorithm is similar to the one discussed in Chapter 3, but importantly now includes coupling between the growth of individual cells and the nutrients in their

environment. In this way, the cells and the solute field surrounding them are allowed to influence each other as the colony expands.

Figure 4.7 shows a series of snapshots from simulations performed using different values of the bulk nutrient concentration u_0: $u_0 = 5.0\,\mathrm{g\,m^{-1}}$ in Figure 4.7-A, and $u_0 = 0.5\,\mathrm{g\,m^{-1}}$ in Figure 4.7-B. Both simulations use the same quasi-2-D domain (L_x = 150 µm, L_y = 5 µm), the same boundary conditions ($\bar{u} = 1$ at $z = L_z$ and zero-flux elsewhere) and are initiated in the same way, by placing 70 randomly-oriented capsule cells at regular intervals along the base of the domain. However, the difference in bulk solute concentration is sufficient to drive a profound change in the shape of the emerging colony.

In both cases, the nutrient supply to the colony is limited, so that only cells towards the top of the colony experience concentrations high enough for rapid growth. However, in Figure 4.7-A there is still sufficient solute to maintain a complete, 5 µm-thick layer of growing cells (black arrows), whereas in Figure 4.7-B the layer is much thinner. This difference is critical – the layer in Figure 4.7-A is thick enough to be stable, whereas the layer in Figure 4.7-B is subject to a surface or "branching" instability. In the latter case, small differences in cell position at the front trigger positive feedback events: cells on the expanding front that are marginally higher than their neighbours receive preferential nutrient access, allowing them to grow rapidly and gain further height, and so on. The resulting colony (Figure 4.7-B, t_3) has a "branched" morphology [105, 186], in contrast to the smooth morphology in the first simulation (Figure 4.7-A, t_3).

This demonstrates that our finished hybrid model can recreate an important and widely-modelled feature of biomass-nutrient interactions [222, 146, 199, 28]: the ability to control the gross morphology of a community by changing the rate at which nutrient is supplied to it.

4.6 Conclusions

In this chapter, we have described the creation of a computational model for describing nutrient-controlled growth in a growing microbial community. We have discussed how community-scale continuum models of nutrient transport can be simplified, discretised and implemented, using the method of finite elements. Using test problems of increasing complexity, we have verified our model implementation, showing that it fulfills stability and consistency criteria under a range of different conditions.

The end product of this work is a flexible, reliable hybrid model that can be applied to simulate competition in a microbial community. Importantly, this model extends previous model paradigms by enabling the simulation of mixtures of different cell shapes, whilst still describing the all-important coupling between the colony and the solute fields around it.

5

Cell shape: a new determinant of spatial patterning in biofilms

Publications and statement of authorship

The work presented in this chapter is an adaptation of an existing publication, written in collaboration with other authors. This work has been published as: *William P. J. Smith, Yohan Davit, James M. Osborne, Wook Kim, Kevin R. Foster, and Joe M. Pitt-Francis. "Cell morphology drives spatial patterning in microbial communities" (Proceedings of the National Academy of Sciences 2016)* [259].

The author contributions for this study are as follows: WPJS, YD, JMO, KRF, and JMP-F designed research; WPJS and WK performed research; WPJS, YD, JMO, WK, KRF, and JMP-F analysed data; and WPJS, YD, JMO, WK, KRF, and JMP-F wrote the paper.

Abstract

The clearest phenotypic characteristic of microbial cells is their shape, but we do not understand how cell shape affects the dense communities, known as biofilms, where many microbes live. Here, we use individual-based modelling to systematically vary cell shape and study its impact in simulated communities. We compete cells with different cell morphologies under a range of conditions and ask how shape affects the patterning and evolutionary fitness of cells within a biofilm. Our models predict that cell shape will strongly influence the fate of a cell lineage: we describe a mechanism through which coccal (round) cells rise to the upper surface of a community, leading to a strong spatial structuring that can be critical for fitness. We test our predictions experimentally using strains of *Escherichia coli* that grow at a similar rate, but which differ in cell shape due to single amino acid changes in the actin homolog MreB. As predicted by our model, cell types strongly sort by shape, with round cells at the top of the colony and rod cells dominating the basal surface and edges. Our work suggests that cell morphology has a strong impact within microbial communities and may offer new ways to engineer the structure of synthetic communities.

5.1 Introduction

In Chapters 3 and 4, we showed how to combine an existing model of microbial biomechanics with a Python-based solute-modelling system. The product of this development is a flexible individual-based modelling (IbM) framework that allows

us to study the effects of cell shape in a microbial community, such as a colony or biofilm, in which large numbers of cells compete for limited resources. Significantly, our framework allows microbial shape to be varied as a simulation parameter: by representing individual cells as capsules instead of spheres, we allow a range of simple microbial shapes to be included and compared as part of the same model.

In this chapter, we apply our framework to perform original and fundamental tests of cell shape effects in microbial communities. We simulate the growth of dual-strain biofilms composed of simple coccal or rod-shaped cells, and demonstrate a relationship between cell shape and community spatial structure. Our analyses identify a new mechanism by which different cell shapes can self-organise into layered structures, thereby providing particular genotypes with preferential access to favourable positions in the colony. In addition, we test the predictions of the model using experiments, in which mutant *Escherichia coli* bacteria of different shapes are cultured together in colonies. Overall, this work demonstrates that differences in cell shape are central to both spatial architecture and fitness within microbial communities.

5.2 Simulating growth of mixed-shape colonies

In this section, we provide a brief recap of the basis of the IbM framework described in Chapters 3 and 4. Figure 5.1 provides an overview of components and processes under consideration, and Tables 5.1 and 5.2 provide a list of the model variables and parameters used in this chapter. We then go onto describe the results of simulations using this model.

Overall, our model is similar in structure to previous IbMs based on spherical cells [222, 152, 199], except that it allows us to study communities containing non-spherical cell shapes. We represent microbial communities as collections of elongating cells on a hard surface (Figure 5.1, t_1 and t_2); each cell is represented by a rigid, elastic capsule, having fixed radius r, variable segment length l, position $\mathbf{p} = (p_x, p_y, p_z)^\top$, and

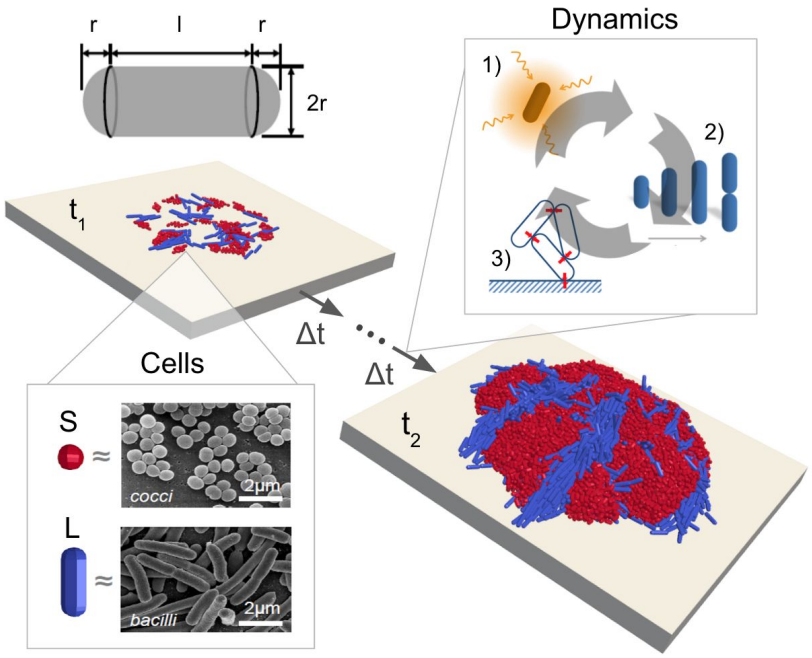

Fig. 5.1 To simulate the growth of a mixed-species microbial colony on a hard surface, we use the IbM framework developed in Chapters 3 and 4. In summary, microbial cells are represented using rigid elastic capsules of variable segment length l and fixed radius r (top left); coccal and bacillar cells are approximated respectively using short (S) and long (L) capsules ('Cells'), modelled on *Staphylococcus aureas* (top) and *Escherichia coli* (bottom) bacteria (SEM micrographs). Colony growth is driven by 3 primary processes ('Dynamics'): cells absorb nutrients from their surroundings (1) in order to grow and divide (2), and repulsive interactions between growing cells lead to the expansion of the colony in 3 dimensions (3). By sequentially updating the cell configuration according to these rules, we simulate the development of colony structure from an initial inoculum of cells (t_1) to a mature colony (t_2). Micrographs provided by the Public Health Image Library [178] and Rocky Mountain Laboratories [237]. Figure reproduced with permission from [259].

orientation $\hat{\mathbf{a}} = (a_x, a_y, a_z)^\top$. Cells absorb diffusing nutrients from their surroundings to grow and divide, causing the community to expand in space (Figure 5.1, 'Dynamics'). We assume cells to be immotile, moving only as a result of elastic repulsion.

Importantly, the capsule representation allows cell shape to be parameterised using a single number: the aspect ratio $AR = 1 + l/2r$. By changing the value of AR, we can model a range of common microbial morphologies, including cocci (round cells with low AR), bacilli (rod-shaped cells with high AR) and coccobacilli (intermediate AR).

Table 5.1 Model variables used in Chapter 5

Variable	Symbol	Units
Cartesian coordinates	x, y, z	μm
Cell volume fraction field	ϕ	
Nutrient field	u	$\mathrm{kg\,m^{-3}}$
For each cell i		
position vector	$\mathbf{p}_i = (p_x, p_y, p_z)^\top$	μm
orientation unit vector	$\hat{\mathbf{a}}_i = (a_x, a_y, a_z)^\top$	μm
segment length	l_i	μm
volume	$V_i = \pi l_i r^2 + \frac{4}{3}\pi r^3$	$\mu\mathrm{m}^3$
local nutrient concentration	$u_i = u(\mathbf{p}_i)$	$\mathrm{kg\,m^{-3}}$
growth rate	$\mu_i = \mu_{\max} u_i/(K + u_i)$	s^{-1}

In this chapter, we represent bacillar and coccal cell shapes using short (S) or long (L) capsules, whose geometries are modelled on those of *S. aureus* and *E. coli* respectively (Figure 5.1, 'cells') [203, 238]. S-type cells have an initial aspect ratio $AR_0 = 1.1$,[1] increasing to a final value $AR_f = 1.7$ at division, whereas L-type cells have $AR_0 = 3.0$ and $AR_f = 5.7$. We also consider shapes intermediate to S and L later on, in Section 5.5.

5.2.1 Simulation protocol

To investigate the impact of cell shape on community growth, we simulated the growth of vertical colony sections in 2 and 3 dimensions. Each simulation was initialised using an inoculum of cells arranged randomly on the base of the domain, with cell axis vectors drawn randomly in the 3-D case. Each inoculum consisted of a 1:1 mixture of two bacterial strains, marked with red and blue colour labels for lineage tracking. Following inoculation, all cells were allowed to grow and divide until the colony reached a fixed maximum height of approximately 30 μm. In 2-D simulations, cell centroids and axes were confined to a plane of base length $L_x = 300$μm, whereas 3-D simulations used a cuboidal domain with base dimensions $L_x = L_y = 40$μm. In both

[1] Note that perfectly spherical cells ($AR_0 = 1.0$) lack a principal axis, which are used to compute spatial relationships between cells. As such, we approximate spherical morphologies with "pseudo-spherical" capsules of $AR_0 = 1.1$.

Table 5.2 Model parameters used in Chapter 5

Parameter	Symbol	Value	Units	Source
Domain size:			µm	[222]
width	L_x	300 (2D) or 40 (3D)		
depth	L_y	1 (2D) or 40 (3D)		
height	L_z	$L_z = \max(p_z) + \delta$		
Cell radius	r	0.48	µm	[238]
Cell birth aspect ratio:	AR_0			This study
S-type		1.1		
L-type		3.0		
Boundary height	δ	40	µm	This study
Nutrient diffusivity	D	2×10^{-9}	$\mathrm{m^2\,s^{-1}}$	[222]
Bulk concentrations:	u_0		$\mathrm{g\,m^{-3}}$	This study
case 1: unlimited		∞		
case 2: limited		5		
Dimensionless parameters	$(\mathscr{D}, \eta)$			This study
case 1: unlimited		(0, 0)		
case 2: limited		(0.01, 0.033)		
Biomass density	ρ	290	$\mathrm{kg\,m^{-3}}$	[222]
Specific growth rate	$\mu_{\max}$	2.8×10^{-4}	$\mathrm{s^{-1}}$	[239]
Uptake saturation constant	K	0.35×10^{-3}	$\mathrm{kg\,m^{-3}}$	[222]
Biomass yield	γ	0.045		[222]
Newton solver tolerance	ε_{n}	1×10^{-3}		This study
Max. Newton solver iterations	N_{iter}	50		[168]
Mesh element size	h	5.0	µm	This study
Division axis noise	$\xi_{\hat{\mathbf{a}}}$	0.1	%	[239]
Division volume noise	ξ_V	0.2	%	[239]
Regularisation weight	Γ	0.002	$\mathrm{m^{-1}}$	[239]
CG Solver tolerance	$\varepsilon_{\mathrm{CG}}$	1×10^{-3}	µm	[239]
Max. contact iterations	N_{Con}	8		[239]
Max. CG solver iterations	N_{CG}	7n		[239]
Cell grid element size	h_{grid}	10	µm	This study
Time step	Δt	15	min	[239]

cases, domains were surrounded by hard walls to approximate repulsive mechanical forces from the basal surface and surrounding sections of the biofilm. We set $\Gamma = 0.04$ throughout the study, so that cell growth would be effectively unconstrained by mechanical forces. As a first approximation, we also allowed all cells to grow exponentially at a maximal growth rate $\mu_{\max}$, representing a scenario where nutrient perfusion in the biofilm is complete and spatially homogeneous. In the next section of this chapter, we remove this assumption in order to model competitive interactions between different cell shapes.

To account for the stochastic noise terms in the model mechanics scheme (see Chapter 3) and inoculation procedure, we increased simulation sample sizes until measurements converged, using the convergence criterion

$$||\langle \mathbf{X} \rangle_N - \langle \mathbf{X} \rangle_{N-1}||_{l2} \; / \; ||\langle \mathbf{X} \rangle_N||_{l2} < \varepsilon_{\mathrm{TOL}}, \tag{5.1}$$

where $\langle \mathbf{X} \rangle_N$ denotes a mean vector of measurements (of a quantity of interest) for a sample size N, and $\varepsilon_{\mathrm{TOL}}$ is a convergence tolerance set to 5%. $||\cdot||_{l2}$ represents the Euclidean norm operation.

In total, ≈ 3000 model simulations were performed in this way, using two NVIDIA Tesla C2075 6GB GDDR5 PCIe workstation graphics cards for simulations without nutrient fields, and on two NVIDIA Quadro K5000 4GB GFX graphics card for simulations including them. Simulations were visualised and checked using Paraview 4.3.1, and the post-processing of results was carried out using MATLAB 2015a.

5.2.2 Cell shape drives spatial patterning within colonies

Figure 5.2 shows representative end-state snapshots of biofilm sections, grown using three 1:1 combinations of S and L cell shapes (SL, SS and LL mixtures, top of Figure 5.2), using the protocol listed above. In these simulations, we found that different spatial structures emerged, depending on the cell shapes that were present.

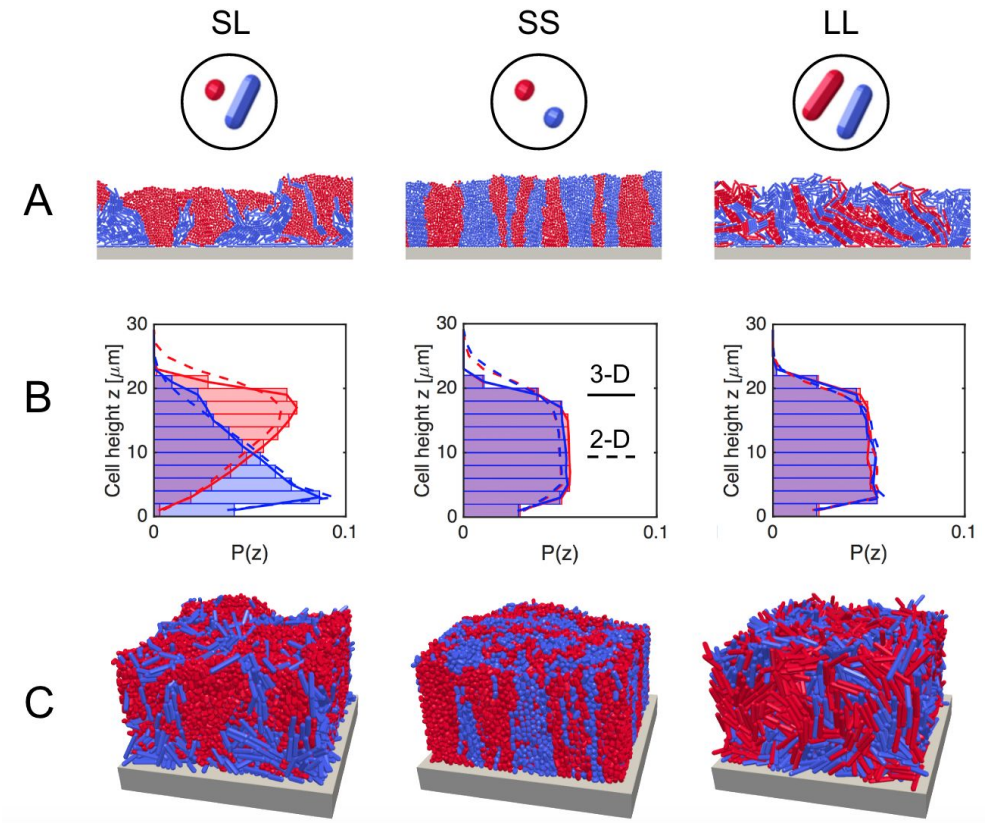

Fig. 5.2 Cell morphology affects self-organisation in simulations of exponential colony growth. A: Sections of 2-D colonies grown from 1:1 mixtures of red- and blue-labeled strains form different spatial patterns depending on whether the strains have a coccal (short, S) or rod-like (long, L) morphology. B: Volume-weighted histograms of cell z-coordinates ($P(z)$) show that SL mixtures develop a layered structure in both 2- and 3-D colonies, with S cells sitting above L cells. In SS and LL control simulations, this layering is absent. C: 3-D simulations, in which cell positions and orientations are no longer confined to the xz plane, produce spatial patterns similar to those shown in 2-D. 20 simulations per case. Figure reproduced with permission from [259].

SL cell mixtures spontaneously developed a layered structure, with groups of red S cells lying atop blue L cells. By contrast, SS mixtures tended to produce smooth, vertical boundaries between adjacent strain groups, with no layering. LL colonies produced a third type of spatial patterning, developing fractal-like interdigitations between adjacent cell groups, as reported in previous modelling studies [238, 267].

In Figure 5.2-B, we show histograms of cell z-coordinates for the two strains: here, $P(z)$ corresponds to the biovolume distribution along the z axis, normalized by total colony volume. This quantifies the tendency for SL colonies to develop layered structures.

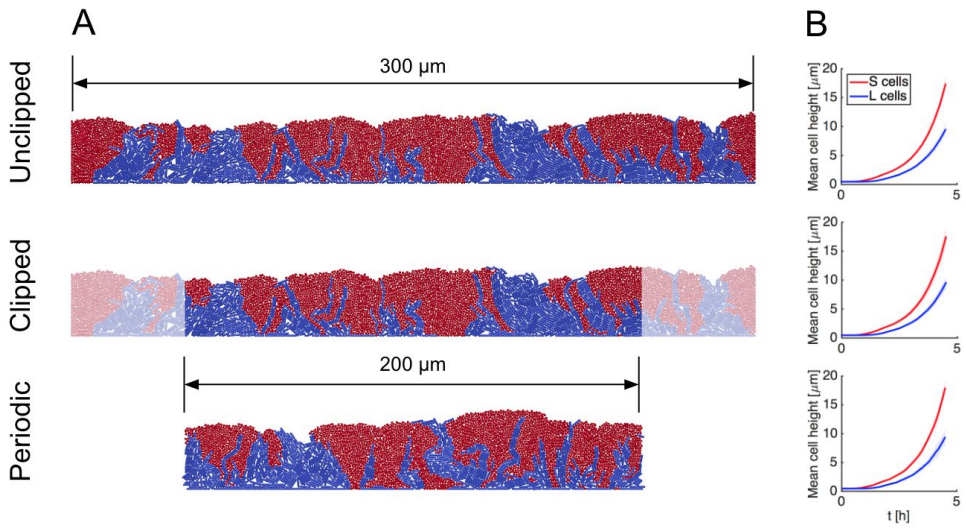

Fig. 5.3 Mixed-shape simulations using hard and periodic mechanical boundaries behave similarly. Here we compare 2-D simulations featuring hard lateral walls (such as those shown in Figures 5.2), before and after excluding cells within 50μm, with periodic analogues of equivalent domain sizes. Colony snapshots (A), taken after 4.5h of growth, show unclipped, clipped and periodic simulations, which produce similar group structures. All three cases produce similar layering dynamics, as quantified by mean strain height traces (B). Sample of 5 simulations under uniform growth conditions. Figure reproduced with permission from [259].

By contrast, the vertical strain distributions seen in SS and LL control colonies are identical, confirming the absence of layering. The same effect is reproduced in 3-D simulations, where cell centers and axes are not confined to the *xz* plane (Figures 5.2-B and 5.2-C).

5.2.3 Layering is independent of lateral boundary conditions

The simulation domains shown in Figure 5.2 are bounded by hard walls on the bottom and sides, which represent the constraining forces imposed by the basal surface and surrounding sections of the colony. In the latter case, the hard wall assumption might be expected to introduce boundary artifacts, because cells close to the sides of the domain face additional constraints to their movement and rotation.

To mitigate these potential boundary artifacts, we used the precaution of excluding cells close to side walls from our analyses (cells within 50 μm of a side wall in the 2-D case, and within 2 μm in 3D). We also repeated walled simulations using periodic boundary conditions which recreate the lateral compressive forces without using hard walls (see Chapter 3 for further details). We show a comparison of these cases in Figure 5.3, which demonstrates that layering dynamics in periodic simulations were very similar to those in Figure 5.2, implying that hard boundaries do not exert a strong influence on the patterning dynamics.

Overall, these observations suggest that individual cell shape is capable of driving significant structural changes in the wider biofilm environment – and in particular, that combinations of differently-shaped cells can drive the formation of layered structures, reported previously in multi-species biofilms [57, 117, 85].

5.3 The competitive value of cell shape

Next, we examined the consequences of layering phenomena on strain competition within the biofilm environment. Because biofilms are typically characterised as highly heterogeneous environments, systematic differences in the positioning of bacterial strains could lead to significant differences in their fitness, offering a competitive advantage to particular cell morphotypes [286, 200, 144].

5.3.1 Modelling nutrient gradients

To test this hypothesis, we repeated the 3-D biofilm growth simulations using nutrient-limited conditions. Instead of allowing all cells to grow at the same rate as before, we coupled each cell's growth rate μ_i to the local concentration u of a rate-limiting nutrient field, evaluated at that cell's centroid $\mathbf{p}_i$. As discussed in Chapter 4 and in previous studies [222, 224, 155, 199], we model this coupling using the Monod

Table 5.3 Solute boundary conditions used in Chapter 5

Set	Boundary	Condition	Description
A	Top: $z = \max(p_z) + \delta$	$u = u_0$	Supply from bulk liquid
	Bottom: $z = 0$	$\nabla u \cdot \hat{\mathbf{n}} = 0$	Zero flux through base
	Left, Right: $x = 0,\ L_x$	$\nabla u \cdot \hat{\mathbf{n}} = 0$	Zero flux through walls
B	Top	$u = 0$	Removal by bulk liquid
	Bottom	$u = u_0$	Supply from base
	Left, Right	$\nabla u \cdot \hat{\mathbf{n}} = 0$	Zero flux through walls

equation $\mu_i = \mu_{\max} u(\mathbf{p}_i)/(K + u(\mathbf{p}_i))$, where $\mu_{\max}$ and K are the maximum specific cell growth rate and the uptake saturation constant, respectively.

By imposing different boundary conditions on the nutrient reaction-diffusion equation, opposing perfusion scenarios can be created: one in which nutrient was supplied from above the colony, and another in which supply came from below. These boundary conditions are listed in Table 5.3. To compute the nutrient field $u = u(x, y, z)$ for a given cell configuration $[\mathbf{p}_1, \ldots, \mathbf{p}_n]$, we solved the RDE (Reaction-Diffusion Equation)

$$D\nabla^2 u = \frac{1}{\gamma}\rho\mu_{\max}\left(\frac{u}{u+K}\right)\phi(\mathbf{p}_1, \ldots, \mathbf{p}_n), \tag{5.2}$$

in dimensionless form, as described previously in Chapter 4. Here, D, γ, ρ, $\mu_{\max}$, K and ϕ correspond to the nutrient diffusivity, the biomass yield per unit solute, the biomass density, the maximum specific nutrient uptake rate, the half-saturation concentration, and the local cell volume fraction, respectively. Nutrient field parameters are listed in Table 5.2; these were chosen so as to create thin growth layers of similar thicknesses in the two perfusion scenarios. In both cases the Damköhler number $\mathscr{D}$ (the ratio of nutrient uptake rate to diffusion rate, as defined in Chapter 4) was set to 0.01.

5.3.2 Shape-driven layering alters strain fitness

The results of the nutrient-limited simulations are shown in Figure 5.4. Figure 5.4-A provides example snapshots of both simulation scenarios, showing colonies grown

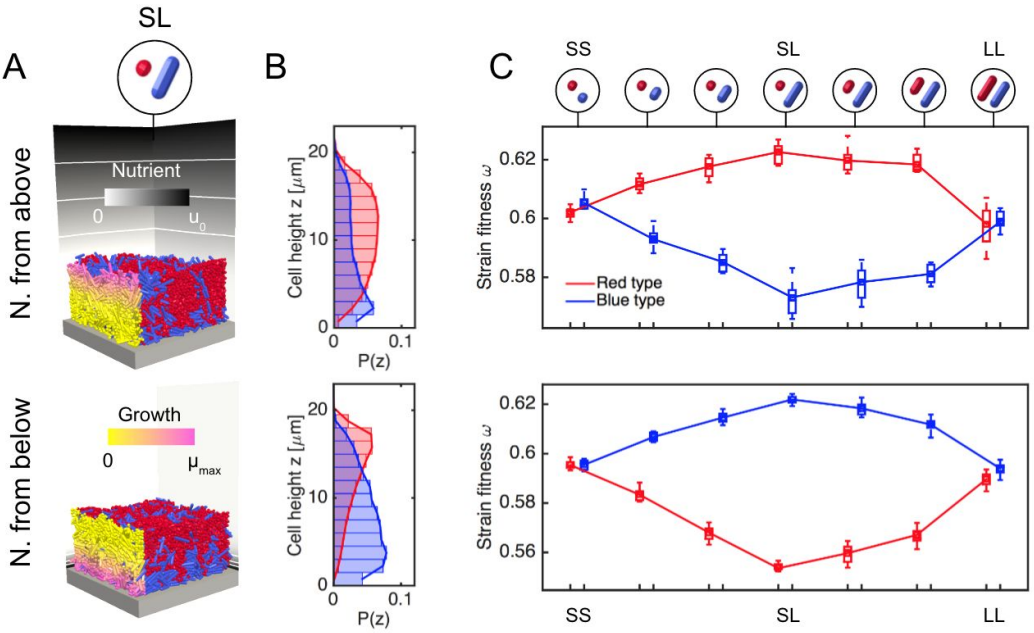

Fig. 5.4 Cell morphology influences strain fitness within colonies. A: Competition between different cell shapes is simulated by growing biofilm sections under nutrient-limited conditions. Nutrients are supplied either from above the colony (first row) or from below (second row). Cells on the left face of the colony are coloured by their growth rate, showing that rapid cellular growth is limited to a thin layer at the top or at the base of the colony, in the two scenarios respectively. Contours on the nutrient field (background) correspond to $u/u_0 = 0.25, 0.50$ and 0.75. B: volume-weighted histograms ($P(z)$) of cell heights in nutrient-limited SL colonies show similar layering effects to those created under homogeneous growth conditions, with S cells (red) growing atop L cells (blue). C: Bar plots of strain fitness show that coccal morphologies outcompete rod-like morphologies in scenarios where nutrients are delivered from above the colony, but that the reverse is true when nutrients are delivered from below. 10 simulations per case; figure reproduced with permission from [259].

from 1:1 SL cell mixtures after 12 hours of growth. Cells in the bulk of the colony are coloured by type as before, but cells on its left face are coloured by their growth rate, confirming that rapid cellular growth is limited to a thin layer at the top or at the base of the colony, in the two scenarios respectively. In Figure 5.4-B, we plot histograms of cell heights in these colonies, showing that S and L cell strains still adopt a layered structure when grown together under nutrient-limited conditions. Cells close to the side walls of the domain are removed from this analysis, as described previously.

To quantify these growth advantages, we used the mean cell division rate as a strain fitness metric ω_i, given by

$$\omega_i = \frac{1}{t_{\text{end}}} \log_2 \left(\frac{\sum_i^n V_i(t_{\text{end}})}{\sum_i^n V_i(0)}, \right) \tag{5.3}$$

where t_{end} refers to the duration of the simulation, V_i denotes the volume of cell i, and n is the number of cells present at a given time. Figure 5.4-C shows the relationship between cell shape and strain fitness in the two nutrient competition scenarios. In this case, colonies were grown using not only SS, SL and LL cell strain mixtures, but also with mixtures of intermediate cell aspect ratios, using the same simulation protocol. The top row of Figure 5.4-C provides a pictorial representation of the cell shapes used. Between the SS and SL cases, the birth aspect ratio of the blue strain is increased through the values 1.1, 1.5, 2.0 and 3.0. Figure 5.4-C shows that the fitnesses of (red) S cells increase at the expense of blue cells, up to a maximum at the SL case. Next, between the SL and LL cases, the aspect ratio of the red strain is increased in the same way, and the fitness differential is reduced to approximately zero. When the nutrient conditions are reversed (Figure 5.4-C, bottom row), so too are the strain fitnesses, this time in favor of L cells.

Importantly, these simulations confirm the hypothesis that strain layering effects can, under limited nutrient conditions, translate into differences in strain fitness. When nutrients are delivered from above the colony, S cells receive preferential nutrient access at the expense of L cells below. S cells are correspondingly afforded an increased growth rate and gain a fitness boost relative to the SS and LL cases where no layering exists. As a result, the number of S cells present in the upper layer of the colony is enhanced, as shown by the cell height histograms in Figure 5.4-B. In cases where nutrients are delivered from below the colony, the fates of S and L cells in SL mixtures are reversed.

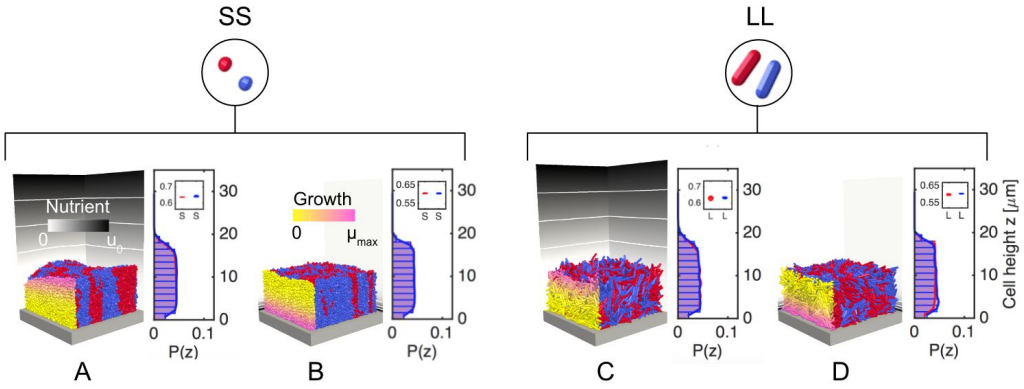

Fig. 5.5 Control simulations show that fitness benefits must result from the heterogeneous colony structure. When the distributions of cell heights are identical, as seen in the SS and LL control simulations above, no fitness difference between strains is observed – regardless of whether nutrients are delivered from above the colony (A, C) or from below (B, D). This demonstrates that neither cell shape has an intrinsic fitness advantage over the other. Figure reproduced with permission from [259].

Finally, Figure 5.5 shows additional colony pictures and cell volume density histograms, corresponding to the control (SS and LL) cases discussed in Figure 5.4. In these cases, no shape driven-layering occurs, and the histograms of each strain overlap almost exactly. Consequently, strain fitnesses are identical, irrespective of the nutrient delivery direction.

5.4 Experimental tests of shape-driven patterning

Having shown that cell shape can affect community development and composition with our model, we then sought to test the predictions of our model experimentally. As discussed in Chapter 2, studying cell shape empirically is challenging, because differently-shaped strains will typically be physiologically different as well, introducing confounding effects. However, the *E. coli* mutants recently identified and described by Monds *et al.* [193] provide a solution to this impasse. Strains in this library are genetically identical except for a point mutation in the gene coding for the cytoskeletal protein MreB. Critically, these mutations cause substantial and stable changes in cell

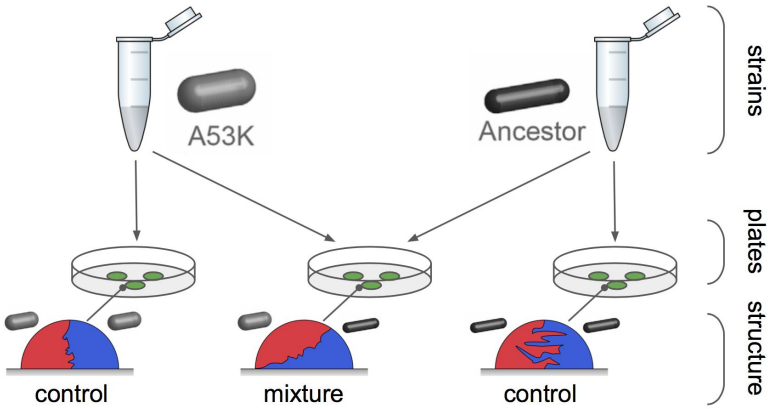

Fig. 5.6 Diagram summarising experimental protocol for testing layering. Fluorescently-labelled short (A53K) and long (Ancestor) cells from the Monds *E. coli* morphotype library are grown in liquid culture (strains) to a fixed density, before being spotted onto agar plates in different combinations (plates). After 48 h growth, colonies growing on the agar are imaged using epifluorescent and confocal laser scanning microscopy.

aspect ratio, without significantly affecting exponential cell growth rates. For example, the specific growth rate μ is reported as 0.519 ± 0.015 h^{-1} for the ancestral (WT) strain, and 0.516 ± 0.007 h^{-1} for mutant REL606mreB A53T [193]. This allows cells of different shapes to be cultured together in set proportions.

In this section, we discuss experiments in which differently-shaped cells from the Monds library are fluorescently labelled and grown together on agar plates. Figure 5.6 shows a diagram depicting this procedure. The resulting colonies are then imaged using two types of microscopy:

- **Epifluorescent microscopy (EM)**, which gives an overhead view of a whole colony and its overall composition;
- **Single-photon confocal laser scanning microscopy (CLSM)**, which reveals the 3-D structure of small colony sections.

We show how the resulting data can be processed to examine shape-driven spatial patterning *in vitro*, as a direct test of our model's predictions. The experiments and

image acquisition described below were performed by our collaborator Wook Kim, whereas we performed the subsequent image analysis.

5.4.1 Experimental protocol

The strains used in these experiments are as follows: *Escherichia coli* REL606 is the parent (WT) strain [162]. A53K (REL606mreB^{A53K}) and A53S (REL606mreB^{A53S}) were previously constructed from REL606 with the respective non-synonymous mutation at the 53rd amino acid residue of the mreB protein [193]. A53K (denoted AK) exhibits the shortest and widest cellular morphology, and A53S (AS) is intermediate, compared to WT. Importantly, these strains exhibit mean aspect ratios of 4.44 (WT), 3.55 (AS) and 2.50 (AK), but share the same specific growth rate, and differ only marginally in lag phase time [193]. All three strains were kindly donated by Kerwyn Huang (Stanford University, CA).

Fluorescent tag plasmids (pmaxRFP or pmaxGFP, Amaxa/Lonza Inc.) were introduced into all three strains for epifluorescence and confocal microscopy, so that each strain expressed either RFP or GFP (Red and Green Fluorescent Protein, respectively). For routine culturing in liquid, cells were grown shaking at 250 rotations per minute in LB (Lysogeny Broth, Thermo-Fisher Scientific) medium at 37°C. For plate cultures, cells were grown on DM (Davis Minimal) medium [162], supplemented with either glucose (175µg mL^{-1}) or lactose (210µg mL^{-1}) as previously described [193] at 37°C. All media were supplemented with kanamycin at 50µg mL^{-1} to maintain plasmids.

Overnight cultures were serially diluted in PBS (Phosphate-Buffered Saline), mixed together in a 1:1 ratio, then spotted in either 1 or 10µL volumes on the surface of DM plates. We observed no significant difference between glucose or lactose supplementation; data reported in this study are from glucose-supplemented plates spotted at 1µL volume. For each combination of cell strains and fluorescent labels, control experiments using reverse labellings were also carried out, and each experiment

was repeated at least twice. Two days following inoculation, mixed-culture colonies were imaged by epifluorescence and confocal laser scanning microscopy as described in previous publications [144, 143].

5.4.2 Experiments corroborate shape-dependent fitness predictions

The array of epifluorescent micrographs shown in Figure 5.7 correspond to overhead views of entire colonies, grown from 1:1 mixtures of different combinations of the AK (short), AS (medium) and WT (long) E. coli strains, as listed above. Each column in the array is labelled according to the strains used; label colours showing which fluorescent label (red or blue) each strain has been tagged with. The images shown are in pseudocolour, with the fluorescence signal from GFP-labeled cells shown in blue (so as to match the strain colour labels used in simulations). The labels 1 and 2 denote repeats of a given experiment.

These images can be used to test a primary prediction of the individual-based model. Nutrients diffuse into colonies from the agar below, similar to the scenario shown in Figure 5.4-A (second row). If mixed-shape colonies really produce layered structures, then this ought to benefit the longer cell type, which is predicted to become concentrated at the base of the colony and thereby secure a richer supply of nutrients. We can confirm this trend in the images shown in Figure 5.7-A, by examining the edge of the colony in each case. In the first column (AK-AK), both cell strains (red and blue) are present at the edge, suggesting a similar strain fitness. As the aspect ratio of the red strain is increased however (cases AK-AS, AK-WT), the blue strain disappears from the edge, implying that its fitness has fallen relative to that of the red strain. When the aspect ratio of the blue strain is then increased in the same way (cases AS-WT, WT-WT), the blue strain reappears at the colony edge, implying that its fitness is once again equal to that of the red strain. These observations are consistent

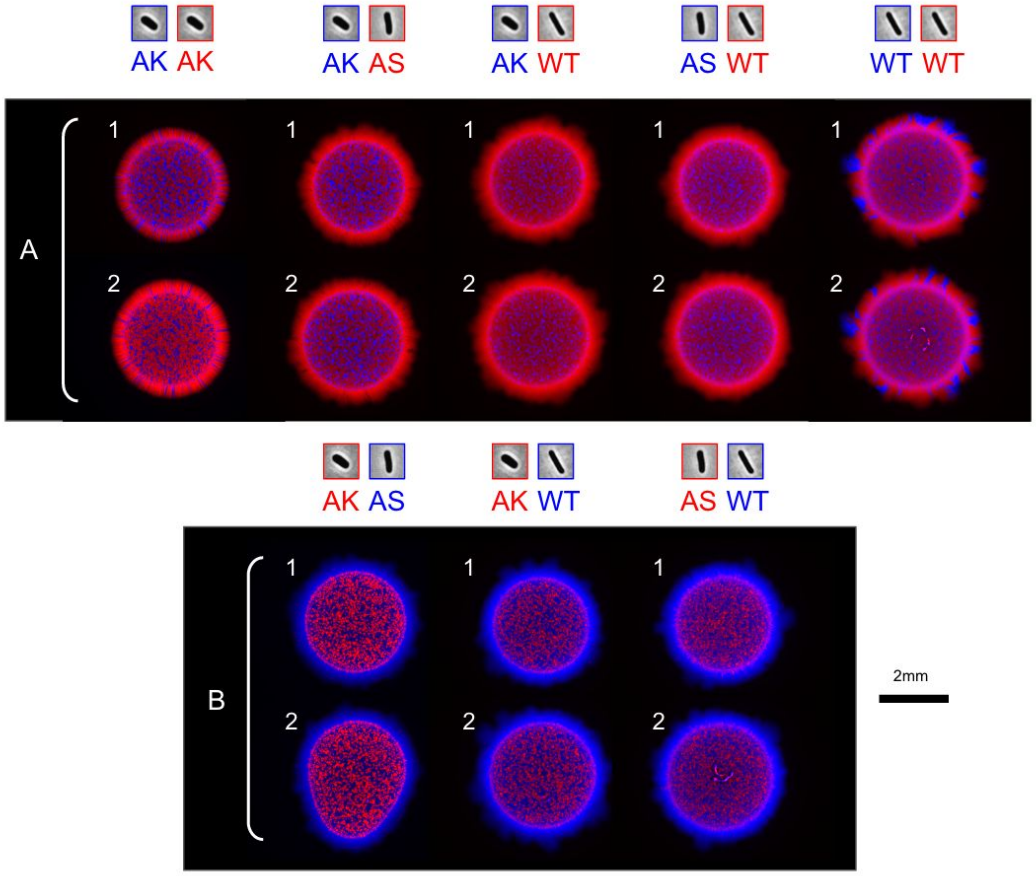

Fig. 5.7 Fluoroescently-labelled bacteria from the Monds library are grown together in colonies, as an experimental test of morphotype-patterning relationships. Pseudocolour images of whole *E. coli* colonies, grown from different binary combinations of AK, AS and WT strains, show that cell shape affects colony edge composition. In each case, two experimental repeats (1, 2) are provided. In A, strains are shown in red (longer cell strain, RFP label) and blue (shorter cell strain, GFP label). As the aspect ratio of the red strain is increased (AK-AK through AK-WT), its presence at the colony edge increases relative to the shorter blue type, implying a fitness benefit for the former. Applying the same procedure to the blue strain (AK-WT through WT-WT) extinguishes the effect. This trend can be seen both in colonies containing mutant strains (AK, AS) and in those containing the ancestral strain (WT) – suggesting that the effect is not caused by mreB mutations *per se*, but by the cell shape changes they produce. In B, red and blue fluorescent labels are reversed, and the same trend appears. Phase contrast cell images (of width 3.5 µm) taken with permission from [193]; figure reproduced with permission from [259].

with the fitness predictions discussed in Figures 5.4 and 5.5, and are also reproduced when the strain colour labels are reversed (Figure 5.7-B).

5.4.3 Spatial patterning controlled by cell shape *in vivo*

Re-imaging the colonies shown in Figure 5.7 using confocal microscopy allows the 3-D spatial structure of each community to be inspected in greater detail. Figure 5.8 depicts high-magnification confocal images ('confocal') of colonies composed of only one morphotype (AK-AK, AS-AS, WT-WT), shown below whole-colony images for comparison ('colony'). Each confocal image shows both the middle layer of the vertical image stack, and that stack's orthogonal projections, as computed using FIJI microscopy software [247]. Following collection, confocal image stacks were enhanced by setting pixel saturation to 1% and by normalising signal to the full intensity range.

The confocal images in Figure 5.8, taken from the edge of each colony, corroborate a second prediction of the model: that inter-strain (red-blue) mixing is strongly dependent on cell aspect ratio. Similarly to Figure 5.2 (SS column), AK-AK colonies show smooth inter-strain boundaries, whereas WT-WT mixtures reproduce the fractal-like interdigitations seen in the model (c.f. Figure 5.2, LL column), again recapitulating the findings of previous studies [238]. The intermediate AS cell shape (c.f. Figure 5.2, center column) produces an intermediate level of mixing, generating fractal-like patterns as in the WT case, but with an apparently lower fractal dimension.

5.4.4 Measuring layering using automated image analysis

The third key prediction made by the model was that mixed-shaped colonies should produce a layered spatial structure, with shorter cells lying atop longer cells. To see if this prediction would hold *in vitro*, we performed additional image analysis on confocal image stacks, to check how the relative abundance of the two strains varied as a function of height in the colony. The (automated) image processing protocol is described below.

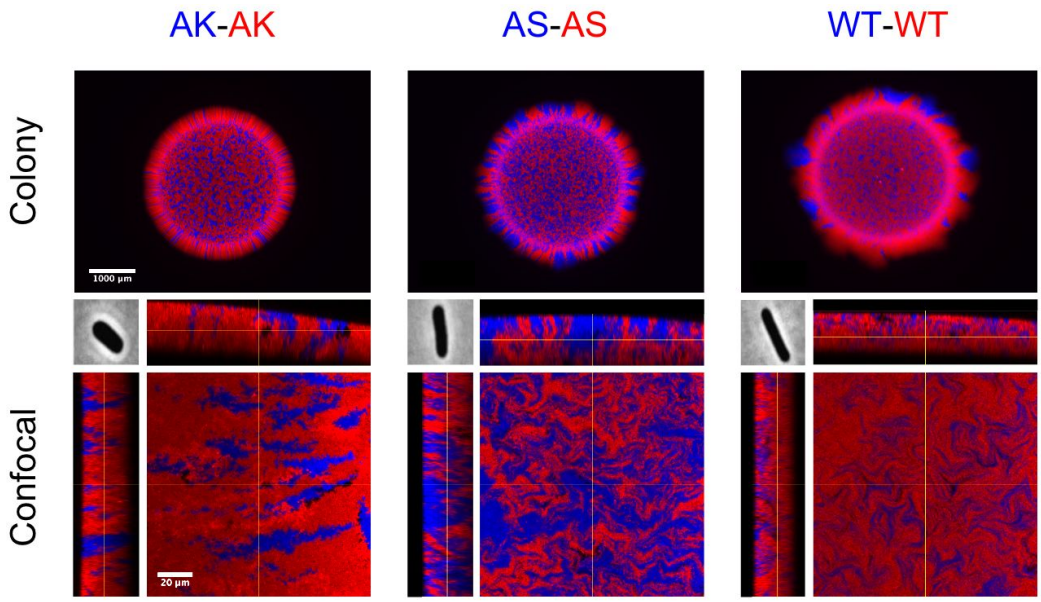

Fig. 5.8 Colonies composed of Monds' AK, AS and WT *E. coli* strains (top row) reproduce spatial patterning predicted in simulations. At higher magnification, representative confocal images of edge sections of each colony are shown alongside orthogonal projections (bottom row). These images corroborate the predictions of our simulations: WT colonies show complex, fractal-like mixing between red and blue cell groups, whereas AK colonies show smoother group boundaries extending vertically through the colony. AS colonies display intermediate behavior, showing patterning of lower fractal dimension than in WT colonies. Images taken after 48h growth in each case, scale bars on top and bottom row correspond to 1mm and 20µm respectively. Phase contrast cell images (of width 3.5 µm) taken with permission from [193]; figure reproduced with permission from [259].

Following enhancement in FIJI (see above), images were then segmented using the MATLAB bioformats plugin, according to the following procedure. For each stack, incomplete or excessively dark images were excluded by removing any layer in which more than 1% of pixels had intensities less than 12% of the maximum, measured in composite grayscale images. These thresholds were chosen manually to optimise the segmentation accuracy. To ensure a sufficient number data points for curve fitting later on, confocal stacks with fewer than 6 images remaining were removed from the analysis outright. In each of the remaining images, the number of GFP-labeled cells was estimated by counting the number of pixels in the green channel data with intensities above a threshold, computed for each individual layer using Otsu's method

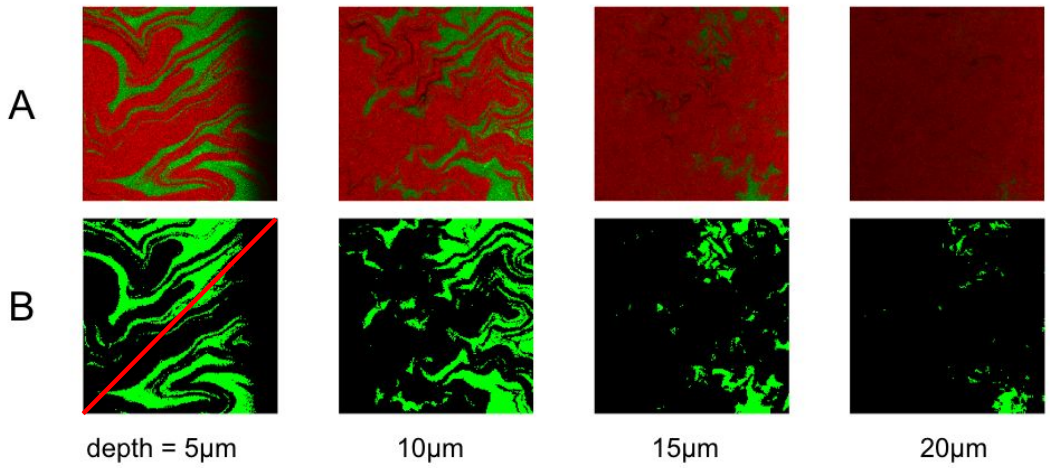

Fig. 5.9 Quantification of cell layering effects using image analysis. Four examples of raw (non-pseudocolour) 2-channel confocal images (A) depict successively-deeper layers of a WT-AK colony, with longer WT cells labelled in red, and shorter AK cells labelled in green. To count the number of AK cells as a function of height in the colony, we first remove images that are incomplete slices (e.g. A, depth 5 μm, and images that have a poor signal-to-noise ratio due to limited laser penetration. The remaining images are segmented using the green channel only to produce binary images (B), from which the green pixel count can be measured as a proxy for AK strain cell volume. Figure reproduced with permission from [259].

[211]. Figure 5.9 shows an example of this segmentation process, applied to confocal images of a WT-AK colony.

5.4.5 Mixed-shape colonies reproduce layering effect

Confocal microscopy data demonstrates that mixing long and short cell strains together can result in the emergence of layered structures. In Figure 5.10-A, we show that WT cells (shown in blue) displace shorter AK cells (red) from the base of the colony. This effect is visible both from side projections of confocal z-stacks (Figure 5.10-A, top row) and from horizontal slices taken at increasing depths in the colony. Because nutrients are supplied from the agar below the colony, we also see an overgrowth of rod-cells at the colony base, as predicted by the second modelling scenario shown in Figure 5.4. Reversing the colour labels produces the same result (Figure 5.10-B),

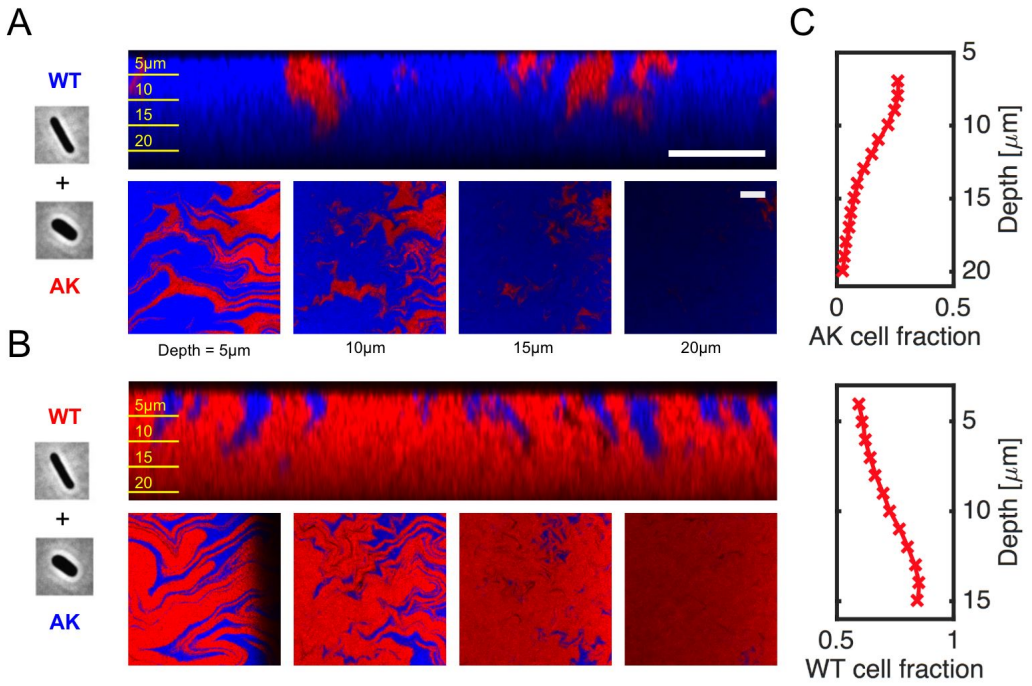

Fig. 5.10 Mixed-morphotype colonies reproduce the layering phenomena predicted by simulations. A: Pseudocolour confocal images show that GFP-labeled WT *E. coli* cells (shown in blue) are able to burrow beneath shorter, wider AK mutants (red), leading to their enrichment at the base of the colony. B: The same is true when fluorescent labels are reversed. Images correspond to vertical colony sections (A,B, top row) and horizontal slices taken at successive depths (A, B, bottom row). C: layering effects can be quantified by measuring the volume fraction of GFP-labelled cells as a function of depth in the colony, using automated image analysis. Cell micrographs in A and B are taken with permission from reference [193]; scale bars correspond to 20 μm. Confocal images and data taken after 48 h growth; figure reproduced with permission from [259].

demonstrating that layering is not an artifact produced by the fluorescent labelling scheme.

In Figure 5.10-C, we use the automated image analysis scheme (discussed above) to quantify the layering effect. By counting the number of blue pixels in each layer of a stack, we estimate the volume fraction of AK (top row) or WT (bottom row) cells as a function of depth in the colony. These traces show an approximately linear reduction in the AK cell fraction (and corresponding increase in WT fraction) within the first

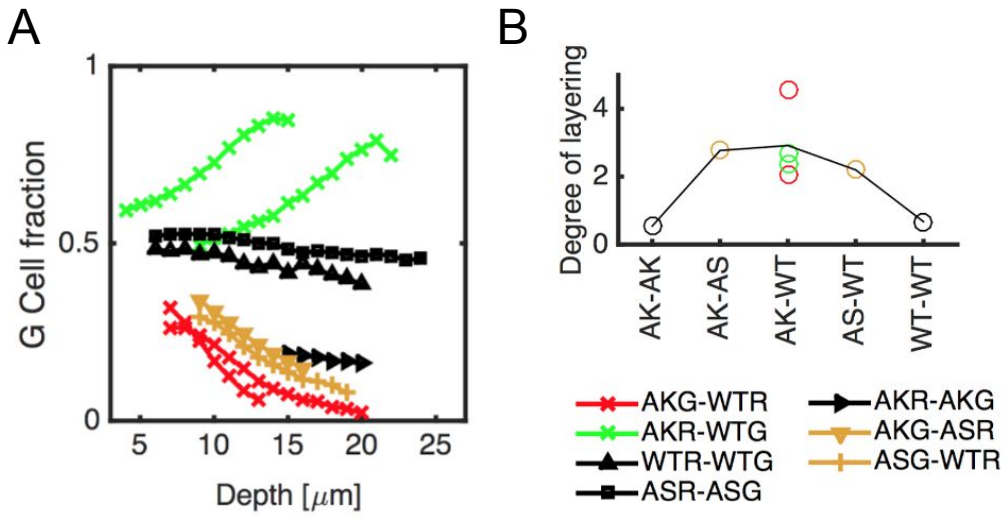

Fig. 5.11 Exploring the relationship between layering and cell shape. In A, we plot the fraction of green pixels in these segmentations as a function of depth in the colony, for various binary cell shape mixtures. Each line corresponds to one segmented confocal stack; lines are coloured red, green, black or orange to denote mixed-morphotype treatments, colour-swapped treatments, single-morphotype controls and intermediate morphotype treatments respectively, as shown in the key (bottom right). The gradients of these traces, computed using linear regression, are plotted in B with data points colour-coded to match (A). Images and data taken after 48 h growth in each case; figure reproduced with permission from [259].

15 µm below the colony surface, which is in agreement with the cell arrangements predicted in Figures 5.2 and 5.4.

5.4.6 Layering is dependent on cell shape differences

Finally, we repeated this analysis with images taken from colonies of other morphotype combinations, including the control colonies shown in Figure 5.8. Figure 5.11-A shows the complete set of green (G) cell fraction traces used. In each case, we quantified inter-strain layering by computing the average slope of these fraction traces, using linear fitting. Figure 5.11-B shows a plot of these gradients ('Degree of layering') against the cell-shape combination used. This shows a strong relationship between differences in cell shape and the degree of layering in the colony across these different genotypes, as predicted by the model.

In summary: in this experimental section, we have shown that microbes from the Monds morphotype library can be grown together in agar plate colonies, enabling an experimental test of our simulations. Although the shapes of the *E. coli* cells used are not identical to those in our model, they nonetheless suffice to create the same qualitative effects: significantly, these experiments corroborate several of the model's key predictions:

- Increased fractal mixing with longer cell shapes in single-shape colonies, in agreement with previous experiments;
- Layering effects in mixed-shape colonies, with shorter cells lying atop longer cells;
- Overall fitness advantage for longer cells in mixed-shape colonies, when limiting nutrients are supplied from the substratum.

Having thus validated the predictions of shape-driven patterning and layering, we will now turn our attention back to the individual-based model, and perform further simulations to investigate the physical mechanisms underlying these phenomena.

5.5 Exploring the mechanisms of layering

How can we explain the shape-dependent spatial patterning observed both in simulations and experiments? In particular, can we devise a physical description of how layering occurs? To address these questions, we performed further simulations using the IbM framework, but this time using variations of a second, simplified simulation protocol.

5.5.1 Simplified simulation protocol for testing layering

To investigate the mechanism of cell layering in SL shape mixtures, we grew 2-D colonies from an inoculum of only two cells placed a fixed distance apart, instead of a randomised inoculum of many cells. This enables us to focus on a single interstrain (red-blue) boundary, and makes it easier to control the initial spacing of cells directly. We also removed the lateral mechanical walls at $x = 0, L_x$ so that colony expansion would be restricted only by the basal surface, and set cell growth rates to a constant value ($\mu_{\max}$) as in Figure 5.2.

Figure 5.12 shows a set of representative simulation snapshots for SL, SS and LL 'colonies' grown for 8 h using this procedure. Measuring the mean heights for each shape combination as a function of time shows the development of a significant strain height difference in the SL case, but not in the SS and LL cases. This shows that the simplified simulation protocol reproduces the essential patterning effects reported in Figure 5.2.

5.5.2 The 'wedge effect': layering through self-organisation

Close examination of the growth of SL colonies, such as the one shown in Figure 5.12, suggests that layering is driven by several interacting processes, summarised in Figure 5.13. In Figure 5.12-A we show two end-state snapshots of the same 2-D SL colony, colouring cells either by their type or by the value of a local pairwise orientational order parameter Φ, adapted from previous studies [276]. Φ_i is defined as

$$\Phi_i = \sum_{j \in J}^{J} c_{i,j} \varphi_{i,j}, \tag{5.4}$$

where $\varphi_{i,j} = 1 - \frac{2}{\pi} \arccos |\hat{\mathbf{a}}_i \cdot \hat{\mathbf{a}}_j|$ measures the degree of alignment between a pair of cell orientation vectors $\hat{\mathbf{a}}_i$ and $\hat{\mathbf{a}}_j$, and $c_{i,j}$ is a Gaussian weighting factor given by $c_{i,j} = \exp\left(-\frac{|\mathbf{p}_i - \mathbf{p}_j|}{2\zeta^2}\right)$, where $\mathbf{p}_i$ and $\mathbf{p}_j$ are the respective cell positions. J refers to the

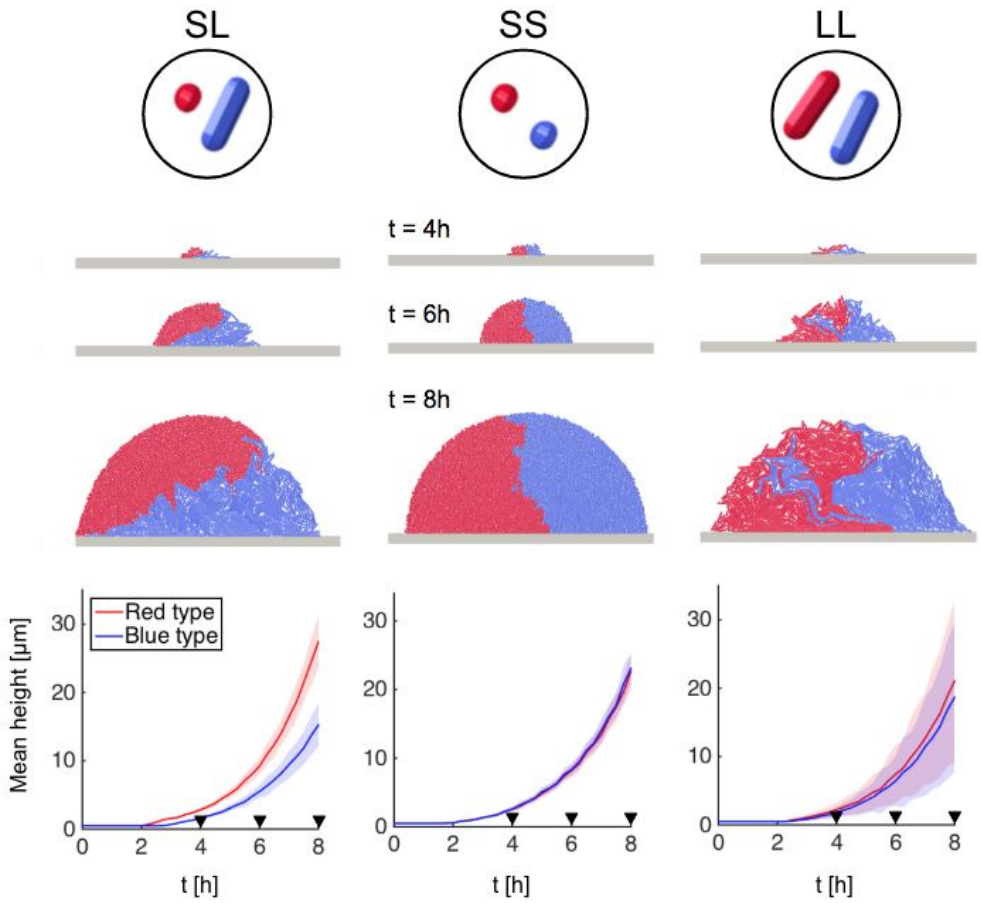

Fig. 5.12 Simplified 2-D simulations allow the physical mechanism of cell sorting to be explored. 2-group simulations using SL, SS and LL colonies form layered, smooth and interdigitated cell distributions respectively. Traces of mean cell height quantify the layering effect over time in SL colonies; black arrows indicate snapshot times. 100 simulations per case; bold lines and shaded areas correspond to mean values and 95% confidence intervals respectively. Figure reproduced with permission from [259].

set of neighbouring cells within range 2ζ of the focal cell i, where $\zeta = 5\,\mu\text{m}$. The value of Φ measured at a focal cell increases when neighbouring cells become aligned with that cell, reaching 1 when all neighbours are perfectly aligned.

As shown in Figure 5.13-A, steric interactions between neighbouring cells in the red S-cell group are weak, and nematic ordering is correspondingly low (Figure 5.14 quantifies this effect as a function of cell shape). The lack of nematic ordering means that the S-cell group expands isotropically, as cells are not elongating or dividing in any particular direction. Consequently, groups of S cells form smooth,

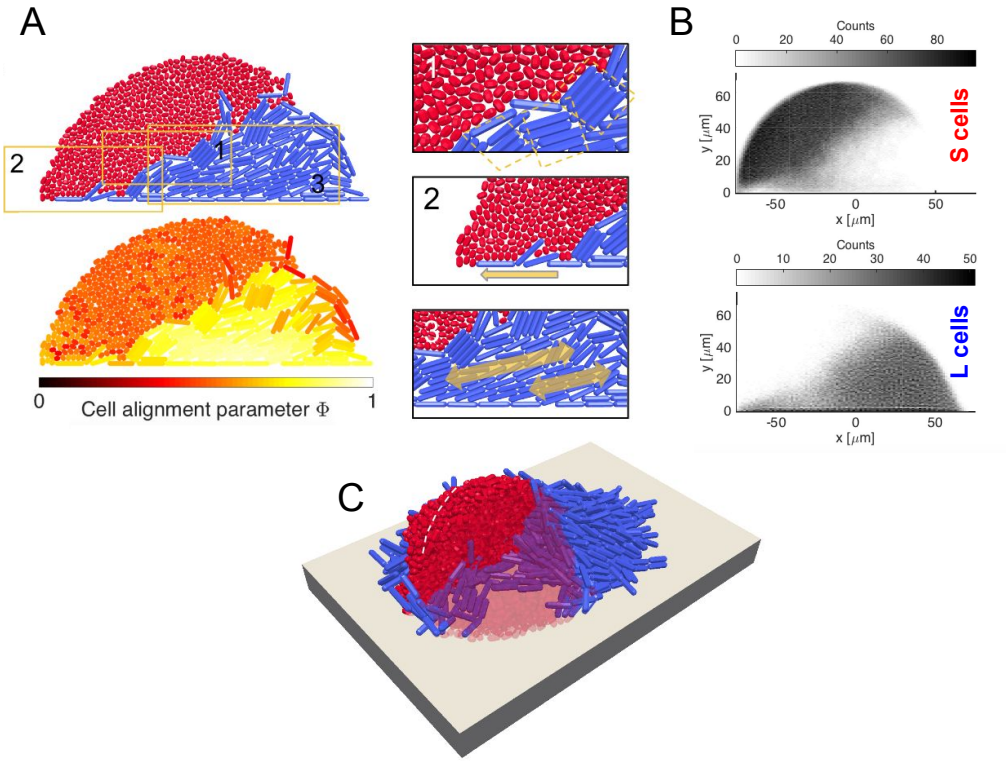

Fig. 5.13 Layering in SL mixtures appears to be driven by the formation of wedge-like arrangements of L cells, which force S cells upward. A: 2-D simulations show that wedges result from steric interactions between cells, which produce high levels of cell-cell and cell-plane alignment in L cells, but not S cells. The tendency for L cells to align together has several effects that are absent in S cell groups, *viz*: rod cells align in cohesive, staggered files (Box 1), which are more robust to growth forces than unaligned spherical cells. Rods near the base of the colony (Box 2) are forced into alignment with the substrate plane, forming a narrow wedge tip at the red-blue clonal boundary. Rod cells to the right of this tip grow laterally (Box 3), driving the wedge under the red cell group. B: 2-D cell density histograms reveal the same group structures in a merged dataset of 100 simulation replicates, confirming that these phenomena are not limited to particular simulation runs. Colormaps correspond to cell counts per histogram bin; 100 bins arranged uniformly along each axis. C: Similar effects are also produced in 3-D simulations. Figure adapted with permission from [259].

symmetric heaps. By contrast, the level of nematic ordering in groups of L cells is very high, due to significant steric interactions between neighbouring cells, as reported in several previous publications [56, 276, 35]. As a result, the growth of the colony is initially highly anisotropic, and the group becomes asymmetric and directional. This

cell growth anisotropy has been reported previously in both experimental [80] and theoretical studies [231, 267].

In light of these observations, we propose that the different group structures created by S and L cell shapes interact to produce layered colony architectures. The flatter, directed L cell groups consistently form wedge-like structures (Figure 5.13-B) that can slide underneath S cell groups, driving the latter upwards, as shown in Figure 5.13-A-1. The basal plane is a vital component of this process: it prevents S cells from being displaced downwards, and increases the degree of nematic ordering in L cells close to the plane, redirecting L group growth towards—and into—the S group.

As shown in Figure 5.13-A-2, L cells are able to burrow beneath S cells because their orientations are templated to this plane: through nematic ordering, L-cell growth remains concertedly lateral, whereas S cells rapidly lose any lateral orientation and are easily displaced upwards. Figure 5.13-A-3 shows that L cells behind the leading edge of the wedge also assist the layering process by providing an expansion force to drive the tip sideways under the S group. Similar behavior is observed in analogous 3-D simulations, as shown in Figure 5.13-C.

5.5.3 Orientational alignment increases with cell aspect ratio

We propose a mechanistic description of layering based on group growth anisotropy, resulting from different degrees of orientational ordering produced by S and L shapes. Figure 5.14 demonstrates these differences by quantifying orientational ordering for a range of different cell shapes. Figure 5.14-A depicts zoomed sections of single-shape colonies, and Figure 5.14-B shows the corresponding mean values of the orientational order parameter Φ in each case. The increase in orientational ordering from approximately 0.50 (random orientations, S cells, ‘a’) to 0.65 (non-random orientations, L cells, ‘d’) supports the above statement that nematic ordering is controlled by shape.

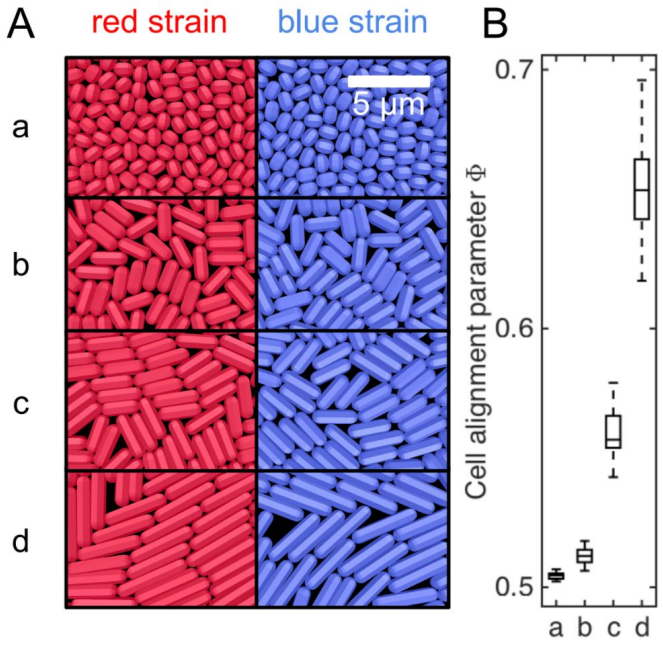

Fig. 5.14 To quantify the effects of cell shape on orientational alignment, we examined binary combinations of cells of four different aspect ratios, ranging from pseudospheres (a-type, equivalent to S) to long rods (d-type, equivalent to L), as shown in Figure 5.4. Cells a through d have an aspect ratio at birth of 1.1, 1.5, 2.0 and 3.0 respectively. Colonies grown using each cell type in isolation (B) show that cell ordering increases with increasing cell aspect ratio, as quantified by population means of the pairwise orientational order parameter Φ. 20 simulations per case.

5.5.4 Layering rate increases with wedge pitch

Further tests support this mechanistic description of colony layering. In Figure 5.15, we examine how layering, measured by the difference in mean heights for red and blue cells ($\Delta z = \langle p_z \rangle_S - \langle p_z \rangle_L$), varies as a function of the initial spacing between the two strains. Plotting the natural logarithm of the strain height differential Δz (Figure 5.15, center) against time reveals that three separate process contribute to the height advantage of the S cells: an initial jump (1) precedes a shallow, sustained climb (2), followed by a steeper climb as soon as the S and L cell groups collide (3).

We attribute these observations to the following processes: lines of S cells buckle earlier than lines of L cells, causing the initial jump (1). Thereafter, L cells continue to preferentially grow along the basal plane instead of upward, leading to a slow increase

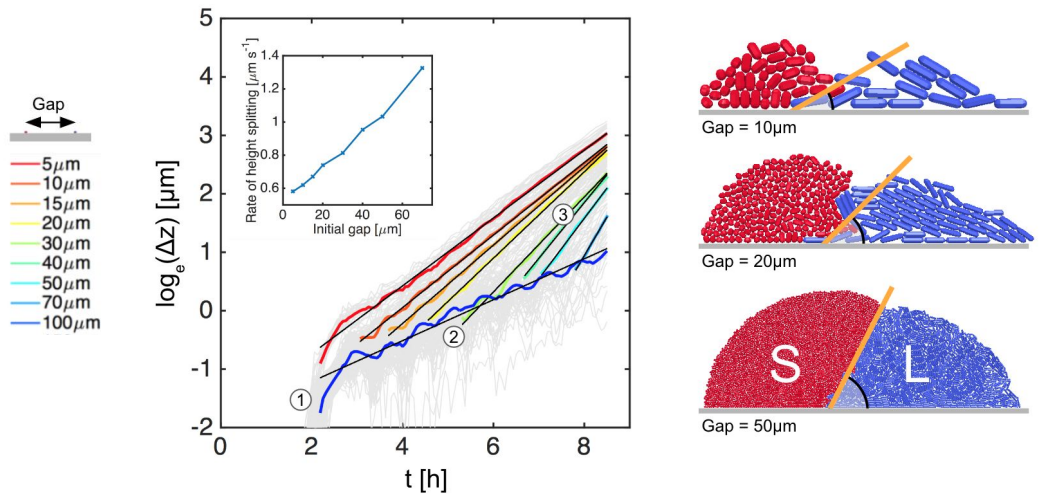

Fig. 5.15 Testing the effects of varying initial spacing between red and blue cell strains ('Gap', left). Logarithmic plots of the strain height differential Δz show three processes contributing to the height differential (center, 1, 2, 3). For each initial gap, eventual collision between S and L cell groups coincides with transition from slow (2) to fast (3) exponential growth in Δz, indicating the onset of layering. Larger initial gaps result in larger groups at the point of collision, increasing the rate of height splitting (inset). This is consistent with proposal that L cell groups behave as wedges, since as larger groups have a steeper edge and therefore produce faster layering (right).

in the height differential (2). Contact between S and L cell groups initiates layering *via* the wedge effect (3). Overall, (3) is the most significant process because it results in a sustained, fast increase in the height differential. Thus, this analysis allows us to untangle contributions to the height differential, distinguishing between intrinsic differences in group properties (1 and 2) and interactions between groups (3).

Further, fitting lines to these traces shows that the rate of height splitting after collision increases with initial gap (Figure 5.15, inset), suggesting that the strain sorting mechanism is dependent on the size of the cell groups at the point of collision. This observation supports the hypothesis that cell sorting is driven by group structure (Figure 5.15, right): increases to the initial gap change the shape of L cell groups from shallow wedges (Gap = 10μm case) to steeper wedges (Gap = 50μm case). As the wedge pitch increases, so too does the rate of spitting.

5.5.5 Layering interrupted by disrupting group structure

If layering is driven by the interaction of contrasting S and L group structures, then it ought to be possible to prevent layering by artificially disrupting this structure. Here we report a test of this idea, based on the simplified two-group protocol. We programmed a set of simulations to trigger a random cell mixing event after an initial period of normal growth. Each mixing event occurred instantaneously at a chosen time t_{event}, and consisted of the following procedure: for each cell i present at time t_{event}, draw a random number $a \in \{0,1\}$. If $a < 0.5$, do nothing. If $a \geq 0.5$, swap the cell type for i to that of the opposite strain (i.e. an S cell becomes an L cell and *vice versa*). Cells converted in this way then either divide (L to S) or elongate (S to L) to adopt the shape of their newly-assigned type.

Figure 5.16 shows the effects of this random mixing for different values of t_{event}. In each case, the mixing protocol removes the height differential, demonstrating successful randomisation of cell locations. Subsequently, the height differential begins to slowly increase again, coinciding with the gradual reformation of group structure, but at a lower rate than in the absence of mixing. If cell layering emerged from interactions between individual S and L cells, then the height differential would be expected to strongly increase following mixing, as this would greatly increase the number of individual contacts between S and L cell shapes. Instead we see the opposite effect, again supporting the hypothesis that sorting results from strain group interactions.

5.5.6 Patterning mechanisms for other shapes

This mechanistic description of group interactions can also explain observations about patterns formed by other shape mixtures. Figure 5.17 shows repeats of the two-group simulations shown in Figure 5.12, performed using the combinations of intermediate cell shapes shown in Figures 5.4 and 5.14. Box plots of mean strain height for each

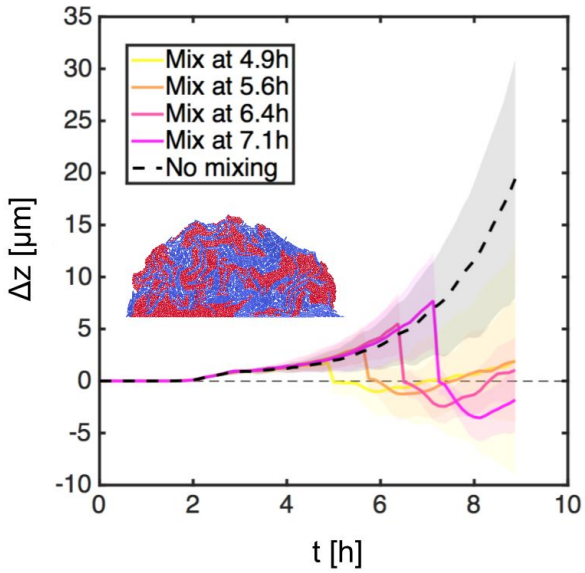

Fig. 5.16 The cell layering mechanism relies on group structure. Repeats of simplified two-group simulations show that the strain height differential Δz does not fully recover following random mixing events at 4.9, 5.6, 6.4 or 7.1 h. At these times, strains are mixed by randomly changing each cell's strain identity with probability 0.5, so that approximately half the S strain population (red) converts to the L-type morphology (blue) and vice-versa. Shortly after mixing, the height differential begins to rise gradually as small groups of L shapes reform surface-hugging group structures, as shown in the inset colony snapshot (8h growth, following a mixing event at 4.9 h). Bold lines and shaded areas correspond to mean values and 95% confidence intervals respectively. All simulations use an initial gap of 6μm. 20 simulations per case; figure reproduced with permission from [259].

shape combination, showing a smooth relationship between the strain layering and cell shape difference (similar to Figure 5.4).

In SS colonies, a smooth vertical boundary is formed because cell orientations are unordered, so that growth forces are not exerted against the neighbouring group in a concerted manner (Figure 5.17, SS). By contrast, when L cell groups meet, neighbouring cells groups concertedly grow into one another, leading to fractal-like interdigitations [238], and much greater variability in mean strain heights (Figure 5.17, LL).

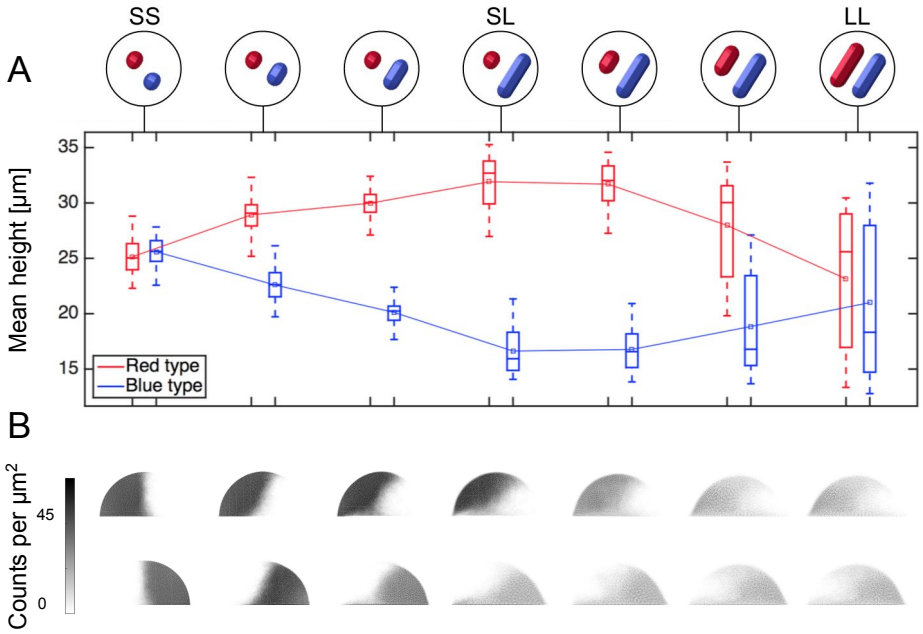

Fig. 5.17 Simulations using intermediate cell shapes show smooth transitions in the degree of cell sorting between SS, SL and LL cases. A: As the aspect ratio of the blue strain is increased, the height differential rises (SS to SL). Applying the same changes to the red strain extinguishes the height differential but leads to greater height variance (SL to LL). Solid lines denote means; boxes and whiskers show interquartile and absolute ranges, respectively. B: As in Figure 5.13-B, 2-D cell density histograms for the red (top row) and blue (bottom) strains provide a statistical picture of colony spatial structure in merged sample of 100 simulations.

5.5.7 Layering is robust to variation in simulation parameters

Having examined the mechanisms underlying shape-driven layering, we sought to evaluate the robustness of this effect with respect to changes in simulation parameters and conditions. For example, one factor that might impact layering is the relative size of the cells involved. Thus far, we had assumed that our S and L cells had identical diameters, given by $2r \approx 1\,\mu\text{m}$. This parameter value is applicable for common laboratory microbes such as coccal *S. aureus* and rod-shaped *E. coli* [203, 238], but other species may differ significantly in size [300].

To test the effects of relative cell size on layering, we repeated our simplified S-L colony simulations using S-type cells of different radii r_S, but identical aspect

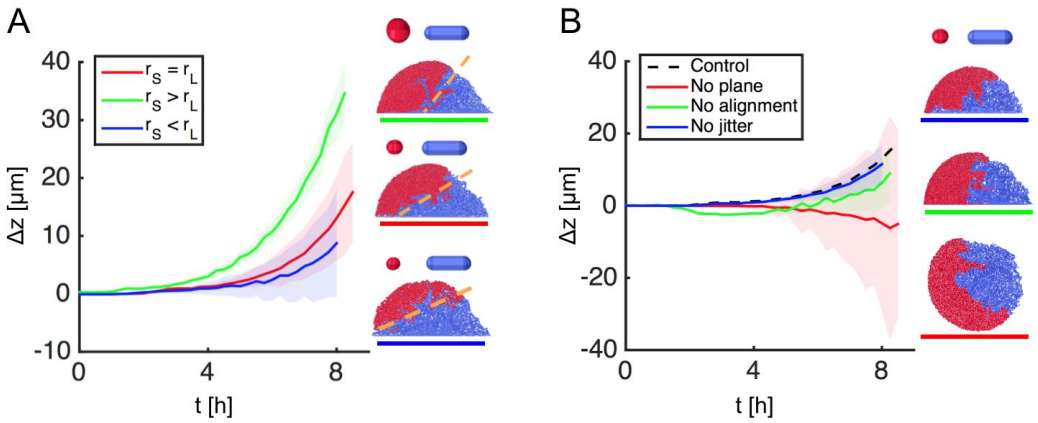

Fig. 5.18 Additional two-group simulations provide further support for the layering mechanism proposed in Figure 5.13. (A): the layering effect, characterised by time traces of mean strain height difference Δz, has a weak dependence on relative cell size, as demonstrated with simulations using modified S-type cells of different radii but identical aspect ratios ($AR_0 = 1.1$). Smaller cells burrow more easily beneath larger ones regardless of shape, which can either attenuate sorting ($r_S > r_L$ case) or enhance it ($r_S < r_L$ case) relative to the original ($r_S = r_L$ case). $r_S = 0.48$, 0.76, and 0.40 µm for red, green and blue traces respectively. (B): Sorting is robust to changes in division orientation noise (no jitter), and to initial cell orientation (no alignment), but is extinguished when the basal plane is removed. Bold lines and shaded areas correspond to mean values and 95% confidence intervals respectively. All simulations use an initial gap of 5µm. 20 simulations per case; figure reproduced with permission from [259].

ratio ($AR_0 = 1.1$), whilst keeping L-cell radii and aspect ratio the same as before ($r_L = 0.48\,\mu$m, $AR_0 = 3.0$). Height differential (Δz) traces for these simulations are plotted in Figure 5.18-A, showing that the degree of layering has a weak dependence on relative cell size. When $r_S > r_L$, individual L cells act as 'ramps' for larger S cells, displacing them from the basal plane and enhancing the height differential Δz (Figure 5.18-A, green trace). Conversely, when $r_S < r_L$ (Figure 5.18-A, blue trace), S cells act as ramps for larger L cells, reducing the height differential relative to the $r_{\text{rod}} = r_{\text{sphere}}$ case (Figure 5.18-A, red trace).

We also wanted to exclude simulation artefacts as potential causes of the layering effect. Firstly, we noted in Chapter 3 that, when a cell divides in CellModeller, its daughters' cell axes are perturbed by small noise terms ('jitter'). Because S cells have

a smaller division volume than L cells, they divide more often for the same intrinsic growth rate μ, and receive more perturbations per unit time. To check the impact of this difference on cell sorting, we ran 20 further 2-D simulations using our SL mixture, this time removing division perturbations for S cells only (i.e. $\xi_a = 0$ for S cells, but $\xi_a = 9\%$ for L cells). The Δz trace shown in Figure 5.18-B ('No jitter') show that this change has essentially no effect on the height differential, eliminating division noise as an explanation for layering. We also found that changing the initial cell orientation, so that both cells' axes were perpendicular to the plane, attenuated the height differential but did not remove it (Figure 5.18-B, 'Alignment'). However, we found that layering was completely removed in that absence of the basal surface, confirming its importance in the layering mechanism (Figure 5.18-B, 'No plane').

In summary, we have proposed that layering occurs because groups of rod-shaped cells form wedge-like structures, which, guided by the basal surface, collectively burrow beneath groups of coccal cells. The necessary group structure is in turn produced by cell-cell and cell-surface steric interactions, which produce nematic ordering in rod-shaped cells but not in coccal cells. Simulations using different initial cell spacings suggest that layering rate can be controlled by the wedge pitch, while simulations using random mixing events show that layering is dependent on the maintenance of group structure. From these findings, we conclude that cell layering is an emergent patterning effect driven by interactions between groups of cells, and does not original from individual cell-cell interactions.

5.6 Discussion

In this chapter, we have used simulations and experiments to show that cell shape can be a determinant of both spatial patterning and composition within a microbial community. In particular, we find that mixtures of rod-shaped and coccal cells can produce layered colony structures, as observed previously in both biotic and abiotic

environments [204, 57]. This indicates a new significance for bacterial cell shape, both as a competitive phenotype in the biofilm context, and as a means for bacteria to influence their environment through collective action.

It is perhaps noteworthy that the modelling and experimental approaches were carried out sequentially, with the experiments recapitulating model predictions immediately without first needing to tune conditions. This observation suggests that the effects reported in this chapter are robust to experimental conditions, and may be common to many existing experimental systems that use mixtures of different cell shapes.

From an evolutionary perspective, our work suggests that the biofilm environment may select for particular cell shapes in specific environments, because of the ways in which they collectively influence biofilm architecture. Given the predominance of the biofilm environment for microbial life [65, 114], any selective effect produced might be expected to have a strong impact on the evolution of bacterial morphology. In natural biofilms, rapid cell growth is often limited to the upper regions of a biofilm [199, 144], which will select for coccal morphologies. Indeed, this may partly explain the ubiquity of the coccal morphology in spite of disadvantages such as decreased nutrient absorption area [300].

In reality, microbial communities are far more intricate than the description used in our simulations. Like all models, our framework makes simplifying assumptions: we deliberately neglect the role of cell motility, detachment and shear forces from the liquid surrounding the colony [155, 220, 224]. The representation of EPS secretions—a hallmark of microbial biofilms—is purely implicit, whereas the inclusion of explicit EPS particles has been shown to influence colony structure in previous studies [144, 103]. Further, *E. coli* biofilms can generate inhomogeneous EPS matrices, as cells can secrete different matrix components according to their physiological state [257].[2]

[2] In a similar vein, it is also possible that the *E. coli* mutants discussed in this chapter *differ* in their production of matrix components (e.g. curli fibers, flagella) [257]. For example, if (say) rates of flagella secretion scaled with cell surface area, longer WT cells might increase their relative adhesivity, allowing them to remain near the base of a colony while shorter AK cells were swept upwards. Recent studies have demonstrated that differential adhesivity can drive stratification in microbial colonies

Consequent inhomogeneities in the mechanical properties (e.g. adhesivity, elasticity) of the matrix could introduce additional self-organisational effects, and alter strain layering in unexpected ways.

However, these omissions allow a degree of realism to be traded for additional control and tractability. Rather than attempting to reproduce the exact dynamics of colony growth, our simulations instead predict the rich dynamics that can emerge when non-spherical cell shapes are introduced to existing modelling paradigms [296, 199]. The fact that these predictions are corroborated by our experiments demonstrates the usefulness of this approach.

Our findings highlight the need for further empirical and theoretical studies to examine mixed-shape colonies in more detail, treating cell shape as a physical variable instead of an incidental attribute. Microbial strains such as those developed by Monds *et al*. [193] will be instrumental to this process, since they allow cellular shape to be varied in isolation of other confounding variables. Likewise, investigating how the predictions of previous theoretical studies are altered by the inclusion of morphological variability will help fully characterise the influences of cell shape in microbial communities. More generally, this work may also suggest new roles for shape and growth anisotropy in other biological systems – ultimately, shape may prove to be an important physical parameter not just for collectives of microbes, but for the morphogenesis of developing tissues and cancer tumors [120, 11].

Finally, although this study considers only antagonistic interactions between microbes, the patterning mechanisms we discuss could also influence other social interactions between microbes. Systems in which spatial patterning facilitates cross-feeding interactions are well-known, and shape-mediated self-organisation could enable cooperating species to develop the requisite colony structure [255, 57, 117, 285, 36, 85]. Further, our results suggest that cell shape can affect the degree of strain mixing within the

[144, 249, 181], and so effects such as these could influence, or even dominate, the layering effects reported here.

colony, which could in turn be used to control selective pressures for or against certain social strategies. For instance, because mixtures of coccal cells produce less genetic mixing than mixtures of rod-shaped cells, cooperative strategies such as enzyme secretion may become more evolutionarily stable [199]. Our findings could therefore help to engineer more productive or stable synthetic microbial consortia, by selecting for community architectures which optimise cellular interactions.

5.7 Conclusions

Microorganisms of different shapes commonly grow together in their dense and genetically diverse communities, known as biofilms. We have used modelling and experiments to study the impact of cell morphology on biofilm architecture and competition. Using the model framework developed in Chapters 3 and 4, we have predicted, described and examined new mechanisms of self-organisation and spatial patterning driven by bacterial cell shape. We have also documented the same patterns emerging in real bacterial colonies. These results suggests that cell shape is a major neglected determinant of patterning and evolutionary fitness within bacterial biofilms.

6

Antibiotic-induced filamentation and its effects in bacterial colonies

Publications and statement of authorship

The work presented in this chapter is an adaptation of an existing manuscript, written in collaboration with other authors. This work has been prepared for publication as:

Isabel Frost, William P. J. Smith, Sara Mitri, Alvaro San Millan, Yohan Davit, James M. Osborne, Joe M. Pitt-Francis, R. Craig MacLean, and Kevin R. Foster. "Cooperation, competition and antibiotic resistance in bacterial colonies" (Submitted to Proceedings of the National Academy of Sciences 2016) [98].

The author contributions for this study are as follows: KRF and RCM conceived the study. IF, SM, ASM, RCM and KRF designed the experimental framework. IF carried out the experiments and microscopy. WPJS, YD, JMO, KRF and JMPF designed the simulation framework. WPJS performed simulations and analysed simulation data. All authors contributed to the manuscript.

Abstract

In the previous chapter, we examined the effects of cell shape on spatial patterning in microbial communities, using our individual-based modelling framework. We tested our model's predictions using genetically-modified *Escherichia coli* bacteria, and concluded that cell shape can be a significant determinant of spatial structure, and strain fitness, in the bulk of a mixed-shape biofilm.

In this chapter, we examine the effects of cell shape in a different context: at the edges of microbial colonies. Within these colonies, antibiotic agents such as carbenicillin can induce morphological changes in susceptible *Pseudomonas aeruginosa* bacteria, creating an additional scenario in which different cell shapes appear and compete in a community. We adapt our model to study this new context, and identify an additional mechanism through which cell morphology can affect both spatial patterning and fitness. Overall, we show how our model can be used to offer mechanistic insight into complex experimental systems.

6.1 Introduction

Altering microbial shape through genetic modification is one route to studying competition between different shapes. The mutant *E. coli* system presented in the previous chapter is an ideal method for investigating the competitive effects of cell morphology, because it allows morphology to be varied in isolation of other phenotypic variables–particularly growth rate–that might also influence competition [193].

However, there are also natural sources of morphological change in microbes, which might tell us more about the roles and function played by cell shape within communities. Most microorganisms have an extensive network of regulation systems to control their cell shape [134, 272], and normally this regulation serves to maintain a fixed, well-defined morphology [305, 46]. However, in certain situations, microbes actively change their morphology [301, 254, 21].

When do these morphological changes occur, and what functions might they serve? Some microbes change their shape as part of their life cycle, reflecting the different tasks cells need to perform at consecutive stages of their development [300, 301]. Other bacteria change their shape in response to particular environmental stimuli: for instance, pathogenic bacteria may change their shape to resist consumption by immune cells [126, 136], and rod-shaped cells may elongate in response to resource shortages in their habitat [300].

A well-known example of an environmentally-driven shape change is microbial filamentation. Filamentation occurs when elongating rod-shaped microbes arrest their cell division (sepatation) machinery, so that cells become progressively longer without also dividing into daughter cells, as per conventional binary division [24]. Filamentation is regarded as a survival strategy that helps microorganisms to cope with environmental stressors, such as ionising radiation or external toxin exposure [184], that might damage their chromosomes. Arresting cell division allows a cell time to effect any necessary repairs to its DNA before errors are passed on to its offspring – whilst simultaneously allowing it to continue absorbing nutrients and expanding in space [137].

Filamentation is a well-known response to antibiotic agents [129, 27], but its consequences in dense bacterial communities have yet to be fully characterised. In this chapter, we turn our attention to filamentation induced by antibiotic exposure, and its effects on competition in bacterial communities. In particular, we use our individual-based framework to model and understand an existing experimental system, used

to study the evolution of antibiotic resistance in bacterial colonies, to examine the competitive effects of cell filamentation at the edges of bacterial colonies.

The structure of this chapter is as follows: first, we report experiments carried out by our collaborator, Isabel Frost, in which antibiotic-resistant bacteria are competed with antibiotic-susceptible bacteria in microbial colonies. Antibiotic exposure induces filamentation only in susceptible bacteria, providing an alternative route to creating mixed-shape microbial communities *in vitro*. Then, using the individual-based framework developed in Chapters 3 and 4 of this thesis, we develop models of shape competition at the colony edge, and devise mechanistic hypotheses to explain the observed enrichment. Importantly, we identify a second mechanism by which cell shape can alter colony spatial structure, by increasing the propensity of elongated cells to branch away from the colony edge.

Overall, both experiments and modelling show that the elongation of antibiotic-susceptible cells coincides with their enrichment at the edges of colonies, suggesting a potential role for filamentation both as a determinant of spatial patterning, and as a functional phenotype.

6.2 Experiments using *P. aeruginosa* bacterial colonies

Here we describe the experimental methods used to create and image colonies of antibiotic-resistant and antibiotic-susceptible bacteria, using similar culture and microscopy techniques to those discussed in Chapter 5. As noted at the beginning of this chapter, these procedures were carried out by Isabel Frost.

6.2.1 Experimental methods

Bacterial strains

Cells of *P. aeruginosa* strain PA01, tagged with yellow and red fluorescent proteins (Yellow Fluorescent Protein and DsRed, respectively), were used as the antibiotic-susceptible ('S') strain. Similarly-labelled, antibiotic-resistant ('R') variants of this strain were created by transforming PA01 with a multidrug resistance plasmid (Rms149, [42, 112]) using electroporation. Transformants were selected on Luria-Bertani (LB) agar plates containing 200 $\mu g\,mL^{-1}$ streptomycin, and transformation was confirmed by PCR and plasmid extraction. Liquid pre-cultures of these strains were incubated at 37 °C and shaken overnight (at 250 RPM) in 3 mL of LB broth (Fisher Scientific, NJ, USA).

Plate cultures

As an initial test of the effects of carbenicillin antibiotic on these microbes, R and S strains were grown together in different combinations, in plate cultures containing progressively higher antibiotic concentrations. These plates were prepared and imaged as follows. Colonies of R and S strains were grown on plates of agar media, containing 25 mL of 1× LB Miller agar (40 $g\,L^{-1}$ of which 15 $g\,L^{-1}$ was agar), and supplemented with 0, 6, 12 and 24 $\mu g\,mL^{-1}$ of carbenicillin. Plates were inoculated using 1:1 mixtures of liquid pre-cultures (see above), mixed in the following combinations: S (red) vs. S (yellow), R (red) vs. R (yellow), and S (yellow) vs. R (red). Each mixture was diluted by one tenth in phosphate-buffered saline (PBS), and then pipetted on an agar plate in a single, 1 µL central drop. Inoculated plates were then grown at 20 °C for six days.

Confocal microscopy and image analysis

After 1, 2, 3 and 4 days' growth, plates were examined using confocal laser scanning microscopy, by cutting individual colonies out of the agar, mounting them on a glass slide, and then imaging with an LSM 700 laser scanning microscope (Zeiss), using 40× and 50× objectives and Zen Black software. Measurements of cell counts and aspect ratios were made by adding 1 µL PBS to the edge of the colony to disperse cells, before analysing captured images using the in-built cell-counting function of FIJI [247].

Liquid culture controls

To investigate the role of community spatial structure in controlling strain interactions, we also grew the R and S strains in liquid shaking culture in the presence of different antibiotic concentrations. Pre-cultures were diluted in 3 mL of fresh LB broth to an OD600 of 0.05 and incubated at the same conditions for 2 hours. Cultures of the strains were then mixed at a ratio of 1:1 in phosphate buffered saline (PBS) with an OD600 of 0.3. Following 10-fold dilution in PBS, 1 µL of the resulting suspension was added per well in a 96 well plate, in triplicate. Wells contained a final total volume of 200 µL LB broth with the same (sub-MIC) carbenicillin concentrations as before (0, 3, 6, 12, 24 $\mu g\,mL^{-1}$. Competitions were run for 12 hours (or 16 hours for antibiotic-free competitions) overnight at 20 °C and 250 RPM.

Fitness and growth measurements

To compute final cell counts in solid culture experiments, colonies grown on competition plates were scraped from the agar and suspended in 1 mL PBS, diluted 10^6 and 10^5-fold and plated out to count colony-forming units (CFU), using fluorescence to differentiate cells labelled with YFP.

Initial ratios were calculated by plating 50 µL of a 10^6-fold dilution of the inocula on LB agar plates. These were incubated overnight at 20 °C, after which CFU were counted, using fluorescence to differentiate cells labelled with YFP. Initial and final counts in liquid culture experiments were measured in the same way, except that here the dilution was 10^5-fold. Further, cells from antibiotic-free liquid competitions were counted using flow cytometry, in order to most accurately measure the fitness cost of the plasmid.

In each case, the relative fitness of the susceptible strain was determined using the formula

$$\omega_S = \ln\left(\frac{N_{S,f}}{N_{S,i}}\right) / \ln\left(\frac{N_{R,f}}{N_{R,i}}\right), \tag{6.1}$$

where $N_{S,i}$ and $N_{S,f}$ are the numbers of susceptible cells before and after the competition, and where $N_{R,i}$ and $N_{R,f}$ are the numbers of resistant cells before and after the competition. Similarly, the number of cell divisions C for each strain $X = R, S$ over the course of a competition was computed using the formula $C_X = \log_2(N_{X,f}/N_{X,i})$.

6.2.2 Experimental results

The collected confocal images of *P. aeruginosa* colonies are shown in Figure 6.1. The presence of the carbenicillin antibiotic (AB) selectively induced morphological changes in susceptible cells: images taken at the colony edge show that, in colonies grown only using the S strain, cells become increasingly filamentous (S+S, Figure 6.1-A) when grown on media prepared with progressively higher AB concentrations [184] – whereas R cells are immune to the effects of AB [112], and maintain a fixed morphology (R+R, Figure 6.1-B) under the same conditions.

Two further effects occurred when the R and S strains are grown together in 1:1 mixtures, as shown in Figure 6.1-C. We observed that, for intermediate antibiotic (AB) dosing (6-12 µg mL^{-1}), the degree of S-cell filamentation was reduced in the presence of the resistant strain. This is to be expected, because the carbenicillin-degrading

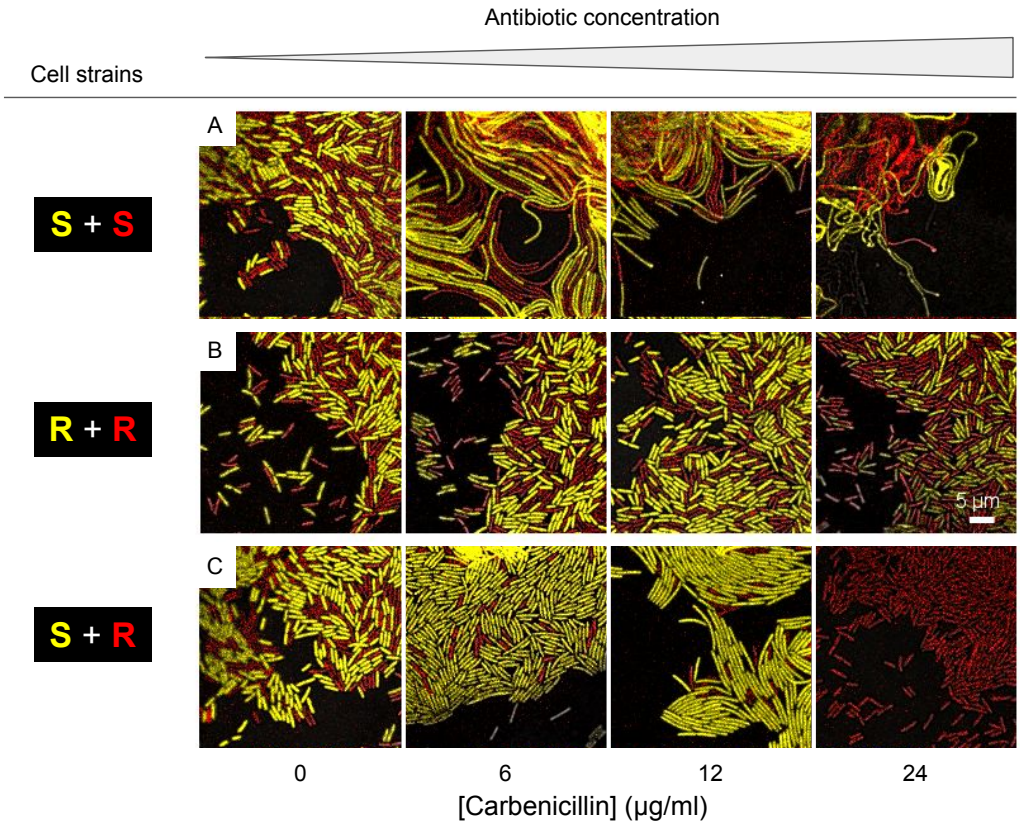

Fig. 6.1 Confocal microscopy images of agar colony edges after two days' growth, showing degree of cell filamentation for increasing concentrations of carbenicillin antibiotic. Strain combinations and fluorescent labels are shown in the left-hand column ('Cell strains'). (S)usceptible cells (A) undergo filamentation at non-zero concentrations of carbenicillin, whereas (R)esistant cells (B) do not. When the two strains are mixed (C), S cells (shown in yellow) filament less than when grown alone, indicating cross-protection. R cells have a marginally lower fitness than S cells in the absence of AB, because of the cost of the resistance plasmid. Surprisingly however, the S strain's advantage appears to increase for intermediate AB concentrations (6-12 $\mu g\,mL^{-1}$), before eventually being wiped out. Figure adapted with permission from reference [98]; images taken using 50× objective lens.

enzymes encoded by the resistance plasmid are extracellular [112], and so R cells degrade AB not only for themselves, but also from their immediate surroundings. Provided they remain sufficiently close to R cells, S cells then receive a degree of "cross-protection" from the deleterious effects of the antibiotic, and exhibit a more moderate stress response with reduced elongation [82, 33, 304].

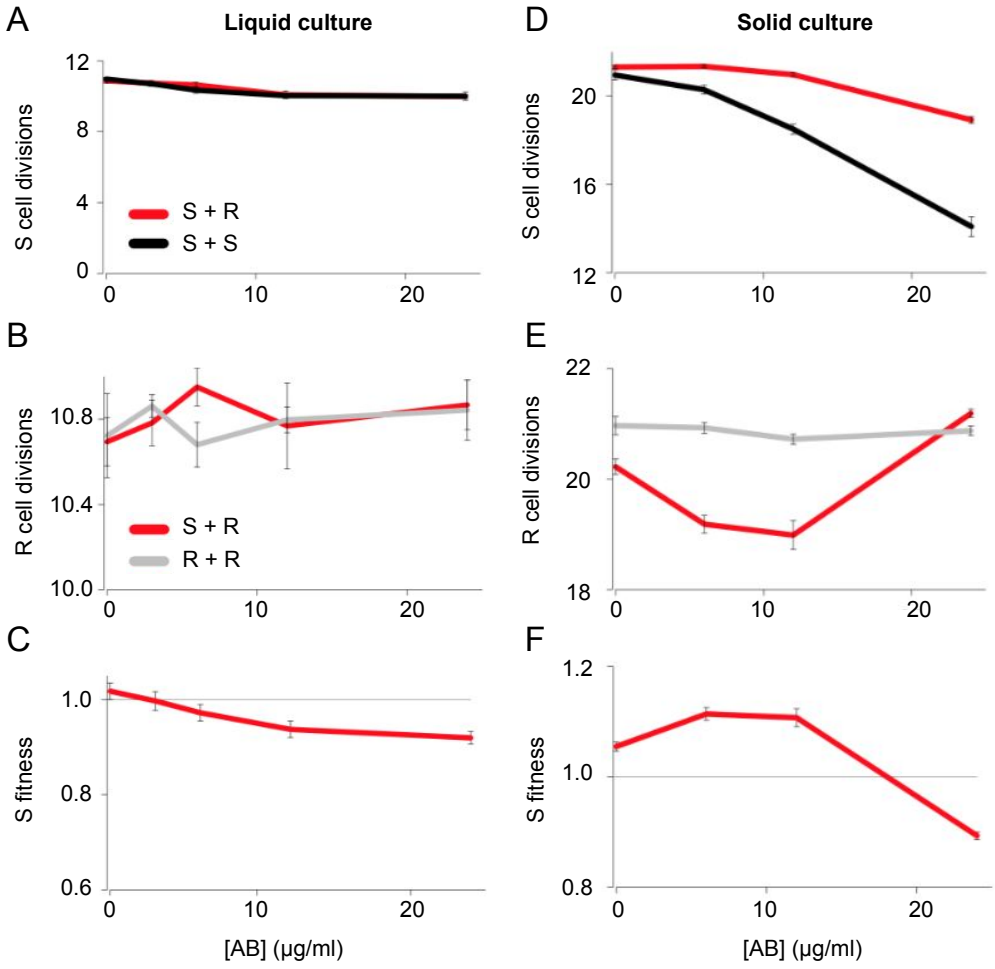

Fig. 6.2 Comparisons of cell growth rates and relative fitness in liquid (A,B,C) and solid (D,E,F) culture experiments. In liquid culture, S cell growth rates (A) decrease with increasing carbenicillin (AB) concentration, while R-strain growth rates (B) remain largely unaffected – irrespective of whether either strain is cultured alone or with the other. Relative fitness calculations (C) show that while $[\mathrm{AB}] = 0$ selects for S (because R bears the cost of the resistance plasmid), all $[\mathrm{AB}] > 0$ select for R. Conversely, in solid culture, S grows faster alongside R than alone (D), indicating cross-protection through extracellular AB degradation, and R grows more slowly with S than alone (E). Intriguingly, in the presence of spatial structure, S fitness for intermediate (6,12) $[\mathrm{AB}]$ is actually greater than for $[\mathrm{AB}] = 0$ (F), and only the highest antibiotic concentrations select for R. Sample sizes: 3 replicates for monoculture (S+S, R+R) and 6 for coculture (R+S) experiments.

However, we also found that S cells were present in higher numbers at the colony edge, even in the presence of intermediate AB concentrations. Only the highest AB concentration used ($24\,\mu g\,ml^{-1}$, Figure 1-C) was sufficient for R cells to completely take over the colony edge. This result was surprising, because filamentation normally indicates cellular damage, and so one might expect significant growth inhibition in S cells whenever it occurs. Instead, it appeared that S cells were actually performing better at the colony edge when they were filamentous.

These results are corroborated by our measurements of cell growth rates and relative fitness in agar colonies. In Figure 6.2, we compare these data with those for liquid culture controls, to examine the effects of community spatial structure on S-R strain interactions. Figure 6.2-A shows that in liquid culture, the S strain grows no better in the presence of R than alone, while in solid culture (6.2-D) S is protected from increases in carbenicillin concentration by R. The R strain in turn is unaffected by S in liquid culture (6.2-B), but actually grows more slowly in its presence in solid culture, for intermediate antibiotic concentrations (6.2-E). Together, these trends drive selection for the R strain for all non-zero antibiotic concentrations in liquid culture competitions (6.2-C) – yet solid cultures can select for the S strain (6.2-F). Perhaps most interestingly, cross protection alone cannot explain why S-cell fitness *increases* with antibiotic concentration in this case, nor why R-cell growth appears to be suppressed in the presence of filamentous S-cells in spatially-structured solid culture.

Filamentation coincides with strain enrichment at the colony edge

Could this unexpected advantage be caused by cell filamentation *per se*? To investigate these result further, S-R colonies were subjected to further analysis. To examine the dynamics of the interactions between S and R cells, 1:1 S-R mixture colonies were grown in triplicate both with and without AB ($12\,\mu g\,mL^{-1}$ carbenicillin) as

described above, and imaged at successive time points, as shown in Figure 6.3. These confocal images of colony edges show that, in the absence of antibiotic, S cells come to dominate the colony edge because they do not pay the cost of expressing the resistance plasmid [112], and so have a faster growth rate under these conditions (Figure 6.3-A, top row). Surprisingly however, they are also able to capture the edge even in the presence of antibiotic (Figure 6.3-A, bottom row).

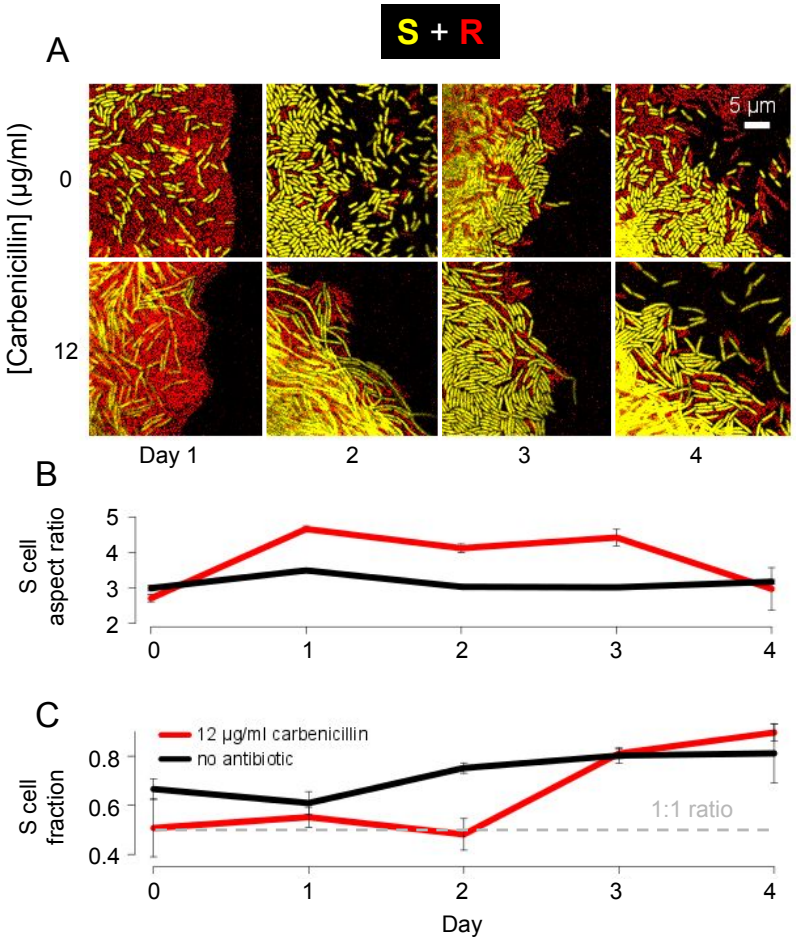

Fig. 6.3 Susceptible (S) cells increase in aspect ratio before outcompeting resistant (R) cells in carbenicillin-treated colonies. As before, yellow S and red R cells were competed in agar colonies, whose edges were imaged during growth on either 0 or 12 µg ml^{-1} carbenicillin (A). Measurements of cell aspect ratios (B) show a transition to filamentous morphology in S cells between days 1 and 3. Following this elongation, the fraction of S cells (C) at the colony edge rises, eventually exceeding the S-cell fraction in the absence of antibiotics, after 3 day's growth. Figure adapted with permission from reference [98]; images taken using 50× objective lens.

Measurements of cell aspect ratios on successive days of colony growth determined that edge capture coincides temporally with the onset of filamentation (Figure 6.3-B). Counting the number of cells of each strain (see Section 6.2.1) showed that the fraction of susceptible cells subsequently increases, actually exceeding the S-cell fraction reached in the absence of antibiotics (Figure 6.3-C).

Overall then, these experimental results suggest that filamentation may offer a competitive edge to S cells when grown alongside R cells, by facilitating 'capture' of the colony edge. The colony edge is an advantageous position to occupy, because it offers the best access to the solutes needed for cell growth [189, 144, 191, 273, 198]. What, then, is the physical mechanism by which filamentous S cells can become enriched there? To study the processes underlying these observations, we devised several models of colony edge growth, using our individual-based framework. We describe these models, and the predictions they make, in the next section.

6.3 Individual-based modelling of the colony edge

In Chapters 4 and 5, we observed that nutrient uptake in microbial communities often creates steep resource gradients, limiting growth to outer boundaries of the community, where resources are most plentiful. In *P. aeruginosa* colonies grown on agar, growth is observed to be restricted to the colony edge [189]. To try and capture this heterogeneous growth in our model, we devised three separate descriptions of limiting solute fields, which we refer to as Models A, B and Z respectively. Models A and B are similar, and examine competition between cells of different shapes at the colony edge. By contrast, Model Z compares cells of the same (coccal) shape, but varies relative cell growth rate. Simulation parameters for each model are summarised in Table 6.1, and are the same as in Chapter 5 unless otherwise stated; boundary conditions are shown in Table 6.2. These models are described below in turn.

Table 6.1 Model parameters used in Chapter 6

Parameter	Symbol	Unit	Value		
			Model A	Model B	Model Z
Nutrient Damköhler num.	$\mathscr{D}_N$		1.0	0.1	0.01 or 0.0001
Oxygen Damköhler num.	$\mathscr{D}_O$		0.1		
Nutrient saturation num.	η_N		0.33	0.33	0.033 or 0.00033
Oxygen saturation num.	η_O		0.33		
Boundary layer width	δ	µm	20	40	40
Domain length (x dim.)	L_x	µm	100	$\max(p_x)+\delta$	$\max(p_x)+\delta$
Domain length (y dim.)	L_y	µm	100	100	300
Domain length (z dim.)	L_z	µm	$\max(p_z)+\delta$	40	
Birth aspect ratio:					
R cells	$AR_{0,R}$		2.5	2.5	
S cells	$AR_{0,S}$		4.5	4.5	
A cells	$AR_{0,A}$				1.1
B cells	$AR_{0,B}$				1.1

Table 6.2 Solute boundary conditions used in Chapter 6

Boundary	Condition		
	Model A	Model B	Model Z
$x=0$	–	–	–
$x=L_x$	–	$\bar{u}_N=1$	$\bar{u}_N=1$
$y=0$	–	–	–
$y=L_y$	–	–	–
$z=0$	$\bar{u}_N=1,\ \bar{\nabla}^2\bar{u}_O\cdot\hat{\mathbf{n}}=0$	–	N/A
$z=L_z$	$\bar{u}_O=1,\ \bar{u}_N=0$	–	N/A

$\hat{\mathbf{n}}$ denotes the unit vector normal to a given boundary;
(–) denotes a zero-flux boundary condition for all solutes.

6.3.1 Model A: dual-field approach

P. aeruginosa bacteria are obligate aerobes, meaning that they require both a carbon substrate and elemental oxygen (O_2) for growth [175]. In agar plate cultures, these resources diffuse into colonies from the agar below and the air above, respectively, so that oxygen concentrations are maximised on the upper surface of the colony, and nutrient concentrations are maximised at the colony base. We hypothesised that, if both of these resources became limiting, then colony growth would be restricted to the colony circumference, which has the best access to both solutes simultaneously.

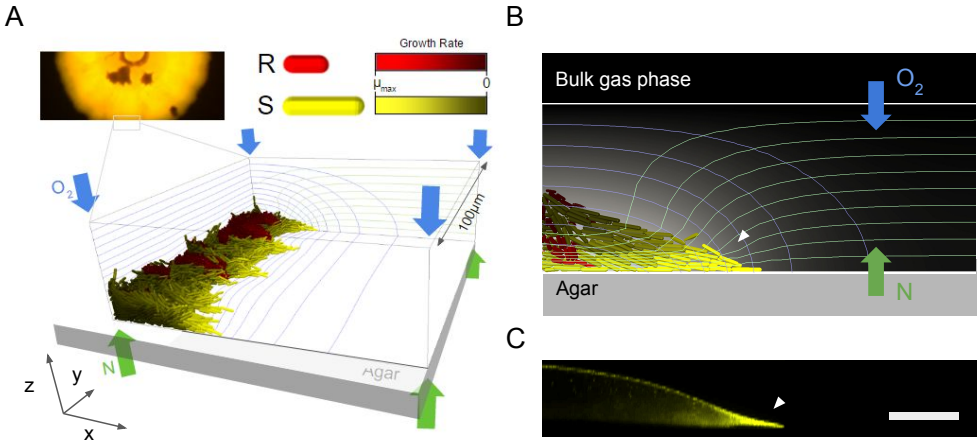

Fig. 6.4 Simulating growth colony edge using Model A. A 100 µm section of the colony edge (A, top left) is modelled using a walled cuboidal domain (A, bottom), containing both discrete cells and continuous chemical fields. Resistant (R) or susceptible (S) cells are represented using short or long capsules, respectively, whose aspect ratio ranges were modelled on those of R- and S-type *P. aeruginosa* bacteria. Cells elongate according to the local concentration of oxygen (O_2, blue contours) and nutrient (N, green contours), which diffuse into the colony from above and below as indicated. Each cell is coloured by its individual growth rate; repulsive elastic forces between growing capsules lead to expansion of the colony edge along the agar surface. Contours mark isoclines in each field in increments of 10%. Both resources are required for growth such that only cells on the outer edge of the colony (B, shown in profile) are able to proliferate, as observed in real *P. aeruginosa* colonies (C). Scale bar equal to 45 µm. Panels A and C taken with permission from references [98] and [191], respectively.

We therefore adapted our Chapter 5 model to create a scenario in which both solutes were required for cellular growth. Figure 6.4 provides a schematic of this model, Model A, indicating the computational domain and boundary conditions used. As shown in Figure 6.4-A, the model domain consists of a walled, 3-dimensional cuboidal domain of dimensions $L_x \times L_y \times L_z$, containing cells at the edge of a colony. Simulations are initialised with a line of capsule cells arranged randomly towards the rear face of this box (at $x = 0$), representing the arrival of the colony edge at time $t = 0$. Cells then grow and divide so that the colony front moves in the radial (x) direction, corresponding to the expansion of the colony as a whole. Mechanical boundaries at the sides and

base of the domain are imposed to represent repulsive forces from the cells around and behind the edge section, and from the agar surface below it.

The cell geometry and mechanics parameters of Model A are identical to those presented in Chapter 5, with two important exceptions. The first is that capsule geometries are now taken from experimental measurements of R- and S-cell aspect ratios at the colony edge (Figure 6.3-B, day 1 data). Capsules representing R and S cells have initial aspect ratios $AR_0 = 2.50$ and 4.50, which increase to final aspect ratios $AR_f = 4.67$ and 8.67 at division, respectively. We chose these values so that the cell-cycle averages of aspect ratios, approximated as $AR_0 + 0.18\,AR_f$, would coincide with the measurements shown in Figure 6.3-B.

The second difference, noted above, is that microbes simultaneously require two solutes—oxygen (O) and nutrient (N)—in order to grow. Thus, the intrinsic growth rate of a cell i is determined by the local concentrations of these solutes, so that its scaled volume $\bar{V}_i = V_i/l^3$ increases according to the dimensionless equation

$$\frac{d\bar{V}_i}{d\bar{t}} = \left(\frac{\bar{u}_{O,i}}{\bar{u}_{O,i}+\eta_O}\right)\left(\frac{\bar{u}_{N,i}}{\bar{u}_{N,i}+\eta_N}\right)\bar{V}_i, \tag{6.2}$$

where $\bar{u}_{O,i}$ and $\bar{u}_{N,i}$ are the dimensionless concentrations of oxygen and nutrient, scaled by their respective bulk concentrations $u_{O,0}$ and $u_{N,0}$, and where $\eta_O = K_O/u_{O,0}$, $\eta_N = K_N/u_{N,0}$ are scaled saturation constants. Time $\bar{t}$ is scaled against the minimum cell division time, $\tau_{\text{growth}} = \ln(2)/\mu$, as described in Chapter 4.

Oxygen and nutrient diffuse into the domain from above and below respectively, as shown in Figure 6.4-B, and their dimensionless concentration fields $\bar{u}_O$ and $\bar{u}_N$ are modelled using the reaction-diffusion equations

$$\bar{\nabla}^2\bar{u}_O = \mathscr{D}_O\left(\frac{\bar{u}_O}{\bar{u}_O+\eta_O}\right)\left(\frac{\bar{u}_N}{\bar{u}_N+\eta_N}\right)\phi(\mathbf{p}_1,\ldots,\mathbf{p}_n), \tag{6.3}$$

$$\bar{\nabla}^2\bar{u}_N = \mathscr{D}_N\left(\frac{\bar{u}_O}{\bar{u}_O+\eta_O}\right)\left(\frac{\bar{u}_N}{\bar{u}_N+\eta_N}\right)\phi(\mathbf{p}_1,\ldots,\mathbf{p}_n), \tag{6.4}$$

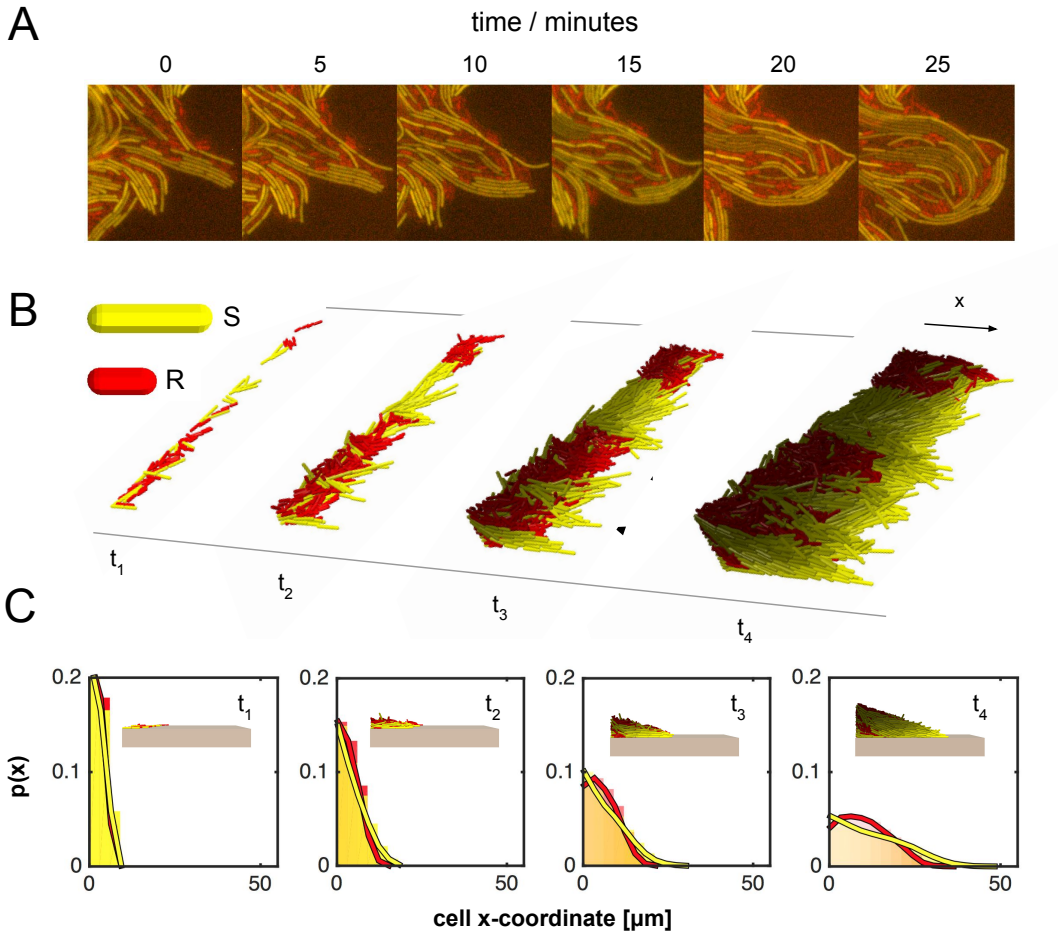

Fig. 6.5 Experiments show that filamentous cells (S, yellow) become enriched at the colony edge (A), and receive an unexpected fitness bonus, when grown alongside non-filamentous cells (R, red). B: IbM simulations using Model A reproduce these observations. Starting from a random configuration of S and R cells mixed in a 1:1 (t_1), radially-oriented S cells instigate branching events (t_2, black arrows), improving their resource access and in turn stimulating further growth (t_3, black arrows). By t_4, S cells have become enriched at the colony edge through positive feedback. C: The shape-driven enrichment process may be quantified using histograms of cell x-coordinates, taken at the same 4 time points as in B. Inset figures show side-on views of the colony edge. Data merged from sample of 20 simulations; times t_1-t_4 correspond to 12, 24, 36 and 56h of growth respectively. Cell colouring schemes are equivalent to those used in Figure 6.4.

where $\mathscr{D}_O$, $\mathscr{D}_N$ are solute Damköhler numbers, and where $\bar{\nabla}^2$ corresponds to the Laplacian operator scaled by cell diameter $l = 1\,\mu\text{m}$. The scalar field $\phi(\mathbf{p}_1, \ldots, \mathbf{p}_n)$ describes the spatial variation in cell volume fraction, computed from the current cell configuration $\mathbf{p}_1, \ldots, \mathbf{p}_n$ as described in Chapter 4. Each simulation timestep, solute fields are computed by solving these coupled PDEs (in non-dimensional form, using the FEniCS finite element library (in-built Newton solver of `Solve()` function [5]).

Filamentation drives enrichment at colony edge

We used Model A to grow 100 µm sections of the colony edge from 1:1 mixtures of R and S cells. Simulations were initiated by randomly placing 20 cells of each type in the area defined by $0 < x \leq 5\,\mu\text{m}$, $0 < y \leq 100\,\mu\text{m}$, representing the leading edge of the colony as it enters the simulation domain. Cells were then allowed to grow and divide so that the colony edge propagated in the radial (x) direction, reaching an average colony volume of $1.043 \times 10^3\ \mu\text{m}^3$ (approximately 6,500 cells) after 56 h. The dimensionless parameters and boundary conditions used in Model A are summarised in tables 6.2 and 6.2.

We found that this model successfully limited growth to the colony edge, as shown in Figure 6.4-B and -C, and that the resulting simulations reproduced the edge enrichment effect observed in our experiments (Figure 6.5-A). The simulation timeseries pictured in Figure 6.5-B shows how, beginning from an equal starting position (t_1), longer S cells (yellow) emerge from the colony front to create fast-growing branches, occluding shorter R cells (red) from the colony edge (t_2-t_3). Consequently, S cells accumulate at the colony edge (t_4), so that the entire front of the colony becomes occupied by S cells. We tracked the enrichment process over time by plotting strain probability distributions ($P(x)$, the likelihood of finding a cell of a given strain at coordinate x) as a function of the radial coordinate x (Figure 6.5-C). Here, each bar in the histogram is coloured according to the average growth rate of cells contained within that bar, so that higher

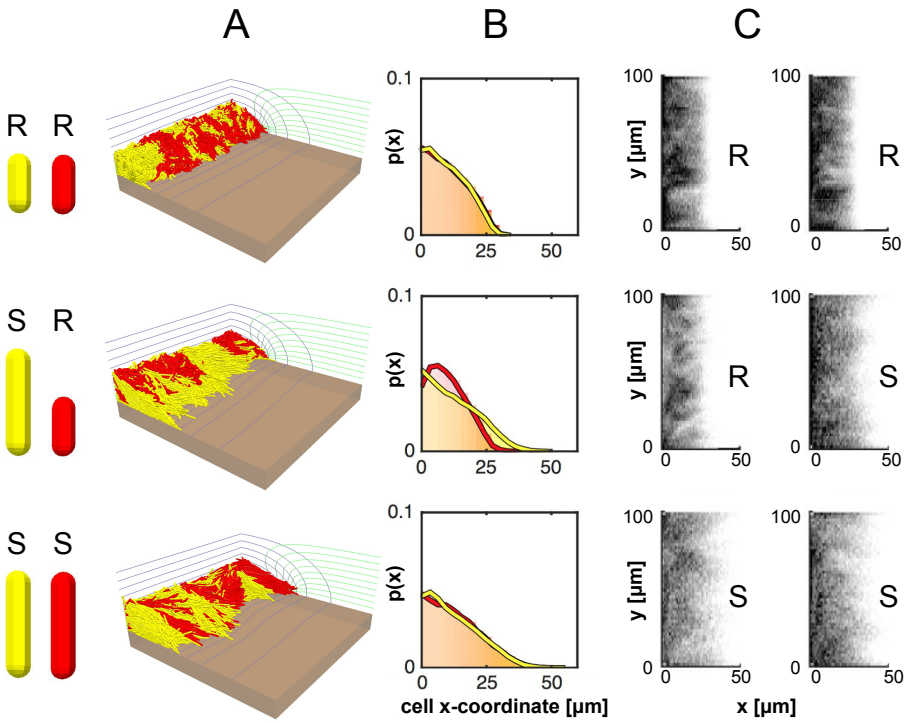

Fig. 6.6 In Model A, cell morphology drives edge enrichment and fitness advantage for susceptible cells in 3D colony edge simulations. Mixtures of short (R) and long (S) aspect ratio cells (SR) behave differently to control simulations where both strains have the same shape (RR, SS). A: The S cell is more sensitive to branching, leading to enrichment at the colony edge when grown alongside R cells. B: Histograms of cell x-coordinate quantify the enrichment of S cells at the colony edge in the SR case only. The spatial structure produces a growth rate advantage for S cells in SR mixtures but not otherwise. C: 2-D cell density histograms confirm that these structural differences disappear in the RR case (neither strain branches) and the SS case (both strains branch). All data taken after 56h of growth, using a merged sample of 10 colonies. Figure adapted with permission from reference [98]; cells in column A coloured by type only with no growth rate shading.

growth rates correspond to bolder colours. Profile snapshots of the colony, highlighting cells by growth rate, show fast-growing S cells dominating the colony edge (Figure 6.5-C, inset). Meanwhile, control simulations show that a difference in the shapes of competed strains is necessary for edge capture. Figure 6.6 shows that enrichment occurs in 1:1 RS competitions, but is absent in SS and RR competition simulations performed in the same way.

6.3.2 Model B: single-field approach

Model A successfully reproduced the observed tendency for longer S cells to accumulate at the growing edge of the colony. However, the dual-field description it uses presupposes simultaneous limitation of two resources.

Therefore, we also tried modelling edge growth limitations using a simpler single-field model (Model B), in which cells depend only on the nutrient stored in the agar for growth. A schematic of the model is provided in Figure 6.7-A. This is effectively the same as the single-field model described in Chapters 4 and 5, except that the computational domain $L_x \times L_y \times L_z$ is rotated, so that nutrient is supplied by a moving boundary to the side of the colony ($x = L_x$) instead of above it. The scaled nutrient concentration field $\bar{u}_N$ is computed by solving the non-dimensional PDE

$$\bar{\nabla}^2 \bar{u}_N = \mathscr{D}_N \left(\frac{\bar{u}_n}{\bar{u}_N + \eta_N} \right) \phi(\mathbf{p}_1, \ldots, \mathbf{p}_n), \tag{6.5}$$

which governs cell growth rates as

$$\frac{d\bar{V}_i}{d\bar{t}} = \left(\frac{\bar{u}_{N,i}}{\bar{u}_{N,i} + \eta_N} \right) \bar{V}_i. \tag{6.6}$$

Instead of assuming the agar to provide a continuous supply of nutrient, Model B supposes that nutrient N is depleted around the colony (owing to uptake by cells), and must therefore diffuse in laterally from the surrounding agar, which behaves as a perfect nutrient source. As the colony expands, so to does the depletion zone; we assume the nutrient source is always a constant distance δ from the colony edge, computed in terms of the largest cell x-coordinate p_x, so that $u_N = u_{N,\text{bulk}}$ at $x = L_x$, and $L_x = \max(p_x) + \delta$. Zero-flux conditions are applied on all other domain boundaries, as summarised in Table 6.2. Note that this description may be thought of as a 3-dimensional analogue of existing 2-D models of colony growth, which use a moving radial boundary condition to represent nutrient depletion in the agar below the colony

[199]. By modelling the same situation in 3-D, we allow cells of different shapes full freedom of movement.

Branching results from longer cell morphology

We performed simulations with Model B, using domains of dimensions $L_y = 100\,\mu\text{m}$, $L_z = 100\,\mu\text{m}$ and $\delta = 40\,\mu\text{m}$, and initialising simulations with random 1:1 inocula of SS, SR and RR strain combinations as before. This time, we also varied the supply of nutrients using the Damköhler number $\mathscr{D}_N$, setting $\mathscr{D}_N = 0.1$ to represent poor nutrient supply (as in Chapter 5) and $\mathscr{D}_N = 0.01$ to represent rich nutrient supply. These parameters are summarised in Table 6.2.

The results of these simulations are shown in Figure 6.7. Under poor nutrient conditions (Figure 6.7-B, C), we found that Model B produced edge enrichment in S-R mixtures, but not in R-R and S-S controls, in agreement with the predictions of Model A (Figure 6.6). One striking outcome here was the marked differences in the overall morphologies of colony edges: under the same conditions, the edges of S-S colonies were much more branched than those of R-R colonies, suggesting that the longer S morphology makes cells more susceptible to branching.

Simulation repeats using a richer nutrient supply ($\mathscr{D}_N = 0.01$), and correspondingly shallower nutrient gradients, corroborate this hypothesis. Under these conditions, almost all cells at the colony edge are able to grow (Figure 6.7-D), and the colony boundary remains stable to branching. As a result, all three shape combinations produce colonies with similar overall morphologies, with a complete absence of edge enrichment in S-R mixtures. In this case, we also observe marginal enrichment of S cells towards the rear wall of the domain, produced by the layering effect discussed in Chapter 5 (Figure 6.7-E, black arrow).

A possible explanation for this effect is shown in Figure 6.8. Suppose an S-type cell and an R-type cell are placed alongside one another, aligned parallel to the x axis.

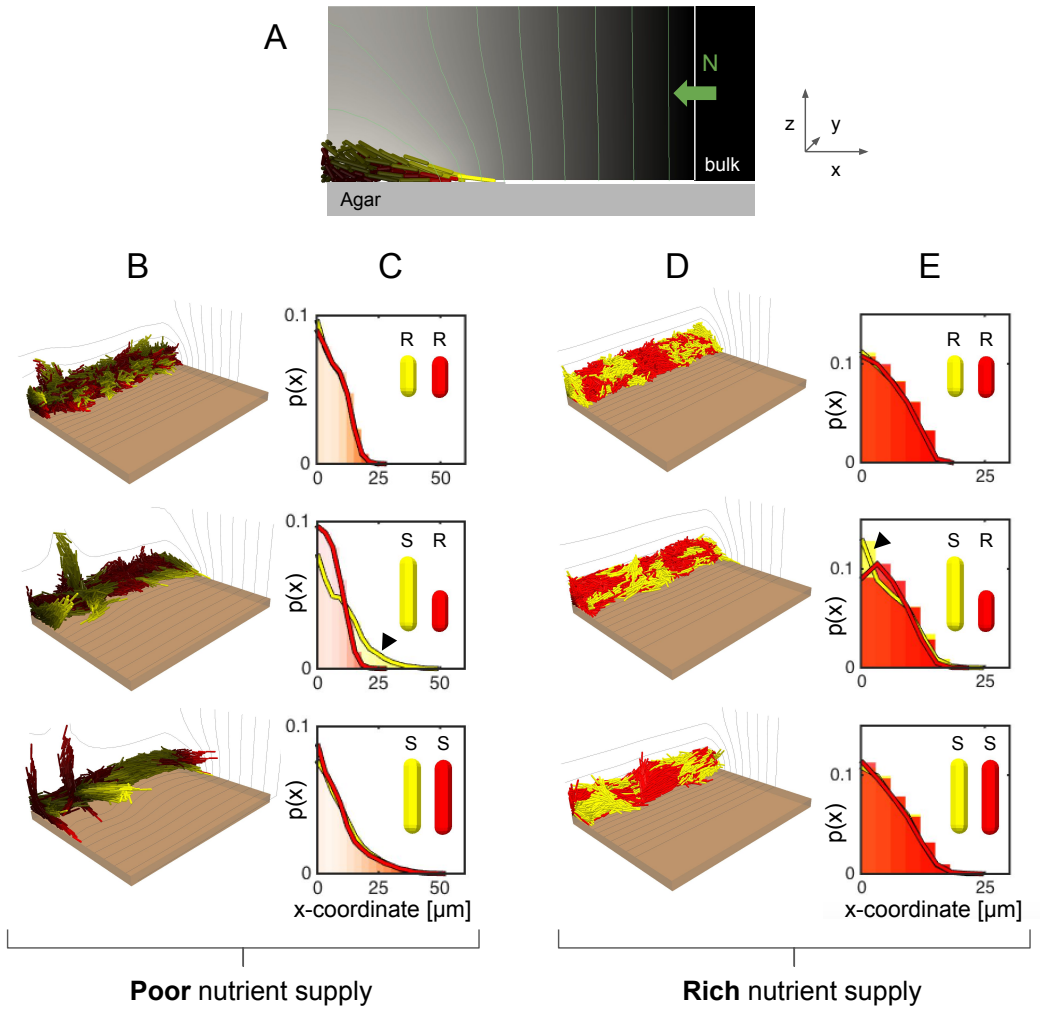

Fig. 6.7 In Model B (A), a single limiting solute (nutrient N) is supplied from a bulk region surrounding the colony. When nutrient supply is limited ('Poor' supply, $\mathscr{D}_N = 0.1$), surface instabilities are produced, and the colony edge becomes branched and irregular (B). S cells branch more than R cells, and become enriched at the colony edge in the SR mixtures (C, black arrow) but not in S-S or R-R controls (C). When nutrient availability is higher ('Rich' supply, $\mathscr{D}_N = 0.01$), no branching occurs, and all three colonies develop similar overall morphologies (D) and spatial strain distributions (E), irrespective of cell shape. Note that branching is more pronounced than in Model A, and is no longer limited to cells close to the agar surface (e.g. B, SR and SS cases). Cell and histogram box colours encode growth rates as in Figures 6.4 and 6.5 respectively; 10 simulations per case.

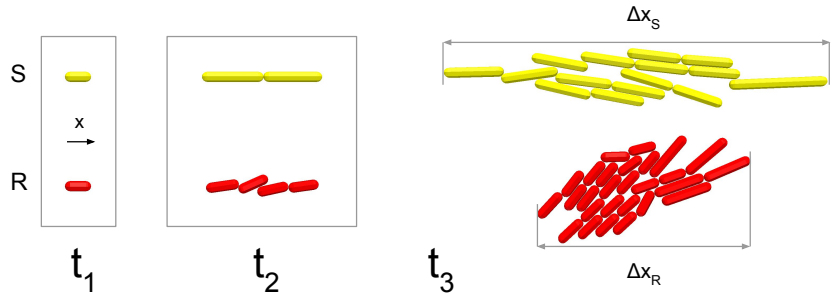

Fig. 6.8 Capsule cells of equal initial volume are placed on a surface, oriented along the x axis (t_1). S (yellow) and R (red) cells are programmed to divide upon reaching volumes V_S and V_R respectively, with $V_S > V_R$. Although both capsule types grow at the same rate μ, longer S cells are more stable with respect to buckling, and deviate less rapidly from their initial alignment (t_2). By maintaining a more consistent orientation, S cells move a longer distance along the x axis than R cells, i.e. $\Delta x_S > \Delta x_R$ (t_3) on short timescales. Images created using CellModeller.

Lines of S cells are more stable with respect to buckling than those of R cells, and so maintain their orientation for longer (Figure 6.8, t_2). Thus, starting at the same position, S cells can travel further than R cells through orientational persistence (Figure 6.8, t_3). If the cells' growth rates are then coupled to local nutrient concentration, and nutrient concentration gradients along x are steep, then the extra distance covered by S cells can translate into a substantial increase in their growth rates, in turn increasing $\Delta x_S/\Delta x_R$ and initiating a runaway branching event. We argue that Models A and B create an enrichment effect through this common mechanism.

6.3.3 Model Z: varying specific growth rates

Models A and B demonstrate that elongation can lead to the enrichment of S cells at the edge of resource-limited S-R colonies, so that they receive a growth rate advantage relative to R cells. Thus, individual-based modelling has provided us with a mechanistic rationale for the experimental observations reported in this chapter: in colonies of S and R bacteria, antibiotic-induced filamentation coincides with increased S-cell counts at the colony edge.

However, this is not the only possible explanation of edge enrichment, and we should also consider alternative hypotheses. For example, Models A and B assume that the intrinsic cell growth rates of S and R cells are the same in the presence of antibiotic, so that S and R cells differ only in cell shape. Actually, this is unlikely to be the case. S cells are expected to grow faster than R cells in the absence of antibiotic, but under high antibiotic concentrations, S cells are killed, and have a lower effective growth rate. As an additional complication, degradation of antibiotic by R cells protects nearby S cells, and may ultimately deplete the supply of antibiotic. Overall then, there are many factors in play that could affect cell growth rates, and it seems unlikely that S and R cells grow at exactly the same rate.

Here we present a third and final model, Model Z, which offers an alternative explanation for edge enrichment based on growth rate differences. The model is effectively a 2-dimensional version of Model B, representing the edge of a 2-strain colony as a laminar sheet of cells measuring, with a single growth-limiting nutrient (N) diffusing into the colony from the bulk agar ahead of it. This time however, the two cell strains (denoted A and B) have identical, coccal shapes, but different growth rates. These may be written in dimensionless form as

$$\frac{d\bar{V}_A}{d\bar{t}} = \kappa\left(\frac{\bar{u}_N}{\bar{u}_N+\eta_N}\right)\bar{V}_A, \quad \frac{d\bar{V}_B}{d\bar{t}} = \left(\frac{\bar{u}_N}{\bar{u}_N+\eta_N}\right)\bar{V}_B, \tag{6.7}$$

where $\bar{V}$ is the cell volume scaled to cell length l^3, $\bar{t}$ is time scaled to the minimum doubling time $\ln(2)/\mu$, $\bar{u}_N$ is nutrient concentration scaled to its value in the bulk agar $u_{N,0}$, η_N is a saturation number $K_N/u_{N,0}$. Here, κ represents the ratio between growth rates of strains A and B: for example, $\kappa = 0.5$ corresponds to a 50% disadvantage for the A strain relative to the B strain. Models A and B assume that $\kappa = 1$.

The corresponding dimensionless PDE for nutrients is

$$\bar{\nabla}^2\bar{u}_N = \mathscr{D}_N\left(\frac{\bar{u}_N}{\bar{u}_N+\eta_N}\right)[\kappa\phi_A+\phi_B], \tag{6.8}$$

where ϕ_A and ϕ_B are the cell volume fractions for A and B strains respectively, and where $\mathscr{D}_N$ is the nutrient Damköhler number as defined above, controlling the steepness of nutrient concentration gradients. Thus, Model Z assumes that A cells consume less nutrient and therefore do not grow as fast as B cells. The boundary conditions for Model Z are similar to those used in Model B. Nutrient is supplied from a perfect source representing the agar ahead of the colony edge, such that $\bar{u}_N = 1$ at $x = L_x$, with $L_x = \max(p_x) + \delta$ as before. All other boundaries are set to be reflecting (zero-flux).

Growth rate differences can also drive edge enrichment

We used Model Z to simulate the growth of 2-strain colonies, shown in Figure 6.9. Horizontal (xy) slices of the colony edge were grown from 1:1 mixtures of A- and B-type capsule cells, shown in red and yellow respectively, placed randomly along the $x = 0$ edge of a 300 µm-wide box. A-type cells were given an intrinsic growth disadvantage by setting $\kappa = 0.95$ (5% disadvantage against B) or $\kappa = 0.90$ (10% disadvantage against B). In each case, the colony was fed with either a plentiful ($\mathscr{D}_N = 0.0001$) or a poor nutrient supply ($\mathscr{D}_N = 0.01$) representing the perfusion conditions present in liquid or solid cultures respectively. Simulations were terminated once the total cell population reached a maximum value of approximately 7.5×10^3 cells, from a starting inoculum of 74 cells.

End-state snapshots of these simulations (Figure 6.9, 'colony slice') show that, when the nutrient supply is limiting ($\mathscr{D}_N$) even a small (5%) growth rate disadvantage leads to enrichment of B-type cells at the leading edge of the colony, as slower-growing A cells are less likely to become locally fixed. Qualitatively, this enrichment increases further when the growth rate disadvantage is raised to 10%. In Figure 6.9 ('Relative fitness'), we also quantify overall cell growth by computing the relative cell fitness for the B-strain,

$$\omega_B/\omega_A = \log\left(\frac{n_B(t_{\text{end}})}{n_B(0)}\right) / \log\left(\frac{n_A(t_{\text{end}})}{n_A(0)}\right), \tag{6.9}$$

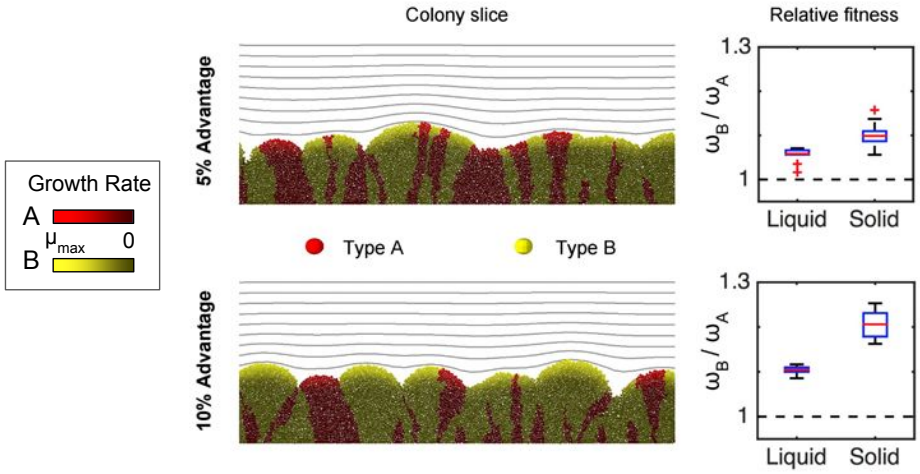

Fig. 6.9 Simulation of colony edge competition using Model Z. Here, A-type cells have either a 5% (top row) or 10% (bottom row) growth rate disadvantage over B-type cells. Simulation screenshots (left) show laminar colony sections grown under nutrient-limited conditions, where rapid cell growth is limited to a thin layer at the edge of the colony. Faster-growing B cells are more likely to become locally fixed and so become enriched at the edge. As before, cells are coloured by type and by growth rate (see legend), so that fast-growing cells appear brightly-coloured; contours correspond to nutrient concentration isoclines in increments of 10%. Plots of relative cell fitness (right) show that the type-B cell growth rate advantage is increased approximately 2-fold under solid culture conditions ($\mathscr{D}_N = 0.01$) relative to 'liquid culture' controls ($\mathscr{D}_N = 0.0001$), in which all cells grow exponentially. Sample of 10 simulations per case; snapshots show the central 200 μm section of the simulation domain.

where $n_A(t)$, $n_B(t)$ denote the numbers of A- and B-type cells present at the beginning ($t = 0$) and end ($t = t_{\text{end}}$) of the simulation. When nutrient perfusion is complete (Figure 6.9, 'Liquid' culture conditions), all of the cells in the simulation can grow exponentially, and so the end-state relative fitness is given by the inverse of the growth rate ratio: 5% and 10% disadvantages for A give mean relative fitnesses $\langle \omega_B/\omega_A \rangle$ of 1.05 and 1.10 respectively. These values are equal to $1/\kappa$ to within 1% accuracy in both cases.

However, when nutrient supply is limiting, the same intrinsic growth rates lead to a larger difference in observed fitnesses (Figure 6.9, 'Solid' culture conditions): 5% and 10% growth rate differences result in mean relative fitnesses $\langle \omega_B/\omega_A \rangle = 1.10$ and

1.21 respectively, approximately doubling the cell fitness advantages measured where nutrient is plentiful. This demonstrates that nutrient limitations can amplify intrinsic growth rate differences: when only the outer edge of the colony can grow, having a higher growth rate is even more valuable, because it increases the probability of becoming fixed at the colony edge.

Thus, Model Z demonstrates that differences in growth rate alone are sufficient to explain the enrichment of a particular strain at the edge of a colony. This gives an alternative to our first hypothesis based on edge branching and the elongated geometry of S cells: if S cells grow faster than R cells (through some unknown combination of cross-protection, antibiotic depletion and R cells paying plasmid expression costs), then they can become enriched at the colony edge.

6.4 Discussion

The edges of bacterial colonies are often characterised by significant resource limitations and fierce competition. Occupying the edge of such a colony can therefore confer a strategic advantage, and strongly influence bacterial competition and evolution. Understanding the physical, chemical and biological processes governing access to the colony edge is therefore of great interest.

In this chapter, we have described experiments in which resistant (R) and susceptible (S) strains of the pathogenic bacterium *P. aeruginosa* compete at the growing edges of agar plate colonies. Within these colonies, exposure to antibiotic induces filamentation in susceptible cells [184], but not in resistant cells [112]. The onset of this selective elongation correlates temporally with enrichment of the S cells at the colony edge – suggesting that cell elongation may benefit S cells by helping them to capture the resource-rich colony edge.

Our individual-based modelling framework provides insight into the processes underlying these phenomena. By devising different models of the colony edge, we have

identified two separate mechanisms through which S cells can accumulate at the colony edge and outcompete their rivals. If S cells are able to maintain a higher growth rate than R cells, they become more numerous in the colony (and, by extension, at the colony edge) over time. When resource limitations allow growth at only the leading edge of the colony, this amplifies the selective pressure favouring the faster-growing phenotype – so that S cells require only a small growth rate advantage in order to secure the colony edge. Cross-protection effects—where S cells benefit from antibiotic degradation by R cells without paying its energetic costs—could confer such a growth rate advantage [82, 33].

Interestingly however, we also find that cell elongation can lead to edge enrichment in the presence of strong resource gradients, by increasing the distance that cells travel through per unit biomass accumulated. By moving further out from the edge, filamentous cells can increase their access to rate-limiting resources, triggering branching events that occlude shorter cells. This mechanism suggests a new importance for cell elongation as an SOS response to cellular damage: instead of being a simple byproduct of division arrest, filamentation may serve an active function, offsetting damage by enabling preferential access to resources at the edge of a colony. In this way, filamentation could also influence the evolution of antibiotic resistance in microbial communities, weakening selection for antibiotic resistance by helping susceptible populations outcompete resistant mutants.

While our models are capable of capturing the enrichment effect, several of their predictions deviate from experimental observations. For example, we model cells as rigid capsules, yet real filamentous bacteria are flexible and can undergo significant bending. The inclusion of cell flexibility might inhibit shape-driven branching, by decreasing the orientational persistence of longer cell shapes. Further, the models do not include any cell-cell or cell-surface adhesion, which could explain why colony fronts appears as monolayers in experiments but have a more wedge-shaped profile in 3-dimensional simulations.

As a method for studying microbial shape in communities, the experimental system we have analysed is also much more complicated than the arrangements reported in Chapter 5. Strain morphologies and growth rates are both coupled to the antibiotic concentrations that individual cells experience, and these couplings are omitted from our models. Ultimately, these additional interactions make it difficult to identify which—if either—of our proposed mechanisms drives the edge enrichment effect seen in experiments. We should also be mindful of plausible alternatives that have yet to be modelled – for example, perhaps filamentous S cells might prevent R cells from reaching the edge through mechanical means [170], forming a cohesive barrier to hold back the resistant phenotype.

In spite of this ambiguity, we argue that both of the mechanistic hypotheses presented in this chapter are potentially interesting effects in their own right. Importantly, our modelling has identified a new mechanism, distinct from the mechanical layering effect reported in Chapter 5, through which cellular shape *per se* can influence spatial patterning and competition in microbial communities. This work highlights the potential relevance of cell shape to a real and important experimental system, and demonstrates the power of individual-based modelling as method for supporting and interpreting observations in community biology.

6.5 Conclusions

In this chapter, we have focused on competition between different cells shapes at the colony edge, adapting our model to examine a real experimental system in which resistant and susceptible cells compete in the presence of antibiotic. Filamentation induced in antibiotic-susceptible cells appears to confer a surprising advantage: preferential access to the colony edge. Using individual-based modelling, we can now rationalise this emergent effect in terms of differential solute gradient sensitivity in different cell shapes. Overall, our findings suggest a new significance for filamentation as a method

for cells to actively resist being out-competed by a resistant population, emphasising the potential impact of cell shape in microbial collectives.

7

Cell shape and microbial warfare *via* toxin secretion

Abstract

In Chapters 5 and 6, we pitted microbes against one another in a competition for nutrients, and examined the ways in which their shapes help them to improve their resource access in dense communities, such as biofilms and colonies. However, microorganisms are by no means passive in their struggle for these vital resources: often as not, communities play host to intense conflict, as microbes fight for supremacy using an arsenal of chemical weaponry.

In this final research chapter, we adapt our individual-based modelling framework to study the role of cell shape within the 'battleground' of a microbial community. We focus on warfare waged using bacteriocins (diffusible toxins), and show how to implement, extend and analyse an existing model of bacteriocin aggression. Our modelling suggests that cell shape can affect the evolution of bacteriocin production under nutrient-limited conditions, but that shape-driven patterning alone does not affect bacteriocin effectiveness.

7.1 Introduction

As we have discussed, microbial communities are highly competitive environments, in which many microbial cells struggle for space [167] and resources [189, 144]. While cooperative interactions can occur in communities, these are generally less prevalent than competitive interactions [94, 64]. In Chapters 5 and 6 of this thesis, we used an individual-based model of this type of competition, known to biologists as

exploitation competition. Individuals interacting *via* exploitation competition harm each other indirectly by consuming shared resources, thereby depriving neighbours of the materials they require.

This type of interaction is only one side of microbial competition, however. It has been suggested that microorganisms actively sense hallmarks of exploitation competition—such as nutrient limitations, toxins, and quorum sensing molecules—and use these cues to regulate aggressive phenotypes that directly harm other microbes in a community [63, 2]. In other words, exploitation competition often leads to a second type of competition [234], known as interference competition, in which competing species or strains fight one another for the resources they require.

Interference competition is highly prevalent in microbial communities, exerting a substantial effect on community structure and stability [1, 2, 141] in collectives such as the human gut microbiome [68]. Consequent arms races [233] have led to the evolution of a formidable array of molecular weapons, with which microbes wage war on their competitors [64]. Weapons in this microscopic armoury include diffusible antibiotics [234], pore-forming 'hole punches' (R-pyocins) [208, 202], temperate viruses [32, 40] and poisoned needles [13, 12]. Microbes have also developed a range of defensive equipment for fending off attacks, using enzymes to degrade toxins [141] and to suppress their production [271, 2].

Bacteriocins are a commonly-studied example of microbial weaponry. These antibiotic agents are small, diffusible polypeptide toxins [145], released by bacteria to attack closely-related strains [67].[1] A defining trait of many human pathogens [128], bacteriocins damage target cells through various mechanisms, including DNA degradation [214], protein synthesis inhibition, and by compromising cell membrane function through depolarisation or lysis [292]. Certain bacteriocins have dual modes of action: for example, Nisin [58] acts both as a transporter inhibitor and as a pore-former [67].

[1] Broad-spectrum bacteriocins are rarer, but also known [180, 58].

Bacteriocin-producing microbes are protected from the effects of their own toxins through the co-expression of immunity proteins [9, 91, 76]. However, bacteriocin production still carries a cost: producer strains must forfeit some of their growth resources in order to synthesise toxins [128, 64], and in some cases must undergo cell suicide (lysis) in order to release the bacteriocin payload into their surroundings [142, 234, 130]. Thus, bacteriocin production is considered a 'spiteful' social trait, in that it harms both the target cell and the producer.

Determining the circumstances under which such traits might evolve, in spite of their costs, is therefore an interesting problem in the field of social evolution, and has received attention in previous theoretical and experimental studies [100, 101, 128]. These studies indicate that selection for bacteriocin-producing phenotypes is strongly affected by community spatial structure, which determines both the lengthscales on which toxins can accumulate, and the degree to which toxin activity is directed against rival strains [43]. Bacteriocins are most useful when competing strains are spatially mixed, and so producers can be put at a disadvantage in segregated biofilms [268].

Bacteriocin production could therefore be of particular interest from the perspective of this thesis, because of its capacity to modulate community spatial structure. By affecting inter-strain mixing, cell shape has the potential to alter biological selection for toxin-producing phenotypes, and thereby affect the evolution of microbial warfare itself. Further, as one of the central processes governing community dynamics [171], bacteriocin production *per se* is amply worthy of study.

With this in mind, we decided to investigate the potential effects of shape on bacteriocin toxin dynamics. In this chapter, we describe an existing model—that of Vanni Bucci *et al*—of bacteriocin production, and implement it in our individual-based framework in order to evaluate the effects of cell shape on interference competition. We also present an extended version of Bucci's model, which considers the implications of toxin degradation, and devise lengthscale analyses to characterise the model's behaviour.

7.2 Modelling interference competition

In recent years, various theoretical models of interference competition have been proposed, using ODE systems [63], cellular automata [142] and individual-based approaches [43] to model the dynamics of bacteriocin production in microbial communities. Other forms of competition, such as the use of type-VI secretion systems [13], are now also being modelled [29, 182].

To test the effects of including interference competition in our framework, we implemented an existing individual-based model of bacteriocin production: namely, that reported by Vanni Bucci *et al*. in 2011.[2] Bucci's model provides a logical extension to the work presented so far in this thesis, considering interactions between bacteriocin-producing and bacteriocin-sensitive strains in a microbial biofilm. Practically speaking, this requires us to add an additional chemical field, describing the concentration of an unspecified bacteriocin toxin, to our hybrid model.

Here, we specify the equations defining this model, before applying dimensional analysis to identify parameter clusters controlling its behaviour. We then go on to describe model simulations, examining how the inclusion of non-spherical shapes influences the dynamics of interference competition under different physical and biological conditions.

7.2.1 The Bucci model

The model of Bucci *et al*., which we will refer to hereafter as the Bucci model, is summarised in Figure 7.1. The model describes the interaction of two microbial strains: a bacteriocin-producing (P) strain in competition with a bacteriocin-sensitive (S) strain (Figure 7.1-A). As in previous chapters, both strains require a nutrient N in order to grow, but additionally P cells convert some fraction f of their nutrient supply into a diffusible toxin T, which inhibits the growth of the S strain.

[2] This study was itself based on an earlier kinetic model by Michael H. F. Wilkinson [284].

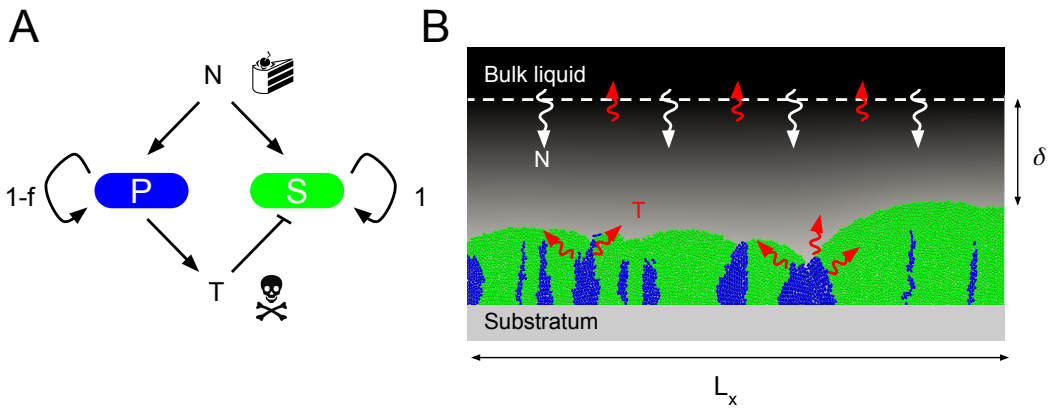

Fig. 7.1 A: In Bucci's individual-based model, a toxin-immune producer strain (P) and a toxin-sensitive strain (S) compete for nutrients (N). Producers invest a fraction f of their resources in the creation of a bacteriocin toxin (T), which inhibits S-cell growth. B: Both strains grow in a 2-D domain of base width L_x, representing a vertical slice through a surface-attached biofilm (blue and green cells) immersed in a liquid bath. Nutrients (white arrows) diffuse down into the biofilm from the well-mixed bulk liquid, through a diffusive boundary layer of thickness δ; toxins diffuse away from groups of P cells (red arrows) and are removed by the bulk liquid.

There are therefore two coupled solute fields (N and T), modelled using two reaction-diffusion equations. As before, we have a PDE to describe the variation in nutrient concentration u_N in Cartesian space $\mathbf{x}$ and time t,

$$\underbrace{\frac{\partial u_N}{\partial t}}_{\text{N accumulation}} = \underbrace{D_N \nabla^2 u_N}_{\text{N diffusion}} - \underbrace{\frac{1}{\gamma}\rho\mu_{\max}\left(\frac{u_N}{u_N + K_N}\right)[\phi_P + \phi_S]}_{\text{N uptake}}, \tag{7.1}$$

where D_N is the nutrient diffusivity, γ the biomass yield per unit nutrient consumed, ρ the cell density, $\mu_{\max}$ the maximum specific cell growth rate, K_N the nutrient saturation constant, and $\phi_P(\mathbf{x},t)$, $\phi_S(\mathbf{x},t)$ the volume fractions for P- and S-type cells respectively. Each term in Equation (7.1) is labelled according to the process it represents. Similarly, for the toxin field we have

$$\underbrace{\frac{\partial u_T}{\partial t}}_{\text{T accumulation}} = \underbrace{D_T \nabla^2 u_T}_{\text{T diffusion}} + \underbrace{\alpha_T f \rho \mu_{\max}\left(\frac{u_N}{u_N + K_N}\right)\phi_P}_{\text{T production}}, \tag{7.2}$$

Table 7.1 Model parameters used in Chapter 7

Parameter	Symbol	Units
Bucci model:		
Bulk nutrient concentration	$u_{N,\text{bulk}}$	$\text{kg}\,\text{m}^{-3}$
Nutrient diffusivity	D_N	$\text{m}^2\,\text{s}^{-1}$
Toxin diffusivity	D_T	$\text{m}^2\,\text{s}^{-1}$
Nutrient uptake Monod constant	K_N	$\text{kg}\,\text{m}^{-3}$
Biomass yield per unit nutrient	γ	
Toxin yield per unit nutrient	α_T	
Maximum specific cell growth rate	$\mu_{\max}$	s^{-1}
Fractional investment in toxin production	f	
Inhibition rate per unit toxin	k_T	$\text{m}^3\,\text{kg}^{-1}\,\text{s}^{-1}$
Extended model:		
S-cell inhibition Monod constant	K_I	$\text{kg}\,\text{m}^{-3}$
Toxin removal Monod constant	K_T	$\text{kg}\,\text{m}^{-3}$
Toxin removal per unit biomass	β_T	
Maximum toxin removal rate	$\nu_{\max}$	s^{-1}

where D_T is the toxin diffusivity, α_T the toxin yield per unit biomass, and f the fractional investment into toxin production. The growth rates for P- and S-type cells, $\frac{dV_P}{dt}$ and $\frac{dV_S}{dt}$, are coupled to the N and T concentration fields according to

$$\frac{dV_{P,i}}{dt} = \left[(1-f)\mu_{\max}\left(\frac{u_{N,i}}{u_{N,i}+K_N}\right)\right]V_{P,i}, \tag{7.3}$$

$$\frac{dV_{S,i}}{dt} = \left[\mu_{\max}\left(\frac{u_{N,i}}{u_{N,i}+K_N}\right) - k_T u_{T,i}\right]V_{S,i}, \tag{7.4}$$

where $V_{X,i}$ represents the volume of a cell of type X and index i, and where $u_{N,i}$ and $u_{T,i}$ are respectively the local concentrations of nutrient and toxin experienced by that cell. k_T is the rate of S-cell growth inhibition per unit toxin, so that S-cell growth is slowed by a factor $u_T k_T$. These parameters and their units are summarised in Table 7.1; likewise, Table 7.2 provides an overview of the model's variables. All other parameters in our individual-based framework (such as those governing the cell mechanics scheme) are as they were in Chapters 5 and 6, unless indicated otherwise here.

Table 7.2 Model variables used in Chapter 7

Variable	Symbol	Units
Cartesian coordinates	$x,\ y,\ z$	μm
Volume fraction fields:		
(P)roducer cells	ϕ_P	
(S)ensitive cells	ϕ_S	
Solute fields:		$\mathrm{kg\,m^{-3}}$
Nutrient (N)	u_N	
Toxin (T)	u_T	
For each cell i:		
position vector	$\mathbf{p}_i = (p_x, p_y, p_z)_i^\top$	μm
orientation unit vector	$\hat{\mathbf{a}}_i = (a_x, a_y, a_z)_i^\top$	μm
segment length	l_i	μm
volume	$V_i = \pi l_i r^2 + \frac{4}{3}\pi r^3$	$\mu\mathrm{m}^3$
local solute concentrations:		$\mathrm{kg\,m^{-3}}$
N	$u_{N,i} = u_N(\mathbf{p}_i)$	
T	$u_{T,i} = u_T(\mathbf{p}_i)$	
growth rates:	μ_i	$\mathrm{s^{-1}}$
P	$\mu_i = (1-f)\mu_{\max} u_{N,i}/(u_{N,i}+K_N)$	
S (Bucci model)	$\mu_i = \mu_{\max} u_{N,i}/(u_{N,i}+K_N) - k_T u_{T,i}$	
S (Extended model)	$\mu_i = \mu_{\max} u_{N,i} K_I/((u_{N,i}+K_N)(K_I+u_{T,i}))$	

Model domain

Equations (7.1) and (7.2) are evaluated on a rectangular domain, shown in Figure 7.1-B. As in Chapter 5, we model a 2-dimensional, vertical section of a biofilm, growing on a solid, impermeable surface ('Substratum'). The biofilm is comprised of many microbial cells (shown in blue and green), which grow and divide according to the nutrient and toxin concentrations they experience (Equations (7.3) and (7.4)). Cells are confined to the model domain using hard mechanical boundaries placed at $z = 0$ (representing the basal surface) and at $x = 0,\ L_x$ (representing repulsion from surrounding sections of the biofilm).

The biofilm is separated from a well-mixed bulk phase (Figure 7.1-B, 'Bulk liquid') by a diffusive boundary layer of thickness δ. The bulk liquid behaves as a perfect source for nutrients (N, white arrows), and as a perfect sink for toxins (T, red arrows)

produced by P-type cells. As the biofilm grows upwards, the diffusive boundary layer moves with it, so that the model domain has a fixed width L_x, but a variable height $L_z = \max(p_x) + \delta$, where $\max(p_x)$ corresponds to the height of the highest cell in the simulation at a given time. The PDE boundary conditions associated with this model are provided in Table 7.3.

Model simplifications

Having defined the basis of the original Bucci model, we also need to specify the ways in which our implementation deviates from it. Overall, our model is a slight simplification of Bucci's, with the following key differences:

- Specific cell growth rates μ_i are always positive, so that cells never decrease in size. In Bucci's model, spherical S cells grow by increasing their radius, but can also decrease in radius when toxin concentrations are high. In our model, all cells are represented as elongating capsules, making it less easy to model cell shrinkage: cell segment lengths can only decrease as far as 0, after which capsule radius must be reduced to shrink the cell's volume further. Since this scheme would be rather complicated, we simply ignore shrinkage altogether.

- We also ignore cell removal processes due to toxin activity or sloughing from the top of the biofilm. In Bucci's model, cells are removed from the simulation if their volume falls below a critical threshold (representing cell death) or if they move too far above the substratum (detachment).

Table 7.3 Solute boundary conditions used in Chapter 7

Boundary	Nutrient field	Toxin field	Description
$z = 0$	$\nabla u_N \cdot \hat{\mathbf{n}} = 0$	$\nabla u_T \cdot \hat{\mathbf{n}} = 0$	Zero flux through base
$z = L_z$	$u_N = u_{N,\text{bulk}}$	$u_T = 0$	Nutrient supply / toxin removal by bulk liquid
$x = 0$	$\nabla u_N \cdot \hat{\mathbf{n}} = 0$	$\nabla u_T \cdot \hat{\mathbf{n}} = 0$	Zero flux through lateral walls
$x = L_x$	$\nabla u_N \cdot \hat{\mathbf{n}} = 0$	$\nabla u_T \cdot \hat{\mathbf{n}} = 0$	

- As noted in Table 7.3, lateral domain boundaries ($x = 0,\ x = L_x$) are reflecting instead of periodic.

Later, in Section 7.2.3, we show that these changes do not have a serious impact on the model's behaviour.

7.2.2 Non-dimensional equations

We carried out dimensional analysis on Equations (7.1)-(7.4), using a similar process to that described in Chapter 4. Here, we use the scaled, dimensionless variables $\bar{V} = V/l^3$, $\bar{t} = t/\tau_{\text{growth}} = t\mu_{\max}/\ln(2)$, and $\bar{u}_N = u_N/u_{N,\text{bulk}}$. When scaling the toxin concentration u_T, there is no imposed reference concentration because $u_{T,\text{bulk}} = 0$. We therefore scale u_T against a 'critical' concentration $\mu_{\max}/k_T$, so that

$$\bar{u}_T = \frac{u_T k_T}{\mu_{\max}} = \frac{\text{Rate of S-cell inhibition}}{\text{Rate of S-cell growth}}. \tag{7.5}$$

At the critical concentration $\bar{u}_T = 1$, S cells are completely inhibited and are unable to grow, no matter how great their nutrient access.

These choices of scaling variables convert Equations (7.1) and (7.2) to non-dimensional form. Assuming, as before [43], that cell growth occurs on much longer timescales than reaction or diffusion (for either solute, N or T), we can compute pseudo-steady state, dimensionless fields $\bar{u}_N$, $\bar{u}_T$ by solving

$$\bar{\nabla}^2 \bar{u}_N = \mathscr{D}_{N,\text{rem}} \left(\frac{\bar{u}_N}{\bar{u}_N + \eta_N} \right) [\phi_P + \phi_S] \tag{7.6}$$

$$\bar{\nabla}^2 \bar{u}_T = \mathscr{D}_{T,\text{prod}} \left(\frac{\bar{u}_N}{\bar{u}_N + \eta_N} \right) \phi_P. \tag{7.7}$$

These equations are controlled by dimensionless parameter clusters: the Damköhler numbers for the nutrient uptake and toxin production reactions, $\mathscr{D}_{N,\text{rem}}$ and $\mathscr{D}_{T,\text{prod}}$,

are given by

$$\mathscr{D}_{N,\text{rem}} = \frac{l^2 \rho \mu_{\max}}{D_N \gamma u_{N,\text{bulk}}}, \qquad \mathscr{D}_{T,\text{prod}} = \frac{l^2 \rho f \alpha k_T}{D_T}, \tag{7.8}$$

and the uptake reaction saturation number $\eta_N = K_N / u_{N,\text{bulk}}$. Similarly, the non-dimensional analogues of the growth equations (7.3, 7.4) are

$$\frac{d\bar{V}_P}{d\bar{t}} = \ln(2) \left[(1-f) \left(\frac{\bar{u}_N}{\bar{u}_N + \eta_N} \right) \right] \bar{V}_P, \tag{7.9}$$

$$\frac{d\bar{V}_S}{d\bar{t}} = \ln(2) \left[\left(\frac{\bar{u}_N}{\bar{u}_N + \eta_N} \right) - \bar{u}_T \right] \bar{V}_S. \tag{7.10}$$

To implement Bucci's model using our IbM framework, we use a similar simulation loop to those described in Chapters 4, 5 and 6. For a given configuration of P and S cells $\{\mathbf{p}_P, \mathbf{p}_S\}$, we compute the cell volume fractions ϕ_P and ϕ_S, and use these to solve the coupled nutrient and toxin PDEs (7.6 and 7.6) with the finite element method described in Chapter 4. Once both fields are solved, we calculate the local nutrient and toxin concentrations at each cell's centroid, and use these to evaluate cell growth rates using Equations (7.9) and (7.10). Following cell growth and division, cell positions are updated using the mechanical relaxation algorithm discussed in Chapter 3.

Overall, our non-dimensionalisation of the Bucci model highlights four parameter groups—$\mathscr{D}_{N,\text{rem}}$, $\mathscr{D}_{T,\text{prod}}$, η_N and f—controlling the behaviour of nutrient and toxin fields, and the response of cells to the concentrations of these solutes. It is instructive to compare these parameter clusters with those used in Bucci's original study [43]. Here, Bucci *et al*. proposed a lengthscale, L_{bac}, as a means to characterise the effective range of a diffusing bacteriocin.[3] L_{bac} is given by

$$L_{\text{bac}} = \frac{\alpha_T k_T \langle m \rangle}{2\pi D_T}, \tag{7.11}$$

[3] A later study performed a similar derivation in more detail, applied to a system involving a diffusing public good enzyme instead of a toxin [197].

where α_T, k_T and D_T are defined as above, and where $\langle m \rangle$ corresponds to the mean biomass of producer cells. We see that this cluster is actually related to the toxin production Damköhler number (Equation (7.8)) by

$$\mathscr{D}_{T,\text{prod}} = f \frac{2\pi l^2}{\langle V \rangle} L_{\text{bac}}, \tag{7.12}$$

where $\langle V \rangle = \langle m \rangle / \rho$ is the mean producer cell volume. This suggests a unity between our non-dimensional scheme and that used in Bucci's original model. In the next section, we examine the effects of varying $\mathscr{D}_{T,\text{prod}}$ on the outcome of a competition involving bacteriocin production.

7.2.3 Simulations using the Bucci Model

To study interference competition in a biofilm, we performed simulations using our implementation of Bucci's individual-based model. As a first test of our implementation, we examined the dynamics of a simple competition scenario, under nutrient-rich conditions ($\mathscr{D}_{N,\text{rem}} = 0.001$ and $\eta_N = 0.033$ as in Chapter 6). We ran simulations using a range of values of toxin production Damköhler number $\mathscr{D}_{T,\text{prod}}$ (between 0 and 0.01), to examine the consequences of making toxin T progressively more effective. We assumed a fixed toxin investment fraction f of 0.3, which is the starting value used in reference [43].

Each simulation was carried out within a 2-dimensional domain of base length $L_x = 200\,\mu\text{m}$ and boundary height $\delta = 40\,\mu\text{m}$, and initialised by randomly distributing a 1:1 inoculum of coccal ($AR_0 = 1.1$) P and S cells (25 cells of each type) along the base of the domain ($z = r$, the cell radius). Following initialisation, all cells were allowed to grow and divide according to Equations (7.9) and (7.10). As described previously, both toxin and nutrient fields (Equations (7.6) and (7.7)) were re-evaluated from the cell configuration after every simulation step, so that cell growth, nutrient and toxin distribution were all coupled. Simulations were run until the community

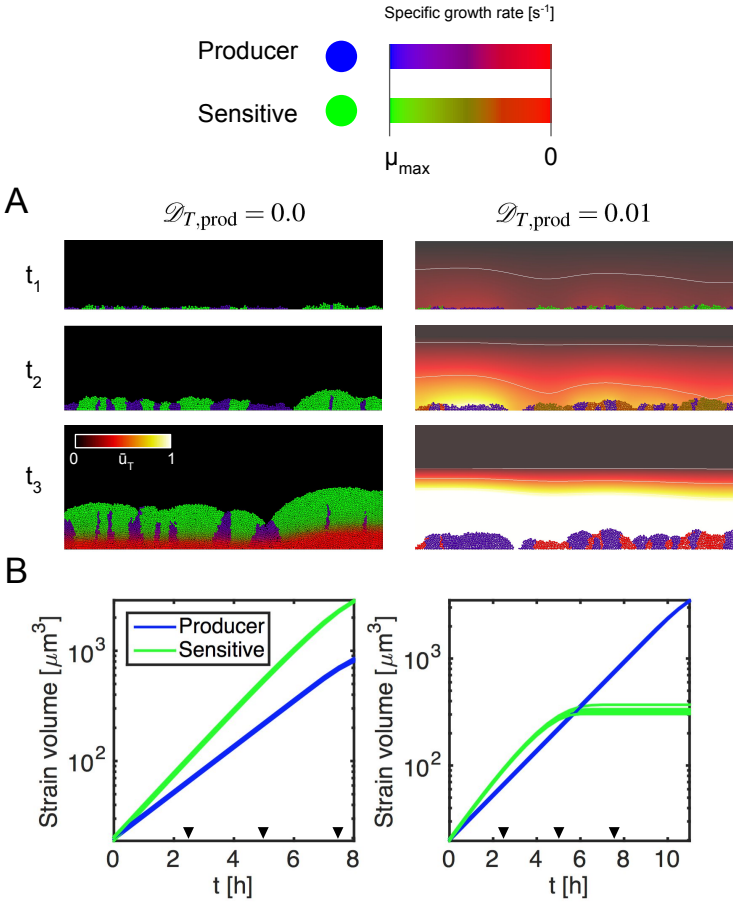

Fig. 7.2 We implemented Bucci's model of bacteriocin warfare using our IbM framework. Simulation snapshots (A) compare development of biofilms grown using low (left column) and high (right) values of the toxin Damköhler number $\mathscr{D}_{T,\mathrm{prod}}$ (0, 0.01 respectively). Strain volume curves (B) show that S cells attain higher volumes in the first case, but that P cells can overtake S-cell growth in the second. Times t_1, t_2 and t_3 correspond to 2.5, 5.0 and 7.5 h of growth, marked with arrows in B. Sample of 5 simulations per case, performed under rich nutrient conditions ($\mathscr{D}_{N,\mathrm{rem}} = 0.001$, $\eta_N = 0.0033$) and with intermediate toxin investment ($f = 0.3$). Strains are coloured by type and growth rate (top); colormaps show toxin concentration fields with contours corresponding to $\bar{u}_T = 0.1$, 0.5 and 0.9.

reached an overall fixed volume of $3.8 \times 10^3 \mu m^3$, equivalent to approximately 5,000 cells, with a sample of 5 simulations per case.

Figure 7.2 shows two examples of simulations in this parameter sweep: one in which the toxin effectiveness was zero (left column, $\mathscr{D}_{T,\mathrm{prod}} = 0$) and one where toxin effectiveness was high (right column, $\mathscr{D}_{T,\mathrm{prod}} = 0.01$). Figure 7.2-A depicts a series of representative snapshots for each case: here, cells are coloured both by their type

and by their relative growth rate (Figure 7.2, top), so that P (blue) and S (green) cells both appear red when their growth is inhibited by toxin (S strain only) or by lack of nutrients (both strains). The snapshots show the upward growth of the biofilm section at successive timepoints (t_1-t_3): when $\mathscr{D}_{T,\mathrm{prod}}$ is low, S cells grow unchecked by toxin, and so outcompete the slower-growing P cells, which waste resources producing ineffective toxin (Figure 7.2-A, left). However, when toxin effectiveness is high (Figure 7.2, right column, $\mathscr{D}_{T,\mathrm{prod}} = 0.01$), P cells are able to inhibit and eventually outgrow S cells.

In Figure 7.2-B, we examine these dynamics by measuring the total cell volume for each strain as a function of time, on semilog axes. Each trace here corresponds to a single simulation. In the absence of the toxin (left column), both strains grow exponentially until the biofilm depth exceeds the maximum penetration of the nutrient – as depicted in Figure 7.2-A (snapshot t_3), which shows that cells at the base of the biofilm (marked in red) are unable to grow owing to lack of nutrient access. When toxin effectiveness is increased, S cells still grow faster than P cells initially (Figure 7.2-B, right column), but eventually become overwhelmed through the accumulation of toxin, and stop growing altogether.

7.2.4 The effects of cell shape on interference competition

Next, we sought to quantify the transition between these two scenarios—victory for sensitives vs. victory for producers—as a function of toxin effectiveness, and to investigate how this competition might be affected by variation in cell morphology. In their 2011 study, Bucci *et al*. characterised such transitions by measuring the change in the producer phenotype frequency, $\Delta P/P_0$, over the course of simulations [43]. $\Delta P/P_0$ is given by

$$\Delta P/P_0 = \frac{P_f - P_0}{P_0}, \tag{7.13}$$

where P_0 and P_f are respectively the initial and final proportions of the producer strain in the biofilm. Here, we calculate these proportions $P(t)$ in terms of the total cell volume of the producer strain at a given time t, i.e.

$$P(t) = \frac{\sum_{i=1}^{n_P} V_i(t)}{\sum_{i=1}^{n_P} V_i(t) + \sum_{i=1}^{n_S} V_i(t)}, \tag{7.14}$$

where V_i is the volume of cell i, and where n_P and n_S are respectively the P- and S-cell populations.

We carried out simulations of bacteriocin competition in biofilms grown either with coccal or rod-shaped microbes. These cell shapes were modelled by setting minimum cell birth aspect ratios, AR_0, to 1.1 for coccal cells, and to 3.5 for rod cells, as in Chapter 5. We examined simulation behaviour over a range of $\mathscr{D}_{T,\text{prod}}$ values (between 0.0 and 0.02), under both nutrient-rich ($\mathscr{D}_{N,\text{rem}} = 0.001$, $\eta_N = 0.0033$) and nutrient-poor ($\mathscr{D}_{N,\text{rem}} = 0.1$, $\eta_N = 0.33$) conditions. Simulations using coccal cells were initiated and terminated as before, and their analogues using rod-shaped cells run for the same number of steps in each case.

Figure 7.3 compares the results of these simulations performed under rich (left column) and poor (right column) nutrient conditions. In Figure 7.3-A, we show simulation snapshots for biofilms comprised of coccal (top row) and rod-shaped cells (bottom), for the same value of $\mathscr{D}_{T,\text{prod}}$ (0.01, as in Figure 7.2, right column). These show that, when nutrients are non-limiting, this value of $\mathscr{D}_{T,\text{prod}}$ is sufficient for bacteriocin-producing cells to dominate the biofilm, irrespective of cell shape. Under these conditions, both coccal and rod-shaped morphologies produce colonies with similar appearances (A) and toxin production response curves (C), whose sigmoidal forms reproduce those of Bucci's original work [43]. Note that, in Figure 7.3-C and D, we have fitted 4-parameter sigmoid curves to each set of data points using the MATLAB function `nlinfit()`.

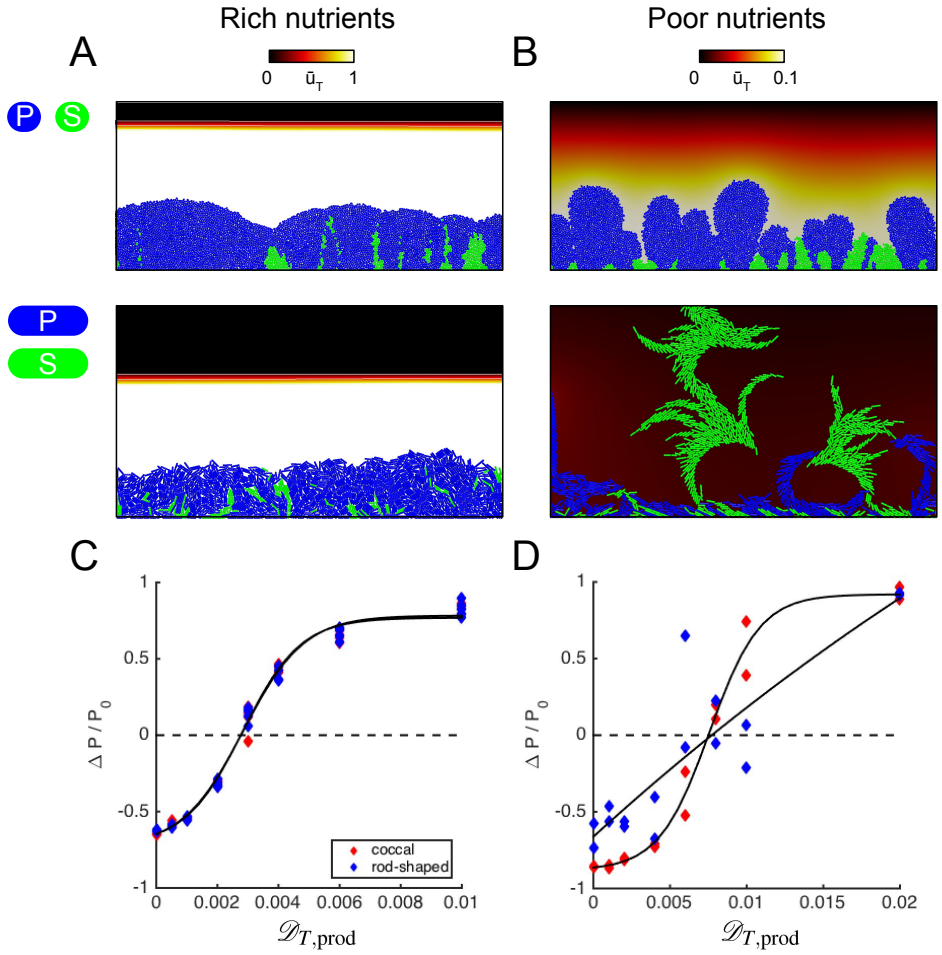

Fig. 7.3 The effects of cell shape in Bucci model simulations, performed under different conditions. A and B compare end-state snapshots of biofilms grown using $\mathscr{D}_{T,\mathrm{prod}} = 0.01$, under rich (A) and poor (B) nutrient conditions, using coccal (top row) or rod-shaped cells (bottom row). Cells are coloured by type only (P: blue; S; green); heatmaps show toxin concentration fields. Simulation outcomes (C,D) in both cases are quantified using $\Delta P/P_0$ (fold-change in producer cell volume, defined in main text) in parameter sweeps over $\mathscr{D}_{T,\mathrm{prod}}$. Red and blue markers denote simulations using coccal or rod-shaped morphologies as shown in legend (C). High and low nutrient concentrations correspond to $\mathscr{D}_{N,\mathrm{rem}} = 0.001$, $\eta_N = 0.0033$, and $\mathscr{D}_{N,\mathrm{rem}} = 0.1$, $\eta_N = 0.33$, respectively; $f = 0.3$ in all cases. Sample of 2 simulations per case.

However, when nutrient supplies are limiting (Figure 7.3-B,D), cell shape can make more of a difference. As shown in (Figure 7.3-B, top), coccal cells produce biofilms with an irregular surface: here, cell growth is limited to the upper surface of the biofilm, and toxin production is much slower owing to the lack of nutrients (note: the colourmap for right-hand column has been set to the range [0, 0.1]). However, P cells

still win overall for this value of $\mathscr{D}_{T,\text{prod}}$. Rod-shaped cells, grown under the same conditions (Figure 7.3-B, bottom), produce a more branched and segregated biofilm. Branches of faster-growing S cells deprive P cells of nutrients required for growth and toxin production, but simulation is also more stochastic, with cells becoming locally fixed at random due to the enhanced branching effect (as described in Chapter 6).

In summary, these simulations show that cell shape can affect bacteriocin interference competition by modulating the spatial structure of a biofilm, in response to nutrient limitations. The increased surface branching produced by rod cells makes it more difficult for producer cells to amass sufficient toxin to outcompete sensitive rivals. We also see that our model implementation is able to reproduce the toxin response curves described in Bucci's original study [43], implying that our modifications do not have a serious effect on the overall behaviour of the model.

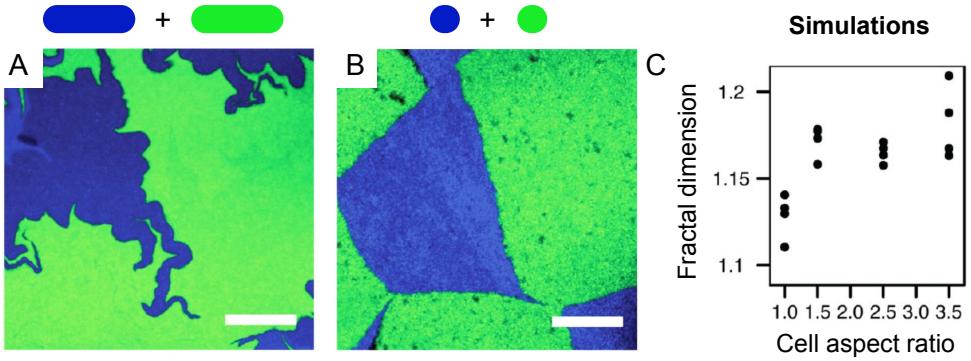

Fig. 7.4 Previous studies show that cell shape controls spatiogenetic patterning in dense microbial communities. Confocal micrographs of 2-strain laminar colonies, composed of rod-shaped (A, BW27783 strain) or coccal (B, KJB24 strain) *Escherichia coli* bacteria, respectively produce interdigitated (A) and smooth (B) patterns at the inter-strain (blue-green) boundary. CellModeller simulations from a previous publication (C) reproduce this dependency, predicting an increase in boundary fractal dimension with cell aspect ratio at birth. Scale bars in A, B correspond to 100 µm; figures adapted with permission from reference [238].

Nevertheless, we found that when nutrients are in rich supply, rod- and coccal-shaped cells perform similarly. This result was unexpected – as discussed in Chapter 5, cell shape is known to alter spatial patterning in microbial communities. Figure 7.4

provides an experimental demonstration of one such shape effect, taken from previous work by Rudge *et al* [238]. Figure 7.4-A shows a confocal image of a laminar, 2-strain microbial colony, with cell lineages marked with green and blue fluorescent labels. This colony is grown from rod-shaped *Escherichia coli* bacteria, which produce fractal-like interdigitations at the inter-strain boundary. By contrast, Figure 7.4-B is grown using a coccal mutant of *E. coli* (KJB24), and shows a smooth interstrain boundary. CellModeller, the mechanics engine on which this thesis is based, is able to recreate these effects *in silico* (Figure 7.4-C), demonstrating that increases in cell length in turn increase the fractal dimension (a measure of pattern complexity) of the inter-strain border.

Overall then, shape affects inter-strain mixing, and our IbM framework has already been shown to capture this effect. If, as we indicated in the introduction, bacteriocin effectiveness is modulated by community spatial structure, should we not expect to see bacteriocin production varying with shape *per se*? Having observed no such effects using the Bucci model, we wondered if this disagreement could be tied to the lengthscales on which bacteriocins were effective. One of the assumptions built into the Bucci model is that the bacteriocin toxin acts catalytically, inhibiting the growth of S cells whilst not being used up in the process. Under these circumstances, toxins are able to diffuse widely through a community (see Figure 7.2), being removed only by the bulk liquid above the biofilm.

This description is likely be representative of some toxins – such as bacteriolysin [67], which catalyse the hydrolysis of the bacterial cell wall. However, some bacteriocins might not behave catalytically if they are consumed as part of their activity, or degraded in the wider environment [216]. As noted in the introduction to this chapter, some bacteria can actively degrade toxins, including bacteriocins, using extra- or intra-cellular enzymes [216, 14]. A key example here are the beta-lactamase enzymes produced by bacteria, which hydrolyse beta-lactam antibiotics (such as penicillin) [166]. Degradational processes such as these are expected to limit the effective range

of a diffusing toxin. We hypothesised that, if sensitive cells were able to rapidly degrade bacteriocin, then it would only be able to penetrate a short distance into a group of sensitive cells, limiting the effects of the toxin to the boundaries between groups of P and S cells. We were keen to test this possibility, since, through the patterning effects described above, cell shape might then control the extent of P-S cell contact and consequent inhibition. To test this hypothesis, we therefore decided to extend Bucci's model to include the degradation of toxin by S cells. We describe these modifications, and their consequences for the model's behaviour, in the next section.

7.3 Extensions to the Bucci model

To examine the effects of toxin removal on bacteriocin effectiveness, we modified Bucci's model in two ways:

1. We added a Monod reaction term to Equation (7.2), so that the toxin would be consumed (or degraded) when interacting with S cells (as shown in Figure 7.5-A).

2. We changed the way in which toxin T inhibits S-cell growth, so that the nutrient uptake rate of S cells was reduced in proportion to their growth inhibition. In other words, when S cells are attacked with toxin, they consume less nutrient. We assume that the toxin-inhibition relationship takes takes the form $K_I/(K_I+u_{T,i})$, where K_I is the toxin concentration at which S-cell growth is reduced by 50%.

7.3.1 Adding toxin removal

The dimensional equations for our extended model are as follows:

$$\underbrace{\frac{\partial u_N}{\partial t}}_{\text{N accumulation}} = \underbrace{D_N \nabla^2 u_N}_{\text{N diffusion}} \underbrace{- \frac{1}{\gamma}\rho\mu_{\max}\left(\frac{u_N}{u_N+K_N}\right)[\phi_P + \left(\frac{K_I}{K_I+u_T}\right)\phi_S]}_{\text{N uptake}}, \tag{7.15}$$

and

$$\underbrace{\frac{\partial u_T}{\partial t}}_{\text{T accumulation}} = \underbrace{D_T \nabla^2 u_T}_{\text{T diffusion}} + \underbrace{f\alpha_T \rho \mu_{\max} \left(\frac{u_N}{u_N + K_N}\right) \phi_P}_{\text{T production by P cells}} - \underbrace{\beta_T \rho \nu_{\max} \left(\frac{u_T}{u_T + K_T}\right) \phi_S}_{\text{T removal by S cells}}. \tag{7.16}$$

In the extended model, the growth equation for P cells remains the same, but for S cells we now have

$$\frac{dV_{S,i}}{dt} = \left[\mu_{\max} \left(\frac{u_{N,i}}{u_{N,i} + K_N}\right) \left(\frac{K_I}{K_I + u_{T,i}}\right)\right] V_{S,i}. \tag{7.17}$$

This model can be converted to a non-dimensional, pseudo-steady state as before, by rewriting the equations using the scaled variables $\bar{u}_N = u_N/u_{N,\text{bulk}}$, $\bar{u}_T = u_T/K_I$, $\bar{t} = t/\tau_{\text{growth}}$, $\bar{x} = x/l$, $\bar{y} = y/l$, $\bar{z} = z/l$ and $\bar{V} = V/l^3$. This gives

$$\bar{\nabla}^2 \bar{u}_N = \mathscr{D}_{N,\text{rem}} \left(\frac{\bar{u}_N}{\bar{u}_N + \eta_N}\right) [\phi_P + \left(\frac{1}{1 + \bar{u}_T}\right) \phi_S], \tag{7.18}$$

$$\bar{\nabla}^2 \bar{u}_T = \mathscr{D}_{T,\text{rem}} \left(\frac{\bar{u}_T}{\bar{u}_T + \eta_T}\right) \phi_S - \mathscr{D}_{T,\text{prod}} \left(\frac{\bar{u}_N}{\bar{u}_N + \eta_N}\right) \phi_P, \tag{7.19}$$

for the nutrient and toxin fields, and

$$\frac{d\bar{V}_{S,i}}{d\bar{t}} = \ln(2) \left[\left(\frac{\bar{u}_{N,i}}{\bar{u}_{N,i} + \eta_N}\right) \left(\frac{1}{1 + \bar{u}_{T,i}}\right)\right] \bar{V}_{S,i}. \tag{7.20}$$

for the S-cell growth equation. The dimensionless equation for P-cell growth (Equation (7.9)) is unchanged from the original model. The equations of the extended model are controlled by the dimensionless control parameters

$$\mathscr{D}_{T,\text{prod}} = \frac{l^2 f \alpha_T \rho \mu_{\max}}{D_T K_I}, \quad \mathscr{D}_{T,\text{rem}} = \frac{l^2 \beta_T \rho \nu_{\max}}{D_T K_I} \tag{7.21}$$

with $\mathscr{D}_{N,\text{rem}}$ defined as before, and with $\eta_N = K_N/u_{N,\text{bulk}}$ and $\eta_T = K_T/K_I$. Note that if we set the toxin reference concentration $K_I = \mu_{\max}/k_T$, then $\mathscr{D}_{T,\text{prod}}$ is then equivalent to the production Damköhler number in the Bucci model.

7.3.2 Predicting model behaviour using fixed cell configurations

We wished to establish whether or not the extended Bucci model was capable of generating different behaviours to those displayed by the original model – and particularly, if the inclusion of toxin removal would limit its effective spatial range.

Therefore, as an initial test of the new model, we examined the spatial distribution of toxin in a biofilm by solving Equation (7.19) for a set of five fixed cell configurations, in the absence of nutrient limitations. Cell configurations consisted of vertical biofilm sections of uniform depth and width $L_x = 200\,\mu\text{m}$, with a regular, alternating arrangement of P and S cells. Each configuration was grown from an inoculum of 48 cells, placed at regular intervals along the domain base ($z = R$) in the repeating sequence (P-P-P-S-S-S), using our individual-based model. All cells were allowed grow at the maximal rate $\mu_{\max}$ until the biofilm reached a height of 45 µm; snapshots of the resulting cell configurations are shown in Figure 7.5-C.

This 'fixed configuration' approach is similar to the PDE solver tests that we described in Chapter 4. We use it again here for three primary reasons: first, keeping the arrangement of cells constant makes it easier to compare solute distributions under different conditions. Second, different fixed configurations can be created and compared according to interest – for example, we tested the effects of changing the size of S- and P-cell groups. Third, solving the PDE for only one cell configuration is much faster than doing so repeatedly as part of an IbM simulation. This allows large areas of parameter space to be explored quickly. The obvious disadvantage is that we lose the feedback between the cell arrangement and the toxin fields, and so we cannot get a sense of

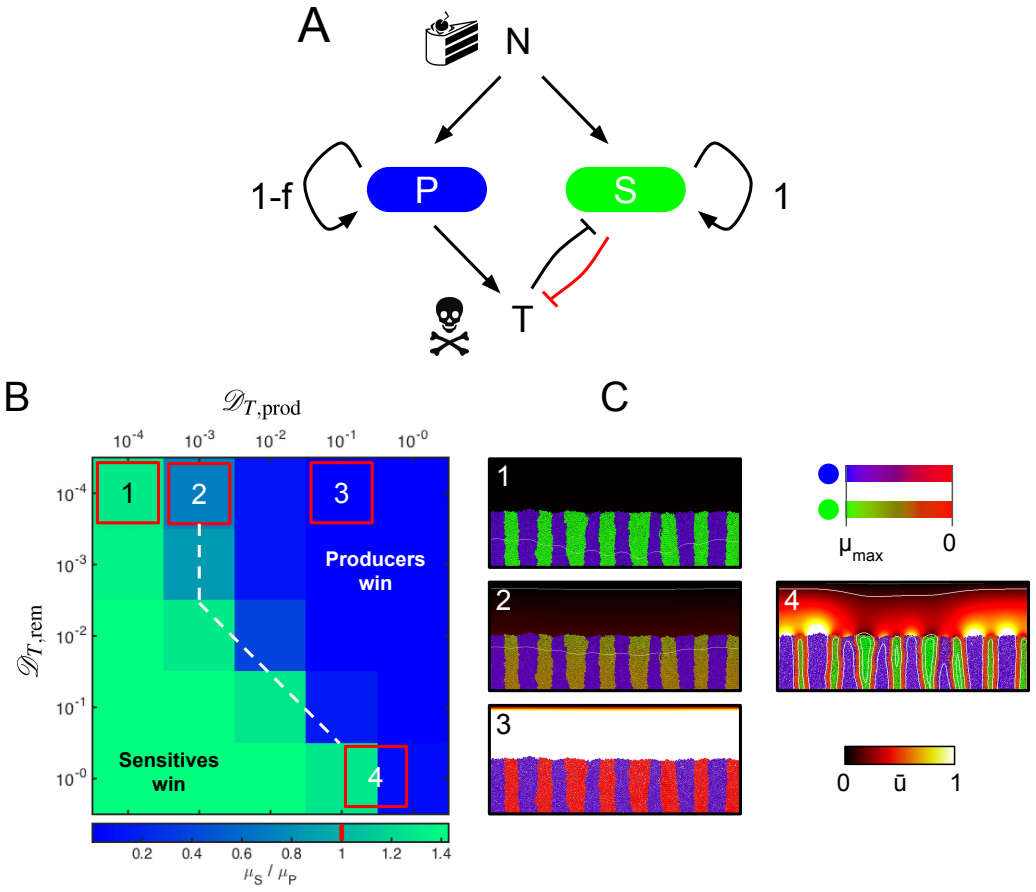

Fig. 7.5 A: schematic showing extended version of Bucci's model, in which S cells can degrade the bacteriocin toxin T (red arrow). B: heatmaps parameter space show PDE behaviour as a function of toxin production and removal Damköhler numbers, computed for fixed cell configurations. Cell growth rates are computed for each PDE solution; each element in the grid is coloured according to the average strain growth rate ratio μ_S/μ_P. C: snapshots of example configurations and fields show complete toxin perfusion for low values of $\mathscr{D}_{T,\mathrm{rem}}$ (1, 2, 3), as seen in the original Bucci model, but predict partial toxin perfusion when both $\mathscr{D}_{T,\mathrm{prod}}$ and $\mathscr{D}_{T,\,\mathrm{rem}}$ are large (4). Numbered boxes in B mark the conditions used for snaphots 1-4. Sample of 5 configurations per case; calculations carried out assuming perfect nutrient perfusion ($\mathscr{D}_{N,\mathrm{rem}} = 0$). Toxin heatmaps and contours are as described in Figure 7.2.

what spatial structures might emerge in the biofilm. It is therefore also necessary to perform fully-coupled simulations, which we discuss later in the next section.

To get a sense of the range of possible behaviours produced by the extended Bucci model, we performed a 2-dimensional parameter sweep (Figure 7.5), varying the two

toxin Damkohler numbers $\mathscr{D}_{T,\text{prod}}$ and $\mathscr{D}_{T,\text{rem}}$ independently through the range 10^{-4} to 1, but keeping the cell configurations (described above) the same in each case.

For the sake of simplicity, we also set $\eta_T = 1$, and assumed nutrient perfusion to be non-limiting ($\bar{u}_T = 1$ over all space) so as to remove the dependency on the nutrient field. In each case, once the toxin field had been computed, we evaluated the growth rate μ of every cell in the configuration using Equations (7.9) and (7.20), again assuming an investment of $f = 0.3$. Boundary conditions for the toxin field were set as before, except that lateral reflecting boundary conditions were replaced with periodic boundary conditions.

Figure 7.5-B shows the results of this parameter sweep as a matrix heatmap, with each grid element coloured according to the relative growth rate of sensitive cells, μ_S/μ_P (averaged over all cells across the sample of 5 configurations). The parameter sweep predicts a transition between regimes in which sensitive cells win ($\mu_S/\mu_P > 1$) and in which producer cells win ($\mu_S/\mu_P < 1$). Interestingly, we found that the nature of the transition varied with location in parameter space. When $\mathscr{D}_{T,\text{rem}}$ was low ($\mathscr{D}_{T,\text{rem}} < 1 \times 10^{-2}$), the transition between outcomes is invariant with respect to $\mathscr{D}_{T,\text{rem}}$, as marked in Figure 7.5-B (vertical section of white dashed line). This picture is consistent with the transition curves we generated for the Bucci model, with relative cell growth rates being controlled by $\mathscr{D}_{T,\text{prod}}$ alone. At higher values of $\mathscr{D}_{T,\text{rem}}$ however, the outcome appears to be controlled by the ratio of the two Damköhler numbers (Figure 7.5-B, diagonal dashed line).

This analysis also suggested the existence of a new type of toxin distribution, distinct from the behaviour of the original Bucci model. To highlight this observation, Figure 7.5-C shows a set of 4 example snapshots, corresponding to the 4 numbered boxes in the parameter space map in Figure 7.5-B, showing toxin fields and cells coloured by type and by growth rate, as before. We found that for low values of $\mathscr{D}_{T,\text{rem}}$, the distribution of toxin through the cell configuration was approximately uniform, so that all S cells in the configuration were equally inhibited – experiencing low (Figure 7.5-C,

Box 1), intermediate (Box 2) or high (Box 3) growth inhibition according to the value of $\mathscr{D}_{T,\text{prod}}$. However, when $\mathscr{D}_{T,\text{prod}}$ and $\mathscr{D}_{T,\text{rem}}$ were both high, we found a second type of behaviour, in which the effect of the toxin was limited to the boundary between adjacent S and P cell groups (Figure 7.5-C, Box 4, corresponding to $\mathscr{D}_{T,\text{prod}} = 0.2$ and $\mathscr{D}_{T,\text{rem}} = 1.0$).

We dubbed these two behaviours 'complete perfusion' (Figure 7.5-C, Boxes 1-3) and 'partial perfusion' (Box 4) respectively. The suggestion of the partial perfusion regime is of potential interest since it confines the effect of the toxin to the inter-strain boundary: the toxin produced is very effective, but is also degraded very effectively, and so cannot penetrate deeply into groups of S cells. As indicated above, cell shape is known to control patterning along the inter-strain boundary, and so interference competition in a partial perfusion scenario might be expected to show a strong dependency on cell shape.

7.3.3 Extended model simulations: testing the effects of cell shape

To investigate this hypothesis further, we ran full simulations using the extended Bucci model, performing a sweep over the same area of parameter space as in Figure 7.5. Simulations were initialised and terminated in the same way as before (Section 7.2.3), and ran either using coccal or rod-shaped cells, to test the effects of cell shape. Instead of measuring relative strain growth rates, we quantified simulation outcome by measuring values of $\Delta P/P_0$ at the end of each simulation, averaging values over a sample of 5 repeats per parameter combination.

Figure 7.6 shows the results of these parameter sweeps. Firstly, for coccal cells (Figure 7.6-A and B) we found similar simulation outcomes to those predicted by our static configuration analysis: the matrix of $\Delta P/P_0$ averages (Figure 7.6-A) has the same overall form as that shown in Figure 7.5, with transitions between S- and P-cell dominance characterised by either a vertical or a diagonal boundary depending on the

value of $\mathscr{D}_{\text{rem},T}$. We were also able to identify partial perfusion behaviour, as shown by end-state simulation snapshots (Figure 7.6-B). Here, Box 1 shows an intermediate case with near-homogenous perfusion; Box 2 (parameters: $\mathscr{D}_{T,\text{prod}} = 0.3$, $\mathscr{D}_{T,\text{rem}} = 1$) shows a more extreme case with S-cell inhibition limited to the inter-strain boundary. Both cases are marked on the parameter space map as before.

Figure 7.6-B shows a further effect of interest: in a partial-perfusion scenario the fate of S and P cells depends strongly on the size of the group in which they find themselves.

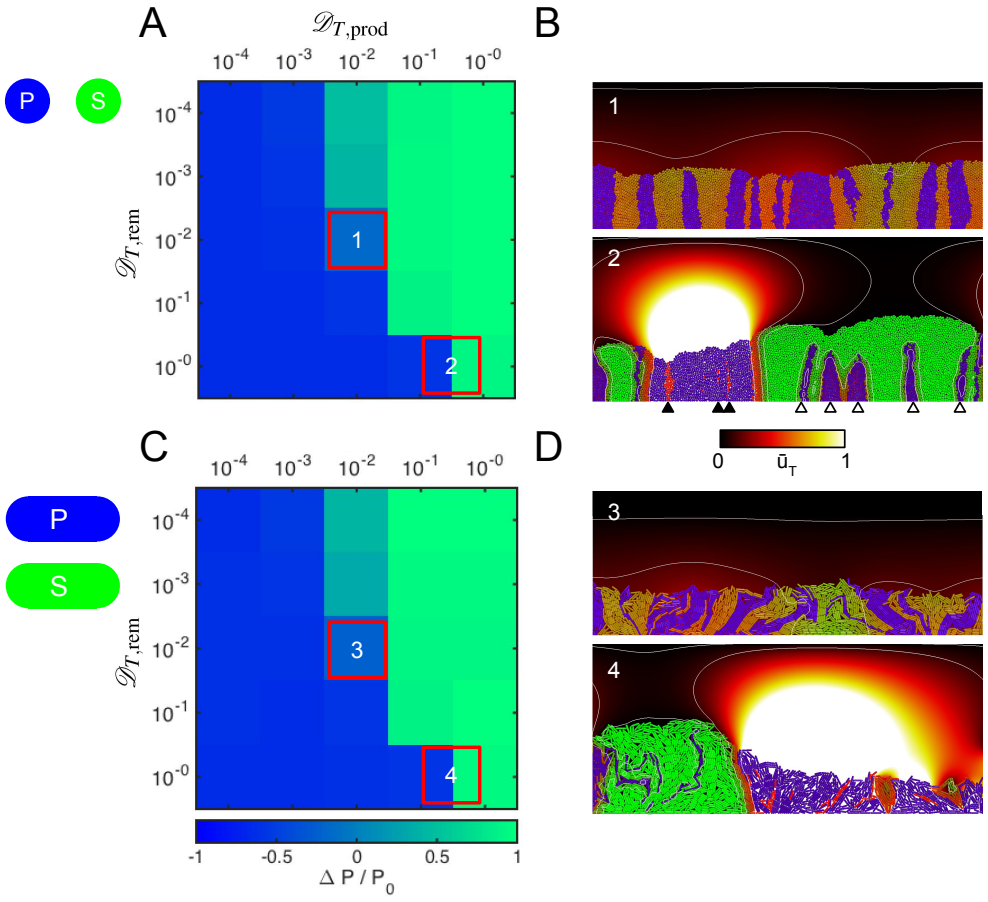

Fig. 7.6 The effects of cell shape in the extended Bucci model. Parameter sweeps (A, C) show simulation outcome (measured by fold-change in producer strain, $\Delta P/P_0$) as a function of control parameters $\mathscr{D}_{T,\text{prod}}$ and $\mathscr{D}_{T,\text{rem}}$, using coccal (A) and rod-shaped cells (C). Simulation snapshots (B, D) for each case confirm the existence of both complete (1,2) and partial (3,4) perfusion regimes as predicted in Figure 7.5. Surprisingly, simulations with rod-shaped cells (A,B) show very similar behaviour to those using coccal cells (C,D). Sample of 5 simulations per case, showing similar overall behaviour to that predicted.

In Figure 7.6-B, Box 2, we see a large group of blue producer cells enveloped in a plume of toxin. Within this group are several small S groups in the process of being cut off from the upper surface of the biofilm (black arrows). These groups are too small to effect rapid toxin removal, and so end up completely inhibited by the high toxin concentrations. Conversely, on the right-hand side of the image we see large groups of S cells that have out-grown smaller groups of P cells (white arrows), which have been unable to produce sufficient toxin to inhibit their competitors. It appears, then, that partial perfusion conditions can increase genetic segregation in biofilms, overwhelming small cell groups whilst preserving larger ones.

Surprisingly however, we found that, when subjected to the same analysis, biofilms composed of rod-shaped cells performed very similarly, producing a virtually-identical outcome matrix (Figure 7.6-C). Likewise, we observed analogous partial perfusion behaviours for the same parameter combinations (Figure 7.6-D). We suggest that this similarity is due to the selection for large group sizes discussed above: the fractal-like patterning seen at the boundaries between rod-shaped groups is lost, because the small and isolated cell groups produced by interdigitation are either inhibited (S surrounded by P) or outgrown (P surrounded by S). Consequently, inter-strain boundaries end up having similar patterning irrespective of cell shape.

7.3.4 Lengthscale analysis

Finally, we sought to explain the behaviour of the extended model, and to create a more quantitative description of the transition between its different outcomes, as observed above. Dimensional analysis of model spatial scales is a powerful analytical tool, often used alongside individual-based modelling [199, 43, 197]. Accordingly, we devised a method of lengthscale analysis to characterise the spatial scales on which different model processes operate.

In Chapter 4, we discussed how Damköhler numbers may be defined both in terms of timescale ratios (the relative timescales of solute diffusion and reaction, $\tau_{\text{diffusion}}$ and τ_{reaction}), or in terms of lengthscale ratios. In the latter case, a given Damköhler number $\mathscr{D}$ may be written as

$$\mathscr{D} = \frac{l^2}{\mathscr{L}^2}, \tag{7.22}$$

where $\mathscr{L}$ is a lengthscale on which solute concentrations change significantly due to reaction and diffusion, relative to the reference concentration used to define $\mathscr{D}$. l is the reference length against which $\mathscr{D}$ is scaled.

In the same way, the two toxin Damköhler numbers, $\mathscr{D}_{T,\text{prod}}$ and $\mathscr{D}_{T,\text{rem}}$, each describe lengthscales over which toxin gradients develop. We can therefore associate each toxin reaction with a characteristic gradient lengthscale $\mathscr{L}$, and write

$$\mathscr{L}_{T,\text{prod}} = \frac{l}{\sqrt{\mathscr{D}_{R,\text{prod}}}} = \sqrt{\frac{D_T K_I}{f \alpha_T \rho \mu_{\max}}}, \tag{7.23}$$

$$\mathscr{L}_{T,\text{rem}} = \frac{l}{\sqrt{\mathscr{D}_{R,\text{rem}}}} = \sqrt{\frac{D_T K_I}{\beta_T \rho \nu_{\max}}}. \tag{7.24}$$

Since we use $l = 1\,\mu\text{m}$, $\mathscr{L}_{T,\text{prod}}$ and $\mathscr{L}_{T,\text{rem}}$ correspond to gradient lengthscales in units of microns – that is, lengthscales over which toxin concentrations vary significantly relative to the reference concentration K_I, due to the toxin production and removal reactions respectively.

The crux of our analysis here is to compare these gradients to other lengthscales characterising structural elements of the biofilm. Here we highlight two important lengthscales, viz:

1. The vertical **system size** $\ell_{\text{sys}} = \max(p_z) + \delta \approx 80\,\mu\text{m}$. ℓ_{sys} controls the distance between the substratum and the bulk phase above the biofilm, and so adjusts the rate at which toxin is removed from the domain by the bulk liquid.

2. The **group size** ℓ_{group}, corresponding to half of the width of a isoclonal group of cells in the biofilm. In the fixed cell configurations shown in Figure 7.5-C, for example, there are 16 cell groups of alternating type arranged along the domain base (length $L_x = 200\,\mu\text{m}$) and so $\ell_{group} = 0.5 \times 200/16 \approx 6\,\mu\text{m}$.

To compare toxin gradient lengthscales $\mathscr{L}_{T,\text{prod}}$ and $\mathscr{L}_{T,\text{rem}}$ with biofilm lengthscales ℓ_{sys} and ℓ_{group}, we return to the fixed-configuration parameter sweeps described in Section 7.3.2. The results of this comparison are shown in Figure 7.7.

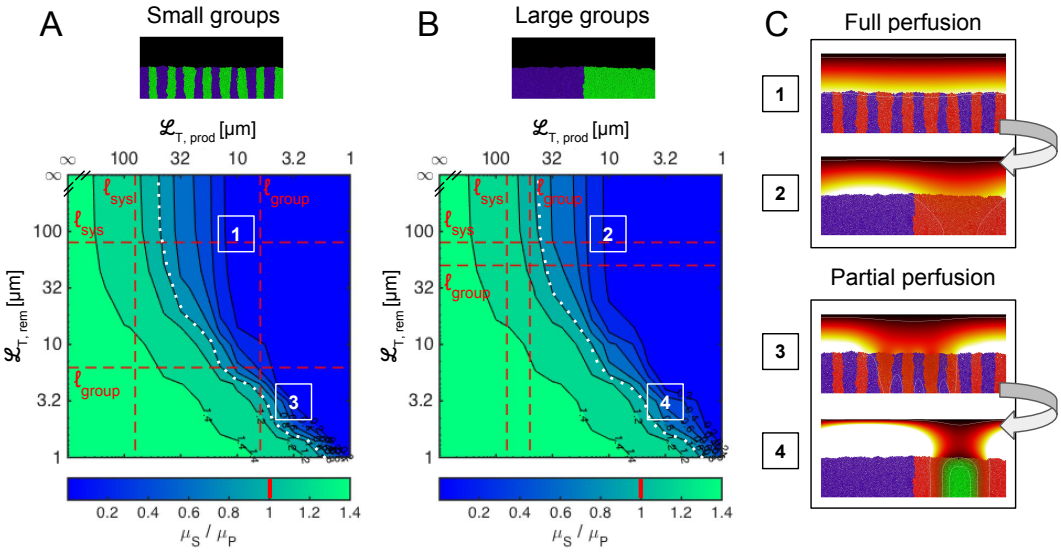

Fig. 7.7 Analysis of lengthscales rationalises transitions between different model behaviours. A: a higher-resolution repeat of the parameter sweep shown in Figure 6-B, plotted as contour map, shows mean strain growth rate ratios (μ_S/μ_P) as a function of toxin production and removal lengthscales, $\mathscr{L}_{\text{prod}}$ and $\mathscr{L}_{\text{rem}}$. These lengthscales can be compared against the system size ℓ_{sys} and the cell group size ℓ_{group} (dashed red lines): toxin degradation by S cells becomes significant when $\mathscr{L}_{\text{rem}} < \ell_{\text{sys}}$, and perfusion becomes incomplete when $\mathscr{L}_{\text{prod}} \approx \mathscr{L}_{\text{rem}} < \ell_{\text{group}}$. The contour $\mu_S = \mu_P$ (dotted white line) marks the transition between S cells winning and P cells winning. B: drawing the same plot for cell configurations with larger group sizes increases ℓ_{group}. C: configuration snapshots compare parameter combinations in which increasing ℓ_{group} maintains full toxin perfusion (1,2) or produces partial perfusion (3,4). Sweep of 100 parameter combinations, with 5 configurations tested per case.

Figure 7.7-A shows a high-resolution repeat of the parameter sweep described in Figure 7.5-B, in which both toxin production and removal Damköhler numbers have been varied independently in the sequence $[0, 1\times10^{-4},\ 5\times10^{-4}, 1\times10^{-3}\ldots5\times10^{-1}, 1]$,

testing 100 parameter combinations in total. For each parameter combination, we solved the extended model toxin PDE (Equation (7.19)) as before, for the same set of 5 fixed cell configurations, and again measured the mean strain growth rate ratio μ_S/μ_P in each case. This time however, we plot these measurements as a shaded contour map, and label the plot axes with the gradient lengthscales $\mathscr{L}$ to which each Damköhler number corresponds (Equations (7.23) and (7.24)). We also annotate the plot with lines (Figure 7.7-A, dashed red lines) marking the fixed lengths ℓ_{sys} and ℓ_{group}, and highlight the 'critical' contour $\mu_S/\mu_P = 1$ (Figure 7.7-A, dotted white line).

We can use the resulting diagram to rationalise the observed behaviour of the extended Bucci model, as follows. Firstly, in the region towards the top of Figure 7.7-A, where $\mathscr{L}_{T,\text{rem}} > \ell_{\text{sys}}$, toxin removal by the bulk liquid predominates toxin removal by S cells. Consequently, the behaviour of the system is independent of the value of $\mathscr{L}_{T,\text{rem}}$, and the $\mu_S = \mu_P$ contour is approximately vertical. We identify this region as representing Bucci's original model: here, toxin removal by S cells is negligible, and the success of P cells is predicted by comparing ℓ_{sys} with $\mathscr{L}_{T,\text{prod}}$. If $\mathscr{L}_{T,\text{prod}} < \ell_{\text{sys}}$, toxin accumulates significantly (i.e. such that $\bar{u}_T \approx 1$) within the biofilm, and S-cell growth is effectively inhibited. We note that the position of the critical contour corroborates this predicted transition point.

Secondly, where $\mathscr{L}_{T,\text{rem}} < \ell_{\text{sys}}$ toxin removal by S cells becomes significant, so that both $\mathscr{L}_{T,\text{prod}}$ and $\mathscr{L}_{T,\text{rem}}$ (i.e. both $\mathscr{D}_{T,\text{prod}}$ and $\mathscr{D}_{T,\text{rem}}$) control relative cell growth rates. Thus, below the horizontal ℓ_{sys} line, the critical contour (Figure 7.7-A, white dotted line) transitions from being vertical to diagonal. In this regime, the metric L_{bac} [43] (Equation (7.11)) is no longer representative of the critical bacteriocin range. To demonstrate this, we note that L_{bac} is inversely proportional to toxin diffusivity D_T. According to Equations (7.23) and (7.24), decreasing toxin diffusivity is equivalent to simultaneously decreasing both $\mathscr{L}_{T,\text{prod}}$ and $\mathscr{L}_{T,\text{rem}}$, i.e. to moving diagonally downwards on Figure 7.7-A. However, if $\mathscr{L}_{T,\text{rem}} < \ell_{\text{sys}}$, relative growth rates become

diagonally invariant, and changes to toxin diffusivity have no effect on bacteriocin performance.

Thirdly, we can identify the conditions necessary to produce partial toxin perfusion, by comparing toxin gradient lengthscales with the cell group size ℓ_{group}. When $\mathscr{L}_{T,\text{prod}} \approx \mathscr{L}_{T,\text{rem}} < \ell_{\text{group}}$ (bottom right of Figure 7.7-A), rapid toxin production is balanced by rapid toxin removal, such that toxin concentrations change rapidly within length ℓ_{group}. Under these circumstances, cells at the edge of an S-cell group experience high toxin concentrations and are strongly inhibited, whereas cells towards the centre of the group are able to grow maximally.

We demonstrate this point further in Figure 7.7-B, which shows a repeat of the same parameter sweep performed with cell configurations of a larger group size ($\ell_{\text{group}} \approx 50\,\mu\text{m}$; a visual comparison of the configurations is provided at the top of Figure 7). Additionally, snapshots comparing toxin and cell growth distributions are shown in Figure 7.7-C, both for the small-group (Boxes 1, 3) and large-group scenario (2, 4). The parameter combinations used to produce each snapshot are marked on the maps in Figures 7.7-A and 7.7-B, and are the same for pairs (1, 2) and (3, 4). The parameter map in Figure 7.7-B has a similar overall appearance to that shown in Figure 7.7-A (since ℓ_{sys} is unchanged). Changing the size of the cell groups has no discernible effect when $\mathscr{L}_{T,\text{prod}},\ \mathscr{L}_{T,\text{rem}} > \ell_{\text{group}}$, as shown in Figure 7.7-C, Cases 1 and 2. However, we see that when $\mathscr{L}_{T,\text{prod}},\ \mathscr{L}_{T,\text{rem}} < \ell_{\text{group}}$, increasing the group size turns a full toxin perfusion into partial perfusion (Figure 7.7-C, Cases 3 and 4).

7.4 Discussion

In this chapter, we have used individual-based simulations and analysis to investigate the effects of cell shape on microbial warfare (interference competition), mediated through diffusing bacteriocin toxins. Using an existing model of bacteriocin production (Bucci's model [43]), we compared biofilm communities grown using different cell

shapes, for different toxin production and nutrient supply regimes. We proposed an extension to this model that includes toxin degradation, predicting new regimes in which toxin range is spatially limited, and no longer described by the lengthscale L_{bac} proposed previously [43]. We have also devised a method of lengthscale analysis that predicts transitions in model behaviour.

Overall, we found that shape can affect the dynamics of interference competition under nutrient-limited conditions, by modulating the transition from smooth to branched colony morphologies. In agreement with our observations in Chapter 6, longer cell shapes produced more branching under the conditions we tested, separating producer and sensitive strains in space, and suppressing toxin production through nutrient capture. However, we find that shape does little to change the effectiveness of toxin production in the absence of nutrient limitations—even when toxin range is limited through removal—in spite of our predictions based on shape-based control of spatial patterning.

We suggest that this is because regimes which limit toxin effect to the boundaries between strains also inhibit the cellular growth normally responsible for fractal patterning, and so cancel out the effects of cell shape. An interesting possibility here is that, if short-ranged secretions were to increase the growth rates of target cells instead of reducing them (e.g. replacing bacteriocin with some a metabolic enzyme [199]), then this might actually enhance spatial mixing, and amplify the effects of shape-driven patterning. Indeed, previous individual-based studies have examined cross-feeding relationships in this way, and found that they lead to increased inter-strain mixing [87].

Aside from the issue of cell shape, the inclusion of toxin degradation could also have a strong influence on community structure and stability. Our observations suggest that short-ranged toxin activity leads to lineage demixing, avoiding the well-mixed communities that favour toxin production, whilst keeping faster-growing non-producers in check through local inhibition. In agreement with recent studies looking at short-ranged inhibition [182], this effect could be characterised further by extending our

modelling to multi-strain biofilms, and repeating the strain diversity measurements reported by Bucci *et al*. in the presence of fast toxin removal [43].

Although it is ultimately a simplification of Bucci's model, our implementation still embodies a lot of complexity that we have yet to fully characterise, because of the intricate coupling between community spatial structure, nutrient availability and toxin perfusion. Including toxin removal in this system adds a new dimension to this complexity, and while our lengthscale analyses go some way to predicting model behaviours when toxin properties are varied, it is important that we also test the model's sensitivity to other parameters, such as the initial cell density and ratio.

In the future, our model could also be used to describe and compare alternative forms of interference competition. As noted in the introduction, microbes wage war with a variety of different weapons, of which bacteriocins are but one example [64]. Whereas bacteriocins can inhibit cells over a wide area when produced *en masse* [52], other common weapons, such as the type-VI secretory system, operate on very short lengthscales. By describing the dynamics of interference competition waged on both long and short spatial scales, our extended model could serve to characterise and compare the physical and ecological conditions in which each strategy is most effective.

7.5 Conclusions

Despite being very common in microbial communities, interference competition is comparatively understudied and poorly understood compared with more positive social interactions. In this chapter, we have applied our individual-based framework to examine the potential role of cell shape in interference competition, mediated through diffusible bacteriocin toxins. By implementing, analysing and extending an existing model of bacteriocin production, we find that cell shape can affect the selection for bacteriocin production when nutrient supplies are limiting, by controlling transitions

between smooth and branched biofilm morphologies. Although we find that the contrasting spatial patterns controlled by cell shape do not affect bacteriocin competition, we argue that the short-ranged toxin interactions produced by our extended model are an interesting phenomenon in their own right, and suggest directions for their future study.

8

Discussion and conclusions

This concluding chapter aims to integrate the work presented in this thesis, examining its significance and impact. We begin by summarising the achievements and findings of our methodology (Chapters 3 and 4) and application chapters (Chapters 5, 6 and 7), before discussing common themes and general conclusions. We comment on the strengths and limitations of our approach, and suggest directions for future research.

8.1 Key findings and achievements

Chapter 3. *Individual-based modelling of biomechanical interactions in a microbial community*

- Individual-based modelling is a powerful and well-established method for studying the development of microbial communities. Most community individual-based models (IbMs) omit non-spherical cell shapes, but recently several methods and representations have emerged that allow their inclusion.
- Of these, we identify the model of Rudge *et al.* [239] as a verified, high-performance framework, capable of modelling different shapes. We describe its formulation and implementation as the open-source software CellModeller.

- To enable the simulation of mixed-shape communities, we implement extensions to CellModeller. We add periodic boundary conditions to limit edge artifacts, and devise growth schemes for growing cells of different shapes at the same rate.

Chapter 4. *Creating a hybrid model of biofilm development*

- Diffusing chemicals mediate many important interactions in microbial communities. CellModeller provides a detailed picture of cell-cell mechanical interactions, but is unable to simulate interactions between cells through chemical solutes. In this chapter, we devise an extension to CellModeller that couples cells' growth rates to their local chemical environment, creating a continuum-discrete (hybrid) model in the style of previous studies.

- We base this extension on established models of cell-solute interactions: focussing on the case of nutrient-limited growth, we show how to solve reaction-diffusion equations using an iterated finite element method, and use dimensional analysis to identify parameter clusters controlling the model.

- We implement this solute transport model using the open-source finite element modelling library FEniCS. We perform parameter sweeps and convergence tests with our implementation, and establish numerical parameters for computing solute fields.

- Overall, the resulting hybrid model combines the mechanically-detailed CellModeller software with a flexible system for solving reaction-diffusion equations (The FEniCS library), joined using a custom Python interface. This framework allows us to vary cell shape as a model parameter, enabling comparative studies of cell shape in a microbial community.

Chapter 5. *Cell shape: a new determinant of spatial patterning in biofilms*

- This chapter contains the primary results of the thesis, recently published in Smith *et al*. [259]. Here we show the first application of our hybrid framework, examining the ways in which cell shape can alter spatial patterning and structure in a dense biofilm community.

- Individual-based modelling predicts that cell shape modulates spatial patterning in microbial communities. In particular, mixed-shape communities produce emergent layered structures, altering cell fitness by changing strains' access to rate-limiting nutrients. Long shapes dominate the colony base and edges, whereas shorter cells rise to the top of the biofilm. Our model also recapitulates the results of previous studies, showing that longer cells produce fractal-like interdigitations between neighbouring cell lineages.

- Further model tests allow the mechanisms of layering and shape-driven patterning to be investigated. We argue that layering is a collective phenomenon produced through the mechanical interaction of groups of differently-shaped cells. Directed by a solid surface, groups of rod-shaped cells grow concertedly along the base of a community, pushing rounder cells upward. These effects appear in both 2-D and 3-D simulations, and are robust to changes in simulation parameters.

- Experimental tests using colonies of differently-shaped *Esherichia coli* bacteria confirm both patterning and layering predictions, and demonstrate a novel route for comparing communities of different shapes *in vitro*. Overall, this establishes a link between cell shape and fitness in dense communities, suggesting a functional value for shapes in collectives.

Chapter 6. *Antibiotic-induced filamentation and its effects in bacterial colonies*

- Bacterial filamentation (elongation) is a common example of morphological change in response to environmental stress. Here we demonstrate the use of our model framework in conjunction with an existing experimental system, used to study competition between antibiotic-resistant and antibiotic-sensitive cells in colonies. We report experiments showing that antibiotic-sensitive bacteria become filamentous in response to antibiotic exposure – but that following this elongation, they appear to actually outcompete resistant cells.

- We devise two models of nutrient-limited growth at the colony edge. These models predict that cell elongation is advantageous, providing cells with a means to congregate at the colony edge ('edge enrichment') where nutrients are most abundant. This demonstrates a second mechanism through which cell shape can affect community morphology – by modulating the stability of the colony front in the presence of steep nutrient gradients.

- Our models can be also used to devise and compare alternative explanations of patterning at the edge of colonies. We propose an alternative model for edge enrichment based on small growth rate advantages for antibiotic-sensitive cells, which we cannot rule out owing to the complexity of the experimental system.

- Overall however, the body of circumstantial evidence points to cell shape *per se* as the root of the enrichment effect. This in turn suggests that filamentation may be more than a passive by-product of the bacterial damage-control response, conferring an active advantage in the presence of strong nutrient competition.

Chapter 7. *Cell shape and microbial warfare via toxin secretion*

- Stiff ecological competition is a hallmark of microbial communities. In this study, we extend our modelling framework to simulate interference competition, with rival strains actively harming one another using diffusing toxins (bacteriocins).

- We implement an existing model (the Bucci model [43]) of bacteriocin production and use it to simulate interference competition in biofilms composed of different cell shapes. We show that shape can affect the favorability of toxin production under limited nutrient conditions through control of biofilm branching. This demonstrates that the branching effect reported in Chapter 6 has direct consequences in mediating social interactions in a community.

- We also propose an extended version of the Bucci model that accounts for toxin removal, through reaction or degradation. These processes can limit the effective range of a toxin, so that its activity is confined to boundaries between rival cell groups. We propose a system of lengthscale analysis, which rationalises transitions in the extended model's behaviour, and defines its relationship to the original Bucci model.

- Our preliminary data suggest that shape-driven patterning alone does not significantly influence the effectiveness of bacteriocin production, in spite of our predictions that it would do so through control of inter-strain mixing. Further work is needed to verify the robustness of this result under different simulation conditions.

8.2 Thesis evaluation

Having summarised the key findings of the thesis, it is instructive to revisit the research questions that we set out in Chapter 2. Broadly speaking, these can be expressed as two interrelated questions: a) [how] does microbial shape affect a community, and b) [how] do communities influence microbial shape? Here we use our findings to address these questions, and comment on their impact for the scientific community.

8.2.1 The influences of microbial shape

To address the first question: our work shows that microbial shape can influence community spatial structure, through several different mechanisms. In addition to recapitulating the nematic ordering [276] and fractal patterning effects [238] associated with polar cells, we have identified two additional mechanisms through which shape can influence the spatial arrangement of cells in a community. Briefly, these are a) the layering effect, in which groups of longer cells burrow beneath shorter cells (Chapter 5, [259]) and b) the branching effect, in which longer cells branch away from a growing community front through chemico-physical feedback (Chapters 6 and 7).

Of these shape-driven processes, we show direct experimental evidence of the layering effect in colonies of *E. coli* bacteria, and circumstantial evidence for the branching effect in competition experiments using *P. aeruginosa*. Both layered and branched architectures are well-known in multispecies communities [36, 285, 192, 199, 28], but were not previously thought to be dependent upon cell shape. Although the two mechanisms are distinct, they ultimately stem from the same fundamental phenomenon: the preservation of orientational order in groups of longer cells, and the loss of orientational order in groups of shorter cells – which itself has been confirmed both theoretically and experimentally [276, 35, 80].

What is the significance of spatial structure produced by shape? The arrangement of microbes in a community is important, because it affects their interactions both with

their surroundings [286], and with one another [43, 198]. Consequently, the spatial patterns produced by different cell shapes can alter relative strain growth rates and biological fitness. By controlling their positions in a community, shape allows groups of microbes to secure better access to rate-limiting resources,[1] and could serve to protect vulnerable cells from attack [43] or exploitation [199].

These results call for a reevaluation of our understanding of community morphogenesis. Conventionally, chemical and biological factors are seen as the major factors governing the development of community spatial structure [287, 115, 116, 28, 87, 189]. While these factors are far from unimportant, our findings emphasise the substantial influence that mechanical interactions exert on community architecture, and how phenotypic changes at the cellular scale can have far-reaching implications. In this perspective, our work stands among numerous recent studies demonstrating the importance of mechanical forces for the emergence of spatial structure [296, 88, 8, 144, 249, 80, 259].

8.2.2 Shaping evolution

So, cell shape can indeed affect microbial communities. Having answered the first of our research questions, it is interesting to speculate on the second question: how do communities affect microbial shape? Having established relationships between fitness and morphology on the timescale of community growth, we can in turn infer that community environments may select for certain morphologies on the timescale of microbial evolution.

How did microbial shape evolve? A current view in microbiology rationalises the different shapes displayed by microorganisms in terms of functions at the individual cell level [300]. In this model, particular shapes are adaptive because they improve individuals' abilities to perform particular tasks, such as absorbing more nutrients, or

[1] Note that nutrient access is one of several possible couplings between cell positioning and fitness: for example, if antibiotic agents were sprayed onto a biofilm, cells in the upper regions of the community would experience the highest antibiotic concentrations, and suffer the most harm [51]. The value of a particular position depends upon the nature of the external environment.

swimming more efficiently [300, 301]. Our findings offer an extension to this view, suggesting that particular shapes may be selected for because of the ordering effects they produce at the community level. Moreover, the significance of the community mode of life—as summarised in Chapter 1—suggests that collective-level fitness effects exert a strong influence on the evolution of microbial shape.[2]

Finally, our findings show that different shapes can convey growth advantages in different contexts. Despite having only considered a very limited (yet still biologically relevant [301]) range of shapes, we find that there is no 'one-shape-fits-all' morphology offering the best result in every community context. In a biofilm growing *in situ*, adopting a coccal morphology might prove advantageous; when competing at the edge of a community, cell elongation could be more beneficial. Since different scenarios select for different shapes, there may be a strong selection for microbes to actively regulate their morphology. This could explain the evolution of the microbial pleiotropy: the tendency for certain microbes to modify their shapes in response to changes in environmental conditions [257, 21]. In short, communities may select for the ability to vary shape, as well as for particular shapes *per se*.

8.2.3 Impact summary

Shape is often regarded as a passive and incidental property of a microbial species, secondary to other considerations such as metabolism and genetics [300, 301, 158]. Our findings demonstrate that the impact of shape in multispecies communities needs to be critically reexamined, as it has the potential to actively alter community dynamics and composition. This is a particularly important message to communicate given that many laboratory models of multispecies communities now involve the co-culture of differently-shaped microbes [298, 57, 262, 204]. While cell shape will not in practice

[2]For instance, phylogenetic studies show that coccal cell morphologies have evolved independently many times [258, 270, 158], and the layering effects we have demonstrated could go some way in explaining this apparent selection.

always matter, this thesis demonstrates that it *can* be important, and its implications in existing experimental and theoretical systems therefore need to be addressed. Now that we know more of shape's significance, the computational and experimental tools developed in this thesis can be used by the wider community, to extend our understanding of shape further.

8.3 Future directions

Here we make some recommendations for future investigation into the community effects of microbial shape.

8.3.1 Model limitations and extensions

Individual-based modelling has provided insight into the emergent effects of cell shape in communities. However, we should be mindful of the limitations of these models, and of aspects of their behaviour that we have yet to fully characterise.

The findings presented in this thesis prompt a number of further questions about cell shape, some of which could be addressed using the model in its current form. For example, in Chapter 5 we showed that coccal cells layer on top of rod-shaped cells, but not on top of similar coccal cells. This suggests that the degree of layering, and its associated fitness benefits, depends on the relative frequencies of different cell shapes. It would be interesting to investigate how shape-driven layering varies with the initial ratio of cell shapes, and the presence of additional shapes and species influence patterning in non-binary (multispecies) communities [191].

There is also ample scope for altering our model, and testing it against other approaches. Two ways forward present themselves here, with two separate motivations. Firstly, as we have discussed previously, there are many features of real microbial communities that our model omits. Including some of these details will help establish how robust

our findings are in the presence of additional processes and interactions, which might reinforce or interfere with phenomena driven by shape. For example, previous studies have shown that EPS secretion [252, 103] and modulation of cell adhesivity [249, 267] can also influence community spatial structure. It is important to determine how these effects—included either through further modifications to CellModeller or through use of other frameworks [88, 267]—interact with shape-driven effects.

The second obvious direction for model change is simplification, motivated by the desire to better understand the mechanisms of shape-driven phenomena. Individual-based approaches can be instructive [197], but also generate large levels of complexity very rapidly. This can make their operation cumbersome and their interpretation ambiguous, compared with simpler, analytical models [135, 108]. Constructing parsimonious models of the novel patterning processes reported in this thesis—shape-driven layering and branching—could offer further insight, helping to isolate the exact physical parameters governing these processes. Approaches based on adapting continuum nematodynamics models [110], used previously to describe microbial shape effects [276, 35], could prove helpful here.

8.3.2 Further influences of cell shape

While this thesis has highlighted some of the ways in which cell shape can influence microbial communities, our work is by no means exhaustive. Shape may yet have further consequences in cell collectives, by modulating community processes and properties in ways we have yet to consider.

In Chapter 7 we concluded that shape-driven patterning did not have a strong influence on interference competition mediated through diffusing toxins – yet other forms of microbial weaponry may prove more sensitive to cell shape. For example, the bacterial T6SS (Type-VI Secretion System)—a molecular machine consisting of a spring-loaded needle [107]—is a very short-ranged weapon, requiring target and producer cells to

be immediately adjacent in order to be effective [13, 12]. Because shape affects the packing arrangements of microbes at high cell densities, the effectiveness of this weapon may then vary with cell morphology. Likewise, bacterial conjugation (transfer of genetic material through cell-cell contact) might display a similar dependency, so that cell shape affects rate of horizontal gene transfer through a community [183, 96]. Additionally, as we noted in Chapter 4, our reaction-diffusion model assumes that cell shape has no effect on solute transport. However, this simplification is unlikely to be true: long cell shapes produce local nematic cell alignment [276], potentially making diffusion in the direction of alignment faster than in other directions. This coupling between media anisotropy and solute transport forms the basis for technologies such as diffusion MRI (Magnetic Resonance Imaging) [132], and previous studies have demonstrated its effects in communities grown in microchambers [56]. An interesting extension to our work, therefore, would be to couple solute diffusion tensors to a metric of local cell alignment, and thereby investigate how solute perfusion varies with cell shape.

Finally, while models can always be simplified or made more complex, they can never be made complete. As the adage goes, 'All models are wrong, but some are useful' [34] – and models are useful insofar as they make interesting and testable predictions. By this metric, our modelling has proven useful – generating unexpected predictions, stimulating new experiments, and expanding our understanding of cell shape as a whole. In spite of its various shortcomings, the general agreement between our model, previous observations, and our own experiments, justifies this approach overall.

8.4 Summary

Microbial communities are ubiquitous, and often contain cells of different shapes – yet to date we know little of the influences of cell shape in this context. In this thesis, we have studied the effects of cell shape in dual-strain communities. Using

individual-based modelling, we have performed systematic comparisons of cell shape effects in biofilms and colonies. Supported by experimental tests, our work predicts and characterises novel mechanisms of self-organisation, demonstrating that shape itself can actively affect the physical, chemical and biological properties of microbial communities. Overall, these findings transform current views of the effects, function and evolution of cell shape.

References

[1] Abrudan, M. I., Brown, S., and Rozen, D. E. (2012). Killing as means of promoting biodiversity. *Biochem. Soc. Trans.*, 40(6):1512–6.

[2] Abrudan, M. I., Smakman, F., Grimbergen, A. J., Westhoff, S., Miller, E. L., van Wezel, G. P., and Rozen, D. E. (2015). Socially mediated induction and suppression of antibiosis during bacterial coexistence. *Proc. Natl. Acad. Sci. U. S. A.*, 112(35):11054–11059.

[3] Alexander, P. and Lundgren, H. P. (2014). *A laboratory manual of analytical methods of protein chemistry*, volume 4. Elsevier.

[4] Allen, M. P., Evans, G. T., Frenkel, D., and Mulder, B. M. (1993). Hard Convex Body Fluids. *Adv. Chem. Phys.*, 86:1–166.

[5] Alnæs, M. S., Blechta, J., Hake, J., Johansson, A., Kehlet, B., Logg, A., Richardson, C., Ring, J., Rognes, E., and Wells, G. N. (2015). The FEniCS Project Version 1.5. *Arch. Numer. Softw.*, 3(100):9–23.

[6] Alpkvist, E., Alpkvista, E., and Klapper, I. (2007). A multidimensional multispecies continuum model for heterogeneous biofilm development. *Bull. Math. Biol.*, 69(2):765–89.

[7] Alpkvist, E., Picioreanu, C., Loosdrecht, M. C. M. V., and Heyden, A. (2006). Three-Dimensional Biofilm Model With Individual Cells and Continuum EPS Matrix. *Biotechnol. Bioeng.*, 94(5):961–979.

[8] Asally, M., Kittisopikul, M., Rué, P., Du, Y., Hu, Z., Çağatay, T., Robinson, A. B., Lu, H., Garcia-Ojalvo, J., and Süel, G. M. (2012). Localized cell death focuses mechanical forces during 3D patterning in a biofilm. *Proc. Natl. Acad. Sci. U. S. A.*, 109(46):18891–6.

[9] Baba, T. and Schneewind, O. (1998). Instruments of microbial warfare: Bacteriocin synthesis, toxicity and immunity. *Trends Microbiol.*, 6(2):66–71.

[10] Bakaletz, L. O. (2007). Bacterial Biofilms in Otitis Media: Evidence and Relevance. *Pediatr. Infect. Dis. J.*, 26(10):1–6.

[11] Basan, M., Elgeti, J., Hannezo, E., Rappel, W.-J., and Levine, H. (2013). Alignment of cellular motility forces with tissue flow as a mechanism for efficient wound healing. *Proc. Natl. Acad. Sci. U. S. A.*, 110(7):2452–2459.

[12] Basler, M., Ho, B. T., and Mekalanos, J. J. (2013). Tit-for-Tat: Type VI Secretion System Counterattack during Bacterial Cell-Cell Interactions. *Cell*, 152(4):884–894.

[13] Basler, M. and Mekalanos, J. J. (2012). Type 6 secretion dynamics within and between bacterial cells. *Science*, 337(6096):815.

[14] Bastos, M. d. C. d. F., Coelho, M. L. í. V., and Santos, O. C. a. d. S. (2015). Resistance to bacteriocins produced by Gram-positive bacteria. *Microbiology*, 161(2015):683–700.

[15] Bayer, E. A., Morag, E., and Lamed, R. (1994). The cellulosome - A treasure-trove for biotechnology. *Trends Biotechnol.*, 12(9):379–386.

[16] Bayley, H. and Cremer, P. S. (2001). Stochastic sensors inspired by biology. *Nature*, 413(6852):226–230.

[17] Be'er, A., Zhang, H. P., Florin, E.-L., Payne, S. M., Ben-Jacob, E., and Swinney, H. L. (2009). Deadly competition between sibling bacterial colonies. *Proc. Natl. Acad. Sci. U. S. A.*, 106(2):428–433.

[18] Begg, K. J. and Donachie, W. D. (1998). Division Planes Alternate in Spherical Cells of Escherichia coli Division Planes Alternate in Spherical Cells of Escherichia coli. *J. Bacteriol.*, 180(9):2564–2567.

[19] Bengmark, S. (2013). Gut microbiota, immune development and function. *Pharmacol. Res.*, 69(1):87–113.

[20] Berg, H. C. and Turner, L. (1979). Movement of microorganisms in viscous environments.

[21] Bergkessel, M., Basta, D. W., and Newman, D. K. (2016). The physiology of growth arrest: uniting molecular and environmental microbiology. *Nat. Rev. Microbiol.*, 14(9):549–562.

[22] Berry, D., Stecher, B., Schintlmeister, A., Reichert, J., Brugiroux, S., Wild, B., Wanek, W., Richter, A., Rauch, I., Decker, T., Loy, A., and Wagner, M. (2013). Host-compound foraging by intestinal microbiota revealed by single-cell stable isotope probing. *Proc. Natl. Acad. Sci. U. S. A.*, 110(12):4720–4725.

[23] Beveridge, T. J., Lawrence, J. R., and Murray, R. G. (2007). Sampling and staining for light microscopy. In *Methods for General and Molecular Microbiology, Third Edition*, pages 19–33. American Society of Microbiology.

[24] Bi, E. and Lutkenhaus, J. (1993). Cell division inhibitors SulA and MinCD prevent formation of the FtsZ ring. *J. Bacteriol.*, 175(4):1118–1125.

[25] Bjarnsholt, T. (2013). The role of bacterial biofilms in chronic infections. *APMIS. Suppl.*, 121(136):1–51.

[26] Blanchard, A. E. and Lu, T. (2015). Bacterial social interactions drive the emergence of differential spatial colony structures. *BMC Syst. Biol.*, 9:59.

[27] Blázquez, J., Gómez-Gómez, J.-M., Oliver, A., Juan, C., Kapur, V., and Martín, S. (2006). Pbp3 inhibition elicits adaptive responses in pseudomonas aeruginosa. *Molecular microbiology*, 62(1):84–99.

[28] Bonachela, J. a., Nadell, C. D., Xavier, J. B., and Levin, S. a. (2011). Universality in Bacterial Colonies. *J. Stat. Phys.*, 144(2):303–315.

[29] Borenstein, D. B. (2015). A multi-agent approach to the evolution of microbial populations in the presence of spatially structured social interaction. (June).

[30] Borenstein, D. B., Meir, Y., Shaevitz, J. W., and Wingreen, N. S. (2013). Non-Local Interaction via Diffusible Resource Prevents Coexistence of Cooperators and Cheaters in a Lattice Model. *PLoS One*, 8(5).

[31] Borenstein, D. B., Ringel, P., Basler, M., and Wingreen, N. S. (2015). Established Microbial Colonies Can Survive Type VI Secretion Assault. *PLoS Comput. Biol.*, 11(10):1–16.

[32] Bossi, L., Fuentes, J. a., Mora, G., and Figueroa-bossi, N. (2003). Prophage Contribution to Bacterial Population Dynamics Prophage Contribution to Bacterial Population Dynamics. *J. Bacteriol.*, 185(21):6467–6471.

[33] Bottery, M. J., Wood, A. J., and Brockhurst, M. A. (2016). Selective conditions for a multidrug resistance plasmid depend on the sociality of antibiotic resistance. *Antimicrob. Agents Chemother.*, 60(4):2524–2527.

[34] Box, G. E. (1979). Robustness in the strategy of scientific model building. *Robustness in statistics*, 1:201–236.

[35] Boyer, D., Mather, W., Mondragón-Palomino, O., Orozco-Fuentes, S., Danino, T., Hasty, J., and Tsimring, L. S. (2011). Buckling instability in ordered bacterial colonies. *Phys. Biol.*, 8(2):026008.

[36] Brenner, K. and Arnold, F. H. (2011). Self-organization, layered structure, and aggregation enhance persistence of a synthetic biofilm consortium. *PLoS One*, 6(2):1–7.

[37] Brenner, S. and Scott, R. (2007). *The mathematical theory of finite element methods*, volume 15. Springer Science & Business Media.

[38] Bressloff, P. C. and Newby, J. M. (2013). Stochastic models of intracellular transport. *Rev. Mod. Phys.*, 85(1):135–196.

[39] Brodie, E. L., DeSantis, T. Z., Parker, J. P. M., Zubietta, I. X., Piceno, Y. M., and Andersen, G. L. (2007). Urban aerosols harbor diverse and dynamic bacterial populations. *Proc. Natl. Acad. Sci. U. S. A.*, 104(1):299–304.

[40] Brown, S. P., Le Chat, L., De Paepe, M., and Taddei, F. (2006). Ecology of Microbial Invasions: Amplification Allows Virus Carriers to Invade More Rapidly When Rare. *Curr. Biol.*, 16(20):2048–2052.

[41] Brüssow, H. (2007). Bacteria between protists and phages: From antipredation strategies to the evolution of pathogenicity. *Mol. Microbiol.*, 65(3):583–589.

[42] Bryan, L. (2012). *Antimicrobial drug resistance*. Elsevier.

[43] Bucci, V., Nadell, C. D., and Xavier, J. B. (2011). The Evolution of Bacteriocin Production in Bacterial Biofilms. *Am. Nat.*, 178(6):E162–E173.

[44] Bucci, V. and Xavier, J. B. (2014). Towards predictive models of the human gut microbiome. *J. Mol. Biol.*, 426(23):3907–3916.

[45] Burns, R. C. and Hardy, R. W. (2012). *Nitrogen fixation in bacteria and higher plants*, volume 21. Springer Science & Business Media.

[46] Cabeen, M. T. and Jacobs-Wagner, C. (2005). Bacterial cell shape. *Nat. Rev. Microbiol.*, 3(8):601–10.

[47] Campbell, N. A., Reece, J. B., and Mitchell, L. G. (1999). Biology, fifth edition.

[48] Carballido-López, R. and Formstone, A. (2007). Shape determination in Bacillus subtilis. *Curr. Opin. Microbiol.*, 10(6):611–616.

[49] Cavanaugh, C. M. (1983). Symbiotic chemoautotrophic bacteria in marine invertebrates from sulphide-rich habitats. *Nature*, 302(5903):58–61.

[50] Celler, K., Hödl, I., Simone, a., Battin, T. J., and Picioreanu, C. (2014). A mass-spring model unveils the morphogenesis of phototrophic Diatoma biofilms. *Sci. Rep.*, 4:3649.

[51] Chambless, J. D., Hunt, S. M., Stewart, P. S., Chambless, J. D., Hunt, S. M., and Stewart, P. S. (2013). A Three-Dimensional Computer Model of Four Hypothetical Mechanisms Protecting Biofilms from Antimicrobials. *Appl. Environ. Microbiol.*, 72(3):2005–2013.

[52] Chao, L. and Levin, B. R. (1981). Structured habitats and the evolution of anticompetitor toxins in bacteria. *Proc. Natl. Acad. Sci. U. S. A.*, 78(10):6324–6328.

[53] Characklis, W. G. (1981). Fouling Biofilm Development: A Process Analysis. *Biotechnol. Bioeng.*, 23(9):1923–1960.

[54] Chen, X., Dong, X., Be'er, A., Swinney, H. L., and Zhang, H. P. (2012). Scale-Invariant Correlations in Dynamic Bacterial Clusters. *Phys. Rev. Lett.*, 108(14):148101.

[55] Cheung, T. (1979). Newton's method for nonlinear ordinary and partial differential equations. *J. Math. Anal. Appl.*, pages 474–485.

[56] Cho, H., Jönsson, H., Campbell, K., Melke, P., Williams, J. W., Jedynak, B., Stevens, A. M., Groisman, A., and Levchenko, A. (2007). Self-organization in high-density bacterial colonies: efficient crowd control. *PLoS Biol.*, 5(11):e302.

[57] Christensen, B. B., Haagensen, J. a. J., Heydorn, A., and Molin, S. (2002). Metabolic commensalism and competition in a two-species microbial consortium. *Appl. Environ. Microbiol.*, 68(5):2495–2502.

[58] Cleveland, J., Montville, T. J., Nes, I. F., and Chikindas, M. L. (2001). Bacteriocins: Safe, natural antimicrobials for food preservation. *Int. J. Food Microbiol.*, 71(1):1–20.

[59] Cocking, E. C. (2003). Endophytic colonization of plant roots by nitrogen-fixing bacteria. *Plant Soil*, pages 169–175.

[60] Coenye, T. and Vandamme, P. (2007). *Burkholderia: molecular microbiology and genomics*. Horizon Scientific Press.

[61] Cooper, S. and Denny, M. W. (1997). A conjecture on the relationship of bacterial shape to motility in rod-shaped bacteria. *FEMS Microbiol. Lett.*, 148(2):227–231.

[62] Cordero, O. X., Ventouras, L.-a., DeLong, E. F., and Polz, M. F. (2012). Public good dynamics drive evolution of iron acquisition strategies in natural bacterioplankton populations. *Proc. Natl. Acad. Sci. U. S. A.*, 109(49):20059–20064.

[63] Cornforth, D. M. and Foster, K. R. (2013). Competition sensing: the social side of bacterial stress responses. *Nat. Rev. Microbiol.*, 11(4):285–93.

[64] Cornforth, D. M. and Foster, K. R. (2015). Antibiotics and the art of bacterial war. *Proc. Natl. Acad. Sci. U. S. A.*, 112(35):10827–10828.

[65] Costerton, J. W., Lewandowski, Z., Caldwell, D. E., Korber, D. R., Sn, S., and Lappin-scott, H. M. (1995). Microbial biofilms. *Annu. Rev. Microbiol.*, 49(1):711–745.

[66] Costerton, J. W., Stewart, P. S., and Greenberg, E. P. (1999). Bacterial biofilms: a common cause of persistent infections. *Science (80-.).*, 284(5418):1318–1322.

[67] Cotter, P. D., Hill, C., and Ross, R. P. (2005). Bacteriocins: Developing Inate Immunity for Food. *Nat. Rev. Microbiol.*, 3(10):777–788.

[68] Coyte, K. Z., Schluter, J., and Foster, K. R. (2015). The ecology of the microbiome: Networks, competition, and stability. *Science (80-.).*, 350(6261):663–666.

[69] Coyte, K. Z., Tabuteau, H., Gaffney, E. A., Foster, K. R., and Durham, W. M. (2016). Microbial competition in porous environments can select against rapid biofilm growth. *Proc. Natl. Acad. Sci. U. S. A.*

[70] Curtis, T. P., Sloan, W. T., and Scannell, J. W. (2002). Estimating prokaryotic diversity and its limits. *Proc Natl Acad Sci U S A*, 99(16):10494–10499.

[71] Darch, S. E., West, S. A., Winzer, K., and Diggle, S. P. (2012). Density-dependent fitness benefits in quorum-sensing bacterial populations. *Proc. Natl. Acad. Sci. U. S. A.*, 109(21):8259–8263.

[72] Davit, Y., Byrne, H., Osborne, J., Pitt-Francis, J., Gavaghan, D., and Quintard, M. (2013). Hydrodynamic dispersion within porous biofilms. *Phys. Rev. E - Stat. Nonlinear, Soft Matter Phys.*, 87(1):24–29.

[73] De Beer, D., Stoodley, P., Roe, F., and Lewandowski, Z. (1994). Effects of biofilm structures on oxygen distribution and mass transport. *Biotechnol. Bioeng.*, 43(11):1131–1138.

[74] Delarue, M., Hartung, J., Schreck, C., Gniewek, P., Hu, L., Herminghaus, S., and Hallatschek, O. (2016). Self-driven jamming in growing microbial populations. *Nature physics*.

[75] Demirci, A., Pometto, A. L., and Ho, K. L. (1997). Ethanol production by Saccharomyces cerevisiae in biofilm reactors. *J. Ind. Microbiol. Biotechnol.*, 19(4):299–304.

[76] Diep, D. B., Skaugen, M., Salehian, Z., Holo, H., and Nes, I. F. (2007). Common mechanisms of target cell recognition and immunity for class II bacteriocins. *Proc. Natl. Acad. Sci. U. S. A.*, 104(7):2384–9.

[77] Dismukes, G. C., Klimov, V. V., Baranov, S. V., Kozlov, Y. N., DasGupta, J., and Tyryshkin, A. (2001). The origin of atmospheric oxygen on Earth: the innovation of oxygenic photosynthesis. *Proc. Natl. Acad. Sci. U. S. A.*, 98(5):2170–5.

[78] Donlan, R. M. (2001). Biofilms and device-associated infections. *Emerg. Infect. Dis.*, 7(2):277–81.

[79] Donlan, R. M. (2002). Biofilms: Microbial life on surfaces. *Emerg. Infect. Dis.*, 8(9):881–890.

[80] Drescher, K., Dunkel, J., Nadell, C. D., van Teeffelen, S., Grnja, I., Wingreen, N. S., Stone, H. A., and Bassler, B. L. (2016). Architectural transitions in Vibrio cholerae biofilms at single-cell resolution. *Proc. Natl. Acad. Sci. U. S. A.*, 113(14):201601702.

[81] Driscoll, T. A., Hale, N., and Trefethen, L. N. (2014). Chebfun Guide.

[82] Dugatkin, L. A., Perlin, M., Lucas, J. S., and Atlas, R. (2005). Group-beneficial traits, frequency-dependent selection and genotypic diversity: an antibiotic resistance paradigm. *Proc. Biol. Sci.*, 272(1558):79–83.

[83] Dusenbery, D. B. (1998). Fitness landscapes for effects of shape on chemotaxis and other behaviors of bacteria. *J. Bacteriol.*, 180(22):5978–5983.

[84] Edwards, N., Beeton, S., Bull, A. T., and Merchuk, J. C. (1989). A novel device for the assessment of shear effects on suspended microbial cultures. *Appl. Microbiol. Biotechnol.*, 30(2):190–195.

[85] Elias, S. and Banin, E. (2012). Multi-species biofilms: Living with friendly neighbors. *FEMS Microbiol. Rev.*, 36(5):990–1004.

[86] Errington, J. (2015). Bacterial morphogenesis and the enigmatic MreB helix. *Nat Rev Micro*, 13(4):241–248.

[87] Estrela, S. and Brown, S. P. (2013). Metabolic and Demographic Feedbacks Shape the Emergent Spatial Structure and Function of Microbial Communities. *PLoS Comput. Biol.*, 9(12):1–12.

[88] Farrell, F. D. C., Hallatschek, O., Marenduzzo, D., and Wacław, B. (2013). Mechanically Driven Growth of Quasi-Two-Dimensional Microbial Colonies. *Phys. Rev. Lett.*, 111(16):1–5.

[89] Ferrer, J., Prats, C., and López, D. (2008). Individual-based modelling: an essential tool for microbiology. *J. Biol. Phys.*, 34(1-2):19–37.

[90] Ferrero, R. L. and Lee, A. (1988). Motility of Campylobacter jejuni in a viscous environment: comparison with conventional rod-shaped bacteria. *J. Gen. Microbiol.*, 134(1):53–59.

[91] Fimland, G., Johnsen, L., Dalhus, B., and Nissen-Meyer, J. (2005). Pediocin-like antimicrobial peptides (class IIa bacteriocins) and their immunity proteins: Biosynthesis, structure, and mode of action. *J. Pept. Sci.*, 11(11):688–696.

[92] Formstone, A. and Errington, J. (2005). A magnesium-dependent mreB null mutant: Implications for the role of mreB in Bacillus subtilis. *Mol. Microbiol.*, 55(6):1646–1657.

[93] Fossum, S., Crooke, E., and Skarstad, K. (2007). Organization of sister origins and replisomes during multifork DNA replication in Escherichia coli. *EMBO J.*, 26(21):4514–4522.

[94] Foster, K. R. and Bell, T. (2012). Competition, not cooperation, dominates interactions among culturable microbial species. *Curr. Biol.*, 22(19):1845–50.

[95] Foster, T. J. (2005). Immune evasion by staphylococci. *Nat.Rev.Microbiol.*, 3(1740-1526 (Print)):948–958.

[96] Freese, P. D., Korolev, K. S., Jiménez, J. I., and Chen, I. a. (2014). Genetic drift suppresses bacterial conjugation in spatially structured populations. *Biophys. J.*, 106(4):944–54.

[97] Frippiat, C. C. and Holeyman, A. E. (2008). A comparative review of upscaling methods for solute transport in heterogeneous porous media. *J. Hydrol.*, 362(1-2):150–176.

[98] Frost, I., Smith, W. P. J., Mitri, S., Millan, A. S., Osborne, J. M., Francis, J. M. P., and Maclean, R. C. (2017). Cooperation, competition and antibiotic resistance in bacterial colonies. *Submitted to Proc. Natl. Acad. Sci. U. S. A.*, pages 1–30.

[99] Gao, G.-J., Blawzdziewicz, J., and O'Hern, C. S. (2007). Enumeration of distinct mechanically stable disk packings in small systems. *Philos. Mag.*, 87(3-5):425–431.

[100] Gardner, A. and West, S. A. (2004). Spite and the scale of competition. *J. Evol. Biol.*, 17(6):1195–1203.

[101] Gardner, A., West, S. A., and Buckling, A. (2004). Bacteriocins, spite and virulence. *Proc. Biol. Sci.*, 271(1547):1529–35.

[102] Geesey, G. G. and Mutch, R. (1978). Sessile bacteria : An important component of the microbial population in small mountain streams. *Am. Soc. Limnol. Oceanogr.*, 23(6):1214–1223.

[103] Ghosh, P., Mondal, J., Ben-Jacob, E., and Levine, H. (2015). Mechanically-driven phase separation in a growing bacterial colony. *Proc. Natl. Acad. Sci. U. S. A.*, 112(17):E2166–E2173.

[104] Gilliam, M. (1997). Identification and roles of non-pathogenic microflora associated with honey bees. *FEM Microbiol. Lett.*, 155(1):1–10.

[105] Golding, I., Kozlovsky, Y., Cohen, I., and Ben-jacob, E. (1998). Studies of bacterial branching growth using reaction–diffusion models for colonial development. *Physica A*, 260:510–554.

[106] Grant, M. a. a., Wacław, B., Allen, R. J., and Cicuta, P. (2014). The role of mechanical forces in the planar-to-bulk transition in growing Escherichia coli microcolonies. *J. R. Soc. Interface*, 11(1):1–13.

[107] Green, E. R. and Mecsas, J. (2015). Bacterial Secretion Systems – An overview. *Microbiol. Spectr.*, 4(1):1–32.

[108] Grimm, V. and Railsback, S. (2005). *Individual-based Modeling and Ecology*. Princeton university press.

[109] Guirard, B. M. (1958). Microbial nutrition. *Annu. Rev. Microbiol.*, 12:247–278.

[110] Gujrati, P. D. and Leonov, A. I. (2010). *Modeling and Simulation in Polymers*. John Wiley & Sons.

[111] Habib, G., Hoen, B., Tornos, P., Thuny, F., Prendergast, B., Vilacosta, I., Moreillon, P., de Jesus Antunes, M., Thilen, U., Lekakis, J., Lengyel, M., Müller, L., Naber, C. K., Nihoyannopoulos, P., Moritz, A., and Zamorano, J. L. (2009). Guidelines on the prevention, diagnosis, and treatment of infective endocarditis. *Eur. Heart J.*, 30(19):2369–413.

[112] Haines, A. S., Jones, K., Cheung, M., and Thomas, C. M. (2005). The IncP-6 plasmid Rms149 consists of a small mobilizable backbone with multiple large insertions. *J. Bacteriol.*, 187(14):4728–4738.

[113] Hale, N. and Trefethen, L. N. (2012). Chebfun and numerical quadrature. *Sci. China Math.*, 55(9):1749–1760.

[114] Hall-Stoodley, L., Costerton, J. W., and Stoodley, P. (2004). Bacterial biofilms: from the natural environment to infectious diseases. *Nat. Rev. Microbiol.*, 2(2):95–108.

[115] Hallatschek, O., Hersen, P., Ramanathan, S., and Nelson, D. R. (2007). Genetic drift at expanding frontiers promotes gene segregation. *Proc. Natl. Acad. Sci. U. S. A.*, 104(50):19926–30.

[116] Hallatschek, O. and Nelson, D. R. (2010). Life at the front of an expanding population. *Evolution (N. Y).*, 64(1):193–206.

[117] Hansen, S. K., Rainey, P. B., Haagensen, J. a. J., and Molin, S. (2007). Evolution of species interactions in a biofilm community. *Nature*, 445(7127):533–536.

[118] Harding, T., Jungblut, A. D., Lovejoy, C., and Vincent, W. F. (2011). Microbes in high arctic snow and implications for the cold biosphere. *Appl. Environ. Microbiol.*, 77(10):3234–3243.

[119] Hays, J. P. and Van Leeuwen, W. (2012). *The Role of New Technologies in Medical Microbiological Research and Diagnosis*. Bentham Science Publishers.

[120] Heisenberg, C. P. and Bellaïche, Y. (2013). Forces in tissue morphogenesis and patterning. *Cell*, 153(5):948–962.

[121] Hellweger, F. L. and Bucci, V. (2009). A bunch of tiny individuals-Individual-based modeling for microbes. *Ecol. Modell.*, 220(1):8–22.

[122] Hellweger, F. L., Clegg, R. J., Clark, J. R., Plugge, C. M., and Kreft, J.-U. (2016). Advancing microbial sciences by individual-based modelling. *Nat. Rev. Microbiol.*, 14(7):461–471.

[123] Hermanowicz, S. W. (2001). A simple 2D biofilm model yields a variety of morphological features. *Math. Biosci.*, 169(1):1–14.

[124] Høiby, N., Bjarnsholt, T., Givskov, M., Molin, S., and Ciofu, O. (2010). Antibiotic resistance of bacterial biofilms. *Int. J. Antimicrob. Agents*, 35(4):322–32.

[125] Hooper, L. V. and Gordon, J. I. (2001). Commensal host-bacterial relationships in the gut. *Science*, 292(5519):1115–1118.

[126] Horvath, D. J., Li, B., Casper, T., Partida-Sanchez, S., Hunstad, D. A., Hultgren, S. J., and Justice, S. S. (2011). Morphological plasticity promotes resistance to phagocyte killing of uropathogenic Escherichia coli. *Microbes Infect.*, 13(5):426–437.

[127] Huntingford, C. (1995). Non-dimensionalisation of the Penman-Monteith model. *J. Hydrol.*, 1694(94):215–232.

[128] Inglis, R. F., Gardner, A., Cornelis, P., and Buckling, A. (2009). Spite and virulence in the bacterium Pseudomonas aeruginosa. *Proc. Natl. Acad. Sci. U. S. A.*, 106(14):5703–7.

[129] Jaimes-Lizcano, Y. A., Hunn, D. D., and Papadopoulos, K. D. (2014). Filamentous Escherichia coli cells swimming in tapered microcapillaries. *Res. Microbiol.*, 165(3):166–174.

[130] James, R., Kleanthous, C., and Moore, G. R. (1996). The biology of E colicins: Paradigms and paradoxes. *Microbiology*, 142(7):1569–1580.

[131] Janules, A., van Loosdrecht, M. C. M., Simone, A., and Picioreanu, C. (2010). Cell flexibility affects the alignment of model myxobacteria. *Biophys. J.*, 99(10):3129–38.

[132] Johansen-Berg, H. and Behrens, T. E. (2013). *Diffusion MRI: from quantitative measurement to in vivo neuroanatomy*. Academic Press.

[133] Johnson, C. (2012). *Numerical solution of partial differential equations by the finite element method*. Courier Corporation.

[134] Jones, L. J. F., Carballido-López, R., and Errington, J. (2001). Control of cell shape in bacteria: Helical, actin-like filaments in Bacillus subtilis. *Cell*, 104(6):913–922.

[135] Judson, O. P. (1994). The rise of the individual-based model in ecology. *Trends Ecol. Evol.*, 9(I):9–14.

[136] Justice, S. S., Hung, C., Theriot, J. A., Fletcher, D. A., Anderson, G. G., Footer, M. J., and Hultgren, S. J. (2004). Differentiation and developmental pathways of uropathogenic Escherichia coli in urinary tract pathogenesis. *Proc. Natl. Acad. Sci. U. S. A.*, 101(5):1333–1338.

[137] Justice, S. S., Hunstad, D. a., Cegelski, L., and Hultgren, S. J. (2008). Morphological plasticity as a bacterial survival strategy. *Nat. Rev. Microbiol.*, 6(2):162–168.

[138] Kallmeyer, J., Pockalny, R., Adhikari, R. R., Smith, D. C., and D'Hondt, S. (2012). Global distribution of microbial abundance and biomass in subseafloor sediment. *Proc. Natl. Acad. Sci. U. S. A.*, 109(40):16213–16216.

[139] Karl, D. (2014). Colorized microbe scanning electron micrograph. http://manoa.hawaii.edu/kaunana/wp-content/uploads/2014/07/4.Colorized_micobe_SEM_web.jpg. [Online; accessed November 01, 2016].

[140] Kelley, C. T. (2003). *Solving nonlinear equations with Newton's method*, volume 1. Siam.

[141] Kelsic, E. D., Zhao, J., Vetsigian, K., and Kishony, R. (2015). Counteraction of antibiotic production and degradation stabilizes microbial communities. *Nature*, 521(7553):516–519.

[142] Kerr, B., Riley, M. A., Feldman, M. W., and Bohannan, B. J. M. (2002). Local dispersal promotes biodiversity in a real-life game of rock-paper-scissors. *Nature*, 418(6894):171–174.

[143] Kim, W., Levy, S. B., and Foster, K. R. (2016). Rapid radiation in bacteria leads to a division of labour. *Nat. Commun.*, 354(1388):1395–1405.

[144] Kim, W., Racimo, F., Schluter, J., Levy, S. B., and Foster, K. R. (2014). Importance of positioning for microbial evolution. *Proc. Natl. Acad. Sci. U. S. A.*, 111(16):E1639–47.

[145] Klaenhammer, T. R. (1988). Bacteriocins of lactic acid bacteria. *Biochimie*, 70(3):337–349.

[146] Klapper, I. and Dockery, J. (2002). Finger Formation in Biofilm Layers. *SIAM J. Appl. Math.*, 62(3):853–869.

[147] Klapper, I. and Dockery, J. (2010). Microbial Biofilms. *SIAM Rev. Soc. Ind. Appl. Math.*, 52(2):221–265.

[148] Klitgord, N. and Segrè, D. (2011). Ecosystems biology of microbial metabolism. *Curr. Opin. Biotechnol.*, 22(4):541–546.

[149] Koch, A. L. (1996). What Size Should A Bacterium Be? A Question of Scale. *Annu. Rev. Microbiol.*, 50(1):317–348.

[150] Kong, H. H. (2011). Skin microbiome: Genomics-based insights into the diversity and role of skin microbes. *Trends Mol. Med.*, 17(6):320–328.

[151] Korolev, K. S., Xavier, J. B., Nelson, D. R., and Foster, K. R. (2011). A quantitative test of population genetics using spatiogenetic patterns in bacterial colonies. *Am. Nat.*, 178(4):538–52.

[152] Kreft, J.-U. (2004). Biofilms promote altruism. *Microbiology*, 150(Pt 8):2751–60.

[153] Kreft, J. U., Booth, G., and Wimpenny, J. W. (1998). BacSim, a simulator for individual-based modelling of bacterial colony growth. *Microbiology*, 144 (Pt 1:3275–87.

[154] Kreft, J.-U., Picioreanu, C., Wimpenny, J. W. T., and van Loosdrecht, M. C. M. (2001). Individual-based modelling of biofilms. *Microbiology*, 147(1):2897–2912.

[155] Kreft, J. U. and Wimpenny, J. W. T. (2001). Effect of EPS on biofilm structure and function as revealed by an individual-based model of biofilm growth. *Water Sci. Technol.*, 43(6):135–141.

[156] Krieger-Liszkay, A., Fufezan, C., and Trebst, A. (2008). Singlet oxygen production in photosystem II and related protection mechanism. *Photosynth. Res.*, 98(1-3):551–564.

[157] Kudrolli, A., Lumay, G., Volfson, D., and Tsimring, L. (2008). Swarming and Swirling in Self-Propelled Polar Granular Rods. *Phys. Rev. Lett.*, 100(5):058001.

[158] Kysela, D. T., Randich, A. M., Caccamo, P. D., and Brun, Y. V. (2016). Diversity Takes Shape: Understanding the Mechanistic and Adaptive Basis of Bacterial Morphology. *PLOS Biol.*, 14(10):e1002565.

[159] Lardon, L. A., Merkey, B. V., Martins, S., Dötsch, A., Picioreanu, C., Kreft, J.-U., and Smets, B. F. (2011). iDynoMiCS: next-generation individual-based modelling of biofilms. *Environ. Microbiol.*, 13(9):2416–34.

[160] Latifi, A., Winson, M. K., Foglino, M., Bycroft, B. W., Stewart, G. S. A. B., Lazdunski, A., and Williams, P. (1995). Multiple homologues of LuxR and LuxI control expression of virulence determinants and secondary metabolites through quorum sensing in Pseudomonas aeruginosa PAO1. *Mol. Microbiol.*, 17(2):333–343.

[161] Lee, W., Lewandowski, Z., Nielsen, P. H., and Hamilton, W. A. (1995). Role of sulfate-reducing bacteria in corrosion of mild steel: A review. *Biofouling*, 8(3):165–194.

[162] Lenski, R. E. ., Rose, M. R. ., Simpson, S. C. ., and Tadler, S. C. . (2016). Long-Term Experimental Evolution in Escherichia coli . I . Adaptation and Divergence During 2,000 Generations. *Am. Soc. Nat.*, 138(6):1315–1341.

[163] Levin, S. a. (2002). Complex Adaptive Systems and the Unknowable. *Bull. Am. Math. Soc.*, 40(1):3–19.

[164] Lindon, J. C., Nicholson, J. K., and Holmes, E. (2011). *The handbook of metabonomics and metabolomics*. Elsevier.

[165] Liu, Y., Sun, J., Peng, L., Wang, D., Dai, X., and Ni, B.-J. (2016). Assessment of Heterotrophic Growth Supported by Soluble Microbial Products in Anammox Biofilm using Multidimensional Modeling. *Sci. Rep.*, 6(February):27576.

[166] Livermore, D. M. (1995). beta-Lactamases in laboratory and clinical resistance. *Clin. Microbiol. Rev.*, 8(4):557–84.

[167] Lloyd, D. P. and Allen, R. J. (2015). Competition for space during bacterial colonization of a surface. *J. R. Soc. Interface*, 12(110):20150608.

[168] Logg, A. and Wells, G. N. (2010). Dolfin. *ACM Trans. Math. Softw.*, 37(2):1–28.

[169] Lozupone, C. a. and Knight, R. (2007). Global patterns in bacterial diversity. *Proc. Natl. Acad. Sci. U. S. A.*, 104(27):11436–11440.

[170] Mailman, M., Schreck, C. F., O'Hern, C. S., and Chakraborty, B. (2009). Jamming in systems composed of frictionless ellipse-shaped particles. *Phys. Rev. Lett.*, 102(25):1–4.

[171] Majeed, H., Gillor, O., Kerr, B., and Riley, M. A. (2011). Competitive interactions in Escherichia coli populations: the role of bacteriocins. *Isme J*, 5(1):71–81.

[172] Marshall, W. F., Young, K. D., Swaffer, M., Wood, E., Nurse, P., Kimura, A., Frankel, J., Wallingford, J., Walbot, V., Qu, X., and Roeder, A. H. K. (2012). What determines cell size? *BMC Biol.*, 10(1):101.

[173] Martens, E. A. and Hallatschek, O. (2011). Interfering waves of adaptation promote spatial mixing. *Genetics*, 189(3):1045–1060.

[174] Martin Oeggerli, with support from School of Life Sciences, F. (2013). Intestinal bacteria. http://ngm.nationalgeographic.com/2013/01/microbes/img/05-intestinal-bacteria-670.jpg. [Online; accessed November 01, 2016].

[175] Martinko, J. M. and Madigan, M. (2005). Brock biology of microorganisms. *ed: Englewood Cliffs, NJ: Prentice Hall. ISBN 0-13-144329-1*.

[176] Martiny, J. B. H., Bohannan, B. J. M., Brown, J. H., Colwell, R. K., Fuhrman, J. a., Green, J. L., Horner-Devine, M. C., Kane, M., Krumins, J. A., Kuske, C. R., Morin, P. J., Naeem, S., Ovreås, L., Reysenbach, A.-L., Smith, V. H., and Staley, J. T. (2006). Microbial biogeography: putting microorganisms on the map. *Nat. Rev. Microbiol.*, 4(February):102–112.

[177] Mather, W., Mondragón-Palomino, O., Danino, T., Hasty, J., and Tsimring, L. S. (2010). Streaming Instability in Growing Cell Populations. *Phys Rev Lett*, 104(20):1–8.

[178] Matthew J. Arduino, J. C. (2007). Staphylococcus aureus scanning electron micrograph (image 6486). https://en.wikipedia.org/wiki/Staphylococcus#/media/File:Staphylococcus_aureus_01.jpg. [Online; accessed July 07, 2016].

[179] Mazzoli, S. (2010). Biofilms in chronic bacterial prostatitis (NIH-II) and in prostatic calcifications. *FEMS Immunol. Med. Microbiol.*, 59(3):337–44.

[180] Mcauliffe, O., Ryan, M. P., Ross, R. P., Hill, C., Auliffe, O. M. C., Ryan, M. P., Ross, R. P., Hill, C., Breeuwer, P., and Abee, T. (1998). Lacticin 3147 , a Broad-Spectrum Bacteriocin Which Selectively Dissipates the Membrane Potential. *Appl. Environ. Microbiol.*, 64(2):439–445.

[181] McLoughlin, K., Schluter, J., Rakoff-Nahoum, S., Smith, A. L., and Foster, K. R. (2016). Host Selection of Microbiota via Differential Adhesion. *Cell Host Microbe*, 19(4):550–559.

[182] McNally, L., Bernardy, E., Thomas, J., Kalziqi, A., Pentz, J. T., Brown, S., Hammer, B., Yunker, P., and Ratcliff, W. (2016). Killing by Type VI secretion drives clonal phase separation and the evolution of cooperation. *bioRxiv*, page 063487.

[183] Merkey, B. V., Lardon, L. a., Seoane, J. M., Kreft, J.-U., and Smets, B. F. (2011). Growth dependence of conjugation explains limited plasmid invasion in biofilms: an individual-based modelling study. *Environ. Microbiol.*, 13(9):2435–52.

[184] Miller, C., Thomsen, L. E., Gaggero, C., Mosseri, R., Ingmer, H., and Cohen, S. N. (2004). SOS response induction by beta-lactams and bacterial defense against antibiotic lethality. *Science*, 305(5690):1629–31.

[185] Miller, M. B. and Bassler, B. L. (2001). Quorum sensing in bacteria. *Annu. Rev. Microbiol.*, 55(1):165–199.

[186] Mimura, M., Sakaguchi, H., and Matsushita, M. (2000). Reaction-diffusion modelling of bacterial colony patterns. *Phys. A Stat. Mech. its Appl.*, 282(1):283–303.

[187] Mirams, G. R., Arthurs, C. J., Bernabeu, M. O., Bordas, R., Cooper, J., Corrias, A., Davit, Y., Dunn, S.-J., Fletcher, A. G., Harvey, D. G., Marsh, M. E., Osborne, J. M., Pathmanathan, P., Pitt-Francis, J., Southern, J., Zemzemi, N., and Gavaghan, D. J. (2013). Chaste: An Open Source C++ Library for Computational Physiology and Biology. *PLoS Comput. Biol.*, 9(3):e1002970.

[188] Mitchell, J. G. and Kogure, K. (2006). Bacterial motility: Links to the environment and a driving force for microbial physics. *FEMS Microbiol. Ecol.*, 55(1):3–16.

[189] Mitri, S., Clarke, E., and Foster, K. R. (2015). Resource limitation drives spatial organization in microbial groups. *ISME J.*, 10(6):1–12.

[190] Mitri, S. and Foster, K. R. (2013). The genotypic view of social interactions in microbial communities. *Annu. Rev. Genet.*, 47:247–73.

[191] Mitri, S., Xavier, J. B., and Foster, K. R. (2011). Social evolution in multispecies biofilms. *Proc. Natl. Acad. Sci. U. S. A.*, 108 Suppl(Supplement_2):10839–46.

[192] Momeni, B., Brileya, K. A., Fields, M. W., and Shou, W. (2013). Strong inter-population cooperation leads to partner intermixing in microbial communities. *Elife*, 2013(2):1–23.

[193] Monds, R. D., Lee, T. K., Colavin, A., Ursell, T., Quan, S., Cooper, T. F., and Huang, K. C. (2014). Systematic Perturbation of Cytoskeletal Function Reveals a Linear Scaling Relationship between Cell Geometry and Fitness. *Cell Rep.*, 9(4):1528–1537.

[194] Monod, J. (1949). The Growth of Bacterial Cultures. *Annu. Rev. M*, 3(Xl):371–394.

[195] Moran, N. A., Baumann, P., Moran, N. A., and Baumann, P. (2000). Bacterial endosymbionts in animals. *Curr. Opin. Microbiol.*, 5274(July):270–275.

[196] Moreau-Marquis, S., Stanton, B. a., and O'Toole, G. a. (2008). Pseudomonas aeruginosa biofilm formation in the cystic fibrosis airway. *Pulm. Pharmacol. Ther.*, 21(4):595–9.

[197] Nadell, C. D., Bucci, V., Drescher, K., Levin, S. a., Bassler, B. L., and Xavier, J. B. (2013). Cutting through the complexity of cell collectives. *Proc. Biol. Sci.*, 280(1755):20122770.

[198] Nadell, C. D., Drescher, K., and Foster, K. R. (2016). Spatial structure, cooperation and competition in biofilms. *Nat. Rev. Microbiol.*, 14(9):589–600.

[199] Nadell, C. D., Foster, K. R., and Xavier, J. B. (2010). Emergence of spatial structure in cell groups and the evolution of cooperation. *PLoS Comput. Biol.*, 6(3):1–9.

[200] Nadell, C. D., Xavier, J. B., and Foster, K. R. (2009). The sociobiology of biofilms. *FEMS Microbiol. Rev.*, 33(1):206–224.

[201] Nadell, C. D., Xavier, J. B., Levin, S. a., and Foster, K. R. (2008). The evolution of quorum sensing in bacterial biofilms. *PLoS Biol.*, 6(1):e14.

[202] Nakayama, K., Takashima, K., Ishihara, H., Shinomiya, T., Kageyama, M., Kanaya, S., Ohnishi, M., Murata, T., Mori, H., and Hayashi, T. (2000). The R-type pyocin of Pseudomonas aeruginosa is related to P2 phage, and the F-type is related to lambda phage. *Mol. Microbiol.*, 38(2):213–231.

[203] Nakayama, M., Shigemune, N., Tsugukuni, T., Tokuda, H., and Miyamoto, T. (2011). Difference of EGCg adhesion on cell surface between Staphylococcus aureus and Escherichia coli visualized by electron microscopy after novel indirect staining with cerium chloride. *J. Microbiol. Methods*, 86(1):97–103.

[204] Nava, G. M., Friedrichsen, H. J., and Stappenbeck, T. S. (2011). Spatial organization of intestinal microbiota in the mouse ascending colon. *ISME J.*, 5(4):627–638.

[205] Neilands, J. B. (1995). Siderophores: Structure and Function of Microbial Iron Transport Compounds. *J. Biol. Chem.*, 270(45):26723–26726.

[206] Nguyen, L., Scherr, N., Gatfield, J., Walburger, A., Pieters, J., and Thompson, C. J. (2007). Antigen 84, an effector of pleiomorphism in Mycobactenum smegmatis. *J. Bacteriol.*, 189(21):7896–7910.

[207] Nicolella, C., Zolezzi, M., Rabino, M., Furfaro, M., and Rovatti, M. (2005). Development of particle-based biofilms for degradation of xenobiotic organic compounds. *Water Res.*, 39(12):2495–504.

[208] Ohsumi, M., Shinomiya, T., and Kageyama, M. (1980). Comparative study on R-type pyocins of Pseudomonas aeruginosa. *J. Biochem.*, 87(4):1119–25.

[209] Oishi, K. and Klavins, E. (2014). Framework for Engineering Finite State Machines in Gene Regulatory Networks. *ACS Synth. Biol.*

[210] Osborn, M. J. and Rothfield, L. (2007). Cell shape determination in Escherichia coli. *Curr. Opin. Microbiol.*, 10(6):606–610.

[211] Otsu, N. (1979). A Threshold Selection Method from Gray-Level Histograms. *IEEE Trans. Syst. Man. Cybern.*, 20(1):62–66.

[212] Pace, N. R. (1997). A molecular view of microbial diversity and the biosphere. *Science*, 276(5313):734–740.

[213] Pai, A., Tanouchi, Y., and You, L. (2012). Optimality and robustness in quorum sensing (QS)-mediated regulation of a costly public good enzyme. *Proc. Natl. Acad. Sci. U. S. A.*, 109(48):19810–5.

[214] Parret, A. H. A. and De Mot, R. (2002). Bacteria killing their own kind: Novel bacteriocins of Pseudomonas and other gamma-proteobacteria. *Trends Microbiol.*, 10(3):107–112.

[215] Pathmanathan, P., Cooper, J., Fletcher, a., Mirams, G., Murray, P., Osborne, J. M., Pitt-Francis, J., Walter, a., and Chapman, S. J. (2009). A computational study of discrete mechanical tissue models. *Phys. Biol.*, 6(3):036001.

[216] Perez, R. H., Zendo, T., and Sonomoto, K. (2014). Novel bacteriocins from lactic acid bacteria (LAB): various structures and applications. *Microb. Cell Fact.*, 13(S3):1–13.

[217] Pernthaler, J., Sattler, B., Šimek, K., Schwarzenbacher, A., and Psenner, R. (1996). Top-down effects on the size-biomass distribution of a freshwater bacterioplankton community. *Aquat. Microb. Ecol.*, 10(3):255–263.

[218] Persat, A., Stone, H. a., and Gitai, Z. (2014). The curved shape of Caulobacter crescentus enhances surface colonization in flow. *Nat. Commun.*, 5(May):3824.

[219] Peruani, F., Deutsch, A., and Bär, M. (2006). Nonequilibrium clustering of self-propelled rods. *Phys. Rev. E*, 74(3):030904.

[220] Picioreanu, C., Kreft, J. U., Klausen, M., Haagensen, J. a. J., Tolker-Nielsen, T., and Molin, S. (2007). Microbial motility involvement in biofilm structure formation - A 3D modelling study. *Water Sci. Technol.*, 55(8-9):337–343.

[221] Picioreanu, C., Loosdrecht, M. C. M. V., and Heijnen, J. J. (2000a). Two-Dimensional Model of Biofilm Detachment Caused by Internal Stress from Liquid Flow. *Biotechnol. Bioeng.*, 72(2):206–218.

[222] Picioreanu, C., van Loosdrecht, M. C., and Heijnen, J. J. (1998). Mathematical modeling of biofilm structure with a hybrid differential-discrete cellular automaton approach. *Biotechnol. Bioeng.*, 58(1):101–16.

[223] Picioreanu, C., van Loosdrecht, M. C., and Heijnen, J. J. (2001). Two-dimensional model of biofilm detachment caused by internal stress from liquid flow. *Biotechnol. Bioeng.*, 72(2):205–18.

[224] Picioreanu, C., Van Loosdrecht, M. C. M., and Heijnen, J. J. (2000b). Effect of diffusive and convective substrate transport on biofilm structure formation: A two-dimensional modeling study. *Biotechnol. Bioeng.*, 69(5):504–515.

[225] Pinho, M. G., Kjos, M., and Veening, J.-W. (2013). How to get (a)round: mechanisms controlling growth and division of coccoid bacteria. *Nat. Rev. Microbiol.*, 11(9):601–14.

[226] Popat, R., Crusz, S. A., Messina, M., Williams, P., West, S. A., and Diggle, S. P. (2012). Quorum-sensing and cheating in bacterial biofilms. *Proc. Biol. Sci.*, 279(1748):4765–4771.

[227] Popławski, N. J., Shirinifard, A., Maciej, S., and Glazier, J. A. (2008). Simulation of Single-Species Bacterial-Biofilm Growth Using The Glazier-Graner-Hogeweg Model and the CompuCell3D Modelling Environment. *Math Biosci Eng*, 5(2):355–388.

[228] Potera, C. (1996). Biofilms invade microbiology. *Science*, 273(5283):1795–1797.

[229] Potera, C. (2013). Forging a Link Between Biofilms and Disease. *Science (80-.).*, 283(5409):1–5.

[230] Rabaey, K., Lissens, G., Siciliano, S. D., and Verstraete, W. (2003). A microbial fuel cell capable of converting glucose to electricity at high rate and efficiency. *Biotechnol. Lett.*, 25(18):1531–5.

[231] Rabani, A., Ariel, G., and Be'er, A. (2013). Collective motion of spherical bacteria. *PLoS One*, 8(12):e83760.

[232] Richards, D. M. and Endres, R. G. (2016). Target shape dependence in a simple model of receptor-mediated endocytosis and phagocytosis. *Proc. Natl. Acad. Sci. U. S. A.*, 113(27):201521974.

[233] Riley, M. a. (1998). Molecular mechanisms of bacteriocin evolution. *Annu. Rev. Genet.*, 32:255–278.

[234] Riley, M. a. (1999). The ecological role of bacteriocins in bacterial competition. *Trends Microbiol.*, 7(99):129–133.

[235] Rittmann, B. E. and Mccarty, P. L. (1980). Model of Steady-State-Biofilm Kinetics. *Biotechnol. Bioeng.*, XXII(10):2343–2357.

[236] Robertson, B. R., O'Rourke, J. L., Neilan, B. A., Vandamme, P., On, S. L. W., Fox, J. G., and Lee, A. (2005). Mucispirillum schaedleri gen. nov., sp. nov., a spiral-shaped bacterium colonizing the mucus layer of the gastrointestinal tract of laboratory rodents. *Int. J. Syst. Evol. Microbiol.*, 55(3):1199–1204.

[237] Rocky Mountain Laboratories, NIAID, N. (2006). Escherichia coli scanning electron micrograph. https://en.wikipedia.org/wiki/Escherichia_coli#/media/File:EscherichiaColi_NIAID.jpg. [Online; accessed July 07, 2016].

[238] Rudge, T. J., Federici, F., Steiner, P. J., Kan, A., and Haseloff, J. (2013). Cell Polarity-Driven Instability Generates Self-Organized, Fractal Patterning of Cell Layers. *ACS Synth. Biol.*, 2(1):705–414.

[239] Rudge, T. J., Steiner, P. J., Phillips, A., and Haseloff, J. (2012). Computational modeling of synthetic microbial biofilms. *ACS Synth. Biol.*, 1(8):345–52.

[240] Ryan, R. P., Germaine, K., Franks, A., Ryan, D. J., and Dowling, D. N. (2008). Bacterial endophytes: Recent developments and applications. *FEMS Microbiol. Lett.*, 278(1):1–9.

[241] Saad, Y. (2003). *Iterative methods for sparse linear systems*. Siam.

[242] Saffman, P. G. and Delbruck, M. (1975). Brownian motion in biological membranes. *Proc. Natl. Acad. Sci. U. S. A.*, 72(8):3111–3113.

[243] Salzman, N. H. (2011). Microbiota-immune system interaction: An uneasy alliance. *Curr. Opin. Microbiol.*, 14(1):99–105.

[244] Sanchez-Vizuete, P., Orgaz, B., Aymerich, S., Le Coq, D., and Briandet, R. (2015). Pathogens protection against the action of disinfectants in multispecies biofilms. *Front. Microbiol.*, 6(JUN):1–12.

[245] Savage, D. F., Afonso, B., Chen, A. H., and Silver, P. a. (2010). Spatially Ordered Dynamics of the Bacterial Carbon Fixation Machinery. *Science (80-.).*, 1641(1):1258–1261.

[246] Schaller, G. and Meyer-Hermann, M. (2005). Multicellular tumor spheroid in an off-lattice Voronoi-delaunay cell model. *Phys. Rev.*, 71(5):51910.

[247] Schindelin, J., Arganda-Carreras, I., Frise, E., Kaynig, V., Longair, M., Pietzsch, T., Preibisch, S., Rueden, C., Saalfeld, S., Schmid, B., et al. (2012). Fiji: an open-source platform for biological-image analysis. *Nature methods*, 9(7):676–682.

[248] Schluter, J. and Foster, K. R. (2012). The evolution of mutualism in gut microbiota via host epithelial selection. *PLoS Biol.*, 10(11):1–9.

[249] Schluter, J., Nadell, C., Bassler, B. L., and Foster, K. R. (2014). Adhesion as a weapon in microbial competition. *ISME J.*, 9(1):139–149.

[250] Schmidt, J. M. (1971). Prosthecate bacteria. *Annu.*, 25(126):93–110.

[251] Schulz, H. N. and Jørgensen, B. B. (2001). Big bacteria. *Annu. Rev. Microbiol.*, 55:105–137.

[252] Schwarz-Linek, J., Winkler, A., Wilson, L. G., Pham, N. T., Schilling, T., and Poon, W. C. K. (2010). Polymer-induced phase separation in Escherichia coli suspensions. *Soft Matter*, 6(18):4540.

[253] Sears, C. L. (2005). A dynamic partnership: Celebrating our gut flora. *Anaerobe*, 11(5):247–251.

[254] Secor, P. R., Sweere, J. M., Michaels, L. A., Malkovskiy, A. V., Lazzareschi, D., Katznelson, E., Rajadas, J., Birnbaum, M. E., Arrigoni, A., Braun, K. R., Evanko, S. P., Stevens, D. A., Kaminsky, W., Singh, P. K., Parks, W. C., and Bollyky, P. L. (2015). Filamentous bacteriophage promote biofilm assembly and function. *Cell Host Microbe*, 18(5):549–559.

[255] Sekiguchi, Y., Kamagata, Y., Nakamura, K., Ohashi, A., and Harada, H. (1999). Fluorescence ln Situ Hybridization Using 16S rRNA-Targeted Oligonucleotides Reveals Localization of Methanogens and Seclected Uncultured Bacteria in Mesophilic and Thermophilic Sludge Granules. *Appl. Environ. Microbiol.*, 65(3):1280–1288.

[256] Sekirov, I. and Finlay, B. B. (2006). Human and microbe: united we stand. *Nat. Med.*, 12(7):736–7.

[257] Serra, D. O., Richter, A. M., Klauck, G., Mika, F., and Hengge, R. (2013). Microanatomy at Cellular Resolution and Spatial Order of Physiological Differentiation in a Bacterial Biofilm. *MBio*, 4(2):1–12.

[258] Siefert, J. L. and Fox, G. E. (1998). Phylogenetic mapping of bacterial morphology. *Microbiology*, 144 (Pt 1(1 998):2803–8.

[259] Smith, W. P. J., Davit, Y., Osborne, J. M., Kim, W., Foster, K. R., and Pitt-Francis, J. M. (2016). Cell morphology drives spatial patterning in microbial communities. *Proc. Natl. Acad. Sci. U. S. A.*, page 201613007.

[260] Sogin, M. L., Morrison, H. G., Huber, J. A., Welch, D. M., Huse, S. M., Neal, P. R., Arrieta, J. M., and Herndl, G. J. (2006). Microbial Diversity in the Deep Sea and the Underexplored "Rare Biosphere". *Handb. Mol. Microb. Ecol. II Metagenomics Differ. Habitats*, 103(30):243–252.

[261] Sokolov, A. and Aranson, I. S. (2012). Physical properties of collective motion in suspensions of bacteria. *Phys. Rev. Lett.*, 109(24):1–5.

[262] Stacy, A., Everett, J., Jorth, P., Trivedi, U., Rumbaugh, K. P., and Whiteley, M. (2014). Bacterial fight-and-flight responses enhance virulence in a polymicrobial infection. *Proc. Natl. Acad. Sci. U. S. A.*, 111(21):7819–24.

[263] Starruss, J., Peruani, F., Bär, M., and Deutsch, A. (2007). Bacterial Swarming Driven by Rod Shape. In Andreas Deutsch, Lutz Brusch, Helen Byrne, Gerda de Vries, H. H., editor, *Math. Model. Biol. Syst. Vol. I*, pages 163–174. Springer.

[264] Stewart, P. S. (2003). Diffusion in Biofilms. *J. Bacteriol.*, 185(5):1485–1491.

[265] Stewart, P. S. and Franklin, M. J. (2008). Physiological heterogeneity in biofilms. *Nat. Rev. Microbiol.*, 6(3):199–210.

[266] Stoodley, P., Lewandowski, Z., Boyle, J., and Lappin-Scott, H. (1999). Structural deformation of bacterial biofilms caused by short-term fluctuations in fluid shear: An in situ investigation of biofilm rheology. *Biotechnol. Bioeng.*, 65(1):83–92.

[267] Storck, T., Picioreanu, C., Virdis, B., and Batstone, D. J. (2014). Variable cell morphology approach for individual-based modeling of microbial communities. *Biophys. J.*, 106(9):2037–48.

[268] Tait, K. and Sutherland, I. W. (2002). Antagonistic interactions amongst bacteriocin-producing enteric bacteria in dual species biofilms. *J. Appl. Microbiol.*, 93(2):345–352.

[269] Takeuchi, S., DiLuzio, W. R., Weibel, D. B., and Whitesides, G. M. (2005). Controlling the shape of filamentous cells of Escherichia coli. *Nano Lett.*, 5(9):1819–23.

[270] Tamames, J., Gonzalez-Moreno, M., Mingorance, J., Valencia, A., and Vicente, M. (2001). Bringing gene order into bacterial shape. *Trends Genet.*, 17(3):124–126.

[271] Tyc, O., van den Berg, M., Gerards, S., van Veen, J. A., Raaijmakers, J. M., de Boer, W., and Garbeva, P. (2014). Impact of interspecific interactions on antimicrobial activity among soil bacteria. *Front. Microbiol.*, 5(OCT):1–10.

[272] Typas, A., Banzhaf, M., Gross, C. A., and Vollmer, W. (2012). From the regulation of peptidoglycan synthesis to bacterial growth and morphology. *Nat Rev Microbiol*, 10(2):123–136.

[273] Van Dyken, J. D., Müller, M. J. I., Mack, K. M. L., and Desai, M. M. (2013). Spatial population expansion promotes the evolution of cooperation in an experimental prisoner's dilemma. *Curr. Biol.*, 23(10):919–923.

[274] van Leeuwenhoek, A. and Hoole, S. (1816). *The Select Works of Antony Van Leeuwenhoek: Containing His Microscopical Discoveries in Many of the Works of Nature*, volume 1. Whittingham and Arliss.

[275] Vicente, M. and Errington, J. (1996). Structure, function and controls in microbial division. *Mol. Microbiol.*, 20(1):1–7.

[276] Volfson, D., Cookson, S., Hasty, J., and Tsimring, L. S. (2008). Biomechanical ordering of dense cell populations. *Proc. Natl. Acad. Sci. U. S. A.*, 105(40):15346–51.

[277] Wagner, J. K., Setayeshgar, S., Sharon, L. A., Reilly, J. P., and Brun, Y. V. (2006). A nutrient uptake role for bacterial cell envelope extensions. *Proc. Natl. Acad. Sci. U. S. A.*, 103(31):11772–11777.

[278] Wang, P., Robert, L., Pelletier, J., Dang, W. L., Taddei, F., Wright, A., and Jun, S. (2010). Robust growth of escherichia coli. *Curr. Biol.*, 20(12):1099–1103.

[279] Wang, Q. and Zhang, T. (2010). Review of mathematical models for biofilms. *Solid State Commun.*, 150(21-22):1009–1022.

[280] Wäsche, S., Horn, H., and Hempel, D. C. (2002). Influence of growth conditions on biofilm development and mass transfer at the bulk/biofilm interface. *Water Res.*, 36(19):4775–4784.

[281] West, S. a., Diggle, S. P., Buckling, A., Gardner, A., Griffin, A. S., West, S. a., Diggle, S. P., Buckling, A., Gardner, A., and Griffin, A. S. (2007). The Social Lives of Microbes. *Annu. Rev. Ecol. Evol. Syst.*, 38(May):53–77.

[282] Whitman, W. B., Coleman, D. C., and Wiebe, W. J. (1998). Prokaryotes: the unseen majority. *Proc Natl Acad Sci U S A*, 95(12):6578–6583.

[283] Widder, S., Allen, R. J., Pfeiffer, T., Curtis, T. P., Wiuf, C., Sloan, W. T., Cordero, O. X., Brown, S. P., Momeni, B., Shou, W., Kettle, H., Flint, H. J., Haas, A. F., Laroche, B., Kreft, J.-u., Rainey, P. B., Freilich, S., Schuster, S., Milferstedt, K., van der Meer, J. R., Groszkopf, T., Huisman, J., Free, A., Picioreanu, C., Quince, C., Klapper, I., Labarthe, S., Smets, B. F., Wang, H., Isaac Newton Institute Fellows, and Soyer, O. S. (2016). Challenges in microbial ecology: building predictive understanding of community function and dynamics. *ISME J.*, 1(1):1–12.

[284] Wilkinson, M. H. F. (2002). Model intestinal microflora in computer simulation: A simulation and modeling package for host-microflora interactions. *IEEE Trans. Biomed. Eng.*, 49(10):1077–1085.

[285] Wilmes, P., Remis, J. P., Hwang, M., Auer, M., Thelen, M. P., and Banfield, J. F. (2009). Natural acidophilic biofilm communities reflect distinct organismal and functional organization. *ISME J.*, 3(2):266–270.

[286] Wimpenny, J., Manz, W., and Szewzyk, U. (2000). Heterogeneity in biofilms. *FEMS Microbiol. Rev.*, 24:661–671.

[287] Wimpenny, J. W. T. and Colasanti, R. (1997). A unifying hypothesis for the structure of microbial biofilms based on cellular automaton models. *FEMS Microbiol. Ecol.*, 22(1):1–16.

[288] Woese, C. R., Kandler, O., and Wheelis, M. L. (1990). Towards a natural system of organisms: proposal for the domains Archaea, Bacteria, and Eucarya. *Proc. Natl. Acad. Sci. U. S. A.*, 87(12):4576–4579.

[289] Wolcott, R. D. and Ehrlich, G. D. (2008). Biofilms and chronic infections. *JAMA*, 299(22):2682–4.

[290] Wood, B. D. (2009). The role of scaling laws in upscaling. *Adv. Water Resour.*, 32(5):723–736.

[291] Wood, B. D., Quintard, M., and Whitaker, S. (2002). Calculation of effective diffusivities for biofilms and tissues. *Biotechnol. Bioeng.*, 77(5):495–516.

[292] Wu, J. a., Wu, J. a., Kusuma, C., Kusuma, C., Mond, J. J., Mond, J. J., Kokai-kun, J. F., and Kokai-kun, J. F. (2003). Lysostaphin Disrupts Staphylococcus aureus and Staphylococcus epidermidis Bio lms on Arti cial Surfaces. *Society*, 47(11):3407–3414.

[293] Xavier, J., Picioreanu, C., and Van Loosdrecht, M. C. M. (2005a). A general description of detachment for multidimensional modelling of biofilms. *Biotechnol. Bioeng.*, 91(6):651–669.

[294] Xavier, J. B. (2011). Social interaction in synthetic and natural microbial communities. *Mol. Syst. Biol.*, 7(483):483.

[295] Xavier, J. B., De Kreuk, M. K., Picioreanu, C., and Van Loosdrecht, M. C. M. (2007). Multi-scale individual-based model of microbial and bioconversion dynamics in aerobic granular sludge. *Environ. Sci. Technol.*, 41(18):6410–7.

[296] Xavier, J. B. and Foster, K. R. (2007). Cooperation and conflict in microbial biofilms. *Proc. Natl. Acad. Sci. U. S. A.*, 104(3):876–81.

[297] Xavier, J. B., Picioreanu, C., and van Loosdrecht, M. C. M. (2005b). A framework for multidimensional modelling of activity and structure of multispecies biofilms. *Environ. Microbiol.*, 7(8):1085–103.

[298] Yang, L., Liu, Y., Markussen, T., Høiby, N., Tolker-Nielsen, T., and Molin, S. (2011). Pattern differentiation in co-culture biofilms formed by Staphylococcus aureus and Pseudomonas aeruginosa. *FEMS Immunol. Med. Microbiol.*, 62(3):339–347.

[299] Young, K. D. (2003). Bacterial shape. *Mol. Microbiol.*, 49(3):571–580.

[300] Young, K. D. (2006). The selective value of bacterial shape. *Microbiol. Mol. Biol. Rev.*, 70(3):660–703.

[301] Young, K. D. (2007). Bacterial morphology: why have different shapes? *Curr. Opin. Microbiol.*, 10(6):596–600.

[302] Young, K. D. (2010). Bacterial Shape: Two-Dimensional Questions and Possibilities. *NIH Public Access*, 64(51):223–240.

[303] Young, K. D. (2016). The bacterial cell wall takes centre stage. *Nature*, 537:622–623.

[304] Yurtsev, E. A., Chao, H. X., Datta, M. S., Artemova, T., and Gore, J. (2013). Bacterial cheating drives the population dynamics of cooperative antibiotic resistance plasmids. *Mol. Syst. Biol.*, 9(683):683.

[305] Zaritsky, A. (1975). On dimensional determination of rod-shaped bacteria. *J. Theor. Biol.*, 54(2):243–248.

[306] Zengler, K. and Palsson, B. O. (2012). A road map for the development of community systems (CoSy) biology. *Nat. Rev. Microbiol.*, 10(5):366–372.

Appendix A

Equations of motion for capsule cells

In this appendix, we provide further derivations pertaining to the model presented in Chapter 3, reproducing work presented in Reference [239]. Specifically, we show how capsule cells respond to an applied impulse, and how to describe the motion of points on a cell's surface. These results are respectively used to formulate cost functions for cell movement and overlap, and are subject to the assumptions stated in Section 3.3.

A.1 Motion of cells in response to impulse

Let the generalised position of a capsule cell be denoted $\tilde{\mathbf{p}} = (\mathbf{p}, \hat{\mathbf{a}}, l)^\top$, where $\mathbf{p}$, $\hat{\mathbf{a}}$ and l represent the cell's position, orientation and length respectively. Moving the capsule corresponds to a change to the general position $\Delta\tilde{\mathbf{p}} = (\Delta\mathbf{p}, \Delta\hat{\mathbf{a}}, \Delta l)^\top$ – i.e. some combination of translation $\Delta\mathbf{p}$, rotation $\Delta\hat{\mathbf{a}}$ and expansion Δl.

Firstly, we need to know how a capsule cell will change its position in response to forces $\mathbf{F}_{\text{lin}}$ and torques $\mathbf{F}_{\text{ang}}$, as well as compressive forces F_c acting along the cell axis. We can break this problem down into the following steps:

1. Relate the movement of an arbitrary point on the capsule's surface to the capsule's velocity;

2. Define the drag forces acting opposing this velocity;

3. Assuming applied forces are always balanced by drag, use Newton's laws to relate time integrals of forces (impulses) to changes in the cell's generalised position.

Consider an arbitrary point on a capsule's surface with position $\mathbf{w}$ relative to the cell's centroid. The velocity of that point $\mathbf{v_w}$ can be related to capsule translation, rotation and expansion velocities (respectively $\mathbf{v}_{\text{lin}}$, $\mathbf{v}_{\text{ang}}$ and v_{gro}), as

$$\mathbf{v_w} = \underbrace{\mathbf{v}_{\text{lin}}}_{\text{translation}} + \underbrace{\mathbf{v}_{\text{ang}} \times \mathbf{w}}_{\text{rotation}} + \underbrace{\left(\frac{1}{2}\frac{\hat{\mathbf{a}} \cdot \mathbf{w}}{\lambda}\hat{\mathbf{a}}\right) v_{\text{gro}}}_{\text{expansion}}, \tag{A.1}$$

where λ denotes the tip-to-tip cell length, $\lambda = l + 2r$, and where r is the capsule radius. To determine how the capsule will move when external forces act on it, we need to consider the drag forces which oppose its motion. As per our starting assumptions, we have:

- The linear drag force acting on an infinitesimal section dl of the cell's length is proportional to that section's velocity $\mathbf{v_w}$, such that

$$d\mathbf{F}_{\text{drag}} = -\zeta \mathbf{v_w} dl, \tag{A.2}$$

  where ζ is a fixed drag coefficient;

- Drag forces dominate cell inertia, so that applied forces are almost instantly counterbalanced by drag forces.

Resistance to translation

When a capsule moves through the medium with a linear velocity $\mathbf{v}_{\text{lin}}$, what drag forces does it experience? Substituting Equation (A.1) into Equation (A.2) gives

$$d\mathbf{F}_{\text{drag}} = -\zeta \left(\mathbf{v}_{\text{lin}} - w\hat{\mathbf{a}} \times \mathbf{v}_{\text{ang}} + \frac{1}{2}\frac{w}{\lambda}\hat{\mathbf{a}} v_{\text{gro}} \right) dl. \tag{A.3}$$

Here we have assumed that the length segments dl all lie in the average position—on the capsule's principal axis—such that $\mathbf{w} = w\hat{\mathbf{a}}$. The total drag force resisting linear movement can then be found by integrating Equation (A.3) over the length of the cell. Of the velocity terms in Equation (A.3), all but the first are odd in l, and so after cancellation we are left with

$$\mathbf{F}_{\text{drag}} = -\zeta \mathbf{v}_{\text{lin}} \int_{-\frac{\lambda}{2}}^{+\frac{\lambda}{2}} dl \tag{A.4}$$

$$= -\zeta \mathbf{v}_{\text{lin}} \lambda. \tag{A.5}$$

If an external linear force $\mathbf{F}_{\text{lin}}$ is applied to the cell, then using the assumption that applied forces are balanced by drag, we have

$$\mathbf{F}_{\text{lin}} = -\mathbf{F}_{\text{drag}} \tag{A.6}$$

$$= \zeta \mathbf{v}_{\text{lin}} \lambda. \tag{A.7}$$

Integrating this applied force over a time interval, $\Delta t = t_1 - t_0$, gives the applied linear impulse, $\mathbf{j}_{\text{lin}}$, and so

$$\mathbf{j}_{\text{lin}} = \int_{t_0}^{t_1} \mathbf{F}_{\text{lin}} dt = \zeta \lambda \int_{t_0}^{t_1} \mathbf{v}_{\text{lin}} dt = \zeta \lambda \Delta \mathbf{p}, \tag{A.8}$$

which rearranges to

$$\Delta \mathbf{p} = \frac{\mathbf{j}_{\text{lin}}}{\zeta \lambda}, \tag{A.9}$$

giving the linear displacement of the cell $\Delta \mathbf{p}$ in response to an applied impulse $\mathbf{j}_{\text{lin}}$.

Resistance to rotation

A similar approach can be used to evaluate the drag forces acting on a rotating cell, and thereby calculate its change in angular position following the application of an external force. Rudge *et al.* [239] showed that the change in a cell's orientation, $\Delta \hat{\mathbf{a}}$, in

response to an angular impulse $\mathbf{j}_{\text{ang}} = \int_{t_0}^{t_1} \mathbf{F}_{\text{ang}}\, dt$, is given by

$$\Delta\hat{\mathbf{a}} = \left(\frac{12\mathbf{P}\mathbf{j}_{\text{ang}}}{\zeta\lambda^3}\right). \tag{A.10}$$

Here, ζ and λ represent the drag coefficient and cell tip-to-tip length as before; $\mathbf{P}$ denotes a 3-by-3 projection matrix[1] defined as

$$\mathbf{P} = \begin{bmatrix} (1-\hat{a}_x^2) & -\hat{a}_x\hat{a}_y & -\hat{a}_x\hat{a}_z \\ -\hat{a}_x\hat{a}_y & (1-\hat{a}_y^2) & -\hat{a}_y\hat{a}_z \\ -\hat{a}_y\hat{a}_z & -\hat{a}_y\hat{a}_z & (1-\hat{a}_z^2) \end{bmatrix}, \tag{A.11}$$

where $\hat{a}_x$, $\hat{a}_y$ and $\hat{a}_z$ correspond to the x, y and z components of the cell axis vector $\hat{\mathbf{a}}$. We note that Equations (A.9) and (A.10) are in keeping with the equations of motion used in other rigid-body dynamics studies [88].

Resistance to expansion

Finally, we need to know how drag forces resist the cell's elongation in the viscous medium. Assuming that cell grows by uniform cell wall expansion along its length at velocity v_{gro}, we can write the compressive force resisting axial cell expansion, F_c, as

$$F_c = \frac{\zeta}{2}\left[\int_0^{+\frac{\lambda}{2}} \left(v_{\text{gro}}\frac{w}{\lambda}\right) dl - \int_{-\frac{\lambda}{2}}^{0} \left(v_{\text{gro}}\frac{w}{\lambda}\right) dl\right] = \frac{\zeta\lambda}{8} v_{\text{gro}}, \tag{A.12}$$

where w denotes position along the cell axis $\hat{\mathbf{a}}$ as before. In order to model the cell's resistance to compression due to its own structural and mechanical properties, we incorporate an additional drag term γ,

$$F_c = \left(\frac{\zeta\lambda}{8} + \gamma\right) v_{\text{gro}}. \tag{A.13}$$

[1] $\mathbf{P}$ serves to project vector $\mathbf{j}_{\text{ang}}$ onto the plane perpendicular to $\hat{\mathbf{a}}$, hence its name.

Integrating over time as before to give the growth impulse j_{gro}, we have

$$j_{\text{gro}} = \int_{t_0}^{t_1} F_c dt = \left(\frac{\zeta\lambda}{8} + \gamma\right) \int_{t_0}^{t_1} \frac{dl}{dt} dt = \left(\frac{\zeta\lambda}{8} + \gamma\right) \Delta l, \tag{A.14}$$

where above we have assumed that $\Delta l \ll l$ so that l can be taken out of the integral. If we also assume that the cell's internal resistance to expansion is much greater than the drag resistance, i.e. that $\frac{\zeta\lambda}{8} \ll \gamma$ (consistent with rigid body behaviour), then this expression further simplifies to

$$\Delta l = \frac{j_{\text{gro}}}{\gamma}. \tag{A.15}$$

Response to generalised impulse

Together, Equations (A.9), (A.10) and (A.15) describe the translation, rotation and contraction of a capsule i, in response to a generalised impulse $\tilde{\mathbf{j}}_i = \left(\mathbf{j}_{\text{lin},i}, \mathbf{j}_{\text{ang},i}, j_{\text{gro},i}\right)^\top$, under the drag conditions we have specified. For each i we can write

$$\Delta\tilde{\mathbf{p}}_i = \begin{bmatrix} \Delta\mathbf{p}_i \\ \Delta\hat{\mathbf{a}}_i \\ \Delta l_i \end{bmatrix} = \begin{bmatrix} \frac{\mathbf{j}_{\text{lin},i}}{\zeta\lambda_i} \\ \frac{12\mathbf{P}_i\mathbf{j}_{\text{ang},i}}{\zeta\lambda_i^3} \\ \frac{j_{\text{gro},i}}{\gamma} \end{bmatrix} = \begin{bmatrix} \frac{\mathbf{I}}{\lambda_i} & 0 & 0 \\ 0 & \frac{12\mathbf{P}_i}{\lambda_i^3} & 0 \\ 0 & 0 & \Gamma \end{bmatrix} \begin{bmatrix} \mathbf{j}_{\text{lin},i} \\ \mathbf{j}_{\text{ang},i} \\ j_{\text{gro},i} \end{bmatrix} = \mathbf{D}_i\,\tilde{\mathbf{j}}_i, \tag{A.16}$$

where $\mathbf{I}$ denotes a 3-by-3 unit matrix. Equation (A.16) therefore defines a linear relationship between changes in generalised cell coordinates $\Delta\tilde{\mathbf{p}}_i$ and applied generalised impulses $\tilde{\mathbf{j}}_i$. Note that above we have approximated the ratio ζ/γ with the parameter Γ, as defined in the starting assumptions.[2] By analogy, we can also write the movements for a system of n cells in the same way,

$$\Delta\tilde{\mathbf{p}} = \mathbf{D}\tilde{\mathbf{j}} \tag{A.17}$$

[2]Note that, in the current CellModeller code, ζ is set to unity by default – i.e. it is factored out of matrix $\mathbf{D}$, such that Γ alone controls the relative weight of the Δl elongation loss factor.

where now $\Delta\tilde{\mathbf{p}} = [\tilde{\mathbf{p}}_1, \ldots, \tilde{\mathbf{p}}_n]^\top$, $\tilde{\mathbf{j}} = [\tilde{\mathbf{j}}_1, \ldots, \tilde{\mathbf{j}}_n]^\top$, and where $\mathbf{D}$ is a $7n$-by-$7n$ block-diagonal matrix of the form

$$\mathbf{D} = \begin{bmatrix} \mathbf{D}_1 & \ldots & 0 \\ \vdots & \ddots & \vdots \\ 0 & \ldots & \mathbf{D}_n \end{bmatrix}. \tag{A.18}$$

A.2 Motion of points on cell surfaces

As stated in Section 3.3, we are interested not only in how cells move, but also in how much they overlap with one another. In order to describe how overlaps between cells vary with an applied impulse, we need to define a relationship between a cell's movement and the motion of a specific point on its surface. As shown in Chapter 3, the motion of these surface points can then be used to parameterise and minimise cell-cell and cell-surface overlap.

If a capsule undergoes a generalised movement $\Delta\tilde{\mathbf{p}} = (\Delta\mathbf{p}, \Delta\hat{\mathbf{a}}, \Delta l)^\top$, how will a point located on its surface move? Let us denote such a point $\mathbf{q}$ in the cell's reference frame and $\mathbf{q}_{\text{lab}}$ in the laboratory frame, such that $\mathbf{q}_{\text{lab}} = \mathbf{p} + \mathbf{q}$. If the cell's displacement is small, its axis vector $\hat{\mathbf{a}}$, projection matrix $\mathbf{P}$ and segment length l will remain approximately constant during the movement, and the displacement of the surface point $\Delta\mathbf{q}_{\text{lab}}$ can be written

$$\Delta\mathbf{q}_{\text{lab}} \approx \underbrace{\Delta\mathbf{p}}_{\text{translation}} + \underbrace{(\Delta\hat{\mathbf{a}} \times \mathbf{q})}_{\text{rotation}} + \underbrace{\frac{\Delta l}{\lambda}(\hat{\mathbf{a}} \cdot \mathbf{q})\mathbf{a}}_{\text{expansion}}. \tag{A.19}$$

Using Equation A.16, we can relate cell movement to an applied impulse $\tilde{\mathbf{j}}$. Substitution gives

$$\Delta\mathbf{q}_{\text{lab}} \approx \frac{1}{\zeta\lambda}\,\mathbf{j}_{\text{lin}} - \left(\mathbf{q} \times \frac{12\mathbf{P}}{\zeta\lambda^3}\,\mathbf{j}_{\text{ang}}\right) + \frac{(\hat{\mathbf{a}} \cdot \mathbf{q})\hat{\mathbf{a}}}{\gamma\lambda}\,j_{\text{gro}}. \tag{A.20}$$

We can also project this movement along any unit vector $\hat{\mathbf{n}}$, giving the displacement of the surface point along that vector, $\Delta q_{\hat{\mathbf{n}}}$, where

$$\Delta q_{\hat{\mathbf{n}}} = \hat{\mathbf{n}} \cdot \left(\frac{1}{\zeta\lambda}\, \mathbf{j}_{\text{lin}} - \left(\mathbf{q} \times \frac{12\mathbf{P}}{\zeta\lambda^3}\, \mathbf{j}_{\text{ang}} \right) + \frac{(\hat{\mathbf{a}} \cdot \mathbf{q})\hat{\mathbf{a}}}{\gamma\lambda}\, j_{\text{gro}} \right) \tag{A.21}$$

$$= \frac{1}{\zeta\lambda_i} \hat{\mathbf{n}} \cdot \mathbf{j}_{\text{lin},i} - \frac{12}{\zeta\lambda^3} (\hat{\mathbf{n}} \times \mathbf{q}) \cdot \mathbf{P}\, \mathbf{j}_{\text{ang}} + \frac{(\hat{\mathbf{n}} \cdot \hat{\mathbf{a}})(\hat{\mathbf{q}} \cdot \hat{\mathbf{a}})}{\gamma\lambda}\, j_{\text{gro}}. \tag{A.22}$$

By analogy with Equation (A.16), we can rewrite this in block matrix form as

$$\Delta q_{\hat{\mathbf{n}}} = \begin{bmatrix} \hat{\mathbf{n}}^\top & -(\hat{\mathbf{n}} \times \mathbf{q})^\top & \frac{(\hat{\mathbf{n}} \cdot \hat{\mathbf{a}})(\hat{\mathbf{q}} \cdot \hat{\mathbf{a}})}{\lambda} \end{bmatrix} \begin{bmatrix} \frac{\mathbf{I}}{\lambda} & 0 & 0 \\ 0 & \frac{12\mathbf{P}}{\lambda^3} & 0 \\ 0 & 0 & \Gamma \end{bmatrix} \begin{bmatrix} \mathbf{j}_{\text{lin}} \\ \mathbf{j}_{\text{ang}} \\ j_{\text{gro}} \end{bmatrix}, \tag{A.23}$$

or in shorthand, for a given cell i,

$$\Delta q_{\hat{\mathbf{n}}} = \left(\mathbf{C}_{\hat{\mathbf{n}},\mathbf{q},i} \mathbf{D}_i \right) \tilde{\mathbf{j}}_i. \tag{A.24}$$

In Equation A.24, the subscripts on vector $\mathbf{C}$ and matrix $\mathbf{D}$ are included as a reminder of the geometric elements on which each term depends. In brief, $\mathbf{C}_{\hat{\mathbf{n}},\mathbf{q},i}$ encapsulates geometric information on the relative orientations of the unit vector $\hat{\mathbf{n}}$, the cell axis vector $\hat{\mathbf{a}}$, and the position of the surface point $\mathbf{q}$ in the cell's reference frame. Meanwhile, matrix $\mathbf{D}_i$ summarises the cell's resistance to changes in generalised position, independent of its orientation.

Appendix B

Alternative formulation of cell mechanics scheme

In Chapter 3, we discussed the formulation of the Rudge model [239], which uses a constraint-based scheme to compute the movements of a system of overlapping capsule cells.

This scheme is written as an energy minimisation problem (Chapter 3, Equation (3.2)), used to compute a set of unknown impulses $\tilde{\mathbf{j}}$, whose application then restores the cell configuration to mechanical equilibrium. As shown in Equation (3.25), Rudge *et al*. formulated this minimisation problem in terms of an elastic potential energy function $E_{\text{overlap}} = |\mathbf{A}\tilde{\mathbf{j}} + \mathbf{d}|^2$, representing the energetic cost of cell-cell overlap, and an additional movement energy function E_{movement}, chosen as

$$E_{\text{movement}} = \frac{1}{\Delta t}\tilde{\mathbf{j}}^{\top}\mathbf{D}\tilde{\mathbf{j}}. \tag{B.1}$$

corresponding to the mechanical work expended in moving cells through the medium. Here, matrices $\mathbf{A}$, $\mathbf{D}$, overlap vector $\mathbf{d}$ and timestep Δt are as defined in Chapter 3. This addition energy term serves as a 'regularising' constraint, allowing a unique solution $\tilde{\mathbf{j}}$ to be found.

One criticism of this scheme is that there is no obvious physical reason why the quantity $E_{\text{overlap}} + E_{\text{movement}}$ (potential energy plus work) should be minimised. In this appendix, we present an alternative regularisation that instead minimises the overall potential energy of the system of cells, and which results in a similar linear system to that used in the original model. Overall, this demonstrates that there are alternative physical interpretations to the constraints used in the Rudge model.

B.1 Assumptions

Here we lay out some assumptions for our alternative formulation.

1. For simplicity, suppose that the cell configuration consists of a set of n elastic disks (instead of capsules) arranged on a plane xy, each having a fixed radius r, index i and stiffness K_A. Each cell has a position $\mathbf{p}_i = (p_x, p_y)^\top$ and two degrees of translational freedom, but cannot rotate or change in size.

2. Initially, cells are placed so that some of their boundaries overlap, producing a total of m overlaps denoted by distance d_k in each case. Overlap distances for the whole system are collected in a vector $\mathbf{d} = (d_1, \ldots, d_m)^\top$.

3. When a cell moves away from its initial position, it is subjected to two types of force:

   (a) A drag force proportional to its velocity $\mathbf{v}_i$, as in Appendix A, Equation (A.2);

   (b) A spring-like restoring force pulling it back to its original position, with stiffness coefficient $K_B \ll K_A$. This force could represent adhesion between a cell and an elastic EPS matrix.

4. Suppose that the cells are moved by the application of a set of n linear impulses $\mathbf{j} = (\mathbf{j}_1, \ldots, \mathbf{j}_n)$, where $\mathbf{j}_i = (j_x, j_y)^\top$. Find $\mathbf{j}$ such that the total potential energy of the system is minimised.

We make Assumption 1 for the sake of brevity; Assumptions 2-4 make the problem equivalent to that discussed in Chapter 3, apart from the addition of the elastic restoring force (Assumption 3.b).

B.2 Derivation

From our starting assumptions, there are two contributions to the total potential energy of the system: elastic potential energy from cell-cell overlap, and elastic potential energy from the restoring forces. Therefore we can write the total potential energy U_{total} as

$$U_{\text{total}} = U_{\text{overlap}} + U_{\text{movement}}. \tag{B.2}$$

First, consider the movement potential U_{movement}. Application of the impulse set $\mathbf{j}$ will change cell positions by $\Delta\mathbf{p}$, adding to the potential energy by

$$U_{\text{movement}} = \frac{K_B}{2}|\Delta\mathbf{p}|^2 \tag{B.3}$$

Assumption 3.a implies that we can write $\Delta\mathbf{p}_i = \mathbf{D}_i\mathbf{j}_i$ by analogy to Equation (A.16) in Appendix A. The terms of matrix $\mathbf{D}_i$ depend on the nature of the drag force in 3.a: for instance, if we assume drag $\mathbf{F}_{\text{drag}}$ to be given by Stokes' law, $\mathbf{F}_{\text{drag},i} = -6\pi\eta r\mathbf{v}_i$, with $\mathbf{v}_i$ the cell's velocity vector, then $\mathbf{D}_i = \mathbf{I}/6\pi\eta r$, with $\mathbf{I}$ a 2-by-2 identity matrix. For a set of n cells, it follows that

$$\Delta\mathbf{p} = \mathbf{D}\mathbf{j}, \tag{B.4}$$

and so we can rewrite Equation (B.3) as

$$U_{\text{movement}} = \frac{K_B}{2}|\mathbf{Dj}|^2. \tag{B.5}$$

Next, consider the energy term U_{overlap} in Equation (B.2). When cells move, the degree to which they overlap will change – let $\mathbf{d}_{\text{res}}$ denote the remaining overlap following impulse application. If cells are elastic as per Assumption 1, then we have

$$U_{\text{overlap}} = \frac{K_A}{2}|\mathbf{d}_{\text{res}}|^2 \tag{B.6}$$

as with Equation (B.3). To relate $\mathbf{d}_{\text{res}}$ to impulses $\mathbf{j}$, we use the result

$$\mathbf{d}_{\text{res}} = \mathbf{Aj} + \mathbf{d} \tag{B.7}$$

by analogy with Equation (3.23) in Chapter 3, where $\mathbf{d}$ is the vector of initial overlaps as per Assumption 2, and where $\mathbf{A}$ is an m-by-$2n$ matrix summarising geometric information on the relative orientations of cells in contact. Substitution of Equation (B.7) into Equation (B.6) yields

$$\frac{K_A}{2}|\mathbf{Aj} + \mathbf{d}|^2, \tag{B.8}$$

which has the same form as Equation (3.24) in Chapter 3. Finally, combining Equations (B.5) and (B.8) gives

$$U_{\text{total}} = U_{overlap} + U_{movement} \tag{B.9}$$

$$= \frac{K_A}{2}|\mathbf{Aj} + \mathbf{d}|^2 + \frac{K_B}{2}|\mathbf{Dj}|^2 \tag{B.10}$$

From our starting assumptions, we choose $\mathbf{j}$ such that

$$\frac{dU_{\text{tot}}}{d\mathbf{j}} = 0, \tag{B.11}$$

which implies

$$\frac{K_A}{2}\frac{d}{d\mathbf{j}}\left(|\mathbf{A}\mathbf{j}+\mathbf{d}|^2\right)+\frac{K_B}{2}\frac{d}{d\mathbf{j}}\left(|\mathbf{D}\mathbf{j}|^2\right)=0. \tag{B.12}$$

Multiplying out the left-hand derivative in equation (B.12), we get

$$\begin{aligned}
\frac{d}{d\mathbf{j}}\left(|\mathbf{A}\mathbf{j}+\mathbf{d}|^2\right) &= \frac{d}{d\mathbf{j}}\left((\mathbf{A}\mathbf{j}+\mathbf{d})^\top(\mathbf{A}\mathbf{j}+\mathbf{d})\right) && \text{(B.13)}\\
&= \frac{d}{d\mathbf{j}}\left(\mathbf{j}^\top\mathbf{A}^\top\mathbf{A}\mathbf{j}\right)+\frac{d}{d\mathbf{j}}\left(\mathbf{j}\mathbf{A}^\top\mathbf{d}\right)+\frac{d}{d\mathbf{j}}\left(\mathbf{d}^\top\mathbf{A}\mathbf{j}\right)+\frac{d}{d\mathbf{j}}\left(\mathbf{d}^\top\mathbf{d}\right) && \text{(B.14)}\\
&= 2\mathbf{A}^\top\mathbf{A}\mathbf{j}+\mathbf{A}^\top\mathbf{d}+\mathbf{A}^\top\mathbf{d}+0 && \text{(B.15)}\\
&= 2\left(\mathbf{A}^\top\mathbf{A}\mathbf{j}+\mathbf{A}^\top\mathbf{d}\right). && \text{(B.16)}
\end{aligned}$$

Likewise, for the right-hand derivative, we obtain

$$\begin{aligned}
\frac{d}{d\mathbf{j}}\left(|\mathbf{D}\mathbf{j}|^2\right) &= \frac{d}{d\mathbf{j}}\left(\mathbf{j}^\top\mathbf{D}^\top\mathbf{D}\mathbf{j}\right) && \text{(B.17)}\\
&= \frac{d}{d\mathbf{j}}\left(\mathbf{j}^\top\mathbf{D}^2\mathbf{j}\right) && \text{(B.18)}\\
&= 2\mathbf{D}^2\mathbf{j}, && \text{(B.19)}
\end{aligned}$$

where above we have used $\mathbf{D}^\top=\mathbf{D}$ to write $\mathbf{D}^\top\mathbf{D}=\mathbf{D}^2$. Substituting Equations (B.16) and (B.19) into (B.12) gives

$$\begin{aligned}
K_A\left(\mathbf{A}^\top\mathbf{A}\mathbf{j}+\mathbf{A}^\top\mathbf{d}\right)+K_B\left(\mathbf{D}^2\mathbf{j}\right)=0, \quad \text{or} && \text{(B.20)}\\
\left(\mathbf{A}^\top\mathbf{A}+\frac{K_B}{K_A}\mathbf{D}^2\right)\mathbf{j}=-\mathbf{A}^\top\mathbf{d}, && \text{(B.21)}
\end{aligned}$$

which is similar to Equation (3.31) in Chapter 3 except for the term in $\mathbf{D}^2$. The spring constant ratio K_B/K_A performs a similar role to $\Gamma/\Delta t$ in Equation (3.31), acting as a weighting coefficient to the regularising drag matrix $\mathbf{D}^2$.